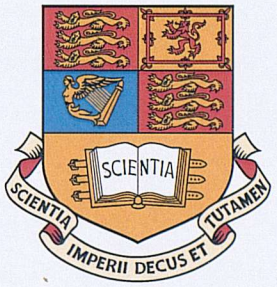
# The Fluid Dynamics of the Helicopter Vortex Ring Phenomenon

by

Gary A. Ahlin




Department of Aeronautics
Imperial College of Science, Technology and Medicine
Prince Consort Road
London SW7 2BY

This thesis is submitted for the degree of Doctor of Philosophy of the University of London

2007

# Abstract

Computational simulations of rotors in axial descent were conducted to obtain new insight into the complex flow physics of the dangerous helicopter flight phenomenon known as the vortex ring state. The simulations were performed using Brown's Vorticity Transport Model which provides a comprehensive description of the aerodynamics of rotorcraft.

The detailed vortex kinematics of the wake of a rotor in axial flight are exposed. Initial, small-scale, 'pairing' of sections of the helical vortex system are shown to lead to large-scale re-orientation of vortex filaments out of a plane that is parallel to the rotor disc. This is shown to be the key mechanism that leads to the disorganisation of the wake. Vortex re-orientation plays an important role in truncating the wake and in precipitating the onset of the vortex ring state. The onset of the vortex ring state marks a significant change in the dominant kinematics of the wake as the vortex kinematics inherent to the helical wake of a rotor, in hover or very low speed descent, switch to approximate the self-induced motions of a group of coaxial vortex rings. It is demonstrated that the velocity field of a hovering rotor has the same toroidal topology as that associated with the vortex ring state.

Increasing the amount by which rotor blades are twisted is shown to postpone both the onset and the cessation of the vortex ring state to higher descent speeds. The root-vortex system is found to play a crucial role in the global dynamics of the rotor wake.

The coupling of the rotor aerodynamics to the local velocity field when a rotor descends with fixed collective pitch is shown to be fundamentally different to that of a descending rotor trimmed to produce nominally constant thrust. A new method of scaling the descent speed and rotor performance parameters is shown to improve the reliability of comparisons of the performance of descending rotors that were operated differently.

# Declaration

I declare that all of the work that is contained within this thesis has been undertaken by the author

Signed.....

Date.....

# Acknowledegements

Firstly, I would like to thank my supervisor, Professor Richard Brown, for his dedication, enthusiasm and expert guidance, without which my research activities would not have been so rewarding. I would also like to thank all of my group mates, who together, made my research experience fun and enjoyable.

I would also like to thank my friends at Clayponds, Imperial College's hall for post-graduate students, where I lived whilst conducting my research, for their support, for their humour, and for their friendship. Without them my time at Imperial would not be so memorable.

Finally, I would like to express my enormous gratitude to my parents, my siblings and also to my girlfriend Pan, for their unyielding support and inexhaustible patience during my research and especially during the writing of this thesis. Indeed, Pan deserves special thanks for keeping me sane and for making my life fun during the sometimes frustrating days, whilst writing this thesis.

This research was partially funded by a U.K. Engineering and Physical Sciences Research Council Grant (No. GR/R/90116/01).

# Contents

**Abstract** 1

**Acknowledgements** 3

**Table of Contents** 4

**List of Figures** 7

**List of Tables** 19

**Nomenclature** 20

**1 Introduction** 23

1.1 An Overview of The Vortex-Ring Phenomenon . . . . . 23

1.2 Hypotheses . . . . . 33

1.3 Synopsis . . . . . 34

1.4 Publications . . . . . 36

**2 CFD Simulations of the Vortex Ring Phenomenon: A Description of the Model** 38

2.1 Introduction . . . . . 38

2.2 The Governing Equations . . . . . 39

2.3 The Vorticity Transport Model . . . . . 41

2.3.1 Numerical Implementation of The Rotor Wake Model . . . . . 42

2.3.1.1 The Computational Grid . . . . . 43

2.3.1.2 Discretisation of the Governing Equations . . . . . 45

2.3.1.3 Flow Variables . . . . . 46

2.3.1.4 The Advection Routine . . . . . 46
2.3.1.5 Computing the Velocity Field . . . . . 49
2.3.1.6 The Rotor Aerodynamic Model . . . . . 53
2.3.1.7 The Rotor Dynamic Model . . . . . 56
2.4 Model Validation . . . . . 58
2.4.1 Experimental Setup . . . . . 63
2.4.2 Numerical Simulation . . . . . 63
2.4.3 Results . . . . . 64
2.5 Dependence on Computational Resolution . . . . . 69
2.5.1 Grid Dependence Test . . . . . 71
2.6 Summary . . . . . 82
2.7 Conventions and Data Processing Methods . . . . . 84
2.7.1 Coordinate System and Conventions . . . . . 84
2.7.2 Data Processing Methods . . . . . 84
2.7.2.1 Data filtering . . . . . 84
2.7.2.2 Calculation of vorticity locus plots . . . . . 85

**3 Vortex Kinematics of the Wake of a Descending Rotor 89**
3.1 Introduction . . . . . 89
3.2 High Resolution Wake Simulations . . . . . 95
3.2.1 Simplification of the rotor model . . . . . 95
3.3 Entry into VRS from the Windmill Brake State . . . . . 96
3.4 Entry into VRS from Hover . . . . . 112
3.5 Discussion . . . . . 126
3.6 Summary . . . . . 128

**4 Effects of Vortex Kinematics on the Velocity Field 131**
4.1 Introduction . . . . . 131
4.2 Effects of Wake Geometry on Velocity Field Topology . . . . . 132
4.3 Wake Geometry and Measures of Rotor Performance . . . . . 145
4.4 The Aerodynamic Origin of Thrust-Settling . . . . . 157
4.5 Effects of Acceleration on the Rotor and its Wake . . . . . 169
4.5.1 Discussion . . . . . 187

4.6 Summary . . . . . 193

**5 Influence of Geometric Blade-Twist and Blade Stall on the Behaviour of the VRS** **196**

5.1 Introduction . . . . . 196

5.2 Blade Twist Effects on Rotor Aerodynamics in the VRS . . . . . 199

5.2.1 Aims of The Investigation . . . . . 204

5.2.2 Description of the Numerical Experiment . . . . . 205

5.2.3 Results . . . . . 206

5.3 Comments on the effects of blade-stall on the VRS . . . . . 243

5.4 Summary . . . . . 251

**6 Effect of the Mode of Operation of the Rotor on VRS Behaviour** **256**

6.1 Introduction . . . . . 256

6.2 Results . . . . . 257

6.3 Discussion . . . . . 272

6.4 Summary . . . . . 284

**7 Conclusions** **287**

**Bibliography** **298**

# List of Figures


1.1 *Image of a rotor in the VRS taken from the work of Drees and Hendal [14]. The flow field is realised by an injection of smoke particles from a rake just beneath the fuselage model. The original image colours have been inverted to improve clarity.* . . . . . 28

2.1 *2D view of 3D computational grid. Image shows the arrangement of nested computational grids with varing cell size,* $\Delta_0$. . . . . 44

2.2 *Overlapping of adjacent grid levels required to maintain monotonicity and conservativeness of the advection scheme at grid interfaces.* . . . . . 45

2.3 *Stencil for calculating flux of vorticity across cell faces.* . . . . . 47

2.4 *Velocity field induced by a Biot-Savart kernel (vortex singularity) and by the Rosenhead-Moore kernal (uniform distribution of vorticity in a cell of width* $\Delta$*).* . . . . . 49

2.5 *Schematic of cluster-cluster interaction approximated by multipole expansion.* 50

2.6 *The velocity field of cluster i is decomposed into the near-field (light grey), the intermediate-field (dark grey) and the far field (white).* . . . . . 52

2.7 *Model of blade aerodynamics and inner vortex lattice.* . . . . . 54

2.8 *Mean thrust vs. descent rate. The graph shows a comparison between the results of a VTM simulation and Gao's experimental data.* . . . . . 65

2.9 *Standard deviation of thrust fluctuations vs. descent rate. The graph shows a comparison between the results of a VTM simulation and Gao's experimental data.* . . . . . 66

2.10 *Calculated mean inflow vs. descent rate: VTM simulated data.* . . . . . 67

2.11 *Mean inflow vs. descent rate: Data from experiments of Washizu et al.* . . . . 68

2.12 *Comparison of the effect of computational cell size, $\Delta_0$, on the thrust coefficient produced by a rotor in descending flight. The thrust signal has been filtered.* . . . . . 72
2.13 *Comparison of the effect of computational cell size, $\Delta_0$, on the standard deviation about the mean thrust of the fluctuations of thrust experienced by a rotor in descending flight.* . . . . . 73
2.14 *Comparison of the effect of computational cell size, $\Delta_0$, on the rotor torque coefficient produced by a rotor in descending flight. The instantaneous profile torque $C_{Q_P}$ has been removed from the data. The torque signal has been filtered.* . . . . . 74
2.15 *From left to right: Vorticity contour plots for a decaying wake after time $\tau = \pi$, $\tau = 18\pi$ and $\tau = 37\pi$ post rotor stoppage. Row (a) shows vorticity contours of the wake where $\Delta_0 = 0.1R$, row (b) $\Delta_0 = 0.05R$, and row (c) $\Delta_0 = 0.05R$. Each snapshot shows the main body of the vortex wake as it convects downstream (positive Z(R)).* . . . . . 76
2.16 *Two-dimensional energy spectra of the lateral velocity component, $v'(\mathbf{x}, t)$. Image (a) shows the energy spectra after time $\tau = \pi$, and image (b) shows the energy spectra after time $\tau = 37\pi$, post rotor stoppage. (Dotted line), $\Delta_0 = 0.1R$; (Dashed line), $\Delta_0 = 0.05R$; (Solid line), $\Delta_0 = 0.025R$.* . . . . . 79
2.17 *Turbulent kinetic energy, k, in the near rotor flow when the rotor was flying in the VRS.* . . . . . 81
2.18 *Two-dimensional energy spectra from a VRS flow, at six different in times in the simulation. In graph (a) rev = 73 (solid line), rev = 78 (dashed line) and rev = 85.5 (dotted line). In graph (b) rev = 164.5 (solid line), rev = 167.5 (dashed line), rev = 181.5 (dotted line). The vertical line denoted as $\kappa \approx R$ marks the wave number that corresponds to a flow scale with a length similar to the rotor radius.* . . . . . 82
2.19 *Schematic representation of the coordinate system of the rotor and the sign conventions used to describe the flow field and rotor trajectories throughout this thesis.* . . . . . 84
2.20 *Image of locus plot of vorticity showing features resulting from the calculation of the locus plot. The image is of a wake of a descending rotor.* . . . . 86

3.1 *Interaction between a pair of axially aligned vortex rings showing their mutually-induced 'leap-frogging' motion (schematic).* . . . . . 90
3.2 *A helix becoming entangled by the action of 'pairing' of its turns (schematic).* 91
3.3 *Schematic of an element of a vortex filament showing swirl and re-orientation axes.* . . . . . 93
3.4 *Schematic of elements of long parallel vortex filaments. Image (a) shows the unperturbed condition and image (b) shows an another instance where there is small perturbation in the lower filament.* . . . . . 94
3.5 *The wake of the simplified rotor in WBS. (Iso-surface of vorticity magnitude.)* 97
3.6 *The wake of the simplified rotor entering the VRS from the WBS. (Iso-surface of vorticity magnitude.)* . . . . . 97
3.7 *The wake of the simplified rotor deep in VRS. (Iso-surface of vorticity magnitude.)* . . . . . 98
3.8 *Snapshot of the wake structure within high speed VRS showing the disruption to the wake as a result of large-amplitude re-orientation of the tip vortex. (Iso-surface of vorticity magnitude.)* . . . . . 100
3.9 *The early stages of vortex re-orientation showing the development of a large-scale 'hair-pin' structure in the tip vortex. (Iso-surface of vorticity magnitude.)* . . . . . 101
3.10 *A view from beneath the rotor showing how re-orientated vortex filaments are wrapped around the core of the ring-like VRS base flow. (Iso-surface of vorticity magnitude.)* . . . . . 101
3.11 *Vorticity field of the wake in VRS, decomposed into components normal and parallel to the disc plane.* . . . . . 103
3.12 *Paths followed by vorticity (a) in the ejection stream and (b) originating at the blade root.* . . . . . 104
3.13 *Particle paths through the time-averaged flow generated by a rotor in high-speed VRS ($\bar{\mu}_z = 1.0$, VTM simulation).* . . . . . 104
3.14 *2D and 3D images of the rotor wake in VRS showing the initiation of a large-scale vortex 'breakaway'.* . . . . . 106
3.15 *Pictorial summary of wake structure in high-speed VRS.* . . . . . 107

3.16 *Variation of the contribution of each vortex component to the overall vorticity in the flow field.* . . . . . 108
3.17 *Statistical spread of vortex filament orientations with respect to the horizontal in WBS and high-speed VRS.* . . . . . 110
3.18 *Example of the non-linear vortex pairing/re-orientation mode occurring in the wake of a hovering rotor.* . . . . . 113
3.19 *Vorticity field of the rotor wake in hover, decomposed into components normal and parallel to the disc plane.* . . . . . 115
3.20 *Vorticity field of the rotor wake in slow descent ($\bar{\mu}_z = 0.2$), decomposed into components normal and parallel to the disc plane.* . . . . . 117
3.21 *Effect on newly generated tip-vortex filaments of an encounter with an upwardly convecting vortex 'fragment'.* . . . . . 119
3.22 *Radial distribution of blade-normal velocity during one rotor revolution. The rotor is descending at a speed of $\bar{\mu}_z = 0.44$. The dark areas represent regions of upward flow.* . . . . . 120
3.23 *Vortical structure of the rotor wake in low-speed VRS. (Iso-surface of vorticity magnitude.)* . . . . . 121
3.24 *Statistical spread of vortex filament orientations with respect to the horizontal in hover and low-speed VRS. Vorticity threshold $\omega/\Omega = 0.5$ (i.e. Survey includes only the strong vorticity in the flow).* . . . . . 122
3.25 *Evolution of tip-vortices in low-speed VRS. (Contour plot of vorticity on a 2D plane through the rotor hub.)* . . . . . 124

4.1 *Iso-surface of the the instantaneous vorticity field (right) of a hovering, single-bladed rotor. The velocity field induced by the vorticity field is shown (left) as contours of downward flow velocity.* . . . . . 134
4.2 *Distribution of instantaneous downward flow velocity along the rotor hub axis. The velocity data has been spatially averaged in the direction parallel to the disc at discrete vertical stations along the wake.* . . . . . 135
4.3 *Normalised integrals of the total vorticity magnitude, $|\widetilde{\omega}|$, and the magnitude of the vertically aligned vorticity $|\widetilde{\omega}_z|$ in the instantaneous wake. The parameter values have been scaled by the magnitude of the total vorticity generated during one rotor revolution.* . . . . . 136

4.4 *2D plots of mean contours of vorticity and the associated induced downward flow in the velocity field. The mean fields were constructed from 120 snapshots over 120 rotor revolutions. The velocity field has been scaled with the mean inflow at hover,* $\lambda_h$. . . . . 138
4.5 *Particle paths in the mean flow field of a hovering rotor. The associated vorticity field is shown as contours beneath the particle paths.* . . . . . 140
4.6 *Particle paths in the mean flow field of a rotor flying steadily at various low descent speeds. The associated vorticity field is shown as contours beneath the particle paths.* . . . . . 142
4.7 *Particle paths in the mean flow field of a rotor flying steadily at various high descent speeds. The associated vorticity field is shown as contours beneath the particle paths.* . . . . . 143
4.8 *Particle paths in the mean flow field of a rotor flying steadily in ascent (left) and in the WBS (right). The associated vorticity field is shown as contours beneath the particle paths.* . . . . . 144
4.9 *Measures of the performance of a rotor in a linearly accelerating axial descent. Measures shown are calculated mean rotor inflow, rotor torque, thrust and standard deviation about the mean thrust of the thrust fluctuations.* . . 146
4.10 *Isosurfaces of vorticity showing the instantaneous geometry of a rotor wake at various descent speeds.* . . . . . 148
4.11 *Contours of the instantaneous induced (left) and induced plus free stream* $(\lambda_i + \mu_z)$, *(right), velocity fields corresponding to markers i to iii. Net velocity fields also show the corresponding velocity vectors on top of the contours.* . . . . . 149
4.12 *Contours of the instantaneous induced (left) and induced plus free stream* $(\lambda_i + \mu_z)$, *(right), velocity fields corresponding to markers iv to vi. Net velocity fields also show the corresponding velocity vectors on top of the contours.* . . . . . 150
4.13 *Isosurfaces of vorticity showing the instantaneous geometry of a rotor wake corresponding to markers vii and viii.* . . . . . 151

4.14 *Contours of the instantaneous induced (left) and induced plus free stream* $(\lambda_i + \mu_z)$*, (right), velocity fields corresponding to markers vii and viii. Net velocity fields also show the corresponding velocity vectors on top of the contours.* . . . . . 152

4.15 *Filtered and raw* $C_T$ *signal as rotor descends.* $C_{T_h}$ *is the rotor thrust coefficient generated in steady hover. The descent rate is scaled by the inflow calculated from* $C_{T_h}$*. (Constant* $\theta_0$ *case.)* . . . . . 158

4.16 *Various representations of wake geometry during hover: Top image: Locus plot; Image second from top: RMS of fluctuations; Bottom two images: instantaneous contours of vorticity. The highest RMS value (black contours) is 10 times higher than the weakest value (contours in lightest hue of grey.* . 160

4.17 *Two dimensional contour plots of the locus of vorticity and RMS of vorticity fluctuations both constructed from 25 rotor revolutions during various intervals of descent speed. Also shown are snapshots of the the corresponding instantaneous vorticity field. The contour plane passes through the hub of the rotor. The highest RMS value (black contours) is 10 times higher than the weakest value (contours in lightest hue of grey).* . . . . . 162

4.18 *Sectional blade loading vs. descent rate scaled by mean thrust at hover, at various blade stations. Blade loading scaled with mean loading,* $C_B/\sigma$*. (Constant* $\theta_0$*).* . . . . . 163

4.19 *On-blade vertical flow velocity (scaled with the theoretical mean inflow at hover) vs. descent rate scaled by mean thrust at hover, at various blade stations. (Constant* $\theta_0$*).* . . . . . 164

4.20 *Estimated rotor torque (less constant profile torque* $C_{Q_0}$*) vs. descent rate scaled by mean thrust at hover. (Constant* $C_T$*).* . . . . . 165

4.21 *Blade loading vs. descent rate scaled by mean thrust at hover, at various blade stations. Blade loading scaled with mean loading,* $C_B/\sigma$ *(Constant* $C_T$*).*165

4.22 *On-blade vertical flow velocity (scaled with the theoretical mean inflow at hover) vs. descent rate scaled by mean thrust at hover, at various blade stations. (Constant* $C_T$*)* . . . . . 166

4.23 *Comparison of wake intensity, $\Sigma$, above and below the rotor vs. descent rate scaled by mean thrust at hover. Wake intensities have been scaled with the wake intensity in the union of the two domains under hovering conditions, $\Sigma_h$. (Constant $\theta_0$)* . . . . . 167
4.24 *Comparison of wake intensity, $\Sigma$, inboard and outboard of the rotor vs. descent rate scaled by mean thrust at hover. Wake intensities have been scaled with the wake intensity in the union of the two domains under hovering conditions, $\Sigma_h$. (Constant $\theta_0$)* . . . . . 168
4.25 *2D vorticity contour plots of the wake geometries during and just after the thrust-settling phenomenon. (Constant $\theta_0$)* . . . . . 169
4.26 *Analytical boundary for VRS onset of Newman* et al. *The boundary is compared with experimental VRS data from the literature. Image taken from Ref.[8].* . . . . . 170
4.27 *Comparison between the thrust histories of four descent acceleration cases, vs. descent speed scaled by the mean inflow of a rotor in hover. Thrust was controlled to be nominally constant at $C_T = 0.00724$. The thrust traces have been artificially separated in the vertical axis for clarity.* . . . . . 175
4.28 *Comparison of standard deviation of the thrust fluctuation histories, $S_{C_T}$, of four descent acceleration cases, vs. descent speed scaled by the mean inflow of a rotor in hover.* . . . . . 177
4.29 *Comparison of the variation of the normalised induced rotor power, $C_P/C_{P_h}$, of four descent acceleration cases, vs. descent speed scaled by the mean inflow of a rotor in hover.* . . . . . 178
4.30 *3D Iso-surfaces and 2D contour plots of locus plots of vorticity in the wake of a rotor undergoing accelerated trajectories. The mean wake from four linear accelerations are shown during four intervals of descent speed. A section of the foregrounds of some iso-surface images have been blanked to provide a view of the inner wake structure. The iso-surface and contour levels are the same in each image.* . . . . . 180
4.31 *Variation of contribution to the total vorticity of the individual vector components of vorticity. Data from the default case, $\dot{\bar{\mu}}_z = \dot{\bar{\mu}}_d$.* . . . . . 182

4.32 *Variation of contribution to the total vorticity of the vertically aligned component of vorticity. Data from all four acceleration cases.* . . . . . 183

4.33 *Visualisations of the vortical rotor wake as the rotor descends with increasing speed over a period of* 20 *revolutions. Two aceleration cases are shown:* $\dot{\bar{\mu}}_z = 2\dot{\bar{\mu}}_d$ *and* $\dot{\bar{\mu}}_z = 8\dot{\bar{\mu}}_d$. *The start points of the two 20 revolution intervals are necessarily different.* . . . . . 186

4.34 *Figure shows mean* $C_P/C_{P_h}$ *vs.* $\mu_z^*$ *from the four acceleration cases. The upper branch of the theoretical induced power curves has been left on this graph to provide an indication of the scale of the deviation from the trend shown in the previous figure of induced power, Fig 4.29.* . . . . . 188

5.1 *Graphs show the variation in the strength, per unit length, of the trailed vortex system caused by variation in blade twist* . . . . . 207

5.2 *Graph shows spanwise distribution of inflow velocity on rotor blades of varying twist rates during hover.* . . . . . 208

5.3 *Mean thrust history of rotors descending through VRS to WBS from hover. Averaging window has width of 1 rev.* . . . . . 209

5.4 *Standard deviation about the mean, of thrust fluctuations as a percentage of the mean thrust at hover, of rotors descending through VRS to WBS from hover. Averaging window has width of 4 revs.* . . . . . 210

5.5 *Normalised total torque,* $(C_Q - C_{Q_p})/C_{Q_h}$, *versus* $\bar{\mu}_z$ *for three rotors each with different blade twist to the other. Width of averaging window is 1 rev.* . 213

5.6 *Locus plots of the geometry of the vorticity field and 2D RMS contour plots of the vorticity field for the three rotors. The 2D plots run vertically through the rotor hub. Plots were computed from 14 snap-shots from 14 contiguous rotor revolutions corresponding to the speed interval:* $0.2 \leq \bar{\mu}_z \leq 0.3$. . . . . 214

5.7 *Locus plots of the geometry of the vorticity field and RMS contour plots of the vorticity field for the three rotors. The 2D RMS plots run vertically through the rotor hub. Plots were computed from 14 snap-shots from 14 contiguous rotor revolutions corresponding to the speed interval:* $0.4 \leq \bar{\mu}_z \leq 0.5$. . . . . 217

5.8 *Locus plots of the geometry of the vorticity field and RMS contour plots of the vorticity field for the three rotors. The 2D plots run vertically through the rotor hub. Plots were computed from 14 snap-shots from 14 contiguous rotor revolutions corresponding to the speed interval:* $0.5 \leq \bar{\mu}_z \leq 0.6$. . . . . 218

5.9 *Iso-surfaces of the instantaneous geometry of the vorticity field produced by a rotor with blade twist of* $\theta_{tw} = -15°$. *The figure shows the convection of the root and tip vortex systems.* . . . . . 220

5.10 *Total speed,* $(\lambda_i + \mu_z)$ *of the flow normal to the rotor disc at several stations along the blade. The data is taken from rotors with twist of* $\theta_{tw} = -15°$, $-25°$ *and* $-35°$. . . . . 221

5.11 *Mean velocity field produced by rotors with blade twist of* $\theta_{tw} = -15°$, $\theta_{tw} = -25°$ *and* $\theta_{tw} = -35°$. *Mean field arises during the speed interval* $0.2 \leq \bar{\mu}_z \leq 0.3$ *(14 rotor revolutions). Direction of free-stream is upwards.* . . . . 226

5.12 *Profiles of mean flow velocity in a plane passing vertically through the rotor hub, arising over descent speed interval* $0.2 \leq \bar{\mu}_z \leq 0.3$. *Direction of free-stream is upwards.* . . . . . 228

5.13 *Mean velocity field produced by rotors with blade twist of* $\theta_{tw} = -15°$, $\theta_{tw} = -25°$ *and* $\theta_{tw} = -35°$. *Mean field arises during the speed interval* $0.4 \leq \bar{\mu}_z \leq 0.5$ *(14 rotor revolutions). Direction of free-stream is upwards.* . . . . 229

5.14 *Profiles of mean flow velocity in a plane passing vertically through the rotor hub, arising over descent speed interval* $0.4 \leq \bar{\mu}_z \leq 0.5$. *Direction of free-stream is upwards.* . . . . . 230

5.15 *Iso-surfaces of the locus of vorticity in rotor wakes in high-speed VRS. Rotors featured have blade twist of* $\theta_{tw} = -15°$ *and* $\theta_{tw} = -35°$. The darker the surface, the stronger the vorticity. . . . . 233

5.16 *Distribution of net speed of vertical flow,* $\lambda_i(r) + \mu_z$, *over rotor blades with different levels of twist. Negative velocities are upward.* . . . . . 235

5.17 *Variation with normalised descent speed of the strengths of the blade tip and root vortices that are trailed from a rotor with blade twist of* $\theta_{tw} = -15°$ *and a rotor with blade twist of* $\theta_{tw} = -35°$. *The data has been filtered using a moving averaging window with a width of 10 rotor revolutions.* . . . . . 237

5.18 *Profiles of mean flow velocity in a plane passing vertically through the rotor hub, arising over descent speed interval of* $1.3 \leq \bar{\mu}_z \leq 1.4$, *for rotor with blade twists of* $\theta_{tw} = -15°$ *and* $\theta_{tw} = -35°$. . . . . 239

5.19 *Profiles of mean flow velocity in a plane passing vertically through the rotor hub, arising over descent speed interval of* $1.5 \leq \bar{\mu}_z \leq 1.6$, *for rotor with blade twists of* $\theta_{tw} = -15°$ *and* $\theta_{tw} = -35°$. . . . . 240

5.20 $C_L - \alpha$ *relationship of a high aspect ratio* ($AR = 30$) *wing without viscous stall representation.* . . . . . 243

5.21 *Spanwise distribution of effective angle of attack vs. normalised descent rate for the rotor comprising blades with* $-15°$ *of twist. Denoted stall characteristics assumed to be those of NACA 0012 aerofoil:* $C_{L_{max}} \approx 1.6$, $\alpha_{e_{stall}} \approx 16°$ . . . . . 247

5.22 *Spanwise distribution of effective angle of attack vs. normalised descent rate for the rotor comprising blades with* $-25°$ *of twist. Denoted stall characteristics assumed to be those of NACA 0012 aerofoil:* $C_{L_{max}} \approx 1.6$, $\alpha_{e_{stall}} \approx 16°$. 248

5.23 *Spanwise distribution of effective angle of attack vs. normalised descent rate for the rotor comprising blades with* $-35°$ *of twist. Denoted stall characteristics assumed to be those of NACA 0012 aerofoil:* $C_{L_{max}} \approx 1.6$, $\alpha_{e_{stall}} \approx 16°$. 249

6.1 *Thrust coefficient, normalised by thrust coefficient arising in hover, from simulations of a rotor operating with either constant collective pitch,* $\theta_0$, *or nominally constant thrust, undergoing an axial descent through the VRS to the WBS from an initial hover.* . . . . . 259

6.2 *Standard deviation of fluctuations of thrust, as a percentage of the mean thrust, from simulations of a rotor operating with either constant collective pitch,* $\theta_0$, *or nominally constant thrust, undergoing an axial descent through the VRS to the WBS from an initial hover.* . . . . . 260

6.3 *Iso-surfaces of the locus of the vorticity field arising over three, pre-VRS, descent speed intervals. The highest (darkest) vorticity level shown is 5 times greater than the lowest level.* . . . . . 262

6.4 *Iso-surfaces of the locus of the vorticity fields arising over four, in-VRS, descent speed intervals. The highest (darkest) vorticity level shown is 5 times greater than the lowest level.* . . . . . 263

6.5 *Iso-surfaces of the locus of the vorticity field arising over a descent speed interval of* $\Delta\bar{\mu}_z = 0.1$. *The highest (darkest) vorticity level shown is 5 times greater than the lowest level.* . . . . . 264

6.6 *Resultant vertical velocities,* $\lambda_z(r) = \lambda_i(r) + \mu_z$, *scaled by the mean inflow at hover, at four blade stations, 0.9R, 0.7R, 0.5R and 0.3R. The results are from the two cases of rotor operational modes.* . . . . . 265

6.7 *Graph of the variation of the strength per unit length of the tip and root vortex systems trailed from the rotor blades with increasing descent rate for two operational mode cases.* . . . . . 268

6.8 *Comparison of the variation of sectional blade loading with descent rate arising on rotors operating under different operational modes.* . . . . . 271

6.9 *Comparison of the spanwise distribution of blade loadings at several descent speeds arising on rotors operating under different operational modes.* . . . . 273

6.10 *Total torque coefficient minus profile torque coefficient, normalised by induced torque coefficient arising in hover, from simulations of a rotor operating with either constant collective pitch,* $\theta_0$, *or controlled thrust. The rotor is undergoing an axial descent through the VRS to the WBS from an initial hover condition.* . . . . . 275

6.11 *Comparison of induced inflow calculated using Washizu's method (Eq. 2.43. Inflow generated by a rotor descending through to the WBS from hover when the thrust is being controlled to be nominally constant or when the collective pitch is being held constant.* . . . . . 276

6.12 *Comparison of induced inflow computed using Washizu's method but with the constant profile torque value replaced with the instantaneous value of profile torque,* $C_{Q_p}$. *Inflow generated by a rotor descending through to the WBS from hover when the thrust is being controlled to be nominally constant or when the collective pitch is being held constant.* . . . . . 278

6.13 *Estimated mean disc inflow using actual profile torque and a descent rate scaled with the instantaneous mean inflow* $\lambda_i$. *Inflow generated by a rotor descending through to the WBS from hover when the thrust is being controlled to be nominally constant or when the collective pitch is being held constant.* . . . . . 279

6.14 *Standard deviation about the mean thrust of the thrust fluctuations vs. descent rate scaled with the instantaneous mean inflow. The thrust was generated by a rotor descending through to the WBS from hover when the thrust is being controlled to be nominally constant or when the collective pitch is being held constant.* . . . . . 281

6.15 *Variation of sectional blade loadings, scaled with the instantaneous mean blade loading with descent rate scaled with the instantaneous mean inflow. Blade loadings are from a rotor descending through to the WBS from hover when the thrust is being controlled to be nominally constant or when the collective pitch is being held constant.* . . . . . 282

6.16 *Variation of rotor torque with descent rate scaled with the instantaneous mean inflow. The torque was generated by a rotor descending through to the WBS from hover when the thrust is being controlled to be nominally constant and when the collective pitch is being held constant.* . . . . . 283

6.17 *Variation of rotor torque scaled with* $2k\lambda_i^3$ vs. *descent rate scaled with the instantaneous mean inflow. The torque was generated by a rotor descending through to the WBS from hover when the thrust is being controlled to be nominally constant and when the collective pitch is being held constant.* . . 283

# List of Tables

2.1 *Rotor definition* . . . . . 63

5.1 *Rotor definition.* . . . . . 205

# Nomenclature

## Rotor System

| | |
|---|---|
| $A$ | : rotor disc area, $\pi R^2$ |
| $c$ | : blade chord |
| $C_B$ | : mean blade loading coefficient |
| $C_B(r)$ | : sectional blade loading coefficient |
| $C_D$ | : drag, scaled by $\frac{1}{2}\rho(\Omega R)^2 c$ |
| $C_L$ | : lift, scaled by $\frac{1}{2}\rho(\Omega R)^2 c$ |
| $C_Q$ | : total rotor torque, scaled by $\rho AR(\Omega R)^2$ |
| $C_{Q_0}$ | : hover based profile torque, scaled by $\rho AR(\Omega R)^2$ |
| $C_{Q_p}$ | : instantaneous profile torque, scaled by $\rho AR(\Omega R)^2$ |
| $C_T$ | : rotor thrust, scaled by $\rho A(\Omega R)^2$ |
| $N$ | : number of blades on rotor |
| $r$ | : radial position on rotor |
| $R$ | : rotor radius |
| $\alpha$ | : aerofoil geometric angle of attack |
| $\alpha_e$ | : aerofoil effective angle of attack |
| $\theta_0$ | : rotor collective pitch |
| $\theta_{tw}$ | : rotor blade twist rate |
| $\lambda_h$ | : mean induced rotor inflow in hover, scaled by $(\Omega R)$ |
| $\lambda_i$ | : instantaneous mean induced rotor inflow, scaled by $(\Omega R)$ |
| $\lambda_z(r)$ | : sectional net vertical flow velocity, scaled by $(\Omega R)$ |
| $\mu_z$ | : normalised descent speed, scaled by $(\Omega R)$ |

$\bar{\mu}_z$ : normalised descent speed, scaled by $(\Omega R)\sqrt{C_T/2}$

$\sigma$ : rotor solidity, $Nc/\pi R$

$\Omega$ : rotor rotational speed

## Fluid Dynamic Model

$F$ : intercell vorticity flux

$M$ : Mach number

$p$ : pressure in the flow

$R_e$ : Reynolds number

$S$ : vorticity source

$t$ : time

$u$ : flow velocity

$u_b$ : flow velocity relative to blade

$W$ : flux weighting function

$\Delta_0$ : cell length

$\Delta t$ : timestep

$\phi$ : wave amplifier function

$\nu$ : kinematic viscosity of the fluid

$\rho$ : flow density

$\omega$ : vorticity

$\omega_b$ : bound vorticity

## Structural Dynamics

$D$ : Energy dissipation

$\mathcal{L}$ : Lagrangian of the system

$q$ : generalised coordinates

$T$ : kinetic energy

$P$ : potential energy

$W$ : work

## Fast Multipole Method

$a_k$ : $k^{th}$ Taylor coefficient of $K_\delta$

$b_k$ : $k^{th}$ Taylor coefficient of $\phi_\delta$

$K$ : Biot-Savart kernel

$K_\delta$ : regularised Biot-Savart kernel

$m_k$ : $k^{th}$ moment of vorticity

$\delta$ : kernel smoothing parameter

## Spectral Analysis

$E$ : Energy spectrum

$k$ : turbulent kinetic energy

$\kappa$ : wave number

## Abbreviations

BET : Blade Element Theory

BVI : Blade Vortex Interaction

CFD : Computational Fluid Dynamics

FMM : Fast Multipole Method

TVD : Total Variational Diminishing

VRS : Vortex Ring State

VTM : Vorticity Transport Model

WAF : Weighted Average Flux

WBS : Windmill Brake State

# Chapter 1

# Introduction

## 1.1 An Overview of The Vortex-Ring Phenomenon

When learning to fly, pilots of rotorcraft are taught to avoid a region of the flight envelope that encompasses a combination of low descent and low forward speed. They will also learn that the location of the boundary around this region of the flight envelope is strongly dependent upon the type of rotorcraft. Crossing the boundary of this region leads to a loss of control effectiveness and an increase in the power required to maintain a steady and adequate thrust. Although flight is possible within this regime, and escape is brought about by a sustained control demand for forward motion, the sudden and uncontrollable loss of altitude [1] sometimes associated with this flight condition becomes important when the vehicle is in close proximity to the ground. The rotorcraft vortex-ring phenomenon, to which the preceding description refers, has received interest within the rotorcraft community since as early as the 1920s, as the recording and analytical treatment of experimental VRS data by Lock *et al.* [2] and subsequently Glauert attests. [3]. However, despite the numerous experimental, analytical and numerical research endevours into this worrying problem of rotorcraft flight, the condition has remained somewhat enigmatic and surprising. Indeed, even as recently as April 2000 the new US-Marine V22 Osprey tilt-rotor aircraft suffered a crash due to an encounter with the VRS [4], an event which appeared to reinvigorate the research effort in this field, especially since the design of the V22 rotors exhibited the modern design trends of incorporating highly twisted and highly loaded blades that were also being implemented on other modern rotorcraft.

The problem appears to lie in the nature of the rotor wake. In all helicopter flight regimes, including axial flight, the helical structure of the wake of a helicopter rotor is inherently unstable to small perturbations to its geometry or strength. The growth rate of disturbances to the rotor wake is, largely, a function of both the strength of the vortical structures within the wake and the pitch of the wake helix, or, in other words, to the relative spacing between adjacent vortex filaments [5, 6]. The effect of the growth of these disturbances is to disorganise the initially structured helical form of the rotor wake. Under normal flight conditions the breakdown of spatial order in the flow occurs in the far field, some distance downstream of the rotor, and the growing disturbances to the wake, are convected away from the rotor at a speed that is dependent on the rotor inflow and the free stream velocity [7, 8]. In descending flight, however, the rate of convection of the perturbations to the wake becomes comparable to their rate of spatial expansion, and thus within a range of descent rates it becomes possible for the influence of the disturbances to reach the rotor [7, 8, 9]. Within this range of descent rates the helical structure of the vorticity field can ultimately break down to yield a highly unsteady toroidal form that is the characterising trait of the VRS flow field. Within the VRS the aerodynamic forces generated by the rotor fluctuate appreciably and erratically in response to the unsteady flow near to the rotor [1, 10, 11, 12].

Particle Image Velocimetry (PIV) has shown [13] that the global geometry of the flow field at the onset of wake breakdown is highly transient, and that the geometry of the wake at any particular instant may be quite different to the geometry of the mean flow. At the onset of the VRS, where the descent rate is approximately half of the rotor downwash velocity, PIV shows the wake to swap intermittently between two geometric forms - one of which is similar to the structure found at hover, and another that resembles a ring, or toroid, of vorticity that bundles up in the vicinity the rotor plane. As the descent rate is increased to near the mean rotor downwash velocity the wake structure becomes more inclined to remain in the second mode and thus the rotor appears to be engulfed in the recirculating flow that characterises the VRS. The unsteadiness of this recirculating flow arises from a recurrent, generally aperiodic, and spatially non-uniform process in which the vorticity within the ring builds up over a number of rotor revolutions and is then ejected into the free-stream [7, 14, 15]. In addition to the highly transient blade loading, the concentration of vorticity near to the rotor during the VRS causes

a reduction in the thrust produced by the rotor if the collective pitch setting is held constant [10, 12, 16], or equivalently, an increase in the power required by the rotor if the thrust is held constant [11]. Hitherto, this effect, known as thrust settling or settling with power, depending on context, was thought to persist throughout the VRS regime. Cessation of the vortex ring state comes about when the descent rate is so high that the recirculating flow near to the rotor can no longer be sustained and the orderly structure of the wake near to the rotor is re-established [3, 17].

The behaviour of a rotor operating within a field of concentrated and highly disorganised vorticity is strongly non-linear. The physics of the growth and transmission of disturbances through the rotor wake is extremely complex, and any attempt to understand these processes is complicated by the presence of long-range interactions between evolving vortex filaments and coupling between the dynamics of the wake and the loading produced on the rotor. The complexity of the VRS is borne out by the varied, counter-intuitive and sometimes conflicting nature of several published reports. A review of the history of the published literature on the VRS reveals several central themes of research. Attention was given to the accurate estimation of steady, mean, rotor performance parameters such as rotor inflow, thrust and power, by Lock [2], Glauert [3], Castles [18] and more recently by Taghizad [19]. These attempts have relied upon analytical treatments of the rotor flow based on the conservation of momentum within a definable stream tube that passes through the rotor disc. However, their analyses were supplemented with constants derived from empirical data. This was done to obtain rotor characteristic curves that matched the experimental data in the region of descent speeds where the momentum theory becomes strictly invalid due to the intractability of defining a suitable stream tube shape for the flow in VRS conditions. Other methods to predict mean rotor performance parameters that have been reported employed linearly decaying vortex tube theories. Wang [20] was the first to propose such a method, and recently, because of the independence from momentum based theories of Wang's method, it was revised and extended by Perry *et al.* [21]. The wake tube, formed from a vertical stack of coaxial vortex rings, could vary in length under the action of both the free stream flow and the linear decay assigned to it. The method provided reasonably good predictions of mean rotor inflow derived from experiments, though the universality of these particular methods have not been demonstrated - only the data from which the empirical constants were derived (or data obtained from

tests with very similar rotors), have been used to validate the models. Apart from the issue of universality, the aforementioned empirically enhanced analytical models give only what is, essentially, time averaged data for the rotor, based upon mean wake length and strength. These models can in no way explicitly provide information regarding the fluid dynamic processes that engender the transition from the tube-like wake form associated with a hovering rotor to the highly unsteady toroidal wake topology that is characteristic of the VRS wake. As a consequence, the unsteadiness observed in rotor thrust and torque measurements is unaccounted for. Such methods are therefore of limited use as tools for understanding the fundamental physics that governs the vortex ring phenomenon.

In an attempt to explore some of the sensitivities of the VRS behaviour to changes in rotor configuration and geometry, numerous experimental investigations have been conducted. Stewart [1] flew several different helicopters into the VRS regime and found the behaviour of each to vary significantly but was unable to identify, from the details of the helicopter designs, a reason for the differences. The effects on the VRS behaviour of rotor disc loading and blade twist were investigated experimentally by Yaggy and Mort [10], Castles and Gray [11], Washizu *et al.* [22], Azuma *et al.* [12] and Gao [16], among others. In some of these experiments, trends in the effects of blade twist were found, though in others, such as in the work of Azuma *et al.*, an investigation into the effects of disc loading revealed no clear patterns of behaviour. In addition, and perhaps more importantly, it has not been possible in many cases to find good agreement between one experiment and another, and in some cases opposing trends are evident, for instance, in terms of the effects of blade-twist on the severity of the fluctuations in thrust. Often, rotors used by one group of researchers to test for twist effects were quite dissimilar to those used by another group of workers performing similar explorations, thus too many unaccounted variables exist between the data sets for rigorous comparisons to be made. Importantly, perhaps, the rotors were sometimes operated in different ways. For instance, Castles and Gray [11] controlled the thrust of their rotors to be nominally constant during a test by varying the collective pitch angle appropriately each time the descent speed was altered. Contrarily, in the tests conducted by Yaggy and Mort [10] and by Washizu *et al.* [22] for instance, the collective pitch angle of their rotors was held constant over the whole range of flight speeds tested, which resulted in an increase in the thrust and thus rotor inflow with descent rate. A further, though obscure, factor that may influence the comparison of data from different

experiments is the possible presence of aerodynamic stall. It is quite possible that, in at least some of the tests, stall may have arisen at high descent speeds undetected, especially when the disc loading was high, or when the collective pitch was held constant. In a manner that is unaccounted for, then, stall would in some way have modified the thrust and the fluctuations of the thrust that was often reported. It is difficult, therefore, to find clearly emerging trends in some aspects of rotor behaviour in the VRS, such as in the effects of variations in rotor blade geometry, in the existing literature. This is despite the numerous tests that have been performed, and it is because of the many variations in the tests and the possible presence of unseen contamination by stall.

In addition, other rotor configurations have been considered. For instance, counter rotating, side by side rotors were studied experimentally by Washizu *et al.* [23], and Betzina [24] and latterly by Abrego, Betzina and Long [25]. The latter two investigations were likely inspired by the problems with the V22 mentioned earlier. In all cases, the characteristic reduction in thrust and the occurrence of large thrust fluctuations experienced by single rotors operating in the VRS was observed. Washizu *et al.* [23] reported that the VRS envelope was slightly larger than for the single rotor that they had previously tested [22]. In addition they also reported that the periodicity in the thrust behaviour observed during the oblique descent of their single model rotor did not arise in the case of the tandem rotor (latterly, periodic fluctuations of the thrust produced by an obliquely descending rotor have also been observed by Stack *et al.* [15]). The observations of Washizu *et al.* [23] suggest that the mutual interference of the tandem rotor wakes modified the dynamics of the flow field. Betzina used an image plane to represent the second rotor. He noted that the image plane caused the rotor to behave differently in the VRS to an isolated rotor. Abrego *et al.* [25] tested a pair of rotors, similar to those of the former work, arranged in close proximity as in a tilt-rotor aircraft configuration. They obtained results suggesting that an image plane does not fully replicate the interference of the second rotor flow field on the first.

The latter three experiments highlight the non-linear and interactional aspects of rotor flows and how they may subtly modify the stability characteristics of the flow field and influence the aerodynamic environment of a rotor operating in or near to the VRS. Indeed, appreciation of the detailed fluid dynamics of the VRS is vital to the complete understanding of the phenomenon. Only a few flow visualisation experiments have been

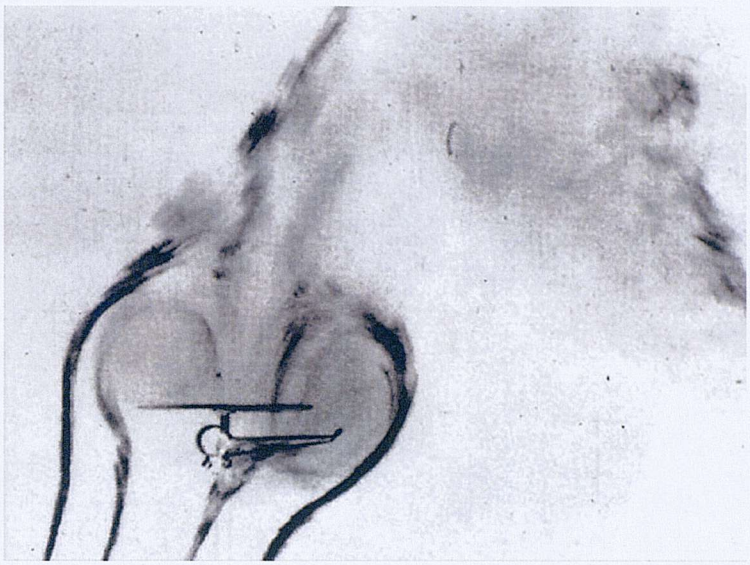


***Figure 1.1:*** *Image of a rotor in the VRS taken from the work of Drees and Hendal [14]. The flow field is realised by an injection of smoke particles from a rake just beneath the fuselage model. The original image colours have been inverted to improve clarity.*

reported, however. Lock and Townsend [26] obtained possibly the first pictures of the VRS flow field by photographing the flow of bubbles around a model screw working in water, though unfortunately the images were limited in detail and thus difficult to interpret. Perhaps the most well known flow visualisation results, though, are those of Drees and Hendal [14], obtained in 1951. Figure 1.1 shows an image of the VRS flow field realised by an injection of smoke particles into the flow near to the rotor. The gross features of the formation and evolution of the wake in the VRS were captured. Leishman [17] has published tantilising images of what appear to be individual vortex filaments bundled beneath the rotor plane in a VRS flow obtained via the shadowgraph technique, though unfortunately he gives little information regarding the evolution of the filaments. Stack *et al.* [15] managed to obtain a reasonable realisation of the flow field via injection of bubbles in the water around their model rotor which was operated in a tow tank, though some of the images are somewhat difficult to interpret. Indeed in all of these flow field studies little information on the fluid dynamic processes at work in the wake of a descending rotor has been communicated. This is probably due to the difficulty in resolving the important fine scale features of the flow well enough, or for long enough to obtain a thorough understanding of the kinematics of the rotor wake. Nonetheless, the visualisations are very useful

for conceptualising the flow field. More recently, Green, Gillies and Brown [13] reported on PIV measurements of a model propeller operating in hover as well as near and within the VRS. Their quantitative realisation of the flow field data allowed a more thorough analysis of the kinematics of the VRS flow field than had been reported before. Analysis of the velocity data using Proper Orthogonal Decomposition (see Holmes *et al.* [27] for instance) revealed the mode swapping behaviour mentioned earlier. This behaviour was associated with the considerable unsteadiness observed in the thrust behaviour just prior to VRS onset.

Even though the quantity and quality of the data obtained from flow visualisation experiments has improved considerably with time, and so yielding the discovery of Green *et al.*, they have not been able to expose the underlying fluid dynamic processes that govern the rotor wake behaviour in descending flight. More progress has been made from the use of computational methods, primarily those that are vortex based. A significant breakthrough was made in the work of Newman, Brown and Perry *et al.* [7] where the CFD method of Brown [28] was used to compute the unsteady flow field of the VRS in order to shed some light on the governing fiuid mechanics. They identified that the VRS occurred due to a sudden catastrophic collapse of the tubular wake structure found in hover and very low speed descent into a toroidal flow field akin to that shown in Fig 1.1. It was noted that the breakdown appeared to be related to the unstable growth of disturbances within the wake, which as a consequence of the increasing descent speed were able to penetrate further up the wake near to the rotor, ultimately causing the total collapse of the wake tube. Previously it has been thought that the coagulation of vorticity at the rotor plane occurred merely as a consequence of the free-steam overcoming the induced downward convection of the wake, which thus held the rotor-tip vortices in the vicinity of the rotor [29]. Such a notion seems strange, since it is not consistent with experimental observations that suggest the VRS starts at a descent speed that is significantly less than the mean inflow velocity of the rotor.

Leishman and co-workers examined the influence of descending flight, thrust and blade twist on the linear stability of the helical vortex system generated by the tips of a rotor [30]. This work was an extension to their work on the linear stability characteristics of rotor wakes in hover and climb [6], this latter work being similar in concept to the more general stability analysis of helical vortex filaments of Widnall [5]. They found that the

growth rates of small perturbations within the wake increased with descent rate, thus implying that the VRS arose in part because of the increased susceptibility of the wake to small disturbances. In addition, they found that an increase in the tip-down blade twist also increased the growth rates of small disturbances whilst an increase in thrust reduced the growth rates. In relation to the rotorcraft community's interest, at the time, in the behaviour of tilt-rotors flying in the VRS, they also calculated that, in the case of tip-vortex systems, the presence of a closely neighbouring wake made both wakes more unstable. The implication was that the wakes of tandem and tilt-rotors would be more susceptible to collapse into the VRS than similar single rotors, as found experimentally by Washizu [23].

Whilst the results of these wake stability analyses are very enlightening, they cannot be relied upon completely, for two reasons. Firstly, the analyses were purely linear which limits their scope as the results cannot be extrapolated to a situation when the excursions of the vortex wake filaments become large and thus their dynamics becomes non-linear. Secondly, the Free Vortex Method (FVM) used for the computations only models the tip vortex. Whilst the tip vortex is generally the more dominant vortex system in a rotor wake, it does not, however, evolve within the flow on its own - there must be some interplay between it and the root vortex system. In addition, an increase in negative blade twist will decrease the strength of the tip-vortex, in favour of the root-vortex, and thereby make it even more important that the root-vortex system is included in an analysis. That said, there is hitherto little in the published literature that explicitly tackles this aspect of the VRS fluid dynamics.

In a further paper on the computational simulations of the VRS, Brown, Line and Ahlin [9] considered the effect of the helicopter fuselage and tail rotor wake on the behaviour of the rotor and its wake in and around the VRS. The rotor was flown at two different, steep angles and thus approached the VRS from different initial conditions. Comparison with results for an isolated rotor showed that the presence of a fuselage strongly influenced the detail character of the VRS and it even admitted a degree of periodicity to the thrust fluctuations that were not evident in the thrust signal of the isolated rotor. In addition, the root vortices could be seen to influence the kinematics of the wake just prior to complete wake breakdown. From simulations of the rotor approaching the VRS regime from a high speed descent, evidence was given that showed clearly how the disorganisation

in the far wake moved towards the rotor as the VRS regime was approached. It was noted though that the complete collapse of the wake appeared to occur far more rapidly than the initial breakdown process in the far wake. Brown *et al.* also noted that the low and high frequency variability in the thrust signal commonly observed in VRS experiments [12, 15] was due to, respectively, the large-scale build up and breakaway of vortex filaments from the vortex toroid, and direct Blade Vortex Interactions (BVI). Despite the general influence that the fuselage had on the behaviour of the main rotor wake, there was no evidence to suggest that it affected the descent speed at which VRS initiated.

The subject of VRS onset has received specific attention in the literature, since its accurate prediction would aid in the design of avoidance systems, etc. The first onset models were based upon the notion that the VRS occurred when the descent speed matched the induced convection speed of the tip-vortices in hover, thus causing them to bunch up beneath the rotor plane. Wolkovitch [29] was the first to derive an onset model on this basis. This notion seems odd though. Using the commencement of thrust settling as the measure of VRS onset, the available experimental data suggests that onset occurs at a descent speed that is significantly lower than the tip-vortex convection speed, and that the induced flow increases with descent speed and thus increases the induced tip vortex convection speed. But, despite the premise and, indeed, the results of Wolkovitch's model being inconsistent with the available experimental data, though, his model was extended by Peters and Chen [31] and quite recently by Taghizad *et al.* [19]. Indeed, Taghizad *et al.* also implemented their extended model into the flight dynamics model of ONERA. Neither the original model nor either of the extended versions of the theory have been employed in the literature elsewhere, however. A model that is more consistent with experimental observation, and, as it turns out, a model that is better related to the actual fluid dynamics of the problem, was derived by Newman *et al.* [7]. They postulated that VRS onset occurs when disturbances in the wake obtain a critical transport velocity that allows them to convect up to the rotor plane and they used momentum theory considerations to express this critical disturbance velocity. The critical velocity was derived from the empirical data of Drees and Hendal. The effect that forward flight has on separating the vortex filaments, and thus moderating the unstable nature of the wake was also accounted for. The resulting model provided very good agreement with experimental data when the measure used to define VRS onset was taken as some low threshold of thrust fluctuations. Indeed, as a

sign of the acceptability of the model, it was later used by Brand *et al.* [32] and Kisor *et al.* [33] as the theoretical marker for VRS onset in their work on the behaviour of the V22 Osprey when flying near to or in the VRS flight regime.

So that the speeds at which the various operational states of one particular descending rotor arise can be compared with those of another, the descent speed has traditionally been scaled with the mean inflow, $\lambda_h$, generated by the rotors at hover, given by $\lambda_h = \sqrt{C_{T_h}/2}$. Nonetheless, it appears from the available experimental and numerical data that the onset speed of VRS of the rotors examined in the literature, varies somewhat. Interestingly, Newman *et al.*'s model [7] matches less well with numerical data [34] for highly twisted blades, possibly because the empirical data on which it is based comes from rotors with blades that were only moderately twisted. In addition, Kisor *et al.* [33] reported that an accelerated descent of the V22 through the theoretical VRS boundary (rather than a slow, incremental, 'quasi-static' approach) engendered a delay, in terms of descent speed, in the arrival of the first signs of, and ultimate collapse into, the VRS. This phenomenon had also been noted to occur in numerical simulations by Newman *et al.* and was researched explicitly quite recently by Ahlin and Brown [8]. It appears then, that the onset speed of the VRS is not universal, at least not when the aforementioned standard scaling parameter is used. Rotor geometry, rotor configuration and also the trajectory of the rotor have all been shown to modify the speed at which the wake will collapse into the VRS. This signifies that the wake behaviour is sensitive to the inflow distribution along the blades and also that there are time dependent features of the wake kinematics that have yet to be fully explained.

The preceding summary of the VRS literature has shown that the research work undertaken up to now has, as a collective, barely scratched the surface of the flow physics that govern the behaviour of the wake of a descending rotor. Indeed, it is known that VRS induces both a loss of mean thrust as well as large, mostly aperiodic thrust variations that have an approximate cycle time of several tens of rotor revolutions [8, 13, 15]. Additionally, it is known that these symptoms of the VRS can cause an alarming loss of control authority in a real flight situation. The fluid dynamic processes that cause these rotor-based effects involve the unstable growth of disturbances within the wake. However, the complex detail of the fluid dynamics have, hitherto, remained obscure due to the difficulties in capturing or isolating the small scale, local fluid kinematics by either experiment

or computation. In addition, the variability between the numerous experimental data sets, and perhaps the inappropriate nature of the standard method of scaling the descent speed of the rotor, has made it difficult, if not impossible, to identify definite trends related to the sensitivities of the phenomenon to important rotor design parameters such as blade loading and blade twist.

## 1.2 Hypotheses

This thesis describes an examination of the detailed fluid mechanics of the rotorcraft vortex ring phenomenon and of some of its sensitivities to rotor design. The thesis is based upon computational simulations, of descending rotors, that have been performed by Brown's Vorticity Transport Model [28, 35].

It is believed that the kinematics of the wake responsible for the disorganisation of the far wake of a hovering rotor are responsible for the truncation of the wake that admits, ultimately, the eventual collapse of the wake upon the onset of VRS. It is also believed that the non-linear, rather than the linear, excursions out of a plane parallel to the rotor of the vortex filaments within the wake are the dominant features of the disorganisation and truncation of the vortical wake and that this re-orientation of vortex filaments is largely responsible for the onset and subsequent evolution of the VRS wake. It is postulated that VRS onset marks the transition in the wake from one type of kinematics, related to the evolution of helical vortex systems, to another type of fluid kinematics, that of a stack of coaxial vortex rings, and that it is this transition that was previously identified as mode switching in Ref. 13. The disorganisation of the wake takes some some to manifest and this is the reason why dynamic flight close to the VRS regime can partially delay and also ameliorate the effects of VRS.

It is also postulated, contrary to previous conjecture in the literature [34], that the VRS is purely a wake dynamic phenomenon and thus does not require feedback from the rotor to cause it to initiate. The way in which the rotor responds to the local velocity field, a topic which has not been explicitly addressed in the literature, is an important, though secondary, feature of the flow physics, however. That is, the operating state of the rotor (constant thrust or constant collective pitch) is of fundamental importance to the behaviour of a rotor in the VRS, but not to the likelihood of VRS initiation.

It is believed that both the onset and the subsequent cessation of the VRS (leading to flight into the WBS) is postponed to higher descent speeds by increasing the magnitude of the geometric twist of rotor blades. In terms of the postponement of VRS onset, it is postulated that this behaviour arises because of the stabilising effect of the increase in inflow velocity in the vicinity of a rotor's root-vortex system that is engendered by an increase in blade twist rate. The postponement to higher descent rates of VRS cessation by an increase in blade twist is achieved because the higher induced flow velocity that an increase in blade twist produces, again in the region of the root-vortex system of the rotor, sustains the vortex ring-like kinematics of the wake to higher descent speeds.

Contrary to received wisdom, it is deemed very likely that the root vortex system of a rotor plays a fundamental role in the VRS physics thus the implication of this is that the inflow distribution is of paramount importance to the way in which the rotor wake behaves during VRS. Also, importantly, omission of the root-vortices of a rotor in a numerical analysis of a rotor in descending flight, at least, is detrimental to the realism achieved by such a simulation.

Finally, it is hypothesised that the standard means of normalising the rotor descent speed, using the mean inflow produced during hover, i.e. $\sqrt{C_{T_h}/2}$, is not satisfactory since it fails to account for the state of the wake at any given descent speed. This is because the rotor inflow changes with descent, and is sensitive to the rotor conflguration, the rotor geometry and the operating conditions of the rotor.

## 1.3 Synopsis

This thesis is arranged as follows. Chapter 2 presents a description of the model used in the present work to simulate the VRS. An exercise is performed to validate the ability of the VTM to faithfully simulate the VRS flow field and the associated rotor aerodynamics against the experimental data of Gao [16]. It is shown that the VTM provides reasonable qualitative agreement with Gao's data. In addition, an assessment of the influence of the size of the computational cell used in a simulation on the results of that simulation is presented. It is also shown how the predicted behaviour of the rotor when in VRS is sensitive to the grid resolution, whilst the predictions of rotor performance during hover or the Windmill Brake State (WBS) are relatively insensitive.

Chapter 3 explores the vortex kinematics of the wake of a descending, idealised, rotor. The evolution of the rotor wake during two different VRS scenarios is examined in detail with special focus on the structure of the vorticity within the flow. It is seen that VRS onset arises in the absence of the aerodynamic feedback between the rotor and the velocity field. In addition, the onset of VRS marks a transition in the dominant dynamics of the evolution of the vorticity field, from that of a helical vortex system to kinematics that approximate those of a stack of co-axial vortex rings. The partial reorientation of tip-vortex filaments from a plane parallel to the rotor to a plane normal to the rotor is shown to be the dominant mechanism that leads to the initial breakdown of the wake into the toroidal form arising in VRS flow and is also the dominant mechanism that is responsible for the repeated disorganisation of the toroidal wake structure during a VRS event.

In Chapter 4, the influence of the vortex kinematics on the velocity field is investigated. A series of studies is presented that look at various aspects of how the global geometry of the vortical wake influences the global and local velocity field and the on-blade aerodynamic environment. It is shown that because the mean vortical wake of a hovering rotor is truncated the associated mean velocity field is also truncated. The importance of this observation is that since the topology of the truncated mean velocity field is actually toroidal, rather than cylindrical as is assumed in the momentum theory for rotor flows, the topology of the velocity field of a hovering rotor is the same as that of a rotor in the VRS. This chapter concludes with an investigation into how the rotor's trajectory (i.e. acceleration effects) can influence the behaviour of the wake and thus how the rotor performance is affected as a result.

Chapter 5 addresses the effects of blade twist and stall on the VRS behaviour and shows the importance of the distribution of the inflow through the rotor and of the dynamics of the root vortex system.

In Chapter 6 the effects of the operational mode of the rotor are examined. It is shown that the way in which a rotor is operated fundamentally affects the manner in which the rotor responds to and behaves within axial descent, such that care must be taken in comparing results from different experiments. An alternative method of normalising the descent speed is presented that caters for the differences caused by the various possible operational modes of the rotor.

Finally, in Chapter 7, the thesis concludes with a general summary and discussion of

the work presented herein, and suggestions for further work are given.

## 1.4 Publications

A number of elements of the research presented in this thesis have been published previously.

In June 2005, a paper reporting upon an analytical and numerical investigation into the influence of acceleration on the speed at which the VRS initiates was presented at the $61^{st}$ Annual Forum of the American Helicopter Society, in Texas, USA [8]. The paper described the derivation of a VRS onset prediction model which extended the model of Newman *et al.* [7] by incorporating terms that accounted for a time-dependent trajectory and related the strength of the disturbance that was postulated to cause wake breakdown, to the strength of the wake when the disturbance was created at the rotor. To both guide and to elaborate upon the modelling assumptions, rotors undergoing oblique, accelerated trajectories were simulated.

In September 2005 a paper [36] reporting on preliminary studies into various aspects of the physics of the VRS was presented at the $31^{st}$ European Rotorcraft Forum in Florence, Italy. The paper featured investigations into the aerodynamic origins of the thrust-settling phenomenon as well as an analysis, based upon numerical simulations, of both the effects of moderate levels of blade twist and of the influence of blade stall, on the behaviour of the rotor in the VRS condition.

In May 2007, the results of research [37] into the detail vortex kinematics responsible for the onset and subsequent development of the VRS were presented at the $63^{rd}$ Annual Forum of the American Helicopter Society, in Virginia, USA. The work involved two high-resolution simulations of a simplified, single-bladed rotor descending into the VRS from different initial flight conditions. A detailed, qualitative analysis of the dominant kinematics of the helical vortex system of the rotor was discussed and the results of a quantitative assessment of the vortical structures within the rotor wake at various stages during the descents were presented. In April 2007 this paper [37] was subtly modified and submitted to the Journal of the American Helicopter Society.

In addition to the previously published work that formed part of this thesis, the author has also contributed to several other papers related to the VRS not explicitly featured

herein.

In June 2004 a paper [9] reporting upon high resolution simulations of isolated rotors and rotors coupled to a generic fuselage and a tail rotor, in descending flight, was presented at the $60^{th}$ Annual Forum of the American Helicopter Society, in Maryland, USA. The work investigated the interference effects that the wake of the helicopter fuselage, in combination with the wake of the tail rotor, had on the behaviour of the main rotor and its wake when in descending flight and when flying within the VRS in particular.

In 2006 the author contributed work to a paper describing an engineering model for mean rotor inflow based upon a vortex-tube element representation of the rotor wake [21]. The paper utilised the mean inflow calculations from the analytical model and time-average flow fields from long duration VTM simulations of a rotor in hover, and when descending at several discrete speeds, to present ideas related to the associated mean topologies adopted by the rotor flow field. The paper was published in the Journal of the American Helicopter Society in July 2007.

# Chapter 2

# CFD Simulations of the Vortex Ring Phenomenon: A Description of the Model

## 2.1 Introduction

As a consequence of the low speed at which a helicopter rotor moves away from the shed and trailed vortices that it creates as a consequence of generating lift, the aerodynamic performance of a helicopter rotor is influenced, fundamentally, by its wake. This is especially true when the rotor operates for extended periods of time enveloped by its vorticity field, such as in the case of the vortex ring state. To model correctly, then, the aerodynamics, aeroacoustics and dynamics of a rotor and any accoutrements, such as a fuselage and empennage, the structure and strength of the vorticity field generated by the surfaces of the rotorcraft, especially those of the rotor, must be adequately represented both temporally and in three-dimensional space. Most Computational Fluid Dynamics (CFD) models used for aerodynamics problems solve the equations of motion of the fluid in terms of the primitive variables, velocity and pressure, using modern numerical techniques to discretise both the equations and the flow domain in which the equations are solved. The magnitude of the error arising from the approximation of the partial differential equations that govern the flow, however, is a function of the number of discretisation points used to define the flow domain and its boundaries. The processing limitations of current high-speed comput-

ers constrain the number of computational grid points that can be used to a level where the flow computation suffers from excessively high levels of numerical diffusion of vortical structures within the flow field. The diffusion arises because vorticity is not an explicitly conserved quantity in such schemes. As a consequence, the resulting spatial smearing of such flow structures leads to a loss of accuracy in the prediction of aerodynamic loads or aeroacoustics, for instance [38]. Although this problem can be alleviated, though not entirely, through the inclusion of many more computational nodes, such a 'brute-force' approach is available to the few with access to high capacity super computing, thus rendering rotorcraft aerodynamics simulation out of the reach of most workers in the field (although, such is the current pace of computer processing development that this problem may not exist for very long).

Since it appears that the correct prediction of the behaviour of the vorticity field is of fundamental importance to rotor flow simulations, it is reasonable to conclude that vorticity should be the quantity that is explicitly conserved in any numerical rotor-flow solver, thus preventing the destruction of vorticity through numerical dissipation. Although, of course, this is by no means a trivial requirement. Such a CFD model has been employed to conduct all of the numerical rotor-flow experiments presented in this thesis. This chapter describes the model and the numerical techniques used to implement it, and presents evidence that confirms the ability of the model to simulate the rotor vortex ring phenomenon.

## 2.2 The Governing Equations

Using the principle of Conservation of Fluid Momentum, the equations of motion for a fluid can be written in differential form in terms of the spatial and temporal gradients of velocity and pressure, as

$$\frac{\partial u}{\partial t} + u \cdot \nabla u = -\frac{1}{\rho}\nabla p + \nu \nabla^2 u \tag{2.1}$$

In general, flows associated with helicopter flight can be assumed to consist of local velocities, $u$, that are but small fractions of the speed at which pressure information, $p$, is transmitted through the fluid. This may not be the case near the tips of rotor blades, however, where speeds can reach or even exceed the speed of sound in the fluid. In such

circumstances, the compressibility effects on the aerodynamic characteristics of aerofoils can be modelled. In general, then, the fluid in which the helicopter is immersed is assumed to be incompressible, and thus the rate of expansion of any fluid element is assumed to be zero, or rather

$$\nabla \cdot u = 0 \tag{2.2}$$

The above velocity-pressure relations form the basis of the approximate Reynolds Averaged equations that are solved by standard CFD techniques for the primitive variable formulation (see Ref. 39 for instance). Since it is the vorticity and velocity fields of a rotor that are of principal interest in this discussion, however, it is pertinent to rewrite equation 2.1 in vorticity-velocity form. Thus, applying the vector identity

$$u \times (\nabla \times u) = \frac{1}{2}\nabla(u \cdot u) - u \cdot \nabla u$$

to Equ. 2.1 and taking the curl of each side of the resulting expression yields the unsteady vorticity transport equation

$$\frac{\partial \omega}{\partial t} + u \cdot \nabla \omega - \omega \cdot \nabla u = \nu \nabla^2 \omega \tag{2.3}$$

where $\omega = \nabla \times u$ is the vorticity and where use of Eq. 2.2 and the corresponding identity

$$\nabla \cdot \omega = 0 \tag{2.4}$$

have also been used. Note that this latter equation expresses Helmoltz's law [40], i.e. that vorticity does not begin or end in the interior of the flow.

The property of zero divergence of the velocity vector places a constraint on the flow such that the velocity field is fixed uniquely by the vorticity field in accordance with a Poisson type equation: taking the curl of the vorticity, such that

$$\nabla \times \omega = \nabla \times \nabla \times u \tag{2.5}$$

which yields

$$\nabla \times \omega = \nabla(\nabla \cdot u) - \nabla^2 u \tag{2.6}$$

but, as seen earlier, $\nabla \cdot u = 0$, and so

$$\nabla^2 u = -\nabla \times \omega \tag{2.7}$$

Equation 2.7 is the differential form of the Biot-Savart equation and the solution of which is given by Green's theorem, and takes the following form:

$$u(x) = -\frac{1}{4\pi} \int_V \frac{(x-y)}{|x-y|^3} \times \omega(y)\, dy \tag{2.8}$$

Rotor flows typically have Reynolds numbers, $Re$, with orders of at least $10^5$ and therefore viscous forces, outside of a thin layer of more slowly moving fluid immediately adjacent to the surfaces of the rotorcraft, may be neglected. In general though it is useful to simplify the governing equations by assuming that the entire flow in which the rotor is immersed is inviscid, such that $\nu\nabla^2\omega = 0$. However, in real flows, the aerodynamic forces generated on the various rotorcraft surfaces accompany the creation of vorticity on those surfaces which subsequently diffuses, and, more strongly, convects into the interior of the flow. Hence, if the flow is assumed to be inviscid, this effect must be accounted for by other means. In general then, a model for the production of vorticity and its subsequent release into the surrounding fluid can be represented by a source term, $S$, of appropriate form. Using the above assumptions to simplify Eq 2.3 the following equation for the transport of vorticity originating from source $S$, is obtained as

$$\frac{\partial\omega}{\partial t} + u \cdot \nabla\omega - \omega \cdot \nabla u = S \tag{2.9}$$

For the work conducted for this thesis, $S$, represents the creation of vorticity corresponding to the generation of aerodynamic loads on the blades of a rotor, only. In general, though, it could represent vorticity generated on any surface, such as a helicopter fuselage, for instance.

## 2.3 The Vorticity Transport Model

The investigations into rotor aerodynamics undertaken for this thesis have been conducted purely by numerical means. The rotor flow solver, the Vorticity Transport Model (VTM) of Brown and Line [35], but originated by Brown [28], was used to conduct all of the rotor simulations featured herein. It was not necessary to further develop the flow solver algorithms used in this model for the purposes of this thesis. On occasion however, some modifications were made in order to make idealisations of the rotor or simply to compute or output flow-field information that was not normally available.

The VTM is a grid based, finite-volume fluid-flow solver designed to simulate the aerodynamics and dynamics of rotorcraft in flight. In accordance with the vorticity transport equation 2.9 the model evolves vorticity, that was first generated on numerically defined surfaces immersed within a fluid, through a three-dimensional computational domain under the action of the local velocity field. The VTM is capable of producing representative, time accurate, simulations of the rotor wake and the rotor aerodynamics and dynamics [35, 41] and of the helicopter body aerodynamics [42]. Hitherto, the VTM has been used for a wide range of rotor applications, in addition to those referenced above, such as the modelling of rotors in ground effect [43], to assess the behaviour of a rotorcraft as it interacts with the wake of an airliner [44] and for VRS studies other than those featured in this thesis, such as Refs. 9 and 34.

The next two sub-sections describe the numerical techniques employed by the VTM to solve the governing fluid flow equations (Eqs 2.9 and 2.8) and to represent the aerodynamics and dynamics of a rotorcraft. Since the model has been described in detail by Brown [28], by Line and Brown [35] and by Line [41], only a summary of the salient features of the VTM will be provided in the following sections. The description comes in two sections since the overall model can be split, conceptually, into two main parts. The first part is the model of the rotor wake and the second is the numerical description of the rotor. The former model evolves vorticity in a computational grid. The latter model, calculates the aerodynamic and dynamic loads generated by the rotor blades as a result of the coupling of the velocity field to the blade aerodynamics, and then interpolates the corresponding vorticity into the aforementioned grid. As will be discussed, the separation of the two models reflects the difficulty in reconciling the relatively rapid evolution of the state of the rotor with the comparatively large time scales associated with the evolution of the surrounding flow field.

### 2.3.1 Numerical Implementation of The Rotor Wake Model

The following subsections provide a summary of the numerical methods used to solve the governing equations and evolve the resulting flow through time.

#### 2.3.1.1 The Computational Grid

The VTM employs a bespoke implementation of the Cartesian Fast Multipole Method (FMM) as a highly efficient means by which the velocity field is calculated. This method, which is described in § 2.3.1.5 of this thesis, does not require any form of condition to be imposed at the boundaries of the flow domain. The evolution, therefore, of the vorticity within the computational grid in accordance with Eq. 2.9 requires only regions, or cells, that contain vorticity at any given time to be included in the computation. In the VTM, the quantity of cells, and hence the memory required by the calculation is minimised by allowing the number of cells to vary as required by the transport of vorticity within the computed flow.

The grid is founded upon a virtual Cartesian stencil upon which cells can be created. Each predefined position on the stencil represents a potential location of a single computational cell, having sides of length $\Delta_0$. The stencil is fixed relative to the rotor hub and may extend to infinity in all directions and thus completely encapsulates the simulated rotorcraft.

As vorticity is introduced to the grid from the rotor via the source term $S$, a cell is created at the corresponding location on the stencil. The numerical scheme employed by the VTM to advect the vorticity through the flow domain requires knowledge of the flow variables in locations immediately adjacent to the cell containing the new vorticity, and thus the immediate neighbours of that cell on the stencil are also created. Once in the grid, a cell therefore already exists for vorticity to be transported into at the next timestep and as the vorticity is transported new neighbouring cells are created. Importantly, however, upon the advection of vorticity from one cell to the next, any cells that are left effectively empty, and which are not immediate neighbours of any cells occupied by vorticity, are removed from the computational domain and thus from the memory of the computer. The grid is therefore able to evolve freely and adaptively with the vorticity in the flow.

The grid structure is effectively boundary free and thus, theoretically, the number of cells within the grid may grow without bound. In reality however, the cell count can become excessively large for the capacity of the computer memory and therefore the computational domain is partitioned into an arrangement of nested grids of varying resolution. The grids are arranged in levels. The rotor is positioned within the lowest grid level, level $i = 0$, in which the cell length is $\Delta_0$, i.e. equal to that of the underlying stencil.

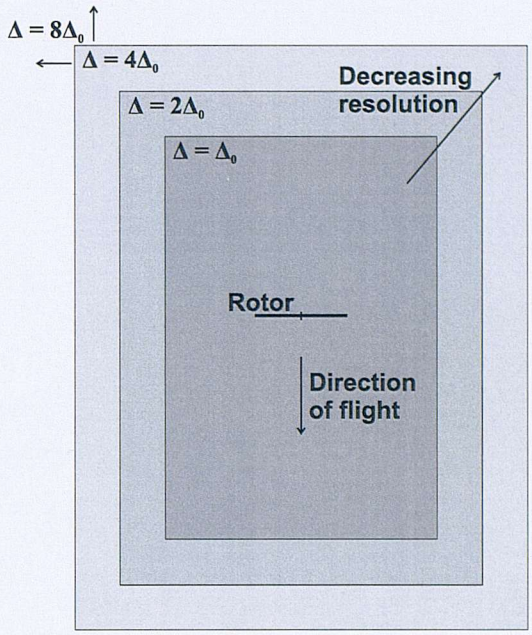



***Figure 2.1:*** *2D view of 3D computational grid. Image shows the arrangement of nested computational grids with varing cell size,* $\Delta_0$.

The grid resolution is then systematically reduced upon moving away from the rotor. At a prescribed distance from the rotor, in each direction, lies the interface between the lowest level grid and the next level, grid level $i = 1$. Here, the resolution of the grid is $2\Delta_0$. This process of doubling the cell length each time the grid level is increased can be repeated, theoretically, to generate any number of grid levels, though in practice just three of four levels are adequate, as shown schematically in Fig. 2.1.

Stable advancement of the solution in explicitly discretised schemes requires that the maximum stable timestep satisfies the Courant-Friedrichs-Lewy (CFL) condition, i.e. $u\Delta t/\Delta x < 1$, where $\Delta x$ is the length of a computational cell. Since, in the VTM, the cell length doubles from one grid level up to the next, the flow on that level can thus be advanced using a timestep that is twice that required on the level below it. The advantage of this approach is that computational effort us focused both temporally and spatially where it is most required, i.e. near to the rotor.

The nested grid arrangement brings with it the problem of maintaining the conservative and monotonic properties of the advection scheme at the grid level interfaces, and thus effective implementation of the nested grid into the VTM requires a means of advecting the vorticity across grid level boundaries. This is achieved as follows: Cells at the interface

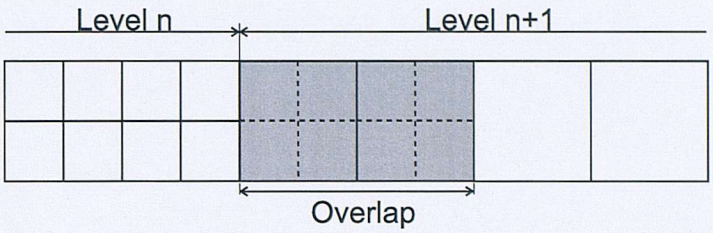



***Figure 2.2:*** *Overlapping of adjacent grid levels required to maintain monotonicity and conservativeness of the advection scheme at grid interfaces.*

between adjacent levels are overlapped, as in Fig. 2.2. The flux of vorticity across the interface is calculated on the finer grid and is then extrapolated onto the coarser grid. This method is conservative and preserves the second order and monotonic properties of the advection scheme at all interfaces.

#### 2.3.1.2 Discretisation of the Governing Equations

The unsteady vorticity transport model 2.9 is integrated in a piecewise manner over the grid stencil to yield

$$[\omega]^{n+1} - [\omega]^n = [u \cdot \nabla\omega]^n_{2^i\Delta t} + [S]^n_{2^i\Delta t} - [\omega \cdot \nabla u]^n_{2^i\Delta t} \tag{2.10}$$

The factor $2^i$ accounts for the different timestep assigned to each grid level, $i$, where $i = 0, 1, 2...$ and where the time at grid level $i = 0$ is discretised into contiguous timesteps of length $\Delta t$, such that the time at the beginning of each timestep is $n\Delta t$, where $n = 0, 1, ....$

The integration of any flow variable, $q(x,t)$ say, over the cell volume, $V_i$, and the duration of the timestep is performed by the following operators:

$$[q]^n = \int_{V_i} q(x, 2^i n\Delta t)\, dx \tag{2.11}$$

and

$$[q]^n_{2^i\Delta t} = \int_n^{n+1} [q]^n\, dt \tag{2.12}$$

Using an appropriate explicit numerical method each operator is approximated to yield a set of algebraic equations written in terms of the flow variables in the immediate vicinity to each computational cell. At the beginning of each timestep, $2^i n\Delta t$, the vorticity distribution $[\omega]^n$ in the wake is used to evaluate the the velocity field $u^n = u([\omega]^n)$ using

the FMM. Once the velocity field is known, operator splitting allows each operator to be applied in the following sequence

$$\begin{aligned} [\omega]^{*} &= [\omega]^{n} + [S]^{n}_{2^i\Delta t} \\ [\omega]^{**} &= [\omega]^{*} + [\omega \cdot \nabla u]^{n}_{2^i\Delta t} \\ [\omega]^{n+1} &= [\omega]^{**} + [u \cdot \nabla \omega]^{n}_{2^i\Delta t} \end{aligned} \tag{2.13}$$

and hence the vorticity field at time $t = (n+1)\Delta t$ is constructed. The sequence is then repeated for all $n \in N$. The flux of vorticity arising as a consequence of stretching is computed by application of Runge-Kutta integration to evaluate $[\omega \cdot \nabla u]^{n}_{2^i\Delta t}$. Using Strang's space-operator splitting technique [45], the three-dimensional problem is decomposed into three one-dimensional problems to which Toro's Weighted-Average-Flux (WAF) scheme [46] is applied to approximate the advection operator $[u \cdot \nabla \omega]^{n}_{2^i\Delta t}$. The WAF scheme is described later in § 2.3.1.4. By their method of construction, the means of approximating each of the operators is second order accurate and thus, overall, the entire explicit numerical scheme just presented is also second order accurate [47].

#### 2.3.1.3 Flow Variables

The WAF method, used in the VTM to advect the vorticity through the grid, requires the velocities normal to the cell faces to compute the inter-cell fluxes and thus the staggered grid arrangement proposed by Harlow and Welsh [48] is implemented to provide the required velocity information. This arrangement avoids the need to interpolate velocity information from the cell centres to the cell interfaces which is especially important since the solenoidal property of the flow will not be preserved otherwise.

#### 2.3.1.4 The Advection Routine

To perform the advection of the vorticity through the grid, the advection equation can be written by omitting the stretching and source terms from Eq. 2.9 to yield

$$\frac{\partial \omega}{\partial t} = u \cdot \nabla \omega \tag{2.14}$$

Using Strang's [45] method of splitting space-operators into their component parts to yield three one-dimensional problems, Eq. 2.14 can then be written in conservative finite-volume

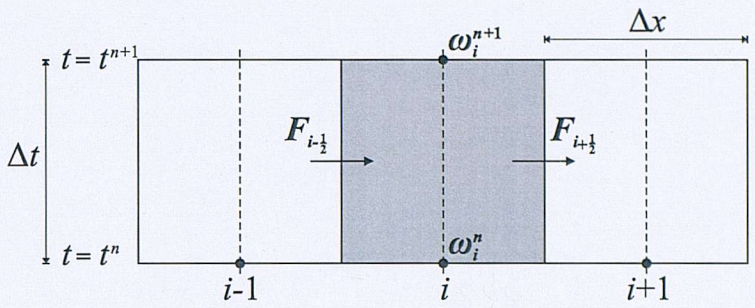



***Figure 2.3:*** *Stencil for calculating flux of vorticity across cell faces.*

form as

$$\omega_i^{n+1} - \omega_i^n = \frac{\Delta t}{\Delta x}(F_{i+\frac{1}{2}} - F_{i-\frac{1}{2}}) \tag{2.15}$$

where $F_{i+\frac{1}{2}}$ and $F_{i-\frac{1}{2}}$ are the flux vectors of vorticity crossing a cell face from the left cell and the right cell, respectively, as shown in Fig 2.3. The value of $\omega_i^n$ is constant across the cell and varies discontinuously between cells.

To define the fluxes, Toro's WAF scheme is used. The WAF method is a second order accurate scheme for solving one-dimensional Riemann-type, gas-dynamic problems where high density gradients due to the presence of shock-waves are present. The method is essentially an extension to Godunov's first-order accurate, conservative, piece-wise constant Riemann solver. Since rotor flows involve steep spatial gradients of vorticity, the WAF scheme can also be used to define flux vectors of vorticity. Consider first the intercell flux $F_{i+\frac{1}{2}}$ of vorticity. In the WAF scheme's treatment of the Reimann problem, an interval $I = [x_i, x_{i+1}]$ is segregated by a wave emanating from position $x_{i+1/2}$ with speed $u_{i+1/2}$ such that the flux vector $F_{i+\frac{1}{2}}$ represents the weighted sum of the values of the two partial fluxes on the left and right side of the wave front, namely, $F^{(1)}_{i+\frac{1}{2}}$ and $F^{(2)}_{i+\frac{1}{2}}$ respectively. The weighted intercell flux is then expressed as follows

$$F_{i+\frac{1}{2}} = W_1 F^{(1)}_{i+\frac{1}{2}} + W_2 F^{(2)}_{i+\frac{1}{2}} \tag{2.16}$$

where the partial fluxes are given by

$$\begin{aligned} F^{(1)}_{i+\frac{1}{2}} &= u^n_{i+1/2}[\omega_i]^n \\ F^{(2)}_{i+\frac{1}{2}} &= u^n_{i+1/2}[\omega_{i+1}]^n \end{aligned} \tag{2.17}$$

The weights, $W_1$ and $W_2$, represent the geometric extents of the two regions either side of the wave front, after time $t = t^n + \Delta t/2$ relative to positions $x = x_i$ and $x = x_{i+1}$

respectively, such that

$$\begin{aligned} W_1 &= \frac{1}{2}(1+\phi) \\ W_2 &= \frac{1}{2}(1-\phi) \end{aligned} \tag{2.18}$$

where the CFL number at the cell interface is given by $\phi = u_{i+1/2}\Delta t/\Delta x$. A similar procedure is carried out to yield the expression for the upwind intercell flux $F_{i-\frac{1}{2}}$, although the velocity on the opposite cell face, namely, $u = u_{i-1/2}$, is used.

To avoid the loss of monotonicity that this higher-order scheme induces, the scheme employs so-called wave-amplifier functions, $\zeta$, which switch in value depending upon the behaviour of the solution [49]. The amplifier functions modify the weighting functions so that Equation 2.19 is re-written to include the wave-amplifiers as

$$\begin{aligned} W_1 &= \frac{1}{2}(1+\zeta\phi) \\ W_2 &= \frac{1}{2}(1-\zeta\phi) \end{aligned} \tag{2.19}$$

where

$$\zeta = \zeta(r^n_{i+\frac{1}{2}}, \phi)$$

and where $r^n_{i+\frac{1}{2}}$ is the vorticity distribution ratio

$$r^n_{i+\frac{1}{2}} = \frac{\omega^n_i - \omega^n_{i-1}}{\omega^n_{i+1} - \omega^n_i}$$

The value of $\zeta$ depends upon the nature of the wave amplifier being used. The VTM uses the SUPERA type amplifier functions in general, as described in [49]. The objective of the amplifier is to avoid loss of monotonicity near large gradients by ensuring that the solution is Total Variational Diminishing, or TVD, which, in general, allows convergence of a consistent conservative numerical scheme. In the discrete sense, TVD is defined as

$$TV(\omega^n) = \sum_{i=-\infty}^{\infty} |\omega^n_{i+1} - \omega^n_i| \tag{2.20}$$

and for the scheme to be fully TVD the wave amplifier functions ensure that the following condition is satisfied

$$TV^{n+1}(\omega) \leq TV^n(\omega). \tag{2.21}$$

#### 2.3.1.5 Computing the Velocity Field

As alluded to earlier in this chapter, the evolution in time of the discretised vorticity transport equation 2.10 requires that the velocity field is known at the beginning of the time step. To compute the velocity field, the Biot-Savart equation 2.8 is approximated as

$$u(x) \approx \int_V K_\delta(x,y) \times \omega(y)\, dy \tag{2.22}$$

where $K_\delta$ is the Rosenhead-Moore regularised Biot-Savart kernel [50, 51] which takes the following form

$$K_\delta(x,y) = -\frac{1}{4\pi} \frac{(x-y)}{(|x-y|^2+\delta^2)^{3/2}} \tag{2.23}$$

The constant regularising parameter $\delta$ is included to account for the fact that the computational cells in the domain each contain a uniform distribution of vorticity, rather than a vortex singularity. The value of $\delta$ is chosen such that the location of the maximum velocity induced by the vorticity in a cell coincides with the edge of the cell, as shown in Fig 2.4.

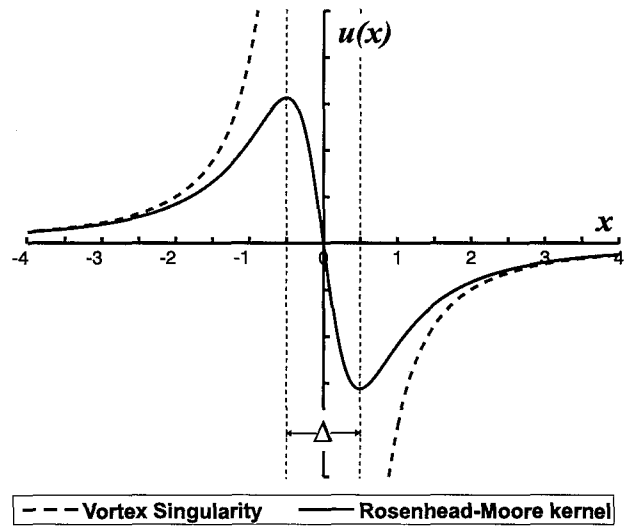



***Figure 2.4:*** *Velocity field induced by a Biot-Savart kernel (vortex singularity) and by the Rosenhead-Moore kernal (uniform distribution of vorticity in a cell of width $\Delta$).*

Simple summation of all the cell to cell Biot-Savart interactions in the computational grid results in a cumbersome $\mathcal{O}(N^2)$ operation. To compute the velocity field efficiently, the VTM employs a fast summation method called the Cartesian Fast Multipole Method (FMM) (See Greengard and Rokhlin [52, 53]). Such a method can be applied to any system where pair-wise interactions between discrete elements in the system domain can

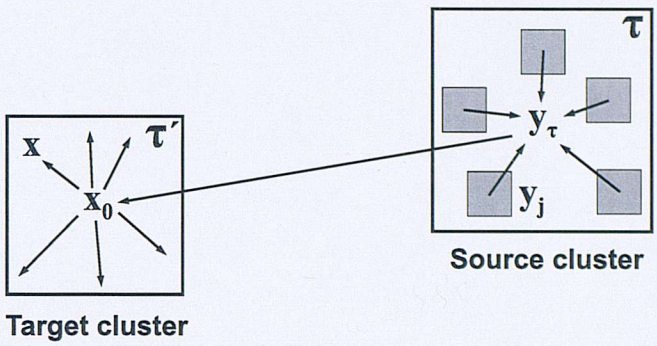



***Figure 2.5:*** *Schematic of cluster-cluster interaction approximated by multipole expansion.*

be represented by a suitable kernel function. The FMM is implemented in a manner that exploits the rectangular topology of the computational grid of the VTM such that the integral in Eq. 2.22 is expanded as an algebraic series, whereas in general, wieldier trigonometric expansions are required. The cost of the calculation is reduced by taking advantage of the fact that the magnitude of Biot-Savart interactions reduce rapidly with distance. This is achieved by grouping multiple, long-range, interactions together so that they can be expressed using a single algebraic series. The accuracy of the calculation is then controlled by the degree of truncation used to form the algebraic series.

The grouping, or clustering, of interactions together and subsequent approximation of their spatial influence is the pivotal concept of the FMM. Figure 2.5 shows this concept schematically.

A number $N_\tau$, of the total number $N$, of computational cells containing vorticity are systematically grouped together in a cluster $\tau$. The vorticity weighted centroid of the cluster lies at $y_\tau$ and the centre of each cell lies at $y_j$. The velocity induced at a point $x_0$ in a second, distant, cluster, $\tau'$, by cluster $\tau$ is calculated using an approximation, via Euler integration, to Eq. 2.22, as follows

$$\mathbf{u}(\mathbf{x_0}) = \sum_{j\in\tau} \mathbf{K}_\delta(\mathbf{x_0}, \mathbf{y_j}) \times \omega_j \tag{2.24}$$

Equation 2.24 is then expanded as a Taylor series about the centre of the source cluster, $\tau$, such as

$$\begin{aligned} \mathbf{u}(\mathbf{x_0}) &= \sum_{j\in\tau} \mathbf{K}_\delta(\mathbf{x_0}, \mathbf{y}_\tau + (\mathbf{y}_j - \mathbf{y}_\tau)) \times \omega_j \\ &= \sum_{j\in\tau} \sum_{k}^{\infty} \frac{1}{\mathbf{k!}} D_y^k \mathbf{K}_\delta(\mathbf{x_0}, \mathbf{y}_\tau)(\mathbf{y}_j - \mathbf{y}_\tau)^k \times \omega_j \end{aligned}$$

and truncating the series at the $p$th term yields the following approximation:

$$\mathbf{u}(\mathbf{x}_0) \approx \sum_{k=0}^{p} \mathbf{a}_k(\mathbf{x}_0, \mathbf{y}_\tau) \times \mathbf{m}_k(\tau) \tag{2.25}$$

The Taylor series expansion is three-dimensional and thus the above expressions include the vectors, $k = (k_1, k_2, k_3)$, $D_y^k = \partial/\partial y_1^{k1} \partial y_2^{k2} \partial y_3^{k3}$, $\mathbf{k!} = k_1! k_2! k_3!$, $\mathbf{x}^k = x_1^{k1} x_2^{k2} x_3^{k3}$ for $k_i \geq 0$, and the subscripts 1, 2 and 3 refer to the three Cartesian directions $x$, $y$ and $z$.

Parameter $\mathbf{a}$ represents tensor functions describing the range of the interactions in cluster $\tau$, and takes the form

$$\mathbf{a}_k(\mathbf{x}_0, \mathbf{y}_\tau) = \frac{1}{\mathbf{k!}} D_y^k \mathbf{K}_\delta(\mathbf{x}_0, \mathbf{y}_\tau) \tag{2.26}$$

and the local distribution of vorticity within $\tau$ is described by a moment function written as

$$\mathbf{m}_k(\tau) = \sum_{j \in \tau} (\mathbf{y}_j - \mathbf{y}_\tau)^k \omega_j \tag{2.27}$$

The above procedure results in a computation with a cost of $\mathcal{O}(N \log N)$. A computation with a cost of $\mathcal{O}(N)$ is achieved by using a truncated Taylor series expansion about the centroid of the target cluster $\tau'$ to represent the discrete velocities in that cluster induced by the source cluster. The spatial derivatives of $\mathbf{u}$ about $\mathbf{x}_0$ are required for this calculation. Thus, differentiating Eq 2.25 with respect to $\mathbf{x}_0$ yields

$$D_x^n \mathbf{u}_0 = (-1)^n \sum_{k=n}^{p} \frac{\mathbf{k!}}{(\mathbf{k}-n)} \mathbf{a}_k(\mathbf{x}_0, \mathbf{y}_\tau) \times \mathbf{m}_{k-n}(\tau) \tag{2.28}$$

and the velocity at a nearby position, $x$, can then be calculated approximately from the series representation about $\mathbf{x}_0$ as

$$\mathbf{u}(x) \approx \mathbf{u}(\mathbf{x}_0) + \sum_{k=1}^{p} \frac{1}{\mathbf{k!}} D_x^k \mathbf{u}(\mathbf{x}_0)(\mathbf{x} - \mathbf{x}_0)^k \tag{2.29}$$

where $n$ is the level of the data structure on which the multipole calculation is being carried out. The derivatives of the velocity field are also projected to a nearby position in a similar fashion.

The vorticity and velocity information is ordered and stored within the computer memory using an octree data structure. In the octree, the solution domain is decomposed hierarchically so that, at the lowest level, eight individual cells are grouped together to form a parent cluster, with the cells known as the children of that cluster. Since they

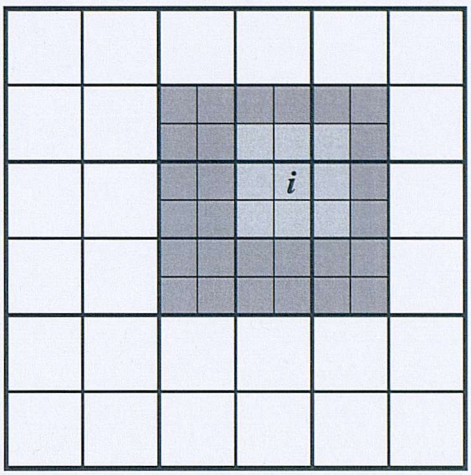



***Figure 2.6:*** *The velocity field of cluster $i$ is decomposed into the near-field (light grey), the intermediate-field (dark grey) and the far field (white).*

represent the lowest level of the structure, they are denoted as the leaves of the tree. At the next level, eight clusters are formed into a larger cluster, thus the smaller clusters are the children of the larger parent. This process is applied recursively until the whole solution domain is contained within a single, parent cluster. This uppermost parent is known as the root of the tree. This method of ordering the information is required by the FMM and also provides an efficient means of managing the creation and destruction of cells that was described earlier.

Application of the FMM commences with a sweep through the octree from the lowermost level, its leaves, to the uppermost level, the root of the data tree, during which the moments, $\mathbf{m}$, are computed using Eq. 2.27. The next stage of the procedure involves a sweep back down from the tree root, to the leaves of the tree, wherein the velocities on each level are calculated. At a cluster, $i$, at a level $n$ in the octree, the velocity is taken to be the sum of far-field, intermediate-field and near-field velocity components. The decomposition of the solution domain into the three fields is shown in Fig. 2.6. The near-field is defined as all the nearest neighbours of cluster $i$. The intermediate-field contains the clusters that are the children of those parents that neighbour the parent of $i$ and which are not in the near-field. The remaining clusters make up the far field. In terms of levels on the octree, the far-field represents level $n+1$, whilst the near and intermediate fields of cluster $i$ are on the $n$th level, and finally, the children of cluster $i$ reside on level $n-1$. Once the velocity due to the vorticity in the far field of cluster $i$ has been computed, the velocity due

to the intermediate-field is then calculated by evaluating the cluster-cluster interactions on level $n$. Once this has been done, the far and intermediate velocity contributions are then summed together and translated to the children of cluster $i$ using Eq. 2.29. These translated far and intermediate components of the velocity field thus become the far-field of the children of cluster $i$, whilst cluster $i$'s near-field becomes the intermediate field of its children. This process of evaluation and subsequent translation of the far and intermediate velocity fields is conducted on all clusters on level $n$, after which the downward sweep through the octree moves to level $n-1$, whereby the process is repeated. Note that the near-field velocity calculation is not generally performed at level $n$. The velocity field due to the vorticity in the near-field is only computed once the lowest level of the octree has been reached, i.e. once the near-field is that of an individual computional cell, and its neighbours are also cells. This contribution to the overall velocity field is computed directly using the Biot-Savart equation, as follows:

$$u(x) = \sum_j \mathbf{K}_\delta(\mathbf{x}, \mathbf{y}_j) \times \omega_j. \tag{2.30}$$

This final calculation, once performed for every cell on the lowest level of the octree, over the complete computational domain, results in the knowledge of the full velocity field by which the vorticity field can then be advected.

#### 2.3.1.6 The Rotor Aerodynamic Model

As a blade on a rotor rotates through the viscous fluid in which it is immersed, vorticity is generated on the blade's surface as a consequence of the spatial gradients of velocity of the flow that arise there. If the chord-wise angle of the blade's incidence to the flow is non-zero then the chord-wise distribution of the vorticity generated over the blade surface will engender a resultant force on the blade that acts normally to the free-stream flow. A variation in the span-wise distribution of the normal forces on the blade will result in the steady trailing of stream-wise vorticity from the trailing edges of the blade. Additionally, changes to the local flow velocity will result in the shedding of span-wise vorticity from the blade as the chord-wise vorticity distribution adjusts to the changing flow conditions.

In the VTM, the flow is generally considered to be inviscid and thus there exists no mechanism to directly create vorticity on the surfaces of rotor blades within the computational flow. Instead, the aforementioned local trailed and shed vorticity, $\omega_b$, is introduced

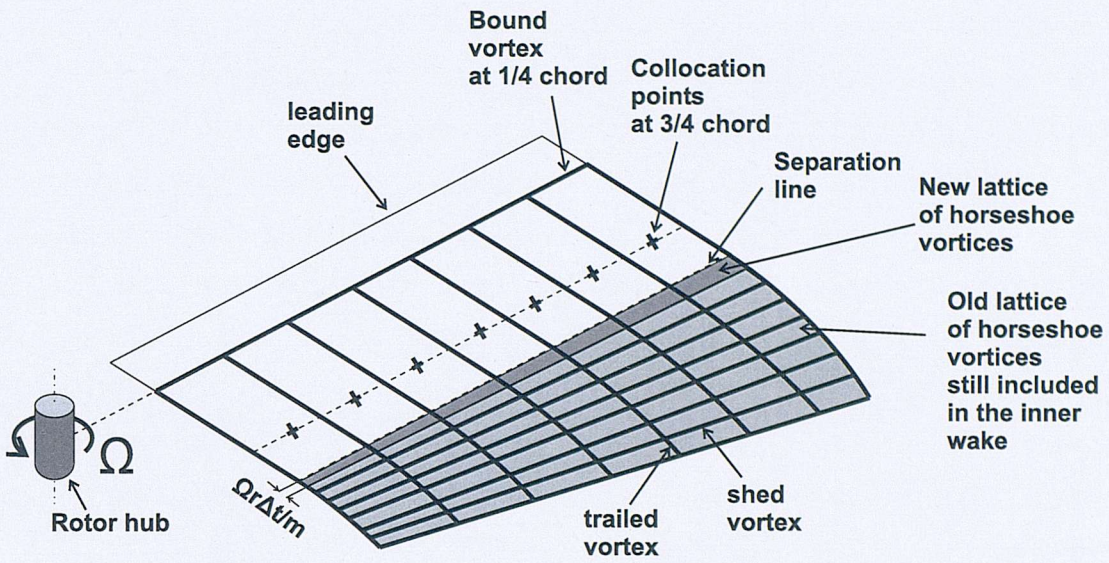



***Figure 2.7:*** *Model of blade aerodynamics and inner vortex lattice.*

into the flow via a vorticity source term, $S$, where

$$S = -\frac{d}{dt}\omega_b + u_b \nabla \cdot \omega_b \tag{2.31}$$

The terms on the right hand side of the equation are the shed and trailed vorticity respectively and $u_b$ is the local flow velocity at a given point on a blade. The vorticity generated on the rotor blades and the aerodynamic forces that result from this process are evaluated in a model that is distinct from the main wake-evolution model. The aforementioned source term is the means by which the two models are coupled together.

The Weissinger-L [54] version of the lifting line model is used to represent the rotor blade aerodynamics. Weissinger's method differs from the original method of Prandtl since it provides a means to represent swept wings, which Prandtl's method does not, and this is useful for modelling rotor blades with complex planform geometry. A schematic of the implementation of the lifting-line model in the VTM is shown in Fig. 2.7. The method represents a rotor blade as a series of connected bound vortex lines that lie along the quarter-chord line of an imaginary, flat, lifting surface. Corresponding to each bound vortex is a collocation point which lies on the three-quarter-chord line of the imaginary surface. Since the vorticity field must be divergence free, each bound vortex trails a stream-wise vortex line from each of its extremities such that the discrete bound and trailing vortices take the form of a horse-shoe. These three vortices are equal in strength, though the two trailing vortices are opposite in sense. The final condition required to

ensure that the vortex system is divergence free is that a vortex parallel to the bound vortex, and with strength equal to the change in strength over some finite time of the bound vortex, though opposite in sense, must be shed into the free-stream. The shed vortex closes off the horse-shoe at the ends of the trailed vortices in the free-stream.

The strength of the horse-shoe vortex system is fixed by the condition that the local flow velocity normal to the imaginary lifting surface at each of the collocation points must be zero. The local flow velocity, $u_b$, is the vectorial sum of the free-stream flow, the blade structural motions, the flow induced by the bound, shed and trailed vortex system on the blades within the rotor-aerodynamic model and the flow induced by the remainder of the rotor wake. The component of the local flow velocity normal to the lifting surface at each of the collocation points is set to zero to yield a set of algebraic equations that are solved to find the strength of each of the discrete bound vortices, $\omega_b$, and hence that of the trailed and shed vortices. Note that the arrangement of the bound vortex line at the quarter-chord and the collocation points at the three-quarter-chord line results in the idealised lifting-line lift-curve slope for an infinite aspect ratio surface of $2\pi \sin(\alpha_e)$, where $\alpha_e$ is the local value of the effective angle of attack at some station along the surface.

Clearly, in order to accurately simulate the aerodynamics of real rotors the full non-linear characteristics of the aerofoil sections, including the effects of Reynolds number, $Re$, and Mach number, $M$, must be modelled. In the VTM, the lift coefficient data, $C_L(\alpha, Re, M)$, for a given aerofoil section is defined in the form of look-up tables or polynominal curve fits generated from experimental data. In addition, as high angles of attack and reverse flow are common features of the rotor operating environment, the $C_L$ vs. $\alpha$ relationship in the full angle of attack range of $0° \leq \alpha \leq 360°$ is accounted for. If the available experimental data for the aerofoil performance does not include the effects of fluid compressibility, then the Prandtl-Glauert compressibility model, $L_\beta$, is applied, in that

$$C_L(\alpha, Re, M) = L_\beta[C_L(\alpha, Re), M] \tag{2.32}$$

where

$$L_\beta(C_L, M) = \frac{C_L}{\sqrt{1 - M^2}}. \tag{2.33}$$

Deviations of the aerofoil performance from that of the idealised lifting-surface are incorporated into the calculation of the strength of the bound vortex at each collocation

point by preconditioning the corresponding normal component of the local flow velocity through use of a scaling factor. The size of the scaling factor is based upon the predicted angle of attack, and so the corresponding lift coefficient for a given aerofoil, at the 1/4 chord line. The effect of the scaling factor is to effectively reduce the normal component of the local flow velocity in oder to mimic the loss of effectiveness of the aerofoil section in its stalled condition. Hence, the consequent strength of the bound vortex is moderated accordingly.

The timescales associated with the evolution of the rotor wake are known to be significantly larger than the timescales associated with the the near-blade unsteady aerodynamics and the accompanying high-frequency rotor-blade dynamics. This poses a significant problem of computational stiffness in the simulation of rotors and their wakes. To overcome this stiffness problem a sub-stepping algorithm is employed in the model of the rotor such that the overall simulation is decomposed, as previously mentioned, into an outer problem (the wake evolution) and an inner problem (the rotor evolution). Division of the global time step $\Delta t$ into $m$ number of sequential substeps allows the calculation of intermediate sources of vorticity as

$$[S]^n_{\Delta t} = \sum_{i=0}^{m-1} [S]^{n+i/m}_{\Delta t_i} \tag{2.34}$$

As the inner problem is advanced by timestep $\Delta t/m$ the blade sweeps round through an arc of angle $\Delta t/m$ radians. As it does so, the intermediate source of shed and trailed vorticity from that sub-step is released from a predefined separation line on the blade as a lattice of horseshoe vortices corresponding to each collocation point along the blade, as shown in the present figure 2.7. The lattice is allowed to advect freely in the flow in accordance with the local velocity field. After $m$ sub-steps, the large vortex lattice, which comprises $m$ number of horseshoe vortices from each collocation point, is interpolated into the main, outer, grid as the total vorticity source $[S]^n_{\Delta t}$.

#### 2.3.1.7 The Rotor Dynamic Model

Real helicopter rotors commonly consist of a complicated set of hinges which allow the blades to flap and lag normal to and parallel to the rotor disc plane, respectively. The mechanical assembly of each pivot often includes a number of springs and dampers and rigid linkages. A further degree of freedom, which is coupled to the former two, is the blade

pitching mechanism which provides the pilot the means to control the aerodynamic forces generated by the rotor. The mechanical method by which the pitching and the flapping and lagging degrees of freedom are coupled together strongly influences the amplitude at which the blades flap and lag out of the disc plane. The rotation of the blades about the rotor hub and the structural motions of the blades, relative to the rotation of the blades about the hub, introduce centrifugal and Coriolis forces into the rotor structural dynamics. The dynamics of real rotor systems are further complicated by bending and twisting of the blades. The resulting mechanical assembly possesses complex and non-linear dynamics when in operation which must be modelled correctly in order to obtain realistic rotor aerodynamic as well as rotor dynamic behaviour from a simulation. The configuration of rotors can vary enormously from one design to another, adding further to the difficulties of modelling these complex mechanical systems.

In the VTM, the simple blades modelled in the simulations featured in this thesis are adequately represented as rigid structures, with a uniformly distributed mass, that pivot about a set of simple hinges and are constrained by idealised springs and dampers. But, the equations of motion for rotor blades are not expressed in the VTM, since a different set of equations will be required each time a new rotor configuration is to be simulated. Instead, the VTM employs the Langrangian dynamic approach (see Ref. 55 for instance) since this provides the necessary generality and flexibility required for comprehensive, yet convenient modelling of widely varying and complex, non-linearly coupled mechanical systems. In essence, the Lagrangian approach represents the various sources of mechanical energy, namely, the kinetic energy $T(q,\dot{q})$, the potential energy $U(q,\dot{q})$, the dissipation $D(q,\dot{q})$ and the work done $Q(q,\dot{q})$, within the system, relative to a set of $p$ generalised coordinates, $q$. The generalised coordinates and their time derivatives are defined as $q = q(q_1, q_2, ..., q_p, t)$ and $\dot{q} = dq/dt$, respectively. Application of Hamilton's principle of minimisation-of-action to the general Lagrangian equation of the system leads to the Euler-Lagrangian equation

$$\frac{d}{dt}\left(\frac{\partial \mathcal{L}}{\partial \dot{q}}\right) - \frac{\partial \mathcal{L}}{\partial q} + \frac{\partial D_t}{\partial \dot{q}} - \int_{t_0}^{t_0+t} \frac{\partial D_t}{\partial \dot{q}}\, dt = Q \tag{2.35}$$

where $\mathcal{L} = T - U$ and $Q$ is the work done on the blades by the aerodynamic forces. Expanding the first term on the left side of Eq. 2.35 to introduce explicitly the indices, $i, j$,

of the generalised coordinates as

$$\frac{d}{dt}\left(\frac{\partial \mathcal{L}}{\partial \dot{q}}\right) = \frac{\partial^2 \mathcal{L}}{\partial \dot{q}_i \partial \dot{q}_j}\ddot{q}_j + \frac{\partial^2 \mathcal{L}}{\partial \dot{q}_i \partial q_j}\dot{q}_j, \tag{2.36}$$

the full Euler-Lagrangian is then written as

$$\frac{\partial^2 \mathcal{L}}{\partial \dot{q}_i \partial \dot{q}_j}\ddot{q}_j + \frac{\partial^2 \mathcal{L}}{\partial \dot{q}_i \partial q_j}\dot{q}_j - \frac{\partial \mathcal{L}}{\partial q_i} + \frac{\partial D_t}{\partial \dot{q}_i} - \int_{t_0}^{t_0+t} \frac{\partial D_t}{\partial \dot{q}_i}\, dt = Q_i. \tag{2.37}$$

Numerical evaluation of Eq. 2.37 allows for the accelerations, $\ddot{q}$, in the system to be solved directly. Upon the completion of this calculation, the state of the coordinates, $q$, are computed via the simple forward difference scheme, such that

$$q^{n+1} = q^n + \dot{q}^n \Delta t \tag{2.38}$$

and

$$\dot{q}^{n+1} = q^n + \ddot{q}^n \Delta t \tag{2.39}$$

The modelling approach provides information regarding the motion of the blades and the associated forces exerted on the rotor hub. The dynamics of the rotor are coupled to the wake model via the source term, $S$, during the calculation of the local flow velocity relative to each collocation point on the blades, as discussed earlier.

## 2.4 Model Validation

The numerical experiments described in this thesis have been designed to reveal behaviours and trends of the physics of the VRS that are general to all rotorcraft; there was no one helicopter type that was the focus of the research, and nor was any one previous VRS experiment the subject of an in-depth investigation. Indeed, in many of the cases presented in this thesis the rotor has been idealised in some way so as to reduce the number of interacting components of the flow physics down to a level which then allows the fundamental processes at work to be exposed - something that is not possible with model rotors in wind tunnels or real helicopters in real flight scenarios. The accuracy to which the aerodynamics of any particular rotor has been modelled becomes unimportant, therefore. However, in an investigation designed to expose previously obscure flow phenomena, one must have confidence in the realism afforded by the method employed to undertake the investigations. In the context of the present research, this means that there must be little

doubt in the ability of the numerical means by which the VTM solves the fundamental equations that govern the flow physics to provide an appropriate level of realism.

Confidence in the method is gained from obtaining good agreement between experimental data and the results of a VTM simulation of the experiment. The accuracy of the VTM has been validated in this way in a number of instances. Recently, Brown and Line [35] conducted a simulation of Caradonna and Tung's well known experiment of a hovering, two-bladed rotor [56]. Good quantitative agreement of the loading distribution along the rotor blades was obtained. An assessment of the simulated tip vortex trajectories showed that they were well matched to the experimentally derived vortex trajectories from the time of inception up to a vortex age of 0.75 rotor revolutions, after which a noteworthy discrepancy in the two data sets became apparent. Since there was evidence of significant unsteadiness in both the real and simulated wakes around the region of the flow where the charted trajectories began to deviate, it was deemed that this unsteadiness was the cause of the deviation. This was a reasonable explanation, to a degree, since any disturbance due to free-stream turbulence or other cause of flow perturbations, such as a mechanical imbalance in the rotor, would grow unstably in the flow with the result that the wake would be subtly different in detail to the simulated wake. Indeed, the logical extension to this postulation is that the details of the wakes of similar rotors, but with slightly different mechanical imperfections and operated in different wind tunnels would display subtly different, time-dependent, wake features. The conclusion to this argument then, is that excellent agreement between data sets of unsteady flow phenomena would be the result of perfect laboratory, and numerical, conditions or of improbably good fortune.

In the same paper, Brown and Line presented information pertaining to a validation of the ability of the VTM to accurately simulate the dynamic, and thus aerodynamic, behaviour of rotors in forward flight. Harris [57] recorded the blade flapping behaviour of an isolated, four-bladed rotor, flying over a range of low forward speeds whilst operating with constant thrust but with no cyclic control, thus the blades were free to flap in response to the free-stream flow, only. In the past this case has been a particularly challenging one to model due to the strong interaction of the rotor wake with the rotor aerodynamics at low forward speeds. In particular, a significant change in wake geometry and thus rotor performance occurs as the advance ratio of a rotor increases from below to above $\mu_x \approx 0.08$. The implication, then, is that to capture the associated rotor aerodynamics and dynamics,

any model must accurately simulate the wake behaviour. Very good agreement with the experimental data was obtained in both the longitudinal and the lateral flapping behaviour at all but the very highest of the forward speeds that were considered. The discrepancy was thought likely to be due to the deficiency of the description of the post-stall lift variation in the blade aerodynamic model, since stall is a possibility on the retreating blade at high-speed forward flight. The conclusion that can be drawn from that particular study is that the VTM simulates both the wake and the rotor behaviour with a high degree of realism, and that the level of realism is reduced only when the limitations of the simple model used to replicate the non-linear aerodynamic performance of an aerofoil are surpassed.

In their paper on the aerodynamics of co-axial rotors, Kim and Brown [58] compared predictions from the VTM of the relationship between the total power demand and the thrust of both a single and a co-axial rotor in hover, with similar results taken from the experiment of Harrington [59]. Accurate prediction of the power requirement requires, in general, an accurate prediction of the rotor inflow distribution. The inflow distribution is strongly dependent upon the structure of the wake in the vicinity of the rotor. The VTM achieved excellent agreement over the full range of thrust and power data considered, in the case of the single rotor. The agreement with the performance of the co-axial rotor was also very good except at the high end of the range of thrust coefficients considered. This discrepancy was attributed to the limitations of the profile drag model employed in that particular simulation.

The foregoing review of some of the validation exercises to which the VTM has been subjected has highlighted a body of evidence that strongly suggests that the VTM can predict the aero-mechanical behaviour of a rotor, when operating under the conditions that were simulated, with a high degree of accuracy. Blade aerodynamics and dynamics measured in experiments have been well matched in simulations performed by the VTM and this must imply that the computed structure and dynamics of the associated wakes have been faithfully represented to the required degree of resolution. That is to say, the dominant fluid dynamic processes at work in the experiments have been accurately replicated by the VTM's solution of the governing equations of the system. Such a demonstration of predictive success may give reason to suspect that any rotor flow phenomenon could be well modelled by the VTM. However, in the validation cases presented, the rotor wake was able to convect quickly away from the rotor and thus faithful description of the

strength and structure of the vorticity field, at distances from the rotor where it has only a relatively small influence on the rotor performance, is of only secondary importance. Since the vorticity field is properly coupled to the velocity field, a lack of accuracy in the prediction of the far wake distribution will arise partly from the extent to which vortical structures are diffused into the surrounding computational domain as they evolve in time. All rotor wakes computed by the VTM exhibit a breakdown of the orderly structure of the flow field some distance from the rotor. Therefore, the character of the perturbations that so evidently arise in the simulated flow field must also play some role in how the flow field evolves, although the way in which the perturbations grow during the computation, upon their inception, must surely be adequately physical since such growth is governed by the vorticity transport equation solved in the VTM. In descending flight, however, especially at speeds sufficient to induce the VRS, the rotor operates within its wake and the disturbances in the wake engender unsteadiness sufficiently close to the rotor to manifest as fluctuations in the blade loading. As a consequence, it is necessary to confirm that the prediction of the long term evolution of the rotor wake in descending flight is also faithful to reality, in essence, if not in exact detail.

Previous to the current work on the VRS using the VTM, several other investigations were undertaken by Brown as part of larger studies into the VRS. Newman, Brown, Perry *et al.* [7] reported the derivation of a simple engineering model to predict the onset of the VRS which was based upon disturbance convection rates. The model showed good agreement with experimental data for the prediction of the descent speed boundary at which the VRS would initiate, although the measure of VRS initiation is a somewhat subjective one. In the paper, the VTM was used to explore some of the VRS physics. Visualisations of the rotor wake when the rotor was descending at various speeds showed that the wake adopted the expected geometries: In a steeply angled descent, at a speed well clear of the VRS onset boundary predicted by the aforementioned engineering model, the geometry of the rotor wake resembled that of a wake of a rotor operating in the WBS, as expected. At a slightly lower descent speed, just outside of the onset speed boundary, the wake form indicated that the rotor was not quite in the VRS, but probably in the turbulent wake state. At a lower descent speed though, which the engineering model suggested should be in the middle of the VRS flight speed envelope, the rotor wake geometry had adopted the toroidal form that the experimental VRS flow-field visualisations of Drees

and Hendal [14] exposed. In a second simulation, the large fluctuations in the rotor thrust signal and the various snapshots of the wake geometry, which showed significant motion of the wake between image frames, indicated that the VTM was able to predict the high levels of unsteadiness in the flow field that has been reported from flight tests and experimental investigations. The fact that the VTM has been shown to replicate expected rotor wake behaviour at a number of descent speeds is suggestive, at least, that the VTM possesses the required faculties for adequate simulation of the rotor vortex ring phenomenon.

Further evidence of the VTM's suitability to simulate the aerodynamics of descending rotors was presented in work by Brown and Leishman *et al.* [34]. In an investigation into the influence of blade twist on the behaviour of a rotor operating in the VRS, that will be discussed at length in Chapter 5 of this thesis, the VTM simulated a rotor descending steeply, from an initial hover, through the VRS and into the WBS whilst operating with nominally constant thrust. As part of their discussion, the thrust signal produced by the rotor during its descent was shown. The sudden increase in thrust fluctuations that are a characteristic of the VRS arose at a descent speed of roughly one half of the mean inflow velocity. That is, the simulated VRS onset speed was similar to that recorded using the same measure, and, importantly, the same rotor, in the experiment of Azuma and Obata [12] and, also, to that predicted by the engineering model of Newman *et al.* [7]. It must be noted that apart from using the same rotor, no attempts were made in the paper of Brown *et al.* [34] to compare results directly. In fact, no mention of the experiment was made in this respect, this is merely the assessment of the present author. In addition, a more subtle agreement with experiment was evident from the simulations. The VTM predicted the same dependency of auto-rotation speed on blade twist rate as that observed by Castles and Gray in their VRS experiment [11] (their experiment will be discussed in detail later, again in Chapter 5 of this thesis). This latter agreement with experiment suggests strongly that the VTM captured both the finer details of the aerodynamic environment around the rotor that arise during the VRS as well as the global aspects of the VRS fluid dynamics.

The existing evidence for the ability of the VTM to accurately simulate the flow field around a rotor and the associated performance of the rotor, as it operates in or near to the VRS flight regime, is convincing, if a little indirect; the VTM has not, hitherto, been used explicitly to predict the behaviour of a specific rotor for which experimental VRS data

| | |
|---|---|
| Blade number, $N$ | 2 |
| Rotor solidity, $\sigma$ | 0.077 |
| Blade twist, $\theta_t$ | $-5.5°$ (linear) |
| blade chord, $c$ | $0.12R$ (constant) |
| root-cut-out | $0.2R$ |

*Table 2.1: Rotor definition*

exists for comparison. Such direct comparison is important, though, in order to provide further evidence in support of the VTM's abilities when a large body of research into the VRS is to be conducted using the VTM as the main research tool. In the remainder of this section, therefore, the results of a numerical simulation of Gao's experimental configuration [16] are compared with his experimental data to show that the VTM is indeed capable of capturing the flow physics of the VRS to a reasonable degree of accuracy.

### 2.4.1 Experimental Setup

In his experiments, Gao [16] used, among others, a two-bladed teetering rotor as defined in Table 2.1. In his tests, the collective pitch was held constant at 10° while the descent speed of the rotor was varied. The attraction of Gao's experiment compared to the many other tests described in the literature is the simplicity of the rotor configurations that Gao tested, together with the relatively low levels of twist incorporated into the blades of his rotor. This last point is important, as it avoids the issues of radial flow and the resultant stall delay that are thought to complicate the behaviour of more highly twisted blades (see Ref. 60 for instance). Gao's experiments have a further advantage in that they were conducted on a whirling tower, rather than in a wind tunnel, and thus contamination by the various wind tunnel effects should be absent. Other physical effects associated with the whirling tower, such as centripetal forcing of the wake and gyroscopic effects on the rotor remain significant unknowns, however (despite Gao's conclusion that these effects would be negligible) but they were not modelled in the VTM simulations.

### 2.4.2 Numerical Simulation

The simulation faithfully modelled the description of the rotor given above, although the rotor blades were assumed to be rigid. It is important to note that, in all of the VTM

simulations discussed in the present work, the range of descent speeds of interest was traversed by flying the rotor at a constant, but small, rate of acceleration ($d\mu_z/dt = 0.0002$ per rotor revolution). Acceleration is known to affect the onset and development of the VRS [8, 33], and this feature of the simulations, although likely to have only a small effect, must be borne in mind when considering the data. The blade aerodynamics were resolved by 20 collocation points in a cosine distribution along each blade. The computation was advanced by a global timestep of $\frac{1}{62}$ of the rotor period. The cell size on the finest grid level was $\Delta_0 = 0.1R$. This grid size provides a rather low resolution of the flow field. However, the simulation required the rotor to remain in hover for at least 40 revolutions prior to the commencement of its descent in order for any unsteadiness in the thrust level due to the start-up of the rotor to disappear. In addition, to avoid the effects that an accelerated descent might engender, the acceleration level selected was necessarily small. Therefore, approximately 400 rotor revolutions were required to complete the simulation: this is a very large number in the context of rotorcraft simulations. On the computers available for the simulations at the time the work was done (2Ghz Pentium processor with 1Gb RAM) the simulation discussed here took approximately 3.5 weeks to complete. Due to the high cost of running this simulation, therefore, it was deemed necessary to determine whether such a low resolution computation would provide the fidelity required to obtain representative results. The matter of the dependency of the results on the computational cell size is discussed in some detail in the section that follows this.

### 2.4.3 Results

Figures 2.8 and 2.9 show direct comparisons between VTM simulations and Gao's experimentally obtained thrust data. The thrust signal is separated into a mean component and a superimposed fluctuation, and, to match with Gao's presentation of his own data, is plotted against non-dimensional descent rate $\bar{\mu}_z = \mu_z/\sqrt{C_{T_h}/2}$. The agreement between simulation and experiment for the mean thrust is both qualitatively and quantitatively reasonable, although there are some differences in detail. For instance, the thrust-settling seen in Gao's data is very subtle and occurs over a smaller range of descent speeds, between $0.63 \leq \bar{\mu}_z \leq 0.78$, than it does in the simulation - between $0.5 \leq \bar{\mu}_z \leq 0.95$. From a qualitative perspective, the VTM results exhibit the distinct rise in thrust level post the thrust-settling episode that is also evident in Gao's data. Interestingly, Gao's results show

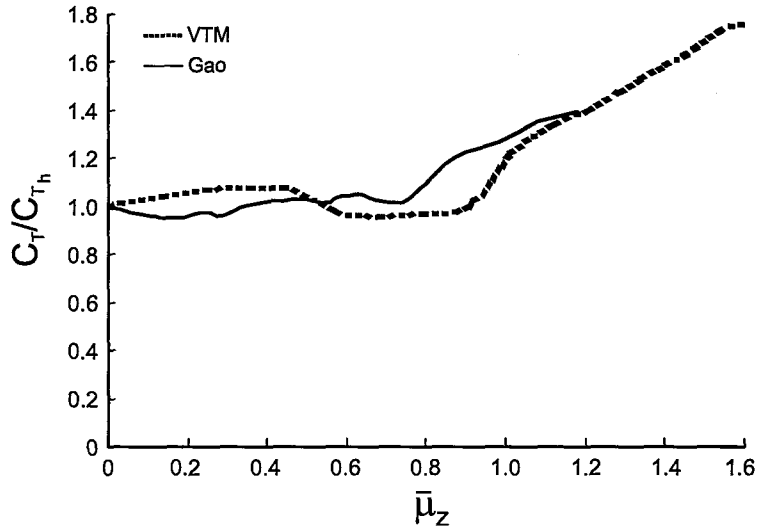



***Figure 2.8:*** *Mean thrust vs. descent rate. The graph shows a comparison between the results of a VTM simulation and Gao's experimental data.*

a dip in the mean $C_T$ during very low speed descent, which seems contrary to the predictions of blade-element theories. The simulation results, however, show the more intuitive variation over the same range of descent rates that is a common feature of other VRS experimental results, such as those of Yaggy and Mort [10] and Azuma and Obata [12].

The fluctuating component of the thrust is represented in Fig. 2.9 as the standard deviation, $S_{C_T}$, of $C_T$ about the mean, expressed as a percentage of the mean $C_T$ occurring at the same descent rate. The figure shows good qualitative agreement between simulation and experiment, particularly with regards to the descent rate at which the fluctuations in rotor thrust attain their greatest amplitude. However, the fluctuations predicted by the VTM are far more severe than those measured in Gao's experiment. Since the blade loading, blade geometry, lock number and the mechanical configuration of the simulated rotor are as those specified by Gao, it is difficult to determine the reasons behind the large discrepancy without more information about the details of the experiment. For instance, an important distinction between the simulation of Gao's experimental system and the real system itself is that the simulated thrust data were obtained by direct integration of the aerodynamic loading on the blades, whereas some degree of attenuation of the time-varying component of the experimental signal is inevitable given the impossibility of constructing an absolutely rigid experimental rig. Discussion, better still, quantification, of this effect is very rare in the experimental VRS literature. Since the qualitative behaviour of the

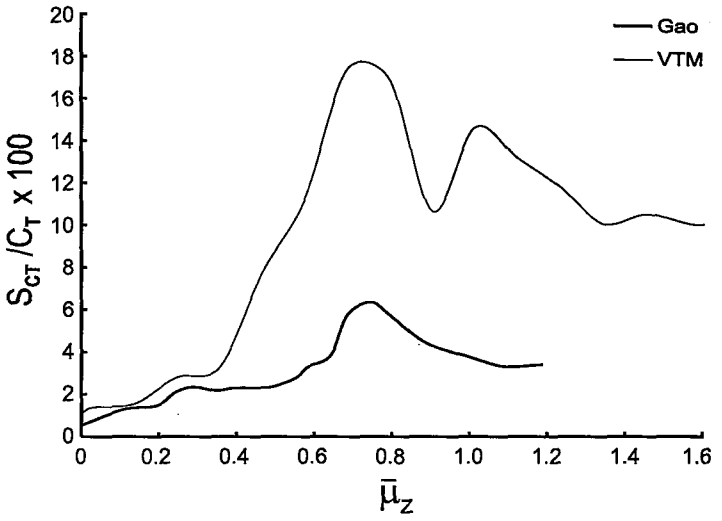



***Figure 2.9:*** *Standard deviation of thrust fluctuations vs. descent rate. The graph shows a comparison between the results of a VTM simulation and Gao's experimental data.*

fluctuating component of the thrust signals are in reasonably close agreement, it is at least conceivable that the gross behaviour of the rotor wake in Gao's experiment is being replicated by the VTM, even if the magnitude of the fluctuations, as measured, are quite different.

Many of the classical experimental and analytical references portray the effects of the VRS on rotor performance by presenting the variation with descent speed of the mean inflow generated by the rotor. The difficulties involved in obtaining the inflow directly from experimental measurement are usually circumvented by deriving this information from measurements of rotor thrust and torque [11, 22]. The identical process can be applied to performance data obtained from the VTM, and predictions can be compared against experimental data for similar rotors.

The approach adopted to obtain the inflow from VTM predictions of thrust and torque follows directly the technique used by Washizu *et al.* [22]. Firstly, the profile torque of the rotor is estimated as

$$C_{Q_0} = C_{Q_h} - C_{T_h}\lambda_h \tag{2.40}$$

where $C_{Q_h}$ and $C_{T_h}$ are the torque and thrust coefficients measured in hover, and $\lambda_h = \sqrt{C_{T_h}/2}$. Then, assuming that the relationships

$$C_P = (C_Q - C_{Q_0}) + C_T\mu_z \tag{2.41}$$

and

$$C_P = C_T \lambda_i \tag{2.42}$$

hold in descending flight, the mean inflow through the rotor is given by

$$\lambda_i = \left( \frac{C_Q - C_{Q_0}}{C_T} + \mu_z \right) \tag{2.43}$$

It should be noted that this analysis assumes that the rotor inflow is distributed uniformly across the rotor disc, and thus produces results that are somewhat at odds with direct measurements of velocity in the plane of the rotor.

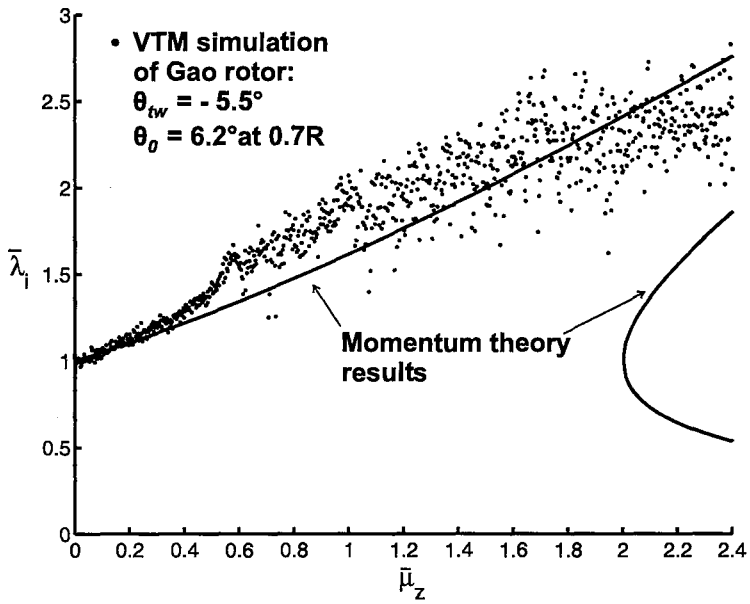



***Figure 2.10:*** *Calculated mean inflow vs. descent rate: VTM simulated data.*

Figure 2.10 shows the variation of normalised inflow, $\bar{\lambda}_i = \lambda_i / \sqrt{C_{T_h}/2}$, obtained using Eq. 2.43 from the thrust and torque data obtained from the VTM simulations of Gao's experiment, as discussed earlier, plotted against, normalised, non-dimensional descent rate $\bar{\mu}_z$. For comparison, Fig. 2.11 shows experimental data obtained by Washizu *et al.* [22] for a three bladed rotor with 8° of twist at various collective pitch settings. Within limits, the variation of inflow with descent rate is traditionally held to be a universal characteristic of the behaviour of all rotors within the VRS. Thus, even though the rotors used in the simulation and in Washizu's experiment are not directly comparable, it can be seen that the simulations capture well the broad characteristics of the measured variation of inflow

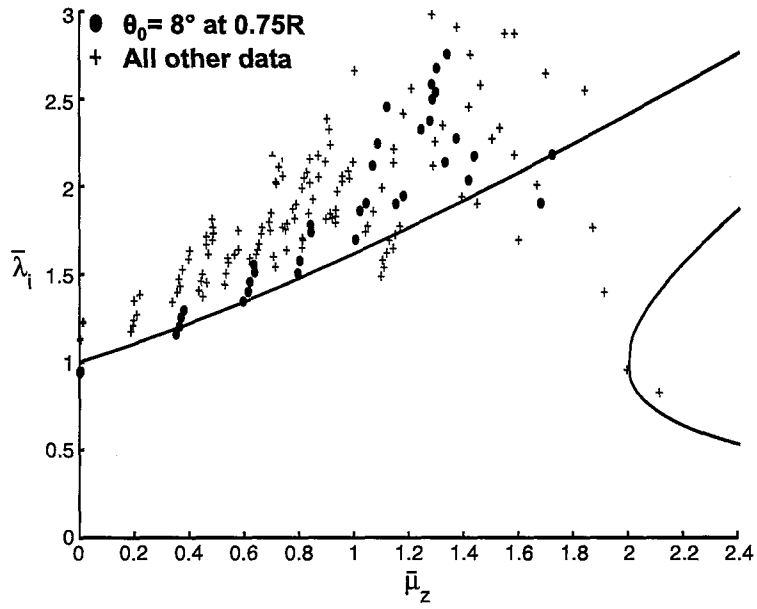



***Figure 2.11:*** *Mean inflow vs. descent rate: Data from experiments of Washizu et al.*

with descent rate, as well as the extent and order of magnitude of the thrust perturbations, represented by the scatter in the data, that was produced by the rotor during its transit through the VRS. It is interesting to note that whereas the VTM significantly over-predicted the thrust fluctuations measured by Gao, it appears from the scatter in the calculated inflow data shown in the two figures that the VTM has captured similar thrust fluctuations as those measured by Washizu *et al.* Such a variance in the trends of the VTM comparisons highlights the difficulty of performing a satisfactorily rigorous model validation exercise.

The foregoing introductory discussion on the predictive capabilities of the VTM along with the direct comparison of simulation and experimental results that followed suggest that the VTM is inherently capable of a reasonably good level of quantitative accuracy in predicting the aerodynamics of rotors in descending flight. Validation is an ongoing process, however, and is certainly not aided by the paucity at present of rigorously-defined, self-consistent data of the quality and resolution required to properly validate modern computational codes.

## 2.5 Dependence on Computational Resolution

As with all aerodynamics research that uses CFD, there is always a compromise between simulation duration and simulation accuracy. The general aim of this thesis was to explore the fundamental fluid dynamic processes that govern many aspects of the rotorcraft vortex ring phenomenon, rather than to investigate the detailed behaviour of a specific rotorcraft when flying in the VRS regime. Arguably, then, an acceptable simulation of the VRS is one that shows the rotor and the wake to possess the expected characteristics at roughly the appropriate descent speeds. This level of acceptability, using a low level of grid resolution, has demonstrably been achieved, as discussed in the preceding section. The properties of the VTM allow, within limits, the choice of computational cell size to be made on the basis of the requirements of the modelling exercise at hand. Therefore, several cell sizes have been used in the various simulations presented in this thesis. The criterion used to select the cell size was largely based upon the level of detail in the flow field that it was necessary to expose, whilst being tempered by the need to keep the simulation run-time to a minimum. To give a further idea of the duration of some of the simulations conducted for this thesis, the high resolution runs of Chapter 3 took approximately four months each, whilst the low-to-medium level resolution simulations featured in Chapter 5 took approximately 5 weeks each. In any case, it is still important to consider how the level to which the flow field is resolved affects the results of the VRS simulations, especially since this flow phenomenon is so highly erratic and so apparently driven by fluid instabilities.

The sensitivity to cell size of VTM simulations has been tested on several occasions in the past. In his paper describing the VTM, Brown [28] tested the stability of the solution to changes in the cell size by examining the effect that grid resolution had on the calculation of inflow distribution through a rotor in forward flight. Results from simulations using 10, 20 and 40 cells per radius, $R$, were compared to an analytical solution. Importantly, the comparison showed convergence of the numerical results to the analytical solution as the cell size was reduced. The inflow distribution calculated in the simulations using the largest cell size showed reasonable agreement with the analytical solution and with the results given by the other two simulations. However, there was a significant difference in the magnitude of the peak inflows over the outer edge of the disc, though the agreement over the rest of the disc was excellent. It was noted, though, that reducing the cell size led to a loss of resolution of the structure of the associated wakes and a smearing of the

distribution of the inflow through the rotor for the same vorticity source into the flow. But, changing the cell size did not qualitatively alter the global form of the solution. It was concluded, therefore, that reducing the cell size merely results in features in the flow field with a scale comparable to the size of the computational cell, not being fully resolved. In a further test of the effects of grid resolution, the loading distribution along a blade of a hovering rotor recorded in the experiments of Caradonna and Tung [56], as discussed earlier, was compared to numerical data from simulations using grid resolutions of 10, 15 and 20 cells per radius along with, respectively, 10, 15 and 20 collocation points evenly distributed along the blades. Once again, convergence to the experimental data with increase in resolution was noted, but the difference between the three sets of numerical results and the experimental data was small, even in the case when only 10 cells per radius were used. Finally, a comparison of the corresponding computed trajectories of the tip-vortices from each of the latter simulations was made with the experimentally correlated tip-vortex geometry for a hovering rotor. It was shown that even when only 10 cells per radius were used, the agreement with the experimentally derived data was good.

Furthermore, in Brown and Line's paper [35] the simulation conducted to examine Harris' forward flight experiment, as discussed earlier, was actually performed twice - with the only difference between the two simulations being the size of the computational cells used. In one simulation, the cell size was $\Delta_0 = 0.016R$ (62.5 cells/R), a high resolution, whilst the other simulation used a cell size of $\Delta_0 = 0.04R$ (25 cells/R), a medium resolution. The evidence provided showed only a small quantitative difference in the results for the flapping dynamics of the rotor blades. Such an outcome strongly suggests that when vorticity is the conserved quantity in a simulation, the prediction of low frequency rotor dynamics, which are largely dependent upon gross and relatively slowly varying features of the wake, are insensitive to the size of the computational grid and hence insensitive to those fine scale features in the flow that are smeared out by low resolution computations. This bodes well for VRS simulations since the global dynamics of the wake appear to have timescales of the order of tens of rotor revolutions [13, 15]. Indeed, in the same study, the effect of losing the finer flow scales was made clear in a comparison of the rotor wake topologies and the azimuthal disc loading. The images of the wakes showed that some of the finer scale features of the tip and root vortices were distinctly under resolved when the cell size was relatively large. The global solution, however, was not affected. The

smearing of the fine tip-vortex features in the low resolution computation manifested as an inability of the computation to capture the high-frequency Blade Vortex Interactions (BVI) induced fluctuations in the loading over the disc. However, the gross features in the loading captured by the high resolution simulation were also present in the less well resolved data.

### 2.5.1 Grid Dependence Test

In order to examine explicitly the possible influence of the size of the computational cell on the outcome of a rotor VRS simulation, two simulations of a rotor undergoing an accelerated descent from hover through the VRS and into the WBS were performed. The rotor operated with nominally constant thrust and its flap and lag dynamics were suppressed, making the rotor completely rigid. This latter aspect of the rotor model was employed simply to reduce the computational cost of the simulation and to remove from the problem an aspect of the flow physics thought not to be of importance in this particular matter. The simulations differed only in the size of the computational cells used. In simulation (a) the cell size was $\Delta_0 = 0.1R$ (10 cells per rotor radius) and in simulation (b) the cell size was $\Delta_0 = 0.05R$ (20 cells per rotor radius). In both cases the number of collocation points used on each blade was 20, which were cosine-distributed along the blades. Figure 2.12 shows a comparison of the thrust signal and Fig. 2.13 shows the standard deviation of the thrust about the mean that were generated during the two simulated descents. In addition, Fig. 2.14 shows a comparison of the rotor torque (less instantaneous profile torque, $C_{Q_P}$) that each rotor shaft was subjected to during each simulation. In each case, the data presented has been filtered using a moving averaging window with a period of four rotor revolutions. This was applied to the raw data to remove the high frequency fluctuations that obscure the main features of the thrust and torque behaviour. This data processing method is described in § 2.7.2.

Comparison of these simple rotor performance measures reveals a clear dependence of the solution on cell size. Consider first the mean thrust data and the standard deviation of the thrust fluctuations. The sudden change from a steady signal to a highly oscillatory signal, and then back to a steady signal again, is generally an indication of the pre-VRS, in VRS and post-VRS conditions, respectively. It is very evident, then, that halving the cell length produces significantly earlier onset of the VRS, though, interestingly, the

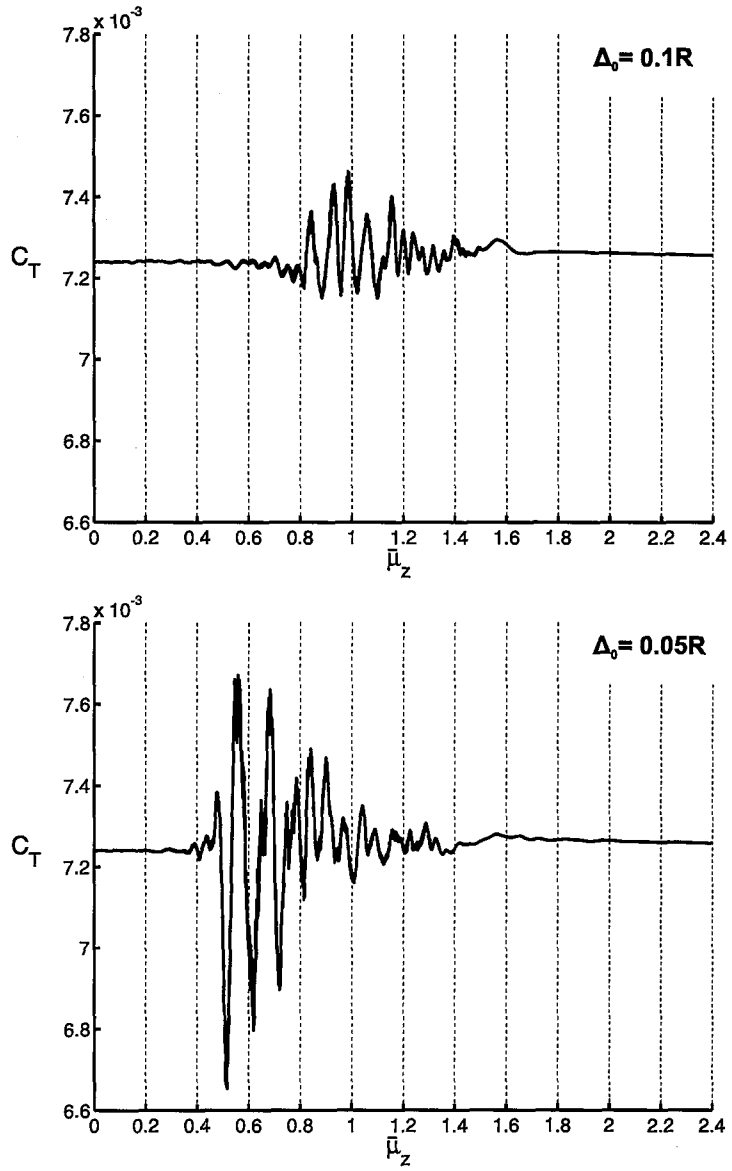



***Figure 2.12:*** *Comparison of the effect of computational cell size, $\Delta_0$, on the thrust coefficient produced by a rotor in descending flight. The thrust signal has been filtered.*

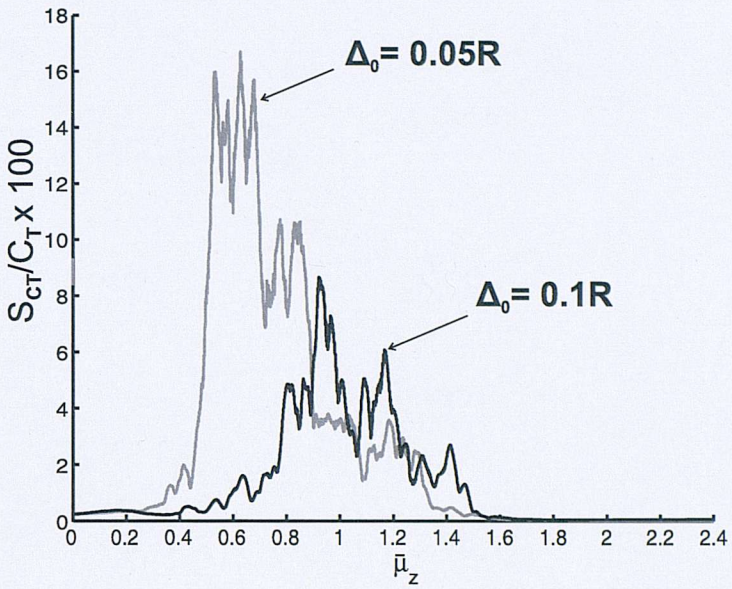



***Figure 2.13:*** *Comparison of the effect of computational cell size, $\Delta_0$, on the standard deviation about the mean thrust of the fluctuations of thrust experienced by a rotor in descending flight.*

cessation of the VRS in this case is only marginally earlier than in case (a). In addition, the magnitude of the thrust fluctuations in case (b) are up to twice as large as those which arose in case (a), the lower resolution simulation.

It can be seen in Fig. 2.14 that when the rotor torque is relatively steady, i.e. pre-VRS and post-VRS, the agreement between the two results is excellent. Only during the inception and subsequent development of the VRS regime do the rotor torque values differ. Since the rotor torque is closely linked to the rotor inflow it may be argued that the mean inflows through the rotors, when the torque is steady, are very similar in magnitude and in distribution.

These simple results are quite illuminating. They suggest that in non-VRS conditions, the predicted rotor performance is largely insensitive to the resolution of the computation, as was alluded to in the earlier discussion on previous grid dependence tests. In hover, low speed descent and high speed descent, where the wake near the rotor is 'quasi-steady' it appears that the global geometry of the wake, or rather, the gross vorticity distribution in the wake is not adversely altered by the cell size, since the gross vorticity distribution is the dominant factor that influences the velocity field near the rotor and thus its performance. Indeed, it is known [17] that the dominant vortical structures near to the rotor in these conditions are relatively ordered and large-scale. Perhaps, though, the cell length becomes

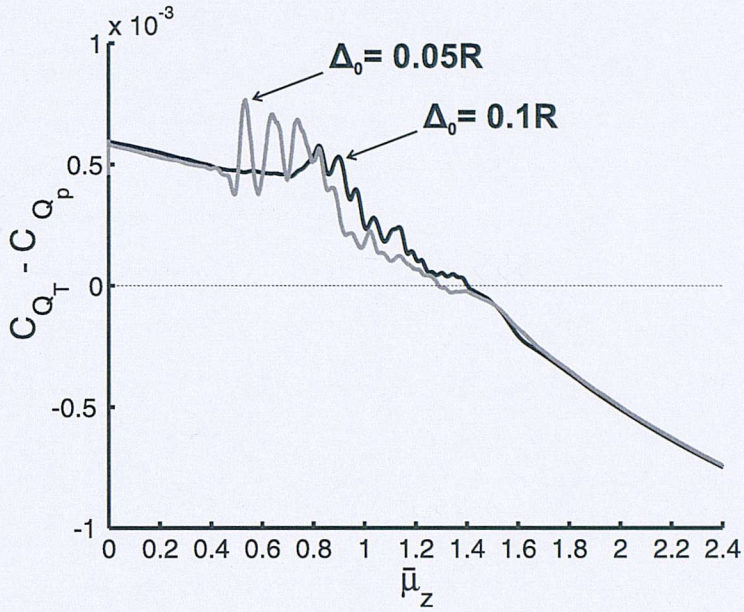



***Figure 2.14:*** *Comparison of the effect of computational cell size, $\Delta_0$, on the rotor torque coefficient produced by a rotor in descending flight. The instantaneous profile torque $C_{Q_P}$ has been removed from the data. The torque signal has been filtered.*

an important issue once the action of the fluid instabilities in the flow has had time to disturb the wake's orderly structure and hence create finer scale flow features. The cell length limits the flow scales that are explicitly evolved by the VTM's numerical solution to the vorticity transport equation, thus as resolution is decreased, the size of the smallest resolvable flow scale will increase. If fine flow scales play an important role in the local evolution of the rotor wake, for instance because they influence the way in which perturbations grow in the flow, then in a flow regime that is driven by the fluid instabilities, such as the VRS, the smallest resolved scale in the flow will become important. It may then be postulated that the outcome of the aforementioned rotor performance comparison indicates that a desensitising of the rotor wake to disturbances in the flow arises as the computational resolution is decreased. This behaviour is, surely, a common feature of dissipative systems, and the VRS flow field is arguably dissipative.

If, in a simulation of a hovering rotor, the rotation of the rotor is impulsively stopped (after an initial period long enough to allow the development of a 'quasi-steady' wake) the subsequent evolution of the flow field, free of any vorticity producing mechanisms, becomes akin to a decaying turbulent flow field. If the simulation is conducted several times, but

each time with a different computational cell length, then the influence of the resolution of the computation on the distribution of kinetic energy over the full range of scales within the flow can be compared, as can the minimum scale resolved in the simulation. Although such an investigation will not explicitly reveal why cell length modifies the solution to a VRS simulation, it will, at the very least, indicate where the differences may lie. In addition, such an investigation will provide information on the manner in which the VTM evolves the different scales within the flow such as whether the cascade of energy through the flow scales is physical, statistically speaking. An investigation of this kind formed part of a final year undergraduate research project, that was partially related to the topic under discussion, and was undertaken by an ERASMUS student from Eidgenössische Technische Hochschule (ETH) in Zurich, Switzerland. The present author designed and supervised the research and conducted the simulations required by the investigation. The source of the work about to be presented can be found in the dissertation by Gerber [61].

Figure 2.15 shows vorticity contours of the rotor wake at three different times after the rotor had been stopped. The state of the wake at the instant when time, $\tau$, was equal to $\pi$ (half a 'virtual' rotor revolution) and also when $\tau = 18\pi$ and when $\tau = 37\pi$. Firstly, the rotor was impulsively started. It was then allowed to rotate and produce lift for twenty revolutions before it was impulsively stopped. Note that the impulsive starting and stopping produced the associated starting and stopping shed vortices thus properly closing the vortex system as required to maintain a divergence free vorticity field. The results from three cases are shown in the figure. In case (a) the cell length was $\Delta_0 = 0.1R$, in case (b) $\Delta_0 = 0.05R$ and in case (c) $\Delta_0 = 0.025R$. As expected, there is a significant difference in the resolution of the tip and root vortices between the three cases. In each case, when $\tau = \pi$ the structure of the wake has not altered much from what would be expected when the rotor was in operation. When $\Delta_0 = 0.1R$, the tip-vortices appear to merge to form a continuous sheet down through the flow. As the cell length decreases however, the sheet is replaced by discrete tip-vortices, most obviously in the case when $\Delta_0 = 0.025R$. This feature of the comparison between the three cases is indicative of the spatial smearing of the finer scale structures in the flow that is engendered by larger cells, as reported by Brown and Line [35] and mentioned earlier. The more remarkable influence of cell size relates to the apparent rate at which the respective wakes are disorganised by the action of the instabilities in the flow. A larger cell size appears to promote later

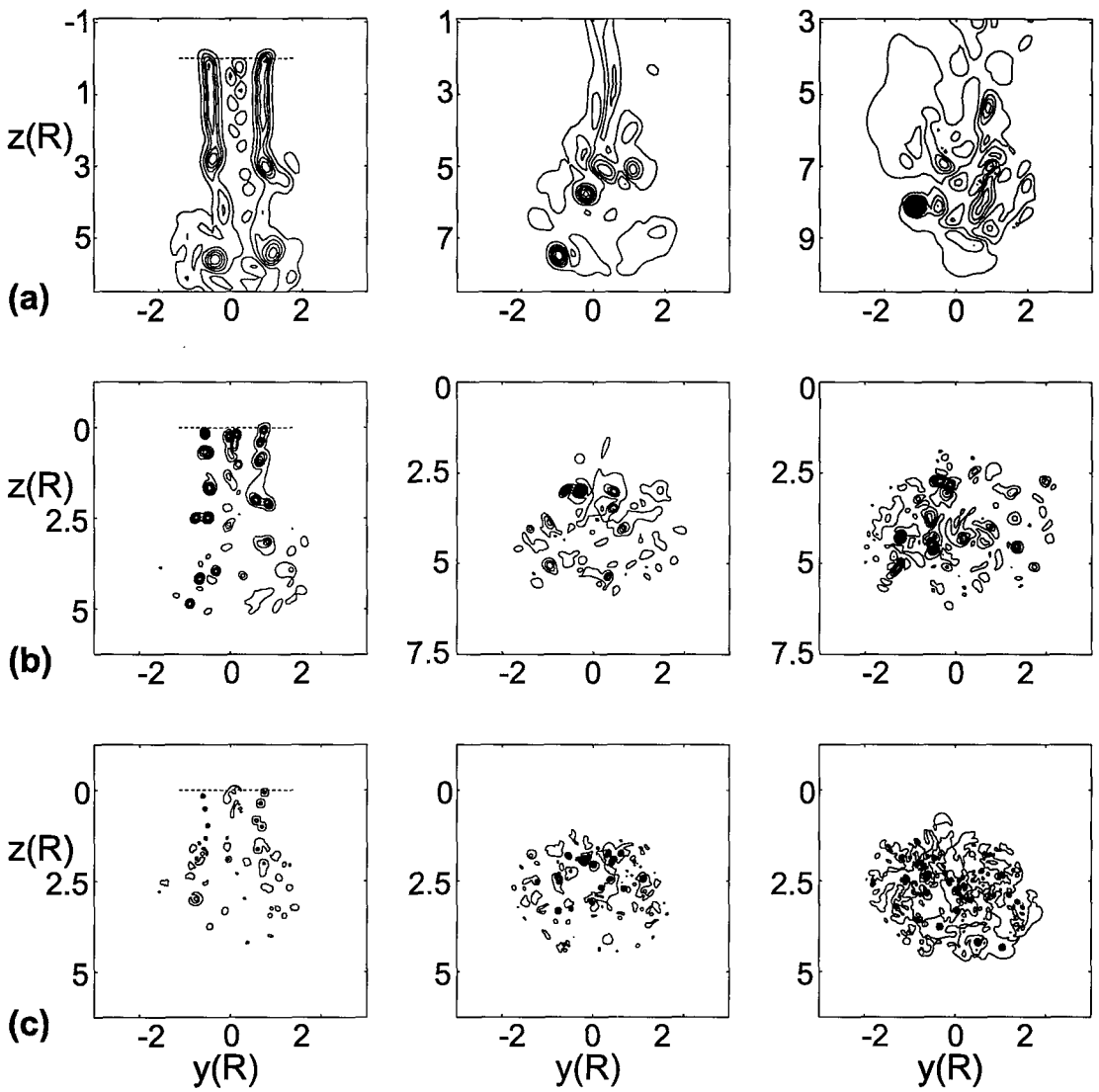



***Figure 2.15:*** *From left to right: Vorticity contour plots for a decaying wake after time $\tau = \pi$, $\tau = 18\pi$ and $\tau = 37\pi$ post rotor stoppage. Row (a) shows vorticity contours of the wake where $\Delta_0 = 0.1R$, row (b) $\Delta_0 = 0.05R$, and row (c) $\Delta_0 = 0.05R$. Each snapshot shows the main body of the vortex wake as it convects downstream (positive Z(R)).*

breakdown of the orderly structure of the wake. This is evident in the images showing the respective states of each wake when $\tau = \pi$. The instabilities in the flow engender breakdown of the wake closer to the rotor as the cell size is reduced. This effect manifests at later times too, as it appears that higher resolution leads to more rapid disorganisation of the computed flow field. That is, the vortex structures within the wake that induce the downward flow responsible for the global downward convection of the wake are rearranged sooner than when the flow structures are more coarsely resolved. This effect is quite likely to be related to the truncation errors inherent in the numerical advection scheme: the magnitude of the truncation errors, which engender spatial smearing, will change with cell size. It is plausible, then, that the relative importance of the truncation error in governing the dynamics of small scale features of the flow (that have scales comparable to the cell size) is modified as the cell size is changed. Perhaps the logical extension of this notion is that a consequence of spatial smearing of flow structures is a modification of the stability characteristics of the computed flow field, i.e. the larger the computational cell, the more stable will be the flow field. This could explain the later onset of the VRS seen in the lower resolution VRS simulation discussed earlier. The exact cause of this apparent desensitising of the flow field that is engendered by spatial smearing requires further investigation, however.

An examination of the way in which kinetic energy is distributed within the flow field provides an indication of the size of the scales within the flow and the way in which the energy is dissipated within it, if at all. Two-dimensional flow velocity data, on a plane normal to the rotor disc and passing through the rotor hub, was used to compute two-dimensional spectra of turbulent kinetic energy (TKE). The spectral method used is defined in the book by Frisch [62] and an example of its implementation can be found in the work of Weinstein and Gurgov [63]. The outcome of applying the method is the 2D energy spectrum, $E$, as a function of the 2D wave number, $\kappa$, where $\kappa = (\kappa_1, \kappa_2)$ and where the indices represent the two Cartesian spatial directions ($z$ and $y$ respectively, in this particular case). The general definition of $E(\kappa)$ can be written as

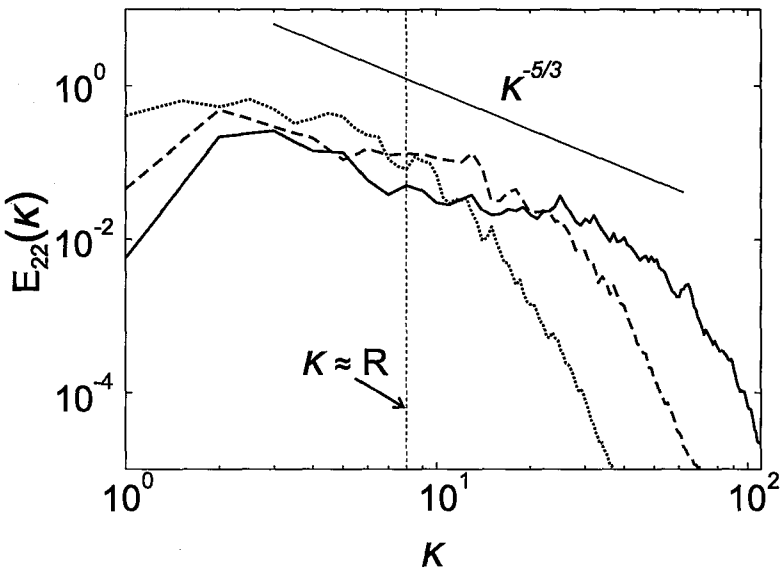
$$k = \frac{1}{2}\left\langle u_i' u_j' \right\rangle = \int_0^\infty E_{i,j}(\kappa)\, d\kappa \tag{2.44}$$

where $k$ is the kinetic energy in the flow.

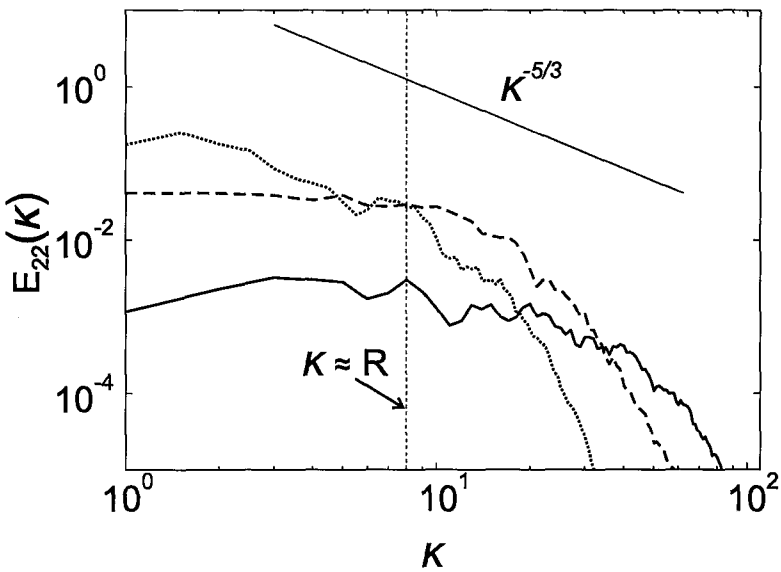
Figure 2.16 shows the energy spectra computed from the cross-stream velocity fluctuations, $v'(\mathbf{x}, t)$, where $\mathbf{x} = (x_1, x_2)$, which gives $E_{22}$ (the downstream velocity components

$u'(\mathbf{x},t)$ yield spectra $E_{11}$.). After approximately 18 'virtual' rotor revolutions the flow exhibited isotropic properties, such that $E_{11} \approx E_{22}$. Dotted lines show the spectra from the simulation when $\Delta_0 = 0.1R$, the dashed lines correspond to the energy distribution arising when $\Delta_0 = 0.05R$, and the solid lines represent the simulation for which the cell length was set to $\Delta_0 = 0.025R$. The graph of Fig. 2.16 (a) shows the distribution of kinetic energy through the flow scales arising when $\tau = \pi$, and the graph of Fig. 2.16 (b) shows the energy distribution at $\tau = 37\pi$. Consider first the curves of Fig. 2.16 (a). It is clear that decreasing the cell size increases the resolved range of energy-containing scales in the flow. This is to be expected since the cell size acts as the limit of the size of the smallest resolvable scale. Accompanying the variation in the cut-off of the flow scale is a variation in the distribution of the kinetic energy in the flow. It appears that relatively more energy is stored in the larger flow scales (where $\kappa < 10^0$) as cell length increases.

Consider now the curves of Fig. 2.16 (b). This figure shows the state of the turbulent kinetic energy distribution some time after the flow became approximately isotropic. In all three cases, it appears that the energy contained in any given scale is generally less than was seen at the earlier time, shown in Fig. 2.16 (a). That is to say, kinetic energy decayed in the flow, which means that the kinetic energy was removed from the simulated flow field, despite the flow field being inviscid. Further evidence of energy dissipation can be seen in the behaviour of the spectra at the smallest scales. If the kinetic energy was conserved within the computational domain, then this would manifest as a build-up or a 'blockage' at the smallest, energy dissipating scales, since the energy cannot be distributed into even smaller scales as they cannot exist due to the limiting factor of the size of a computational cell. If an energy blockage was present, the gradients of the curves at the higher values of $\kappa$ would not progressively become steeper, as they appear to do so in the figure. As no such blockage is evident, the conclusion is that the numerical scheme used in the VTM is dissipating the energy. It should be noted though that it does not necessarily follow that the energy is lost at the grid level, it could be lost at all scales. The notion of kinetic energy dissipation is not consistent with the physics of an inviscid flow field - the total kinetic energy in the flow field must be conserved if it cannot be transformed by viscous processes into heat. This means that the numerical implementation of the VTM must possess dissipative properties overall. The result of such a dissipative property would be an implicit, and inadvertent, model of the sub-grid scale




(a) Energy spectra, $E_{22}$, after time $\tau = \pi$




(b) Energy spectra, $E_{22}$, after time $\tau = 37\pi$

***Figure 2.16:*** *Two-dimensional energy spectra of the lateral velocity component, $v'(\mathbf{x}, t)$. Image (a) shows the energy spectra after time $\tau = \pi$, and image (b) shows the energy spectra after time $\tau = 37\pi$, post rotor stoppage. (Dotted line), $\Delta_0 = 0.1R$; (Dashed line), $\Delta_0 = 0.05R$; (Solid line), $\Delta_0 = 0.025R$.*

flow. A further possible method of energy dissipation is that of vortex annihilation, though this is arguably representative of a real, physical process, rather than just an artefact of the VTM's numerics (see Morton [64], for instance). Due to the finite resolution of scales in the computed flow, discrete vortices with opposite sign can be advected into the same cell under the right conditions. The computation will result in the sum of the two discrete vortices being left in the cell at the end of the timestep - vorticity and thus kinetic energy will be removed from the computation. Dissipation is, however, a physical mechanism and is arguably an essential characteristic of systems that behave in an irreversible or even chaotic way. It may be conjectured therefore that the dissipative character of the VTM, in terms of it having effectively an implicit sub-grid model for dissipation, is governed by the details of the numerical method and this is a fundamental reason why the model can represent the fluid dynamics of the VRS in a realistic manner. Indeed, the cause of the dissipation of energy in the computation is a topic of on-going research on the properties of the VTM, though initial investigations are reported by Gerber [61].

The thin solid line in the Fig 2.16 denoted as $\kappa^{-5/3}$ represents rate of decay of turbulent kinetic energy through a range of scales in high Reynolds number flows, as predicted by Kolmogorov. This range of scales is often termed the 'inertial subrange' since over these scales the transfer of kinetic energy arises due to largely inviscid fluid processes rather than the viscous processes which become dominant at the smaller scales. The decay processes within this range were found to be independent of the method by which the turbulence was initially generated, and it is thus a universal constant of such flows (See Batchelor [65] for instance). So, whilst it is difficult to discern from the present figure a significant range of scales over which the energy in the VTM simulations is distributed in accordance with the $\kappa^{-5/3}$ law, it is noteworthy that the spectra, do, in general, resemble the classical TKE spectrum of decaying turbulent flows of initially high Reynolds number. This suggests that the VTM evolves these flow scales in a realistic manner, even if the method of energy dissipation is an incidental by-product of the numerical scheme.

As an extension to this examination, it is interesting to assess the spectrum of TKE found in a VRS flow, as computed by the VTM. A simulation was conducted of a rotor operating in a fully developed VRS, for a duration of 200 rotor revolutions. The turbulent kinetic energy, $k$, in the flow around the rotor was calculated for each available data set from the fluctuating components of the vertical and lateral velocities, with the mean flow

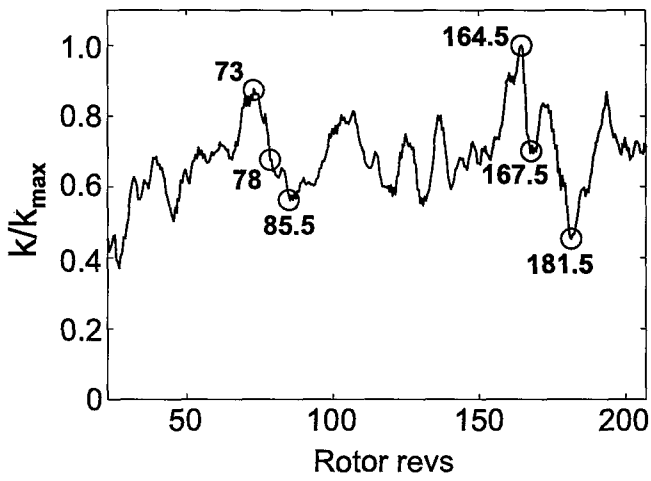



***Figure 2.17:*** *Turbulent kinetic energy, k, in the near rotor flow when the rotor was flying in the VRS.*

removed. The cell length used for the computation was $\Delta_0 = 0.05R$. Figure 2.17 shows a plot of $k/k_{max}$ vs. rotor revolutions. The figure shows that the kinetic energy computed from the 2D velocity fluctuations is oscillatory and aperiodic, which is commensurate with several observations in the literature of the amalgamation and breakaway of vorticity from around the rotor during the VRS. Several minima and maxima are highlighted. The energy spectra corresponding to the velocity field at those times are presented in Fig. 2.18.

It is significant that the variation in total kinetic energy seen in Fig 2.17 manifests, in all cases, merely as a variation in the energy contained in the flow scales that are larger than the fundamental characteristic scale in the flow, that of the rotor radius, $R$. The corresponding wave number is marked on the energy spectra in Fig 2.18. This indicates that the large fluctuations of total kinetic energy correspond to the shedding of the larger scale structures in the flow. The importance of this notion will become evident in Chapter 3 of this thesis. It is also pertinent to highlight the distribution of the kinetic energy over the resolved flow scales. The part of the slope that has a negative gradient adheres even less to Kolmogorov's decay law in the inertial subrange than was seen earlier in the decaying rotor wake. This is perhaps unsurprising since this flow field has a constant input of energy from the rotor and thus is hardly likely to show signs of homogeneity. This implies though, that the VRS is an event which is dominated by the kinematics of large scale vortical structures. The smaller scale features in the flow that may arise are

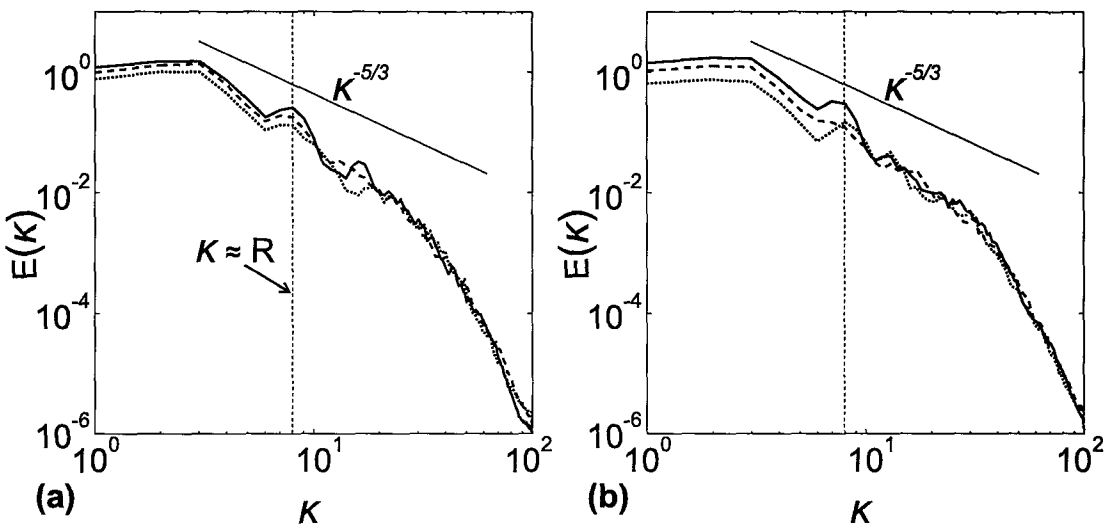



***Figure 2.18:*** *Two-dimensional energy spectra from a VRS flow, at six different in times in the simulation. In graph (a) rev = 73 (solid line), rev = 78 (dashed line) and rev = 85.5 (dotted line). In graph (b) rev = 164.5 (solid line), rev = 167.5 (dashed line), rev = 181.5 (dotted line). The vertical line denoted as $\kappa \approx R$ marks the wave number that corresponds to a flow scale with a length similar to the rotor radius.*

generally convected up away from the rotor, as will also be seen in Chapter 3. It may be deduced therefore that some of the energy in the VRS wake, at least in the region around the rotor that was interrogated by the energy spectrum calculation, is dissipated via the action of the free-stream convection, as well as by a cascade of energy through to the smallest resolvable flow scales where dissipation occurs.

## 2.6 Summary

The governing equations of the system to be studied and the numerical methods by which they are solved in the VTM have been presented. It has been shown that the VTM, which models rotor aerodynamics using an advanced lifting line method and a finite volume based method to solve the vorticity-velocity form of the Navier-Stokes equations, provides accurate predictions of the aerodynamic and dynamic behaviour of a rotor in both hovering and forward flight. More pertinent to this thesis is that the VTM has also been shown to be capable of reasonable quantitative and qualitative prediction of the rotorcraft vortex ring phenomenon. A strong dependence of the solution on computational cell size has

been highlighted, however. The global dynamics of the VRS is captured even when the computational fidelity is relatively low. But, it appears that the sensitivity of the wake to the instabilities in the flow field are reduced as cell size increases and this, possibly, occurs because small-scale flow features that manifest as disturbances in the flow are not resolved, or indeed, contain less kinetic energy than do the same scales when computed on a finer grid. The implication of this sensitivity to the small scale features, of what is a strongly non-linear and dissipative wake system, is that only a computation that directly resolves scales down to near molecular level where kinetic energy is transformed to thermal energy under the action of viscosity, or alternatively that accurately models the viscous processes using a sub-grid-scale model, will provide a true representation of the full range of dynamics of the rotor wake when in the VRS. Nonetheless, it appears that the vorticity conserving properties of the VTM allows the gross features and large-scale dynamics of the VRS to be examined, even when the computational resolution is low. A flow field computed at low resolution still possesses the unstable flow processes that admit VRS-like behaviour, as was suggested by the low resolution validation simulations. Although, perhaps, a low resolution wake contains fewer or weaker disturbances, but they still engender the VRS in descending flight. Therefore, since many of the simulations that were undertaken for this thesis required very long running times, the determination of the cell size to be used was dependent upon the level of fidelity required by the investigation. To expose the details of the wake kinematics, the resolution employed was set sufficiently high to resolve individual tip and root vortices and maintain them as discrete structures in the flow for long periods. If knowledge of the gross performance of the rotor, only, was required, then the cell length defined was relatively large, since the rotor performance is relatively insensitive to spatial smearing of the vortical structures.

## 2.7 Conventions and Data Processing Methods

### 2.7.1 Coordinate System and Conventions

Figure 2.19 shows a schematic of the rotor-disc, its coordinate system, and the sign conventions that have been adopted throughout this thesis.

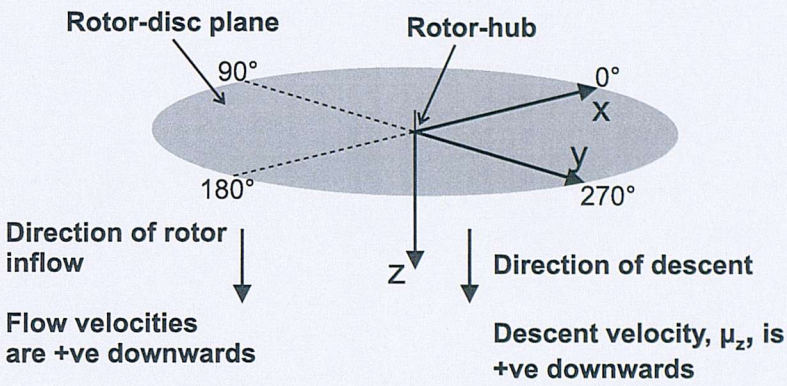



*Figure 2.19: Schematic representation of the coordinate system of the rotor and the sign conventions used to describe the flow field and rotor trajectories throughout this thesis.*

### 2.7.2 Data Processing Methods

#### 2.7.2.1 Data filtering

Throughout this thesis there are numerous instances where the rotor performance data that was generated during a simulation, such as thrust, is presented. The aerodynamic environment in which a descending rotor operates is highly unsteady, and the gross trends that arise in the various measures of rotor performance can be obscured by large fluctuations. The frequencies of some of the fluctuations are equal to or much higher than the rotor-blade passing frequency. Such information may be useful for investigations into rotor vibrations, for instance, but the time-scales involved in the dynamics of the VRS that are of interest to the studies reported in this thesis, are very much greater [13, 15] than the time-scales of the aforementioned high-frequency effects. Where necessary, therefore, the high frequency fluctuations in the rotor performance data have been suppressed. The suppression method involved taking the average of the performance data, such as the thrust signal, over a given number, or 'window', of rotor revolutions within the data set. Starting

from the beginning of the data set in each case, the averaging window was passed over the entire signal in incremental, contiguous steps. The process was stopped when the centre of the window was half the width of the window from the end of the data set. During the simulations, the data was output at every timestep, thus the window-stepping interval was one timestep. The width of this averaging window will be defined when necessary within each section of the thesis, but it ranged from around 10 to 25 revolutions.

#### 2.7.2.2 Calculation of vorticity locus plots

There is a second common data processing technique used throughout this thesis that requires explanation here. On numerous occasions the vorticity field arising at a particular phase of a rotor's descent is visualised. But, there are two problems associated with such visualisations. Firstly, as will be seen, the flow field is highly unsteady and thus one snap-shot of the vorticity field may look somewhat dissimilar to another snap-shot taken some short time later, even if the flight speed is steady. This leads us to the second problem to be dealt with: in most cases in this thesis, the simulations conducted were of a rotor operating in a linearly accelerated descent, post an initial period of hover or flight in the steady 'windmill brake' condition. Generally, therefore, the problem is to present representative images of a highly unsteady wake from a rotor flying with constantly changing speed that can be fairly compared to the wake of another rotor that has either slightly different geometry or operates under different conditions. The solution, implemented here, is to plot the average of a series of snap-shots of the wake. As was mentioned previously accelerated descents were used for the sake of minimising the duration of the computations. As will be discussed in detail in Chapter 4 though, acceleration modifies the VRS dynamics and thus in most cases the acceleration was kept as low as was acceptable in terms of the requirement to minimise simulation run times. The acceleration level was selected on the basis that VRS onset had to occur at a normalised descent rate that was similar to that seen in the majority of experiments and past numerical work reported in the literature, and also, that the characteristic VRS dynamics, such as large-scale vortex shedding, were captured. As a consequence, except in the initial, steady phases of the rotor's trajectory, the averaging process typically included snap-shots of a constantly evolving wake. A reasonable impression of the state of the rotor wake at a given phase in the rotor's descent was thus obtained by taking the average of a series of contiguous snapshots, the quantity

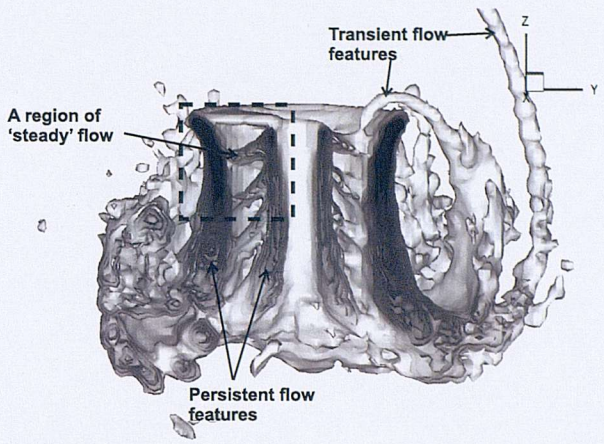



***Figure 2.20:*** *Image of locus plot of vorticity showing features resulting from the calculation of the locus plot. The image is of a wake of a descending rotor.*

of which was big enough to allow persistent features in the flow to remain coherent within the averaged image but for unsteady structures to be weakened or removed from the result altogether. On the other hand, the number of snapshots included in the averaged series was not so large as to include any large changes in the geometric state of the wake. For example, at some stage in the descent of the rotor into the VRS the initially tubular form of the wake collapses down into a toroid of vorticity about the rotor. Generally, the rate of collapse of the wake was rapid compared to the rate of change of the descent velocity, but it was by no means instantaneous and so much care was taken to avoid including both states in a single averaging process where possible.

The image processing technique involved taking the average of $n$ values of vorticity occurring in each cell within the computational domain, over $n$ snap-shots. Typically only one snap-shot per rotor revolution was available, and the number of snap-shots used ranged between 10 to 25. This number of snap-shots is low due to the necessary constraints placed on the simulations. Averaging over such a small number of snap-shots from an unsteady and, importantly, an evolving flow field leads to the emergence of features in the resulting wake image that need interpretation. To aid the discussion, an example of an outcome of the averaging process is shown in Fig. 2.20. The figure shows the result of performing the aforementioned averaging calculation over a normalised descent speed interval, $\Delta\bar{\mu}_z$, of $\Delta\bar{\mu}_z = 0.1$, or in other words, over 14 rotor revolutions in this particular case. The rotor was in low speed descent and thus had not entered the VRS during the selected interval.

There are three important features that emerge from the averaging process. These features will be named as steady, persistent and transient and are defined in terms of a reference frame that translates with the rotor. In essence, the result of the averaging process, in graphical terms, is the locus of the paths followed by the elements of vorticity within the flow. From herein, therefore, the plots of the average state of the vorticity field will be called vorticity locus plots, rather than, for instance, 'mean vorticity fields'. Now, although rotor flows cannot be rigorously defined as steady, the term in this instance is used in a relative sense - the flow near to a hovering rotor is steady relative to the flow disturbed by the products of fluid instability in the far field or relative to the flow near a rotor in the VRS. Thus, if the variation of the strength and velocity of the vorticity that passes through some small but finite region of the flow domain over the duration of the averaging interval, is small, then the extent of the spread of the paths followed by elements of vorticity within that region will be narrow, or rather, comparable to the size of the structures in question. The result of averaging the vorticity field in this region, therefore, is the appearance of a coherent structure with sharp, well defined boundaries, that closely resembled any one of the snap-shots included in the ensemble. This flow is defined as steady. In the figure, an example of a region of flow that can be defined in this way lies in the near field of the rotor. Although only a low-to-medium level resolution was used in the simulation from which this image was extracted, i.e. there were 20 computational cells per rotor radius, the steadiness of the flow just beneath the rotor has allowed the tip and root vortex tubes and even the inboard vortex sheet to be realised with sharp, well defined edges. Importantly, the average strength of the steady features are approximately equal to the strength of the instantaneous structures from which they are constructed.

A second class of emerging feature is the persistent feature. Such a feature is actually just an artefact of the averaging process, but it is nonetheless a desirable product of the calculation. That is, very few or none of the flow structures that passed through the region of the feature actually resembled the feature exactly. This is a gross, rather than a detailed, representation of a region of the flow. A persistent feature is the locus of the *varying* paths of elements of vorticity passing through a given region. But, importantly, whilst the paths taken through a region by a series of vortex elements may differ significantly, the structure of those elements varies little. So the region taken up by a persistent feature will be larger than any one of the structures that passed through that region and it will also, generally,

be weaker than any of those structures, unlike in the case of steady flow; the strength and geometric properties of the structures that passed through a region will be smeared over the region by the averaging process. Importantly, this feature is so named because it represents a region of the flow in which, in the majority of snap-shots, a vortical structure was present in the region. Persistent flow features are highlighted in the figure. Where the path followed by the tip-vortices begins to broaden is where perturbations growing unstably in the flow begin to modify, somewhat erratically, the path followed by individual elements of vorticity. The result is a region of flow that is wider and appears less coherent and weaker than the steady region of flow immediately above it and just below the rotor.

The final class of feature, the transient, or non-persistent feature of the averaged vorticity field is again, an artefact of the averaging process. A transient feature represents the trajectory of a highly mobile fluid structure that convected along a path not closely followed by any other structures within the averaging interval. That is, the transient feature represents a region of flow where the number of times that elements of vorticity passed through that region was small compared to the number of snap-shots used in the averaging process. Therefore, the strength of the feature will be a function of the strength of the vortex structure, of its convection speed, and of the number of snap-shots used in the averaged series. An excellent example of such a feature is highlighted in the figure: the trajectory followed by a fragment of vorticity, as it is recirculated from the far wake back through the rotor, is realised by the averaging process.

It is possible, during the construction of the image resulting from the averaging process, to show only strong levels of vorticity in the image, such that weak persistent features, and most transient features, will not be plotted. The result would be an image that included only the strong and steady structures and the strong, and thus probably important, persistent features. However, as in the image shown in the present figure, it is often necessary to set the iso-surface (or contour) level sufficiently low to reveal important but weaker structures, such as the inboard sheet vortices, for instance. Therefore, without much undue and somewhat arbitrary additional post-processing of the data, some of the less physical artefacts of the averaging process will be displayed in the images. Nonetheless the resulting image plots are, as a consequence, rich with information. Indeed, much utility can be obtained from the presence in the images of weak persistent features or the transient features, if some care is taken to interpret the images properly.

# Chapter 3

# Vortex Kinematics of the Wake of a Descending Rotor

## 3.1 Introduction

In the introduction to this thesis it was mentioned that despite the eighty or so years of research into the VRS that has been undertaken little is known about the detailed wake dynamics responsible for both the onset of VRS and the subsequent evolution and resulting structure of the rotor wake once it has broken down and enveloped the rotor. This chapter describes two high resolution simulations of a single-bladed, idealised rotor approaching and operating within the VRS. The work reveals the vortex kinematics that are responsible for the collapse of the helical geometry of a rotor operating in hover or the windmill brake state into the toroidal geometry that is characteristic of the VRS. Also, extended flight at constant speed within the VRS reveals the mechanisms that lead to both small-scale and large-scale wake breakdown events. Finally, the structure of the vorticity field is analysed in order to expose the level of coherence that is able to persist in the highly unsteady VRS flow field. This work has resulted in the discovery of numerous interesting and important features of the fluid dynamics of the vortex ring phenomenon.

It is reasonable to presume that the physics of the VRS is best considered in terms of the non-linear, time-varying and mutually-induced motions of the coherent vortical structures of the wake. The dynamics of the helical tip vortex, because of its high relative strength, dominates the behaviour of the wake, although the inboard sheet and root vortex

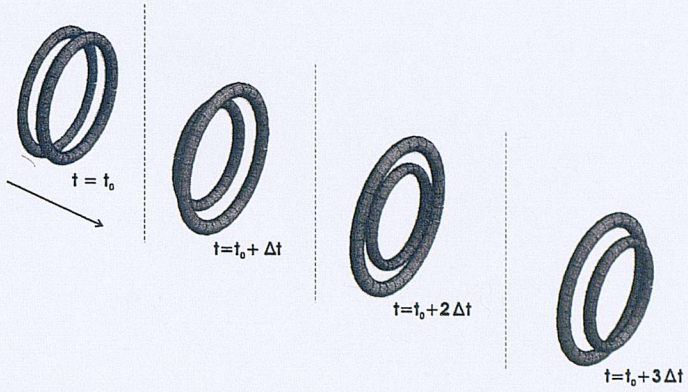



***Figure 3.1:*** *Interaction between a pair of axially aligned vortex rings showing their mutually-induced 'leap-frogging' motion (schematic).*

appear to be the source of many of the subtle differences in behaviour between different rotor systems. Widnall's analysis of the linear stability of helical vortex filaments revealed the existence of three modes of instability [5]. Small geometric perturbations to the helix will grow either through a mode with wave length equal to just a few core-diameters, or as a very long wave that acts over a distance of several helix diameters. A third growth mode, that Widnall termed the 'mutual-inductance' mode, manifests as an interaction between immediately adjacent turns of the helix. This third mode resembles, in the linear, small excursion range, the 'leap-frogging' phenomenon that is characteristic of the interaction of two or more axially aligned vortex loops, as illustrated in Fig. 3.1. The first and third modes of instability have been observed in the wake of a rotor. Bhagwat and Leishman [6] analysed the helical tip-vortex system generated by a helicopter rotor and implicated the mutual-inductance instability, or 'vortex pairing' mode, as the major cause of VRS initiation. This was because, in their free-wake simulations, this instability appeared to lead to a 'bundling' of vortex filaments into rings that move gradually upwards toward the rotor as the rotor descent speed is increased immediately preceding the onset of the VRS.

Widnall, and Bhagwat and Leishman, showed how perturbations to the geometry of long helical vortex systems can grow exponentially, at least for small disturbance amplitudes. The problem with direct application of these results to understanding the onset of the VRS lies in the underlying linearity of the analysis, however. Linear analysis provides no clear information on the actual kinematics of the vortical filaments outside the range of small excursions, and thus the end result of the growth of these linear instability modes

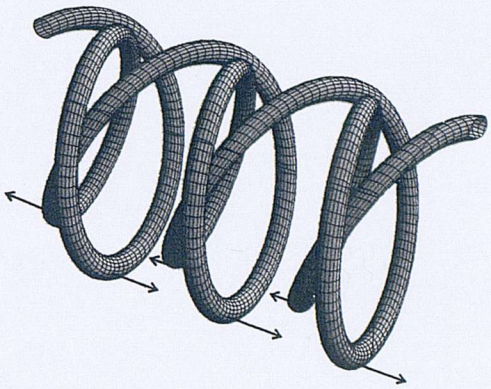


***Figure 3.2:*** *A helix becoming entangled by the action of 'pairing' of its turns (schematic).*

cannot be determined. In particular, the growth of the perturbations cannot be limitless, yet no information can be provided by a linear analysis on the geometry that the disorganised filaments of the wake adopt after finite time. The mutual induction mode may look like leap-frogging* in the linear range, but for any finite amplitude disturbance the geometric constraint imposed by Kelvins's laws on the helical, rather than ring-like, structure of the wake means that the dynamics cannot be entirely equivalent to leap-frogging. This constraint, as depicted in Fig. 3.2, results in entanglement and significant distortion of individual turns of the helix once the dynamics reaches appreciable amplitude.

The aim of the present work is thus to study the VRS from beyond the point where a linear stability analysis ceases to provide insight, and hence to contribute to an understanding of the vortex dynamics that cause the onset of the VRS and the subsequent structural fluctuations within the rotor wake.

Of particular interest in the present work is the vortex 'stretching' term, $\omega \cdot \nabla u$, on the left side of the vorticity transport equation given in Eq. 2.9. Inspection of this term reveals how velocity gradients in the flow rotate and dilate individual vortex filaments. Upon expansion of the term, and writing it with respect to three Cartesian components of a vortex filament and with respect to a Lagrangian reference frame, the result is as follows:

*Henceforth, the term 'leap-frogging' will refer to the axial overlapping of axially aligned vortex rings, which is not the result of a fluid instability, whilst the term 'vortex-pairing' will be used in the context of the interaction of adjacent sections of turns of a helical vortex, which is, indeed, a manifestation of a fluid instability.

$$\frac{D}{Dt}\omega_x = \omega_x\frac{\partial u}{\partial x} + \omega_y\frac{\partial u}{\partial y} + \omega_z\frac{\partial u}{\partial z} \tag{3.1a}$$

$$\frac{D}{Dt}\omega_y = \omega_x\frac{\partial v}{\partial x} + \omega_y\frac{\partial v}{\partial y} + \omega_z\frac{\partial v}{\partial z} \tag{3.1b}$$

$$\frac{D}{Dt}\omega_z = \omega_x\frac{\partial w}{\partial x} + \omega_y\frac{\partial w}{\partial y} + \omega_z\frac{\partial w}{\partial z} \tag{3.1c}$$

where the velocity vector $\mathbf{u} = (u, v, w)$ and where $\mathbf{u} = \mathbf{u}(x, y, z, t)$. Gradients of velocity in the direction parallel to the longitudinal axis of a vortex filament will produce axial stretching or compression of the filament, which, in a solenoidal flow such as this, necessarily intensifies or weakens the vorticity, respectively. The effect of dilatation on the vortical structure of the rotor wake in various flight conditions, including the VRS, was investigated by Ananthan *et al.* [66]. In this paper, the authors did not expose the effect of stretching, and the consequent increase in the induced flow velocity, on the wake kinematics. Instead, they showed that the prevalence of vortex filament dilation that occurs when the wake is in the VRS is significantly greater than that arising in the flow field of a hovering rotor.

It was hypothesised in the introduction to this thesis that the local re-orientation of vortex filaments, rather than the dilation of filaments as considered by Ananthan *et al.*, is of fundamental importance to the global dynamics of the wake of a rotor in axial flight. Figure 3.3 shows a schematic of an axis system for an element of a vortex filament. Spatial gradients of velocity acting obliquely to the swirl axis of a vortex filament[†], induces rotation of the filament about an axis that is perpendicular to both the plane in which the gradient exists and the swirl axis. Importantly, as the filament is re-orientated, the spatial plane in which it induces a flow is also re-orientated (though, of course this plane is orthogonal to the swirl axis), and thus re-orientation of a vortex filament will influence the velocity of the flow induced by a wake system such as that of a rotor. To further highlight the importance of the off-axis velocity gradient terms in Eq.'s 3.1a and b, the following brief discussion shows how the form of the stretching term allows the off-axis gradients to drive the evolution of a vortex system subject to a small geometric perturbation, in addition to causing mere re-orientation of a single filament. Consider two parallel vortex elements each of which are part of either a vortex line stretching out to infinity in either

[†]From herein, velocity gradients that act obliquely to the swirl axis of a vortex filament will be referred to as 'off-axis' velocity gradients.

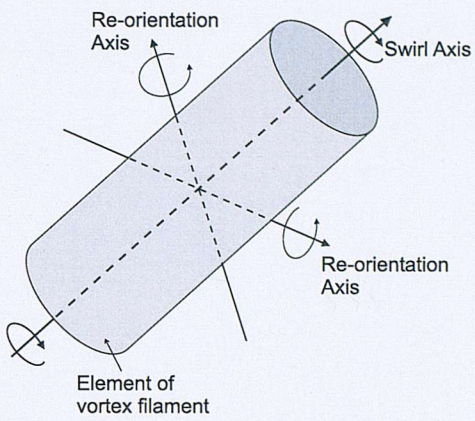
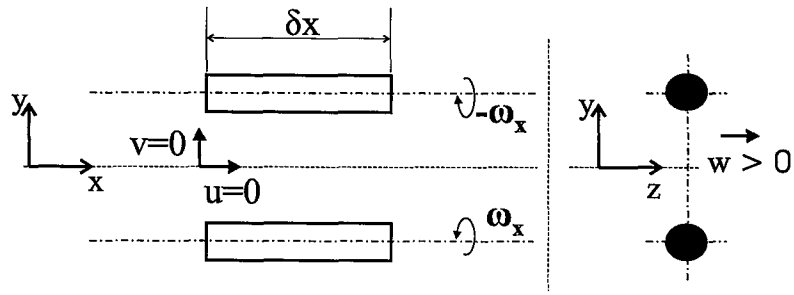
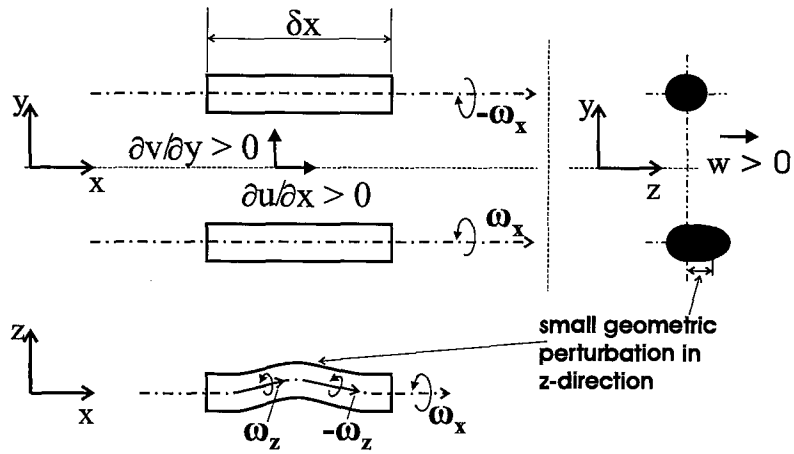



***Figure 3.3:*** *Schematic of an element of a vortex filament showing swirl and re-orientation axes.*

direction, or are filaments on opposing sides of a closed vortex loop, as shown in Fig. 3.4 (a). There is no free-stream flow and, initially, only vorticity parallel to the $x$-axis exists, and so velocity components $u$ and $v$ are equal to zero. The vortex filaments induce a velocity in the $z$-direction, which is non-uniform along the $y$-axis. Thus, in the plane that passes through the two filaments, the z-wise velocity component $w(y) > 0$, and also, the velocity gradients $\partial w/\partial y$ and $\partial w/\partial z$ are the only velocity gradients to be non zero at the outset. In the next instance, shown in image (b) of the figure, allow that a small spatial perturbation, parallel to the $z$-axis, exists on the bottom element, such that a small, positive and negative, component of vorticity in the $z$ direction, is produced in the vortex element, and thus in that location, $\omega_z \neq 0$ also. The small value of the z-wise vorticity component, $\omega_z$, will of course induce small velocities that will have components in the directions parallel to both the $x$ and $y$ axes and therefore, the velocity gradients $\partial u/\partial x$ and $\partial v/\partial x$ will become non-zero as a result. Inspection of Eq. 3.1b shows that this flow condition will rotate the element to produce a $y$-component of vorticity, also. The generation of non-zero velocity gradient $\partial v/\partial x$ that accompanies the creation of vorticity $\omega_y$ in the lower element will be reflected in the upper element. This is because, as inspection of Eq. 3.1b reveals, the product of $-\omega_x \partial v/\partial x$ will result in the generation of a small component of vorticity in the direction of the $y$-axis of that element too. It will, though, be of opposite sign since $\omega_x$ is negative in the upper element. From this discussion, it can be seen how a small perturbation can start a series of local re-orientation events and that, arguably, these small, local excursions will grow in time and may ultimately engender significant restructuring of the original geometry of the vortex filaments. What




(a) Vortex elements at $t = t_0$.




(b) Vortex elements at $t = t_0 + \Delta t$.

***Figure 3.4:*** *Schematic of elements of long parallel vortex filaments. Image (a) shows the unperturbed condition and image (b) shows an another instance where there is small perturbation in the lower filament.*

has been described is an unstable growth mechanism and thus it can be seen how the stretching term of the vorticity transport equation plays a significant role in governing the stability characteristics of a system of vortices, as well as governing the simple re-orientation of vortex filaments. This argument therefore strengthens the aforementioned hypothesis that re-orientation of strong, coherent vortex filaments out of a plane parallel to the rotor-disc is the major characterising mechanism of wake breakdown leading to the VRS. This is because it not only precipitates breakdown but will also strongly influence the strength of the induced downwash in the wake of the rotor. Hence, particular attention is paid in the following sections of this chapter to the kinematics of the vorticity in the flow field.

## 3.2 High Resolution Wake Simulations

The evolution of the wake structure in the VRS was studied via two high-resolution computational simulations using the VTM. In the first simulation, the rotor was decelerated from the windmill brake state (WBS) into the VRS, after which its descent speed was held constant. In this simulation, the computational cell size was set to $\Delta_0 = 0.016R$ (62.5 cells per blade radius). The relatively high resolution afforded by this cell size allowed the evolution of individual tip-vortex filaments to be exposed even when the rotor operated deep within the VRS. In the second simulation, the rotor began its flight in hover and then was accelerated into descending flight until it reached a speed that would take it just into the VRS regime. The computational cell size was set to $\Delta_0 = 0.02R$ (50 cells per blade radius). This cell size was chosen since exploratory runs showed it to be sufficient to give clarity to the dominant vortical structures. As a reminder, since practical rotor flows are generally associated with high Reynolds numbers, the simulated flow was assumed to be inviscid and therefore, it is only the vortex kinematics that contributes to the large-scale dissipation of the orderly structure of the wake that is shown here.

### 3.2.1 Simplification of the rotor model

To allow the fundamental kinematical mechanisms that underly the VRS to be identified, the complexity of the system being simulated was reduced to a minimum. The rotor had just one blade to minimise any obscuration of the motion of individual vortex filaments. In addition, the flap and lag dynamics of the blade were suppressed so that no geometric or strength perturbations to the wake could stem from any irregular motion of its source. Importantly, it is believed that the inherent coupling of the wake dynamics to the blade aerodynamics is an additional, modifying component of the physics of the VRS, rather than a fundamental aspect of the phenomenon that is necessary for VRS to arise. Hence the aerodynamic coupling between rotor and wake was removed by prescribing the bound vorticity, $\omega_b$, to have the same, constant value along the length of the blade for the entire duration of each simulation. It can be inferred from the source equation of Eq. 2.31 that the blade thus generated a wake consisting solely of a tip vortex and a root vortex, both having the same strength at their source. The magnitude of the bound vorticity on the blade was prescribed so that the rotor generated a thrust coefficient of $C_T = 0.005$ when

in hover.

It should be noted that the behaviour of only one particular rotor is investigated and thus much of the small scale detail of the flow that is exposed in the simulations will likely be specific to that rotor alone. Nevertheless, the general physics that underly the vortex dynamics in the wake of this particular rotor should apply equally well to all other types of rotor, no matter what their geometries, blade loading or number of blades.

## 3.3 Entry into VRS from the Windmill Brake State

Figures 3.5, 3.6 and 3.7 show the development of the simplified rotor wake as the rotor moves from the windmill brake state, where the thrust-normalised descent velocity, $\bar{\mu}_z = \mu_z/\sqrt{C_{T_h}/2}$, was equal to 2.1, into a regime that is deep within the VRS. This was achieved via a linear reduction of the descent velocity, over a period of 10 rotor revolutions, to a normalised descent velocity $\bar{\mu}_z = 0.9$. This descent speed was then held constant for the remainder of the simulation.

Visualisations of the simulated flow field show clearly the very complicated vortex dynamics that lead to VRS initiation from the WBS. As the descent speed is reduced, the two or so helical filaments that are closest to the rotor expand radially outwards. These filaments also induce those filaments above them to move inwards (Fig. 3.6) - this reduction in diameter increases the self-induced convection speed of these filaments thus causing them to move downwards against the free-stream. Initially, this quasi-symmetrical motion resembles the leap-frogging process shown in Fig. 3.1, with the necessary radial expansion and compression of the axially compacted helical turns being clearly apparent (Fig. 3.7). Soon afterwards, though, larger, out-of-plane motions begin to occur; the disturbances in the vorticity field start to grow non-linearly and degeneration of the wake into full VRS ensues. Once in the VRS, three, though sometimes just two, and occasionally as many as four, coherent turns of the helical vortex can be seen to persist just above the rotor plane. This suggests that the non-linear growth of perturbations takes some finite time to manifest. Without the existence of these coherent filaments lying parallel to the rotor plane, though, the ring-like recirculation pattern that is almost universally taken to indicate the existence of VRS conditions on the rotor, would almost certainly not arise. As the descent speed of the rotor becomes constant, a repeating pattern of behaviour emerges,

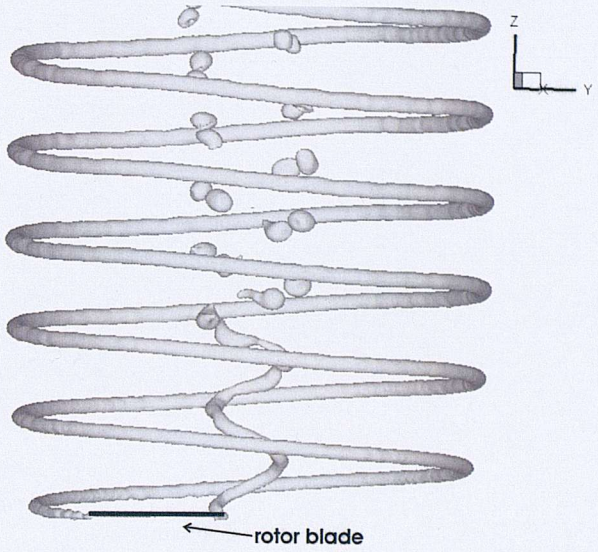



***Figure 3.5:*** *The wake of the simplified rotor in WBS. (Iso-surface of vorticity magnitude.)*

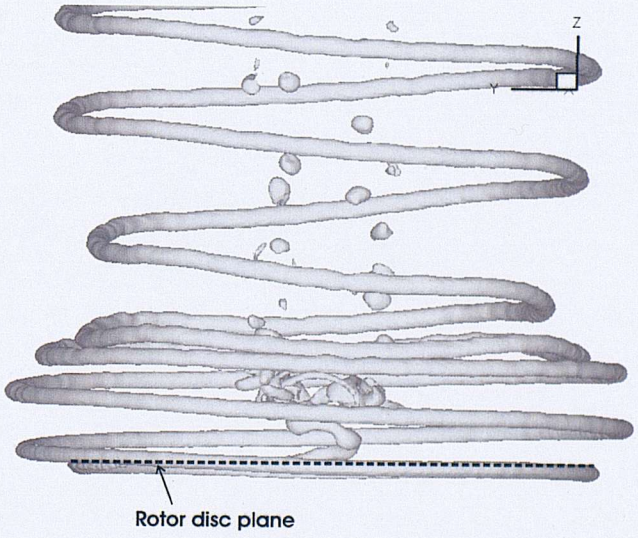



***Figure 3.6:*** *The wake of the simplified rotor entering the VRS from the WBS. (Iso-surface of vorticity magnitude.)*

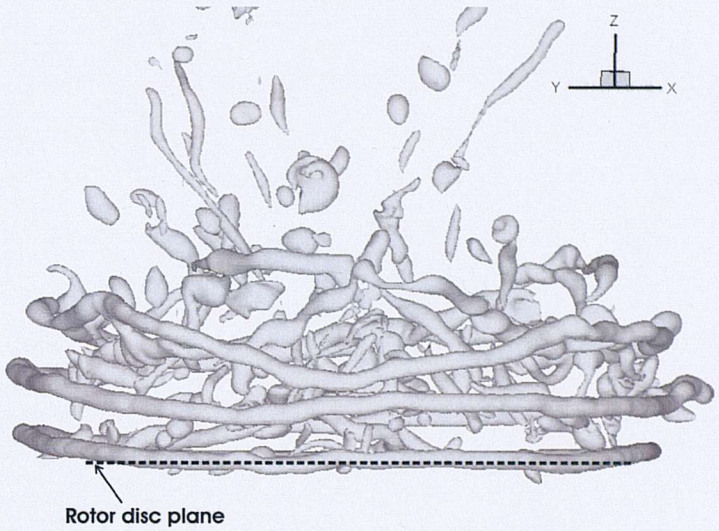



***Figure 3.7:*** *The wake of the simplified rotor deep in VRS. (Iso-surface of vorticity magnitude.)*

although the flow field is so unsteady and interactional that the vortex kinematics do often deviate quite significantly from the mean behaviour.

The helical vortex system approximates a stack of closely spaced and axially aligned vortex rings that has been longitudinally compressed by the resultant velocity field; this structure might be termed the 'base flow' of the vortex ring state. The ring-like structures comprising the base-flow, generally three in this particular simulation, evolve in a way that is approximately analogous to the evolution of three axially aligned vortex rings, of the same sign, in an otherwise quiescent flow field. The leading ring is forced to expand and slow down by the velocity field of the two rings behind, as they accelerate toward it. The second, middle ring also expands by the action of the third, trailing ring which reduces in radius as it moves through the middle ring on its way toward and through the leading ring. The leading ring thus becomes the middle ring and the middle ring, which has since become the trailing ring in the stack, is compressed and accelerated once more down toward the leading ring, passing through the middle ring as it does so.

With this concept of a VRS base flow in mind, the dominant vortex motions that occur to disrupt it can be described more fully. In the absence of hydrodynamic instabilities and viscosity, this 'leap-frogging' process would continue unabated [67]. In the case of the rotor flow simulated here though, this simple process is modified by three factors. The presence of the free-stream flow, which opposes and effectively prohibits the mutually-induced axial

convection of the system of rings, is the first modifying factor. In the pure case described earlier the system of rings would propagate forward through the flow. With the rotor in the VRS, though, the free-stream flow opposes the natural propagation of the stack of rings and effectively traps it near the plane of the rotor. An observer on the rotor sees the leap-frogging process described above as essentially a re-circulation of the filaments within the stack.

The second modifying factor is the presence of flow instabilities, in particular the 'pairing' instability of helical vortex systems and the short-wave instability that is common to both helical and ring vortices. These instabilities cause the growth of small perturbations to the geometry of the compacted rotor vortex filaments within the base flow of the VRS, resulting in significant disruption to the orderliness of its structure. As a new tip-vortex filament is produced by the rotor it immediately begins to expand radially as a result of the velocity field that is induced by the vortex 'rings' above it, whilst it is convected upwards by the free-stream flow. As it travels to the top of the stack of rings it develops irregularities in its form that are due, largely, to the development of the short-wave instability mode. As disturbances in the ring grow, the rings above and below it are also influenced, usually modifying locally the shape and trajectory of those rings too. The manner in which this process occurs around the circumference of each ring varies in detail, though not in essence, so that each infinitesimal section of each ring is acted upon slightly differently. The differences in the form of the perturbations are superimposed onto the gross dynamics of the vortices in the stack, such that no section of any particular ring resembles that of any other. The form and size of the growing perturbations appear to determine, to a large degree, the future kinematics of each ring, both locally and, ultimately, globally. When the new ring in question becomes the top ring, in the stack of still relatively coherent rings, it has developed large deviations from its original shape. Its radius has also been reduced by the action of the velocity field that is induced by the stack of coherent rings below it. Generally, the ring is then advected back down into the stack as if it were part of the unperturbed base flow. By the time it gets to the top of the stack, though, the shape of the ring is far from regular. Different parts of it are thus convected down into the stack at different rates. The non-uniform radial velocity near the top edge of the set of rings exacerbates any deviations from the ring-like geometry and causes long sections of the ring to be very rapidly re-oriented from lying almost parallel to the rotor

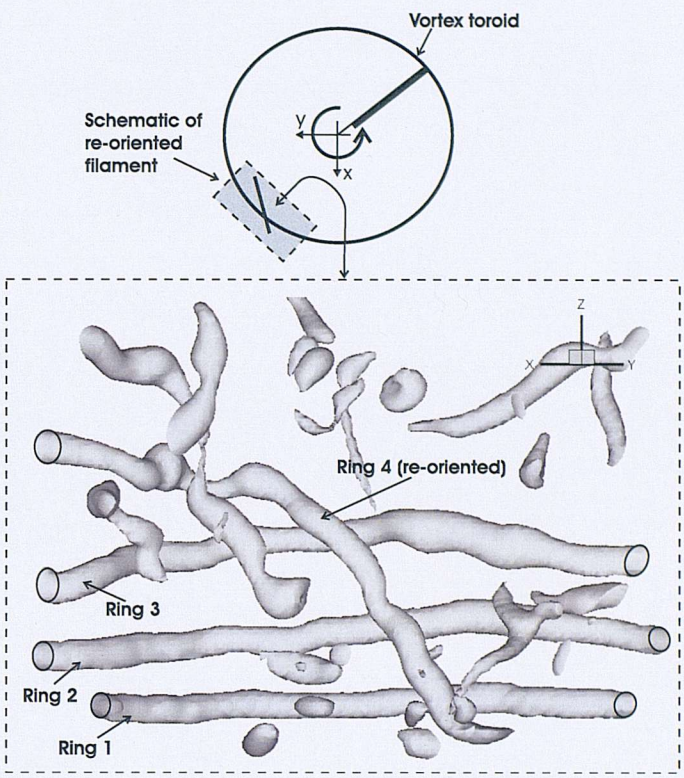



***Figure 3.8:*** *Snapshot of the wake structure within high speed VRS showing the disruption to the wake as a result of large-amplitude re-orientation of the tip vortex. (Iso-surface of vorticity magnitude.)*

plane to an almost perpendicular orientation relative to the rotor plane. An example of one of these large-angle excursions in progress is shown in Fig. 3.8 where the relative order of the first three rings in the stack is in strong contrast to the geometry of the strongly re-oriented fourth ring. The extensive deformation to the vortex filament that is shown in this figure begins as a large-radius 'hair-pin' like structure, such as that shown in Fig. 3.9.

The third modifying factor arises from the geometric difference between a set of rings and a compacted helix; as illustrated in Fig. 3.2, the turns of a helix cannot pass through one another without becoming entangled. This entanglement manifests itself, as shown in Fig. 3.10, in the legs of these hair-pin structures, i.e. the almost-vertical sections of the once ring-like vortex, wrap themselves in spiral fashion around the core of the toroid-like base flow. This process leads very quickly to the complete destruction of the original structure of the vortex loop. The combination of multiple such events yields the rather

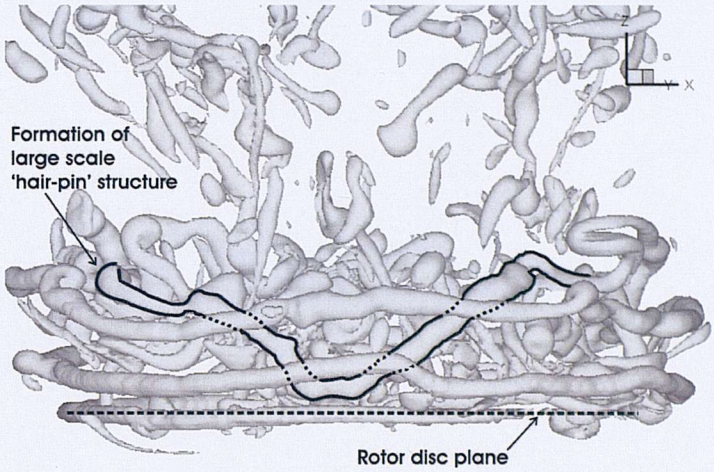



***Figure 3.9:*** *The early stages of vortex re-orientation showing the development of a large-scale 'hair-pin' structure in the tip vortex. (Iso-surface of vorticity magnitude.)*

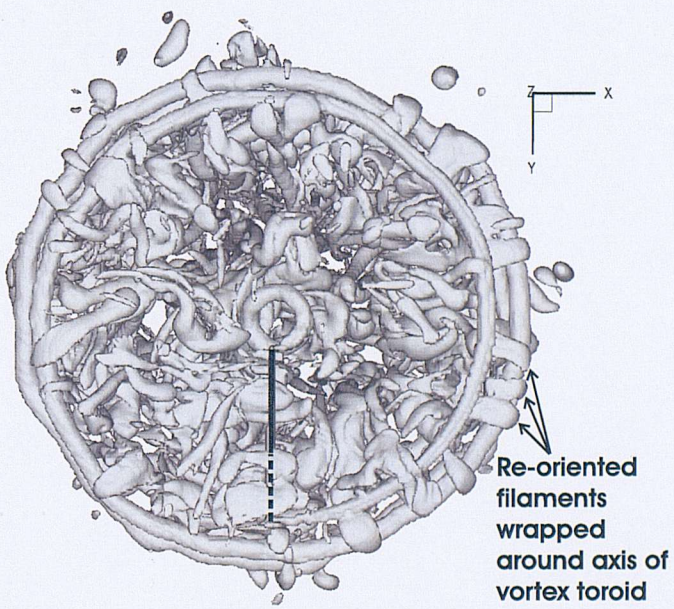


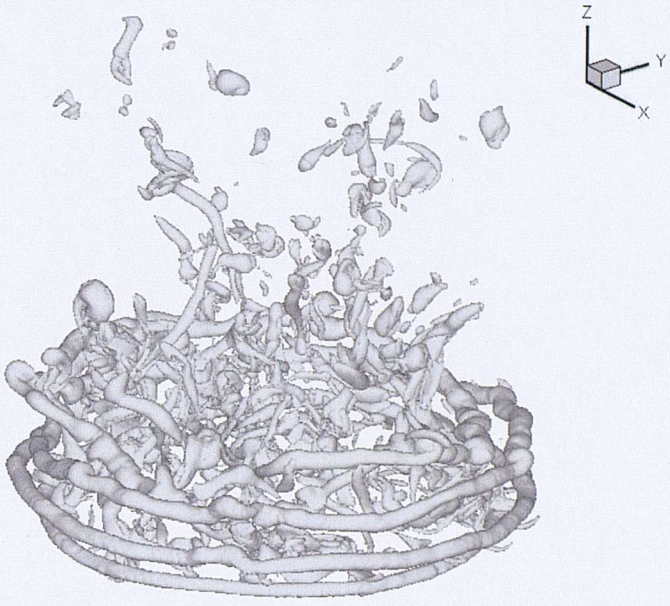

***Figure 3.10:*** *A view from beneath the rotor showing how re-orientated vortex filaments are wrapped around the core of the ring-like VRS base flow. (Iso-surface of vorticity magnitude.)*

intricate radial spoke-like structure to the wake shown in this figure.

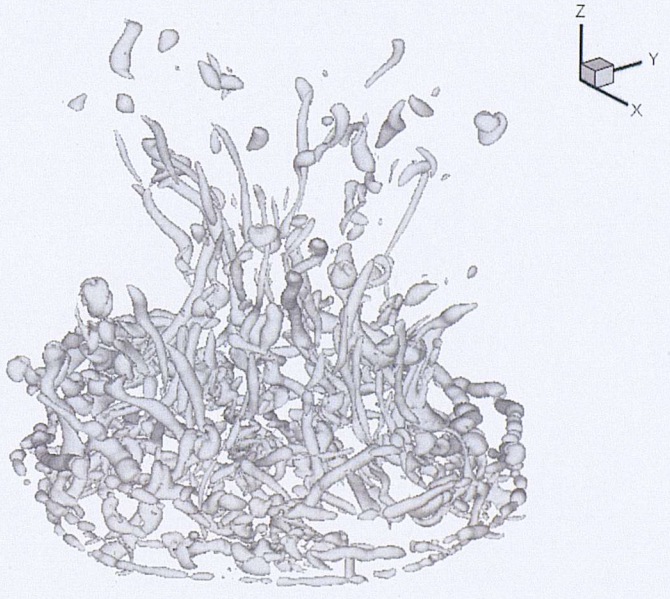
Once the vortex rings have been broken up by the re-orientation process described above, the resulting vortex structures do not remain indefinitely within the toroidal base flow. Figure 3.7 showed the existence of a continuous stream of vorticity into the flow downstream of the rotor that originates from just above the toroid. The diameter of this stream, which is roughly co-axial with the rotor, appears to be approximately two thirds of the rotor's diameter.

Figure 3.11 shows a decomposition of the vorticity field into the components of vorticity that are aligned parallel to the disc-plane (Fig. 3.11(a)) and the component of vorticity that is aligned normal to the disc-plane (Fig. 3.11(b)). The same value of vorticity magnitude was used to create the iso-surfaces in both figures to allow a comparison of the relative contributions of each component to the overall vorticity in the flow. This value was set relatively high to remove the clutter of weaker, more dislocated vortex elements from the image. These figures show clearly that there is much disorder, even amongst the stronger vortical elements within the flow field. This disorder is certainly to be expected, given the underlying instability of the vortex elements to perturbations to their geometry, but somewhat more remarkable is the existence of large, coherent filaments of mostly vertically-orientated vorticity both within the circumference of the rotor disc and in the ejection stream. Indeed, the vorticity in the ejection stream appears to consist mostly of vertically-orientated vorticity, indicating the presence of significant structure within this part of the flow.

Several previous studies [13, 68] have commented on the existence of a central up-flow through the rotor disc when in the VRS. There is some evidence for the existence of an upward flow through the root of the rotor that was simulated in this study. The general trajectory of the root vortices is indicated in Fig. 3.12 where it is seen that, in this particular case, these vortices are initially convected slightly upwards away from the disc plane before being swept radially outwards, and finally downwards into the recirculating base-flow that is associated with the tip-vortex system. The central stream of ejected vorticity thus does not consist primarily of root vorticity, as might be inferred from its location and geometry. For purposes of illustration, Fig. 3.13 shows a set of particle paths through the time-averaged flow around a rotor (of somewhat different geometry to that simulated in this study, though) that is descending at a very similar normalised




(a) Components of vorticity parallel to disc plane.




(b) Component of vorticity normal to disc plane.

***Figure 3.11:*** *Vorticity field of the wake in VRS, decomposed into components normal and parallel to the disc plane.*

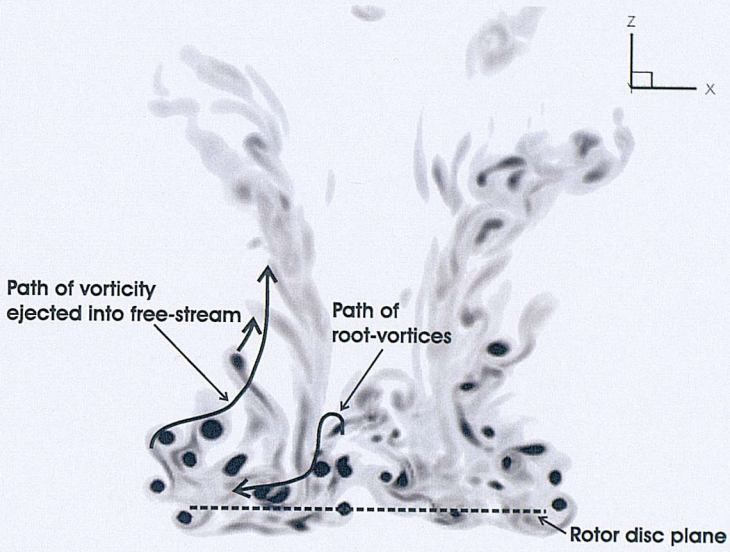



***Figure 3.12:*** *Paths followed by vorticity (a) in the ejection stream and (b) originating at the blade root.*

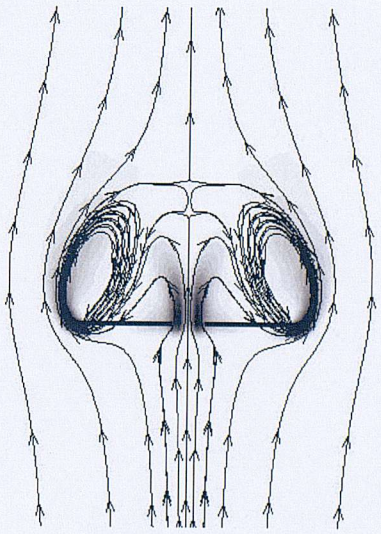


***Figure 3.13:*** *Particle paths through the time-averaged flow generated by a rotor in high-speed VRS ($\bar{\mu}_z = 1.0$, VTM simulation).*

speed ($\bar{\mu}_z = 1.0$). This figure shows the existence, in the mean, of an extended, toroidal, recirculating region of flow around the tips of the rotor that gives way, some distance outboard, to an upwardly-directed flow. Shown in Fig. 3.12 is the path that in general is taken by the vorticity that is ejected up through the central stream. Indeed, the vorticity in the ejection stream appears to be comprised entirely of those elements of the disintegrating, toroidal base flow that move far enough towards the periphery of the recirculating region to be entrained into the outer flow instead of being convected back down into the toroidal base flow.

Long-term observations of the simulated flow-field reveal that there is a second, less frequent and far more aperiodic mechanism whereby vorticity is ejected from the flow near the rotor. This mechanism is likely to correspond to the 'vortex breakaway' process that has been observed in several experimental studies of the VRS (see Stack *et al.* [15] for instance). The high resolution of the current simulation allows the kinematics underlying this process to be examined in greater detail than has been experimentally possible to date. A breakaway event usually follows the coincidental, near simultaneous re-orientation of neighbouring parts of two adjacent vortex loops within the stack of three or so coherent structures that exist within the base flow. The sections of the two adjacent vortex loops that are left near the top of the stack, after this process has resulted in appreciable distortion, do not necessarily follow the normal recirculating trajectory that would take them back down into the toroidal flow, or even into the central ejection stream. Instead, on occasion, they begin to orbit around each other as shown in Fig. 3.14. A small number of rotor revolutions then generally elapses before the intertwined pair of filaments are suddenly ejected almost straight upwards from the top of the toroid and away into the free-stream. The violence of the ejection is most likely a consequence of the high mutually-induced velocity of the filaments involved in the process. The first image at top left of Fig. 3.14 shows a two dimensional contour plot of vorticity on a plane that passes through the rotor hub. Captured in the plot is a sectional view through the wake just prior to an ejection event as two vortex filaments, marked 'a' and 'b', begin to orbit around each other. The 3D image at bottom left reveals the structure of the two co-orbiting filaments in more detail. The set of images at right shows the structure of the wake three rotor revolutions later, by which time filament 'b' has been ejected into the flow downstream of the rotor. The 3D image at bottom right shows how the two co-orbiting filaments deform

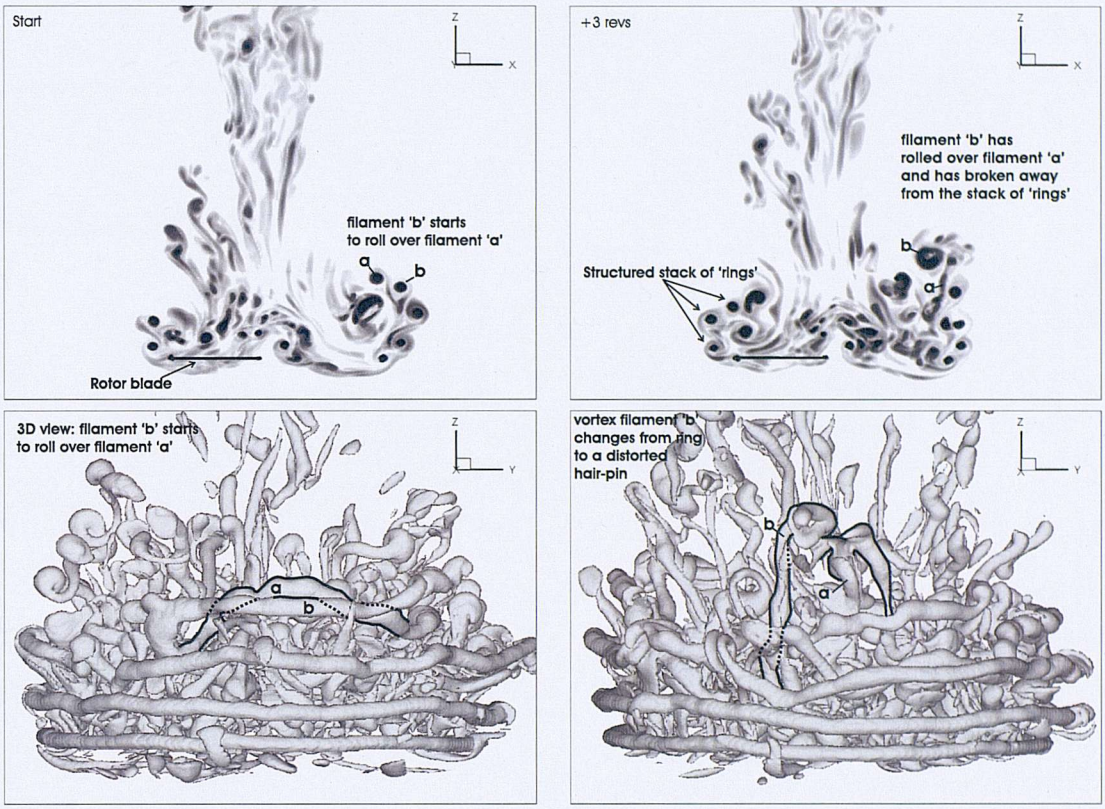



***Figure 3.14:*** *2D and 3D images of the rotor wake in VRS showing the initiation of a large-scale vortex 'breakaway'.*

into a tight hair-pin like structure during the ejection process. These large-scale ejections of vorticity into the flow downstream of the rotor tend to disrupt the normal evolution of the stack of coherent vortex rings within the base flow for several rotor revolutions by causing subsequent turns of the wake to follow a similar process. Eventually, though, some semblance of order in the base flow is re-established following the creation of fresh vorticity at the base of the stack by the passage of the rotor blade beneath the disturbed region.

Much has been made hitherto of the re-orientation of the vortex filaments, or more precisely, the local conversion of horizontally- to vertically-aligned vorticity. This is partly because this re-orientation process is the non-linear, large-amplitude continuation of the development of the linear modes of instability that were highlighted by Widnall [5], and Bhagwat and Leishman [6]. These re-orientations are not just passive, inconsequential events though; filament rotation has important consequences for the velocity field that is induced by the rotor. The induction of vertical inflow through the rotor is dependent only

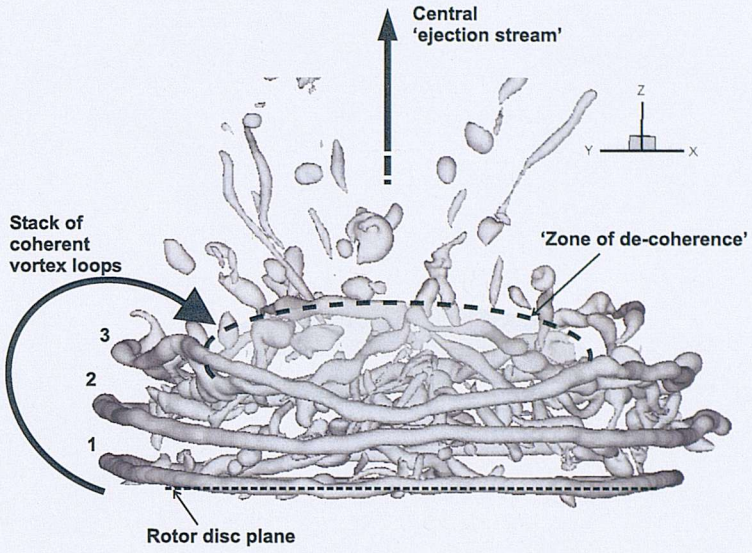



***Figure 3.15:*** *Pictorial summary of wake structure in high-speed VRS.*

on the component of vorticity that lies co-planar with the rotor disc. This follows simply from the fact that a vortex element induces a velocity that has direction perpendicular to its swirl axis. Filament re-orientation is thus an important and influential process since it removes from the flow a significant quantity of vorticity that contributes to the propagation of wake vorticity downwards into the flow below the rotor. In other words, as the components of vorticity $\omega_x$ and $\omega_y$ oriented parallel to the rotor plane are partially converted into vorticity $\omega_z$ oriented normal to the rotor plane, the velocity of local downward flow decreases and the system must therefore lose some of its ability to generate a tubular wake structure beneath the rotor plane. This observation, which is examined explicitly in Chapter 4 of this thesis, has particularly important consequences for the interpretation of the simulation to be presented in the following section of the chapter, where re-orientation of vortex filaments is implicated as the prime factor leading to the collapse of the ostensibly tubular wake into the toroidal structure that is characteristic to the VRS. The present simulation of the more orderly transition into the VRS from WBS allows a less cluttered analysis of the wake kinematics, however. The structure of the wake in high-speed VRS is summarised in Fig. 3.15 which shows the vortical system associated with the rotor essentially to comprise a stack of coherent, recirculating vortex rings, a region in the centre of the wake where the ring-like vortex structures lose their form under the action of the

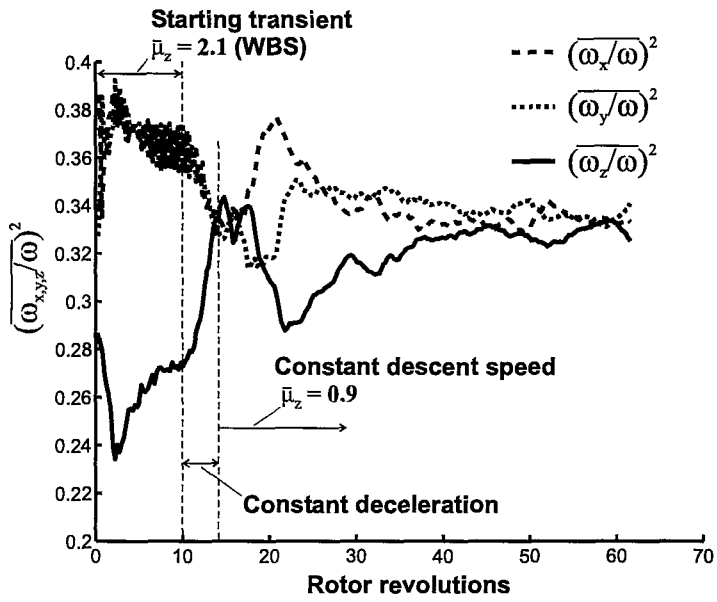


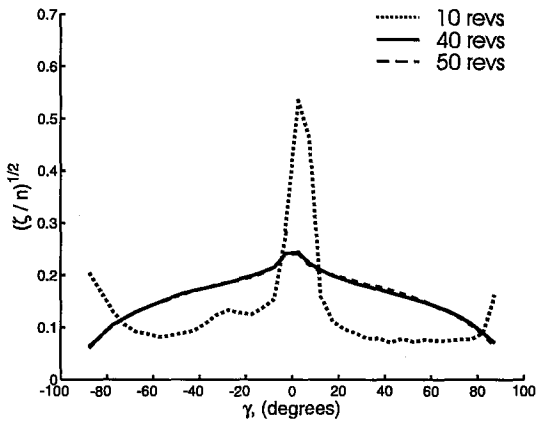

***Figure 3.16:*** *Variation of the contribution of each vortex component to the overall vorticity in the flow field.*

velocity gradients in the flow field, and, finally, an almost continuous stream of ejected vorticity up the centre of the wake.

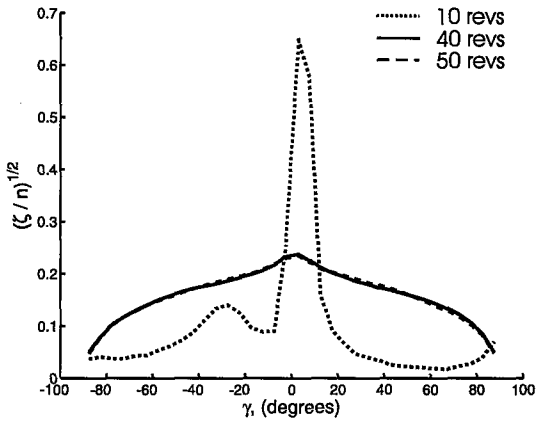
In addition to the preceding qualitative description, a quantitative assessment of the kinematics of the flow field can be conducted by evaluating the variations in strength of the vorticity components with time during the transition from WBS to VRS, and by surveying the orientation angles with respect to the rotor plane that are adopted by the vortex filaments within the wake. Shown in Fig. 3.16 is the variation with time of the relative contribution of each component of the vorticity to the overall vorticity within a box encompassing the entire diameter of the rotor and extending a rotor radius above the disc-plane. For the first 10 rotor revolutions of the simulation, the descent speed was held constant with the rotor in the WBS. Figure 3.16 shows that the contribution of the vertical vorticity component to the overall vorticity in this phase of the simulation, at approximately 27% (this value includes a significant contribution from the tip vorticity as well as from the equally strong though more steeply inclined root vorticity), to be somewhat lower than that of the combined contributions of the two horizontal vorticity components. The rotor was then decelerated into the VRS. The figure shows the contributions of $\omega_x$ and $\omega_y$ to fall slightly as a result, but the contribution of $\omega_z$ to the overall vorticity to rise sharply. This is evidence of the increasing effectiveness of the wake instability in inducing

re-orientation of vortex filaments during the deceleration. Just after the stage where the deceleration ends there is a period of transients whilst the wake settles and the VRS behaviour develops. Once the VRS has fully developed (between revolutions 40 and 45), the contribution of the vertical vorticity component to the total vorticity reaches an ultimate value that is approximately equal to the contributions of the two horizontal components. Although, these values fluctuate somewhat due to the unsteadiness of the flow field. In other words, whilst the majority of the vortex filaments within the wake at this descent speed remain co-planar with the rotor disc, roughly one third, rather than one quarter as in the WBS, of the total vorticity near the rotor is made up of vorticity that does not contribute to the generation of inflow through the system.

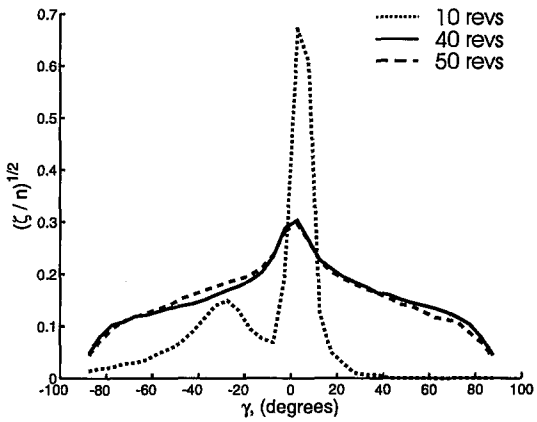
To extend this examination of how the orientations of vortex filaments change as the rotor moves from the WBS to the VRS, the statistical spread of orientation angles with respect to the rotor disc plane, given by $\gamma = \sin^{-1}(\omega_z/|\omega|)$, that were adopted by the vortical filaments in the wake was calculated at different times during the simulation. Figure 3.17 shows the frequency of occurrence, denoted by $\zeta$, of vortex filaments oriented within 5° angular intervals between angles $-90°$ and 90°, divided by the total number of occurrences, $n$, in the overall range. The square-root of the frequency of occurrence is plotted simply to improve the clarity of the presentation. Each graph compares the spread of angles after 10 rotor revolutions (in WBS) and after 40 rotor revolutions and 50 rotor revolutions (during VRS). Each plot differs from the other by the minimum magnitude of vorticity that is included in the frequency count. This 'filtering' of the data was conducted to gain an understanding of how the orientations of the strong, coherent structures differ from that of the fog of low-level vorticity in the flow-field. With the system in the WBS (i.e. after 10 rotor revolutions), several distinct peaks, corresponding to favoured filament orientations within the flow, can be identified. Given the relatively ordered wake within this flight condition, as shown in Fig. 3.5, positive orientation angles can generally be associated with vortex filaments that have been trailed from the tips of the blades, whilst, because of the opposite sense of their vorticity, negative angles correspond to the vortex filaments that stem from the root of the blade. As a useful check case, the data in each graph of Fig. 3.17 with the system in the WBS can thus be interpreted as revealing the predominant contribution of the tip vorticity, oriented in the interval between $+5°$ and $+10°$, and the root vorticity, oriented in the interval between $-40°$ and $-20°$, to the




(a) Vorticity threshold $\omega/\Omega = 0.001$ (i.e. The survey includes virtually all the vorticity in the flow).




(b) Vorticity threshold $\omega/\Omega = 0.05$ (i.e. The survey includes only the intermediate to strong vorticity in the flow).




(c) Vorticity threshold $\omega/\Omega = 0.5$ (i.e. The survey includes only the strong vorticity in the flow).

***Figure 3.17:*** *Statistical spread of vortex filament orientations with respect to the horizontal in WBS and high-speed VRS.*

structure of the flow. The breadth of the peak associated with the root vorticity compared to the peak associated with the tip vortex is most likely a consequence of the disruption of the structure of the root vortex by the action of short-wavelength instabilities that is clearly visible in Fig. 3.5. Instances of filaments with other orientations within the WBS are comparatively rare, aside from, curiously, a significant concentration of very weak vortex filaments (Fig. 3.17(a)) with orientations within the intervals $-90°$ to $-85°$ and $+85°$ to $+90°$. It is quite likely that this feature of the distribution is simply an artefact of the overall second order accuracy of the VTM.

A similar analysis of the wake with the rotor in the VRS (i.e after 40 rotor revolutions) shows a general decrease in the number of filaments aligned parallel to the disc and a substantial increase in the number of filaments aligned more obliquely to the rotor plane compared to the situation in the WBS. Within the VRS, however, the considerable mixing of the root-vortex and tip-vortex filaments renders invalid the clear distinction between the physical source of filaments with positive and negative orientation angles that can be made in the WBS. The apparent symmetry between the spread of filaments with positive and negative orientation angles within the VRS, and the relative breadth of the distribution of filament orientations within the wake, is extremely interesting. Such symmetry is entirely consistent with the predominance of a process within the wake whereby the vortex filaments are forced to undergo continuous end-over-end rotation. As described above, the re-orientation process transforms a source of vortex filaments with near-zero orientation angles (the vorticity in the base flow) into filaments with larger orientation angles with respect to the disc plane. There is no inherent property of the vortex kinematics that precludes, locally, the reverse process, however – that is, the conversion of filaments with larger orientation angles back into filaments with smaller orientation angles with respect to the disc plane. The distinct, but near-linear tail-off in the frequency of vortex filaments with larger orientation angles with respect to the rotor plane is consistent, in fact, with the near-equilibrium of the forward and reverse processes. Certainly, comparing the frequency distributions that are obtained at 40 and 50 rotor revolutions into the simulation shows that the preferred distribution of vortex filament orientations remains a fairly constant feature of the structure of the rotor wake when in the VRS, and supports this notion of at least a statistical equilibrium within the flow. The much stronger tail-off in the frequency of filaments with the highest orientation angles is consistent with the structure presented

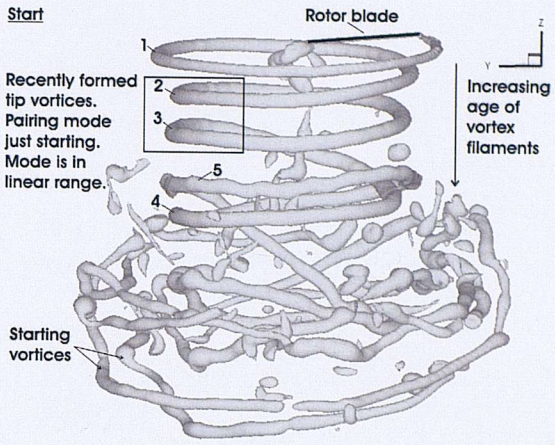
in Fig. 3.11 which shows filaments with almost normal orientation to the rotor plane to predominate in the stream of vorticity that has been ejected from the toroidal, VRS base flow and captured by the free-stream.

## 3.4 Entry into VRS from Hover

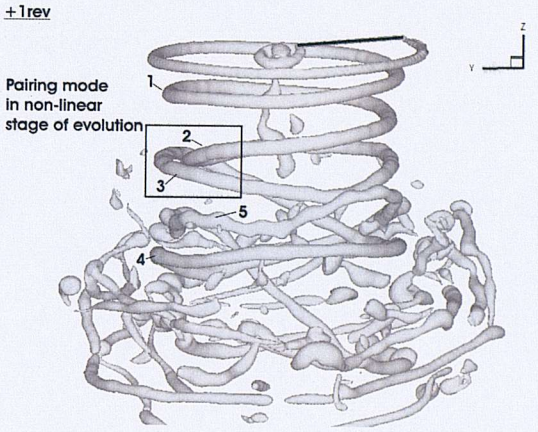
The kinematics of the vortical flow field that lead to the onset of the vortex ring state when the descent commences from hover instead of WBS were also investigated using the simplified rotor described earlier. The trajectory of the rotor comprised an initial 20 rotor revolutions with the rotor in hover to allow sufficient time for a fully developed wake to form. The hover phase was followed by an accelerated descent, over a duration of 28 rotor revolutions, ending with the rotor in low-speed VRS, at a normalised descent rate $\bar{\mu}_z = 0.45$. Twenty three rotor revolutions were then captured with the rotor descent speed held constant at this value.

Visualisations of the three-dimensional structure of the vorticity field that is generated by the rotor in hover, as presented in Fig. 3.18, show the clear influence on the geometry of the rotor wake of both the vortex pairing instability and the short-wave instability that are known to influence very strongly the kinematics of helical vortex filaments [5, 6]. The manner in which the ultimate, non-linear manifestation of the pairing mode diverges from its initial, linear, 'leap-frogging', form is also very clearly evident. The figure shows the evolution of the wake of the hovering rotor, starting from the 15th revolution of the simulation, i.e. from when a reasonably well-developed wake had become established beneath the rotor.

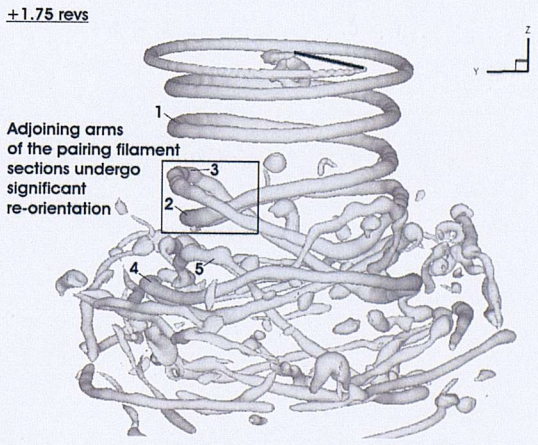
Figure 3.18(a) shows the existence of an ordered near-field consisting of vortex filaments generated during the three most recent turns of the rotor. These filaments are convected downwards into the wake, but are preceded by two older segments of the tip vortex (denoted as '4' and '5' in the figure) that have interacted significantly with each other as a result of the vortex pairing instability. Focusing upon the sections of the tip vortex within the box in Fig. 3.18(a), it is clear that at this early stage in their evolution the geometry of elements '2' and '3' appears largely unaffected by any flow instability, save for the very subtle outward motion of the lower of the two elements. The slight distortion to element '3' indicates the initiation of the self-induction, or 'pairing', mode of instability. At this




(a)




(b)

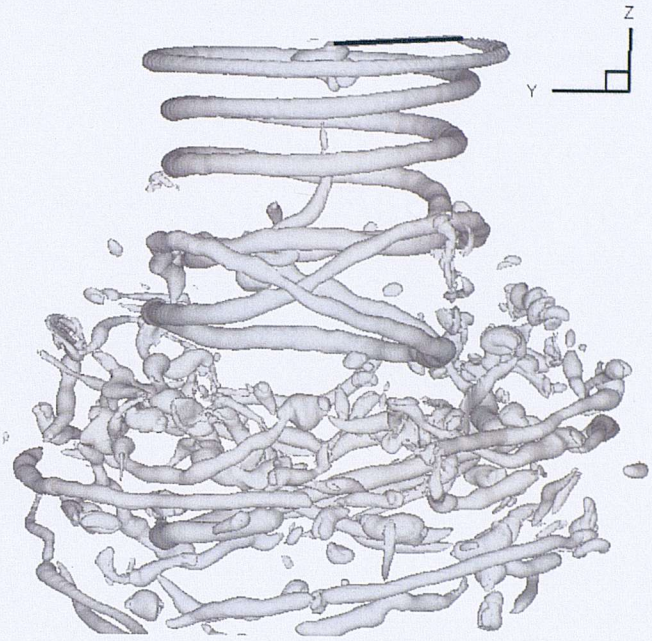



(c)

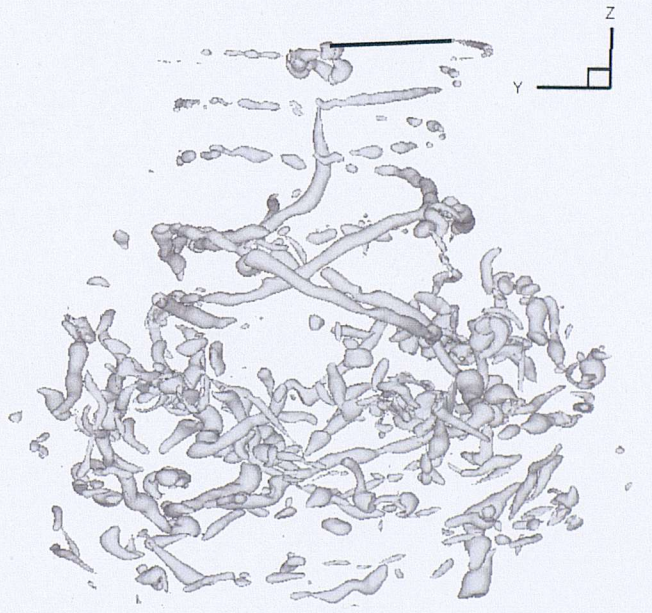
***Figure 3.18:*** *Example of the non-linear vortex pairing/re-orientation mode occurring in the wake of a hovering rotor.*

early stage, the deformations to the filaments resemble reasonably closely the distortions that would result from the early stages of vortex-ring 'leap-frogging'. Fig 3.18(b) shows the structure of the wake after it has developed for a further rotor revolution. This image shows segments '2' and '3' to be in the process of rotating about one another. Although the two segments still lie approximately in the same plane, and thus it is arguable that the relative motion of these segments is still similar in form to the leap-frogging mode, the arms of the turns of the helix to which they belong have been rotated significantly out of their original orientation. The re-orientation of these sections of the vortex is a natural result of the constraint imposed on the deformed geometry of the wake by the helical, rather than ring-like, geometry of the tip vortex, as described earlier. Figure 3.18(c) shows the geometry of the wake a further three quarters of a rotor revolution on from the geometry shown in Fig. 3.18(b). In this final image, the perturbation to the geometry of the originally helical vortex segments has proceeded well into the non-linear regime, to the extent that these segments of the tip vortex have begun to lose coherence both through their own mutual interaction and by interactions with other nearby elements of the wake. Indeed, the products of earlier, similar large-scale disruptions to the structure of parts of the tip vortex system can be seen in the far wake. This process, whereby small perturbations to the structure of the vortex are amplified through the non-linear action of this pairing/re-orientation mechanism, is continuous and repetitive, and results in the almost total annihilation of any structure to the helical vorticity distribution in the far wake of the rotor.

Figure 3.19 shows the vorticity field in the wake of the hovering rotor at the end of its 20th revolution. In this pair of images, the vorticity in the wake has been decomposed into its components parallel to the disc plane (Fig. 3.19(a)), and its component normal to the disc plane (Fig. 3.19(b)) in similar fashion to the data presented earlier in Fig. 3.11. A comparison of the two images shows significant rotation of the helical tip vortex towards a disc-normal orientation by the time the tip vortex has aged by several rotor turns. As described earlier, the re-orientation of the filaments leads to a distinct reduction in the ability of the vorticity some distance below the rotor to contribute to the sustainment of the helical wake structure below the rotor disc. Although there is evidence in Fig. 3.19(b) for re-orientation on a much smaller length scale as a result of the influence of the short-wave instability mode, it is primarily the pairing mode that is responsible for the loss of




(a) Components of vorticity parallel to disc plane.



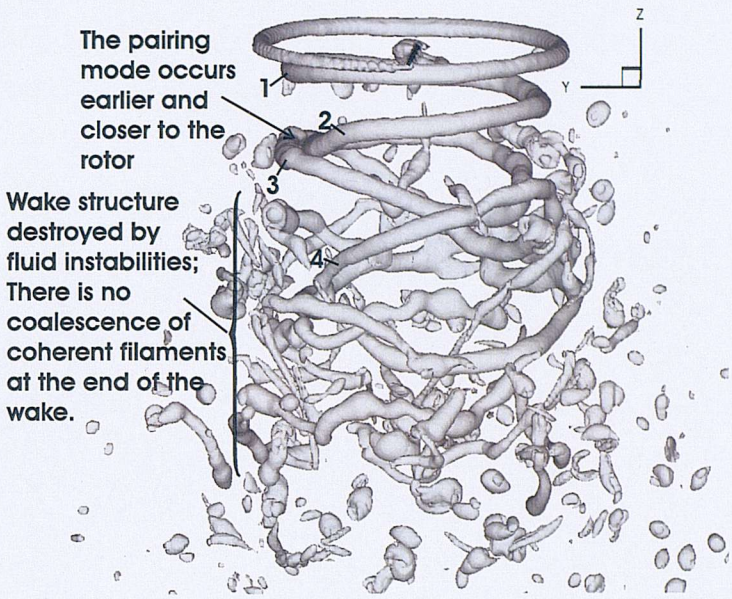

(b) Component of vorticity normal to disc plane.

***Figure 3.19:*** *Vorticity field of the rotor wake in hover, decomposed into components normal and parallel to the disc plane.*

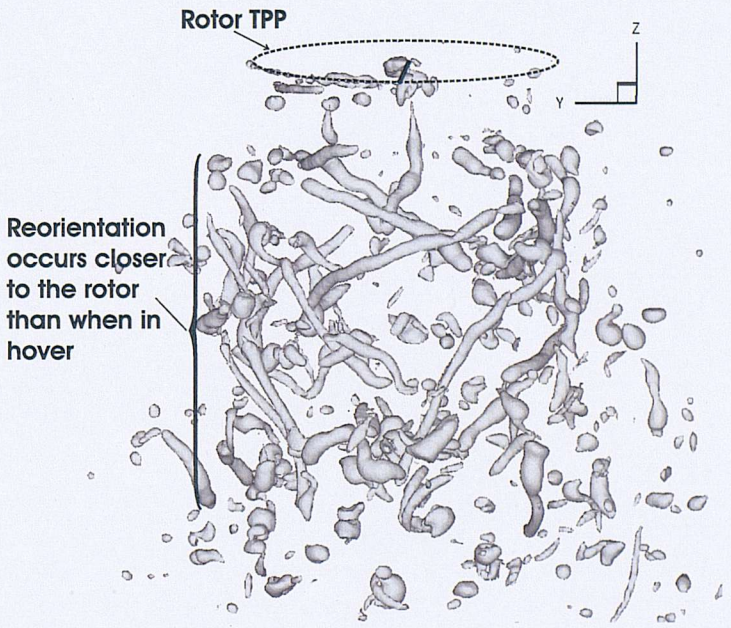
coherence of the vortical structures in the wake. It is thus eminently arguable that it is the vortex kinematics of the wake, and the filament re-orientation in particular, rather than an inherently viscous mechanism, that is responsible for the structural decay and consequent truncation of the wake that has been observed experimentally [13, 69].

As described above, the wake is effectively truncated by the loss of coherence in the turns of the helix, several rotor radii downstream of the disc plane. This implies, then, that it is the rate of growth of the fluid instabilities within the system that governs the length of the wake for a given inflow through the rotor. If the rotor thus descends slowly enough, the helical, hover-like form of the wake can still be maintained for some distance below the rotor. All else being equal, the pitch of the helical wake in low-speed descent is reduced compared to the case in hover. Simplistically this is because in descending flight, the tip vortices travel a reduced distance, during a single revolution of the rotor, under the competing influences of their self-induced advection and the opposing free stream flow, compared to when the rotor is in hover. Bhagwat and Leishman [6] showed that the distance between the vortex filaments was the primary factor governing the growth rate of perturbations in the flow. Thus, as the rotor descends, the pairing which leads to re-orientation and the ultimate destruction of any coherence to the structure of the wake some distance below the rotor, occurs at an earlier tip-vortex age than it does with the rotor in hover. Effective truncation of the wake thus occurs closer to the rotor than it would if this dependency did not exist. This can be seen clearly by comparing the decomposition of the vorticity into components parallel and normal to the disc plane for the rotor in hover, shown in Fig. 3.19, with a similar decomposition of the vorticity generated by the rotor in slow descent as shown in Fig. 3.20.

Unlike in hover, though, the presence of the upwardly-directed free stream occasionally results in fragments of highly disordered vorticity being convected towards the disc plane from the far wake where they were created. In hover these fragments are generally confined to the far-field and simply convect haphazardly around, at the whim of the locally fluctuating velocity field in the region of the exhausted flow. Some of these upwardly-convecting fragments of tangled and highly disorganised vorticity interact very strongly with the more ordered sections of the wake closer to the rotor if they happen to pass close by. These interactions are, on occasion, highly disruptive as they can engender short-wave perturbations of significant amplitude in recently generated tip-vortices, as is




(a) Components of vorticity parallel to disc plane.




(b) Component of vorticity normal to disc plane.

***Figure 3.20:*** *Vorticity field of the rotor wake in slow descent ($\bar{\mu}_z = 0.2$), decomposed into components normal and parallel to the disc plane.*

demonstrated in Fig. 3.21. This mechanism thus appears to provide a means by which the wake might bypass the linear phase of the growth of small perturbations, to lead to an even earlier disruption to the structure of the wake than if this mechanism were absent.

Considerable blade vortex interaction is also evident in the figure and this too appears to exacerbate the breakdown of the structure of the wake as it too seems to initiate earlier non-linear growth of perturbations. The effect of the BVI on the normal velocity of the flow impinging on the rotor blade is depicted in Fig. 3.22 where it produces a significant area of upward flow local to the BVI. Also shown in this figure is the disruption to the distribution of the blade-normal flow velocity caused by the vortex 'fragment' encounter, described above. This is evidence that the thrust produced on a rotor operating in, or near to, the VRS will be effected by wake breakdown in a direct way through an encounter with the fragmented vorticity.

When the descent acceleration ceases and the descent speed of the rotor thus becomes constant (at $\bar{\mu}_z = 0.45$ in this simulation) there is considerable delay in the response of the structure of the wake to the change in acceleration. Indeed, it takes several rotor revolutions, post the cessation of the acceleration, for the wake to adopt the form exhibited in Fig. 3.23; the tubular shape of the wake is no longer in evidence and so the rotor, by this stage, is judged to have entered the vortex ring state, albeit at a much lower descent rate than in the simulation described previously. The figure shows two images of the vorticity field, some 20 rotor revolutions after the descent speed had become constant. The first image shows an iso-surface of the vorticity distribution in the wake with the value used to generate the surface set very low so that much of the weak vortical structure is exposed. The wake appears to consist mostly of fragmented vortex filaments, orientated orthogonally to the core of a large toroid of vorticity about which they recirculate. The second image, again showing an iso-surface of vorticity, but with the surface value set high enough to retain only the strongest features of the vorticity field, shows that, beneath the weak, fragmented layer of vorticity, the wake consists of a highly compacted helix comprising just two definite, coherent, turns of the tip vortex. A third turn is still evident, though it has been significantly deformed by the highly unsteady and non-uniform local velocity field. Over a period of time, the individual turns of the helix are transformed into other less recognisable structures which are then entrained into the recirculating flow around the vortical toroid. The results of this process can be seen very clearly in

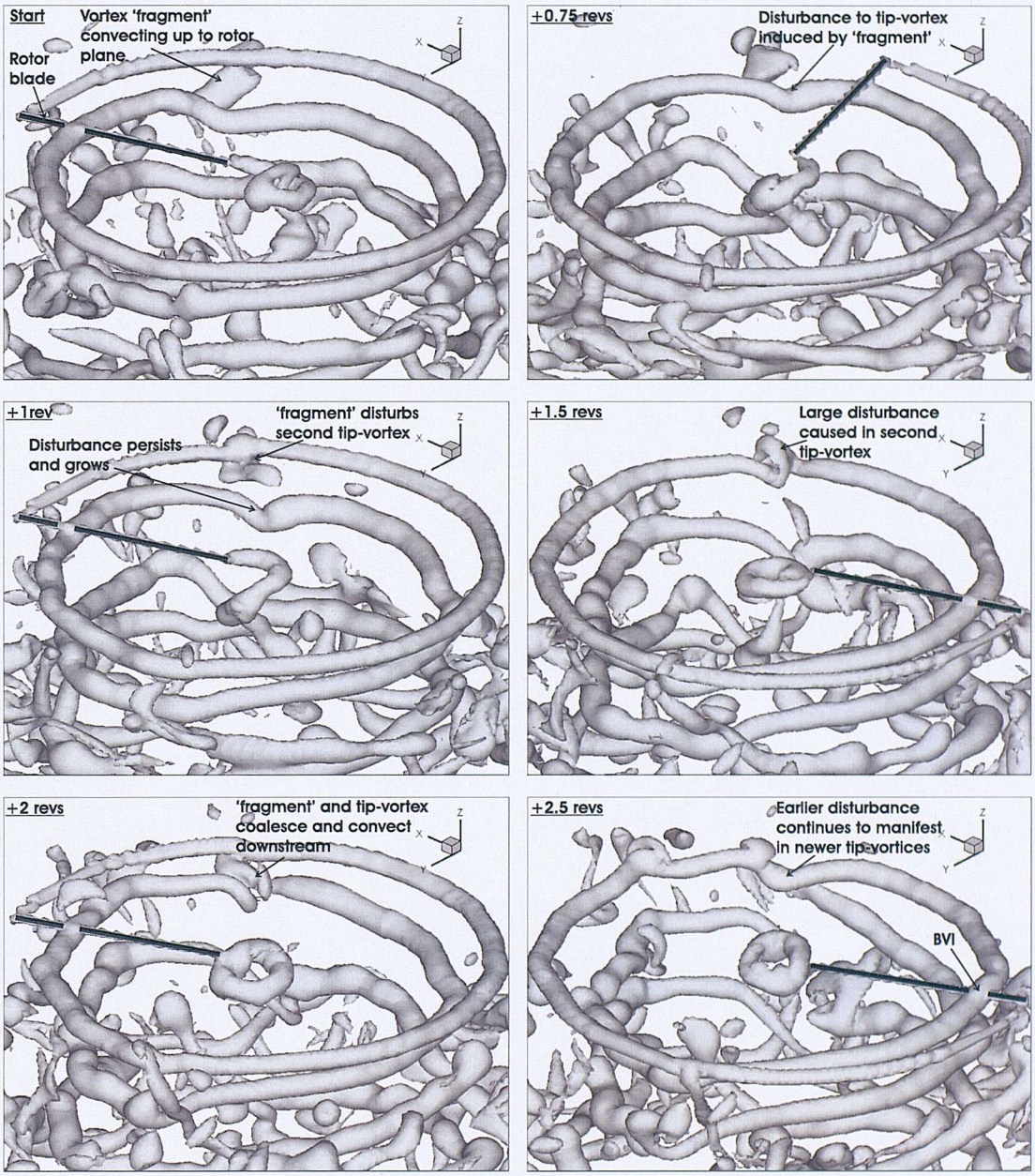



***Figure 3.21:*** *Effect on newly generated tip-vortex filaments of an encounter with an upwardly convecting vortex 'fragment'.*

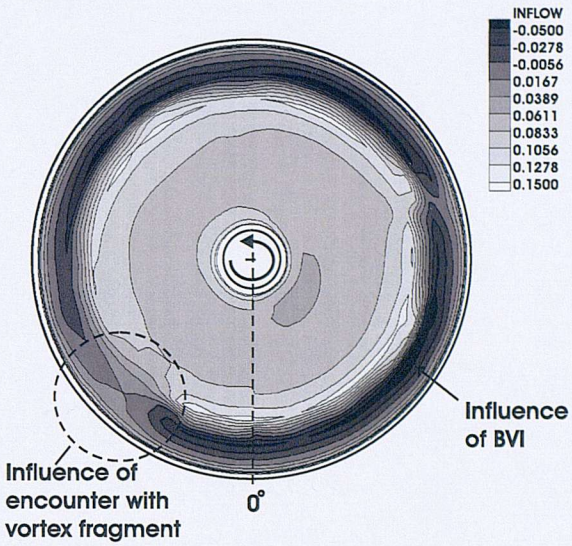
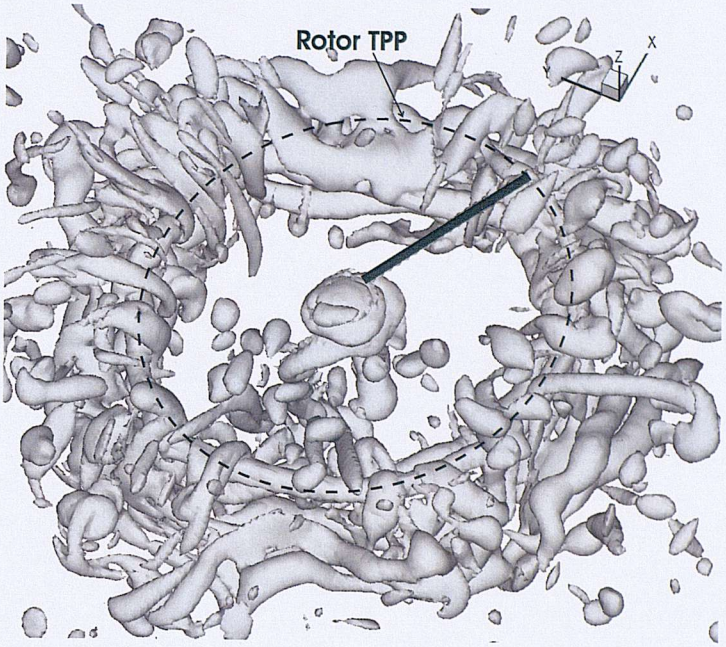


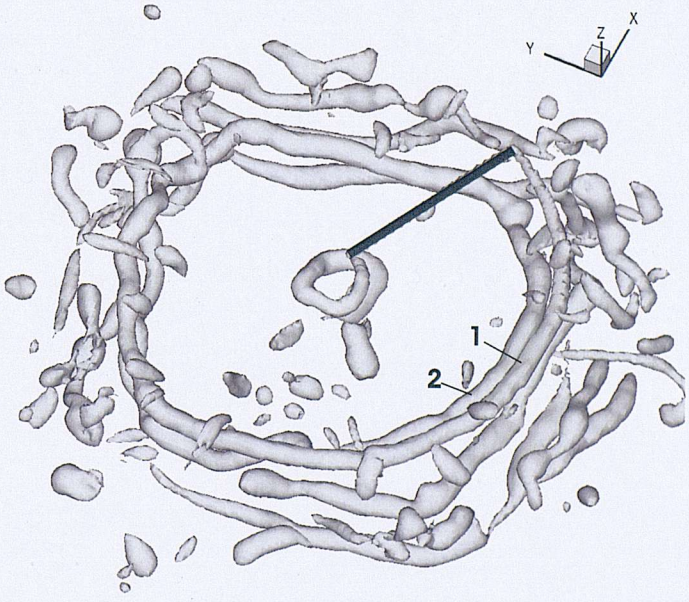

***Figure 3.22:*** *Radial distribution of blade-normal velocity during one rotor revolution. The rotor is descending at a speed of $\bar{\mu}_z = 0.44$. The dark areas represent regions of upward flow.*

Fig. 3.23(a). Little vorticity appears to escape from the recirculatory current, however, unless it happens to be convected sufficiently far out from the circumference of the toroid that it is captured by the free-stream and drawn upwards and away from the rotor; the large-scale ejections of vorticity that are a distinct characteristic of the high-speed VRS appear to be absent in low-speed VRS.

A survey of the orientation angles adopted by the vortex filaments in the wake, as shown in Fig. 3.24, reveals a strong similarity in the underlying structure to the flow fields of the low- and high-speed VRS – despite the subtle differences in their underlying kinematics. The figure shows the frequency of occurrence of vortex filaments that are oriented at a given angle $\gamma$ to the rotor plane, within a box that entirely encompasses the rotor and has a width of four rotor radii. In the vertical direction, the box extended one rotor radius both below and above the rotor disc; this volume was sufficient to capture all the near-field vorticity in the flow. The curves represent the spread of filament-orientation angles after 20 rotor revolutions (i.e. at the end of the hover phase), after 32 rotor revolutions (i.e with the rotor in low-speed, pre-VRS descent at $\bar{\mu}_z = 0.2$) and after 60 rotor revolutions (i.e 12 rotor revolutions post cessation of acceleration, with the rotor in low-speed VRS at $\bar{\mu}_z = 0.45$). The distribution of filament orientations at all descent rates shows a distinct peak of orientation angles within the interval $-5°$ to $0°$; this peak is associated with the




(a) Iso-surface value set to reveal the overall wake structure.




(b) Iso-surface value set to reveal only the strongest structures in the flow.

***Figure 3.23:*** *Vortical structure of the rotor wake in low-speed VRS. (Iso-surface of vorticity magnitude.)*

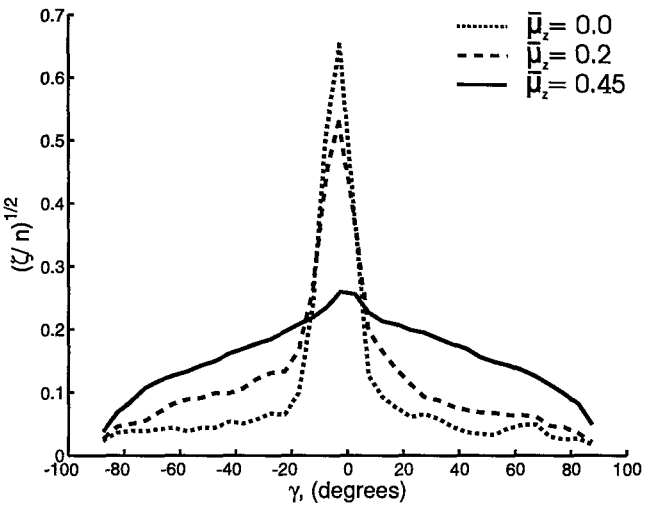



***Figure 3.24:*** *Statistical spread of vortex filament orientations with respect to the horizontal in hover and low-speed VRS. Vorticity threshold* $\omega/\Omega = 0.5$ *(i.e. Survey includes only the strong vorticity in the flow).*

tip-vortex of the rotor. The reduction in the height of this peak as the descent rate of the rotor is increased is clear evidence for the increasing loss of coherence of the tip vortex structure as VRS is approached. The qualitatively very similar distribution of orientations that is adopted by the vortex filaments both in low-speed VRS and in high-speed VRS (see Fig. 3.17(c)) shows that the influence of the instabilities in both systems is to yield fundamentally the same outcome in terms of the resultant structure of the vorticity within the rotor wake.

The vortical wake in low-speed VRS, then, consists of a compacted helix comprising just a few closely spaced turns, each of which are short-lived due to the growth of the many and seemingly random perturbations imposed upon it by the highly non-uniform velocity field near the rotor. The geometry of the helix exhibits numerous manifestations of the action of the short-wave instability; the resultant perturbations can reach appreciable amplitude as early on as just one quarter of a revolution following the generation of the affected segment of the wake. This form of disturbance is not inherent only to the VRS flow, though – all vortex filaments within a rotor wake are subject to the short-wavelength instability notwithstanding the flight condition of the rotor. Indeed, the simulation reveals a more significant difference between the general, global kinematics of the wake in low-speed VRS and the wake in hover or in very low-speed, pre-VRS descent. The wake in

low-speed VRS, in strong contrast with the situation in the higher speed VRS that was described earlier, shows scant evidence of the pairing of sections of adjacent vortex turns and the accompanying large-scale re-orientation of vorticity that is the dominant mode of relative filament motion in the flow field of a hovering rotor. As in high-speed VRS, the dominant motion in low-speed VRS is still similar to that of an axially-compressed stack of axially aligned, recirculating vortex rings, save for the modifications to that flow that result from the underlying helical, rather than ring-like geometry of the rotor wake. Unlike in the high-speed VRS, each newly generated tip-vortex filament finds itself to be the trailing loop, rather than the *leading* loop, in a stack of two or three co-orbiting ring-like structures; the somewhat different balance between the free stream and the velocity field that is induced by the stack of vortex loops results in the newly-formed vortex filament being advected downwards, below the rotor, rather than upwards as in the higher-speed VRS. The older vortex loops below the new filament expand and slow, and at some point their downward trajectory is arrested by the action of the free-stream in opposition to their induced flow. At this juncture, the direction of travel of the leading loop reverses and it then advects back up towards the rotor and has a radius sufficient to allow it to pass *outside* of the younger filaments moving down through it. Figure 3.25 charts the course of a series of such vortex loops. From the images it is clear how the rotating rings together form a toroid-like structure just below the rotor disc. The downward and outward circulation of the loops around the toroid results in a recirculating flow structure that has a generally smaller diameter than the equivalent structure that is formed by the upward and inward circulation of the coherent vortex loops in higher-speed VRS. Note though the very strong effect of the inherent flow instabilities on the number of vortex loops in the recirculating flow – this number remains relatively constant with time. Even though new, coherent segments of the tip vortex are continually being produced by the rotor, their ring-like structure persists for only a few rotor revolutions. The compacting action of the free stream in opposition to the induced flow appears to restrict this process of continual ring generation and eventual structural decay to within the spatial confines of the toroid itself, and also suppresses the large-amplitude spatial distortions of the flow field that are necessary for significant, individual, large-scale re-orientations of the vortex filaments to occur.

At some stage in the descent, then, there is a switch from one gross kinematic mode

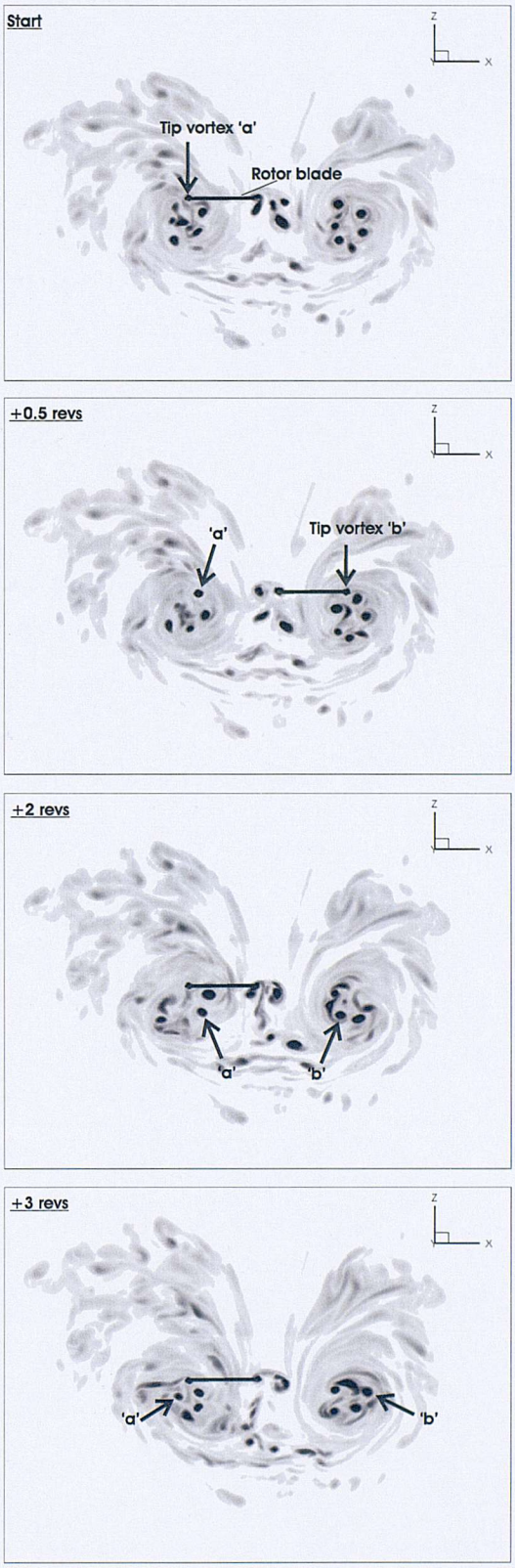



***Figure 3.25:*** *Evolution of tip-vortices in low-speed VRS. (Contour plot of vorticity on a 2D plane through the rotor hub.)*

to another: the pairing of helical turns, which is a mode of wake instability, gives way at some rate of descent to the approximate 'leap-frogging' motion of several, coaxial ring-like structures. This kinematics is not a mode of instability. In the low-speed VRS, then, the dominant mode of fluid instability appears to be short-wave, although the effects on the kinematics of the essentially helical form of the wake are still evident. This transition of the dominant wake dynamics may be used to mark the change from what is sometimes termed 'incipient' VRS, where the wake structure is largely tubular, though unsteady, to the fully-developed vortex ring state. Observations of the simulated wake suggest that the switch only occurs once *two* conditions have been met: firstly, the number of coherent turns left in the helix must be appropriate to allow the wake system to evolve in recirculatory fashion as a set of rings, rather than as a helix. Secondly, the magnitude of the opposing free-stream velocity must be approximately equal to, or larger than, the downward convection velocity of the leading (oldest) coherent tip-vortex filament, such that the body of the wake is unable to convect far from the rotor plane and thus form a tube-like structure as in hover. This criterion leads to a hypothesis that may explain the geometric fluctuation of the vortical wake, as characterised by Green *et al.* [13], whereby, at descent speeds that are too low to maintain the wake in the VRS, the structure of the wake is seen to switch intermittently between an elongated, helical geometry, which Green *et al.* referred to as a "tubular" form, and a toroidal geometry. The toroid subsequently breaks down, however, usually after just a few tens of rotor revolutions, allowing the re-formation of the tubular wake structure. So, this switching may happen if there are sufficient perturbations, in strength and number, to the structure of the tubular wake to lead to a rapid loss of coherence in the leading helical turns, thus causing the wake to lose its capacity to produce the local downwash velocity required to sustain the tubular form, with consequent collapse of the wake into its toroidal form. The toroid would eventually change back into a tubular form, though, because, although the structure and number of turns, or rings, in the wake might admit leap-frogging (as distinct from pairing), the free-stream velocity might not be sufficient to maintain the required spatial density of coherent vortex rings necessary for such motion to continue. In this case, the induced downwash would convect the rings back down away from the rotor, reforming the tube, and readmitting vortex 'pairing' as the dominant kinematic mode within the wake.

## 3.5 Discussion

In both instances of VRS that have been presented in this chapter, the underlying kinematic behaviour has been shown to be similar to the natural motion of a set of axially aligned vortex rings. That said, though, in the case where the low-speed VRS was approached from hover, the VRS dynamics that ultimately developed had, first, to transmute from a wake motion that was driven by the vortex mutual inductance, or 'pairing' mode of instability inherent to helical vortex systems. The wake structures and kinematics that arise in high- and low-speed VRS differ in subtle though important and interesting ways. In high speed VRS, the vortical toroid sits above the rotor plane and consists generally of three or four strong and coherent, closely-stacked helical turns of the tip vortex which approximate vortex rings both in their form and in their behaviour. The stack of rings that constitutes the base flow of the low-speed VRS lies beneath the rotor however, and three-dimensional flow visualisations have shown that this base flow consists of generally fewer ring-like vortex filaments than in the high-speed instance. The difference in the positions relative to the rotor that are adopted by the two wakes appears to govern the nature of the processes that destroy the coherence in their structures. When the wake is above the rotor, large-scale breakdown arises from long-range filament re-orientations, although the short-wave instability mode nonetheless plays an important role. Generally though, large hairpin-like vortex filaments are formed, as a result of these re-orientations, and the apices of these hairpins are either convected back down into the toroid or are induced to convect above it and away into the free stream – the eventual fate of any particular structure being dependent upon the way in which it interacts with other nearby vortex filaments. This process limits the number of rings that remain coherent within the high-speed VRS wake. In the low-speed case, however, the primary cause of the loss of coherence and ultimate break-up of the tip-vortex filaments appears to be the non-linear growth, along their length, of short-wave disturbances. In addition, the strain histories of the ring-like vortices in the two systems are quite different: in the low-speed VRS the helical loops undergo an initial radial compression which is followed by a radial expansion, whilst the opposite occurs in the high-speed case. The strain history of a convecting vortex ring appears to be an important factor that influences the evolution of perturbations to its geometry [67] and it is quite possible that the observed variances in vortex filament strain history between the two cases may contribute to the kinematic differences between high-speed and low-

speed VRS observed in the present work – although this is pure conjecture at this stage. What is certain, though, is that in the low-speed case, flow disturbances are convected up towards the rotor and its newly generated vortex filaments. Conversely, in the high-speed case, disordered vorticity and locally unsteady flow is blown upwards and away from the rotor, though indeed some highly disrupted vorticity may recirculate for some time prior to being ejected. This observation raises the possibility that the difference in the number of coherent turns that generally arise in the two base flows may be due to the variation in the number and strength of the perturbations that the tip-vortices are subjected to at any one time. Indeed, from the wake images shown in this chapter, the youngest filaments in the low-speed VRS flow field seem to be far more disrupted than their counterparts in the higher speed VRS. In this vein, the non-linear bypass mechanism mentioned earlier may play an important role in low-speed VRS in accelerating the disruption of the orderly structure of the youngest parts of the wake.

The simulations presented in this chapter were of a single-bladed rotor that trailed tip and root vortices of constant and equal strength into the flow field. In addition, the blade aerodynamics were uncoupled from the velocity field. It is possible that such simplifications could influence the generality of the findings of this work. The wake of a multi-bladed rotor operating under the same flight conditions may well comprise a different number of coherent ring-like vortex structures than that of the single rotor featured here. The number of rings that can persist in such a system is likely, though, to be equally dependent upon the form, amplitude and growth rate of the perturbations in the flow field. The simulations presented here have exposed, albeit qualitatively, the form that those perturbations may take and the manner in which they might evolve, and hence the fundamental dynamics of the wake generated by any rotor operating in the VRS. In summary, the behaviour of a multi-bladed rotor should not differ greatly from that of a single bladed rotor; the details will be different but the essence of the governing physics must be the same.

The aerodynamic coupling of the blade loads to the unsteady velocity field of the flow will cause the strength and distribution of the bound circulation on the blades to vary in time. The manner in which the strength and distribution of vorticity that is trailed from the rotor changes in response to the fluctuating velocity field will depend upon blade geometry and the mode of operation of the rotor, i.e. constant, or rather, controlled thrust (as

in real flight) or constant collective pitch (as in wind tunnel tests). In the simplified computations presented here, the evolving vorticity field induces unsteadiness in the velocity field but, since there is no feedback from the rotor, the velocity fluctuations have no effect on the resultant strength of the vorticity field at its point of creation. In the real system, as the tip-vortex strength changes so therefore will the growth rate of any perturbations to the wake. Arguably, this effect will alter the number of persisting, coherent rings that arise in the VRS wake from one moment to another, and will also affect the rate at which the wake breaks down. In the absence of this feedback mechanism, the detailed history of the wakes computed here will differ somewhat from that of a more comprehensively-modelled rotor system. Such detractions miss the point of the present study, however. The simplified treatment of the rotor, wake geometry and aerodynamic feedback was purposely introduced in order to isolate the dominant effects of the kinematics of the vortical structures produced by a rotor on the breakdown of the wake and the subsequent onset of, and behaviour within, the VRS. To this extent, the simulations presented here capture the essence of these processes although, undoubtedly, the behaviour of the system will be modified somewhat in the presence of other, possibly competing, physical effects.

## 3.6 Summary

The results of high-resolution computational simulations of a simplified, single-bladed rotor that was flown into the VRS both from hover and from the windmill brake state, have been presented.

Some previous studies have suggested that the loading on the rotor may mediate the non-linear feedback of the local velocity field into the strength of the wake, and that this feedback may be at the root of the eventual global breakdown of the wake into the toroidal form found in the VRS [30, 34]. In this study, the feedback between rotor and wake was eliminated by prescribing the bound vorticity on the rotor blade to be constant for all time, yet the large-scale collapse of the wake from a tubular form into the toroidal form that is a characteristic of the VRS was shown still to occur. This shows conclusively that the aerodynamic feedback between the rotor and wake is at most a modifying feature of a flow phenomenon that arises, fundamentally, from the dynamics of the vorticity in the wake under the influence of its inherent fluid instabilities.

When the VRS is approached from the WBS the wake is transformed from an ordered helix, of large pitch, into a compacted helix resembling a toroid of vorticity that lies just above the rotor plane. Considerable and persistent coherence of vortical structures has been identified in the wake of a rotor operating in high-speed VRS. The toroid appears to consist of a number of tip-vortex filaments that are roughly co-planar with the rotor, and that exhibit, approximately, the dynamics of a stack of axially-aligned vortex rings. There is a repeating kinematic process that resembles the 'leap-frogging' interaction between discrete vortex rings, where the most recently generated vortex filament expands and passes over those that are moving downward within its circumference. This motion is modified by the non-linear growth of the fluid instabilities that are inherent to a helical vortex system and by the geometric constraint that is imposed by the helical, rather than ring-like form of the vortical wake. Large-scale re-orientations of tip-vortex filaments, from roughly parallel to the rotor plane into an orientation that is approximately normal to the rotor disc, play a significant role in the vortex kinematics and leads to significant disruption of the orderly structure of the wake. The numerous short-wave perturbations that also grow on the filaments appear to facilitate and expedite the initiation of the larger-scale re-orientations. The general motion of the helical turns that form the structure of the toroid in *low-speed* VRS is also akin to that of a stack of axially aligned vortex rings, but in this case the toroid lies below the plane of the rotor. The dominant vortex pairing behaviour is all but suppressed by the compacting action of the free-stream, however, and the short-wave mode of instability becomes the primary cause of the disruption to the coherent structure of the wake.

Despite the highly unsteady and erratic behaviour of the flow fields in both high- and low-speed VRS, the vorticity distributions in both cases actually possess significant structure. In particular there is a statistical tendency of the vortex filaments, even after their initial helical geometry has been significantly disrupted by the action of the fiuid dynamic instabilities within the flow, to adopt a range of preferred orientations with respect to the plane of the rotor rather than to be oriented randomly in the fluid that surrounds the rotor. Indeed, by far the majority of filaments are oriented non-parallel with respect to the plane of the rotor disc.

The non-linear continuation of the initially linear growth of the perturbation modes identified by Widnall [5], and Bhagwat and Leishman [6] has been investigated. The linear

'pairing' of adjacent sections of the helical tip-vortices results in large-scale, longitudinal rotation of those parts of the filaments that are immediately connected to the pairing sections. Rotation of vortex filaments out of the plane of the rotor locally reduces the ability of the wake to propagate downwards into the flow below the rotor. The re-orientation of vortex filaments associated with the non-linear development of the pairing mode is implicated as the primary cause of the truncation of the wake of a hovering or slowly descending rotor.

The transition of the geometry of the wake from its tubular, hover-like form to the toroidal form that is characteristic of low-speed VRS is accompanied by a switch in the dominant kinematics associated with the coherent vortex-filaments in the flow. The kinematics of the wake when in the tubular form is dominated by the vortex pairing mode and the subsequent large-scale re-orientation and disruption of the far-wake. At a certain descent speed, though, the disruption of the far-wake truncates the wake sufficiently to allow the dominant kinematics to swap into a mode that is characterised by the 'leap-frogging' or recirculation of the coherent, ring-like, structures within the flow. In this mode, the wake adopts the toroidal form that is characteristic of the vortex ring state.

# Chapter 4

# Effects of Vortex Kinematics on the Velocity Field

## 4.1 Introduction

In Chapter 3, the vorticity field was examined in detail in order to expose the vortex kinematics responsible for the onset and ensuing development of the rotor vortex ring phenomenon. Various effects on the velocity field were implied from the behaviour of the vortical wake without recourse to the actual induced velocity field that results from the vortex motions. Such an omission was not detrimental to the rigour of work since the assumed behaviours were readily implied from the properties of the Biot-Savart equation and the extrapolations of resulting behaviours were kept quite general. Nonetheless, knowledge of the local velocity field that arises during the axial flight of a rotor can provide significant insight into observed effects that the vorticity field alone cannot provide. This chapter presents four related studies on the effects that local or global vortex kinematics have on, either, the global velocity field or on the rotor blade aerodynamic environment and hence the rotor loads produced by the rotor. The work in this thesis is based, mostly, on rotors following unsteady trajectories. That is, generally, the translational velocity of the rotor was changed linearly post an initial steady 'settling' condition. Hence, in the final section of this chapter, the effect that an accelerated descent has on the wake kinematics, and thus the velocity field local to the rotor is assessed.

## 4.2 Effects of Wake Geometry on Velocity Field Topology

Although classical momentum theory and other, more advanced 'fixed wake' theories assume that the wake of a hovering rotor stretches, semi-infinitely, beneath the rotor (in the direction of the rotor inflow) it has long been known [13, 15, 17, 69] that the wake actually truncates at a distance of just a few rotor radii from the rotor disc plane. (Practical experience of standing at various distances from a cooling fan whilst feeling the strength of the blowing air suggests this to be the case.) Indeed, numerous experimental investigations have shown, to varying degrees of clarity, the truncation of the wake of a hovering rotor. The more highly resolved of the flow visualisations [13, 17] have shown the geometry of the far wake to deviate significantly from the classical steam-tube envisioned by practitioners of momentum theory, and this deviation has often been associated with the vortex 'pairing' phenomenon which was realised in three-dimensions in Chapter 3. Nonetheless, the ultimate fate of of the vortical wake structure has remained obscure due to the limitations of the visualisation methods used.

Previous attempts to render the flow behaviour visible through use of computational methods did not result in many greater successes than those achieved by the experimentalists, however. It appears that the primitive variable CFD techniques used hitherto for rotor flow simulations have, generally, suffered from excessive numerical diffusion of the important rotational flow [38] since it is not explicitly conserved. So, although the eventual reduction of downwash velocity and the associated radial expansion of the wake near its end has been predicted by these methods [70], the numerical diffusion of the vorticity in the wake has prevented the satisfactory revelation of the vortex kinematics responsible for the predicted effects. Leishman [17] and other practitioners of the free-vortex wake method have loosely associated the mechanism of truncation of the vortical wake of a hovering rotor with the aforementioned pairing instability [30] and have thus managed to capture the gross wake geometry observed in experiments. Unfortunately, the corresponding velocity fleld is rarely seen to accompany the vorticity data. It seems likely though, due to the limitations of the degree of freedom afforded to the vortex filaments defined in the free-wake methods, that the proper evolution of the wake structure is unlikely to be achieved - a presumption made in the light of the previously unseen vortex kinematics uncovered by the VTM in Chapter 3 of this thesis.

In the discussion that follows it will be demonstrated how, at a given instant of hovering

flight, the disorganisation of vortical structures in the far wake due to fluid instabilities truncates not only the vorticity field but also the corresponding velocity field. It is then suggested how the effects that the vortex kinematics have on the velocity field at one instant in time also serve to render a truncated mean flow field. The important result of this analysis is the appearance of a toroidal topology in the mean velocity field, i.e. that truncation of the wake by fluid instabilities leads to recirculatory flow, even in the hover condition. Therefore the study shows that there is no difference between the flow topology arising in the hover condition and that which arises in the vortex ring condition, contrary to the received wisdom.

Figure 4.1 shows both the vortical wake and the induced velocity field of the simplified rotor used in the low-speed VRS simulations of chapter 3, 20 revolutions from rotor-start-up (immediately after this point the rotor began to descend). The velocity field, on the left of the figure, shows contours of downward induced velocity, $\lambda_z$, normalised by the mean rotor inflow, $\lambda_h$, as defined in chapter 2. The axes are in terms of rotor radii. The image on the right of the figure shows iso-surfaces of the strong vortical structures in the wake. These instantaneous images can be examined to at least glean a connection between the observable vortex kinematics and its corresponding induced velocity field. Examination of the figure, then, shows that the velocity at the disc plane is not quite unity, i.e. it is not equal to the calculated mean inflow, $\lambda_h$, but this is due to the effect of the unsteadiness of the flow and the non-uniform distribution of the vorticity in the near field. From the vertical station $z = 0$ to $z = 2$ the velocity contours show that the velocity within the helical wake system does not reach a magnitude of twice the inflow velocity over any appreciable region, as classical momentum theory predicts for a constant strength wake tube of semi-infinite length. Since the momentum theory of a rotor wake assumes the vorticity distribution down the length of the wake to be uniform, and because it is a theory for steady flow, some discrepancy is to be expected, however. In this instantaneous case the vorticity is not distributed uniformly down the length of the wake, as will be shown later. After a distance of around $2R$ down from the rotor, the speed of the downward flow reduces. This behaviour coincides with what is arguably the end of the coherent, structured region of the vorticity field, the end being demarcated by a group of strongly interfering vortex filaments that appear to be undergoing significant pairing and re-orientation. Below this region, the instability mechanisms in the wake appear to

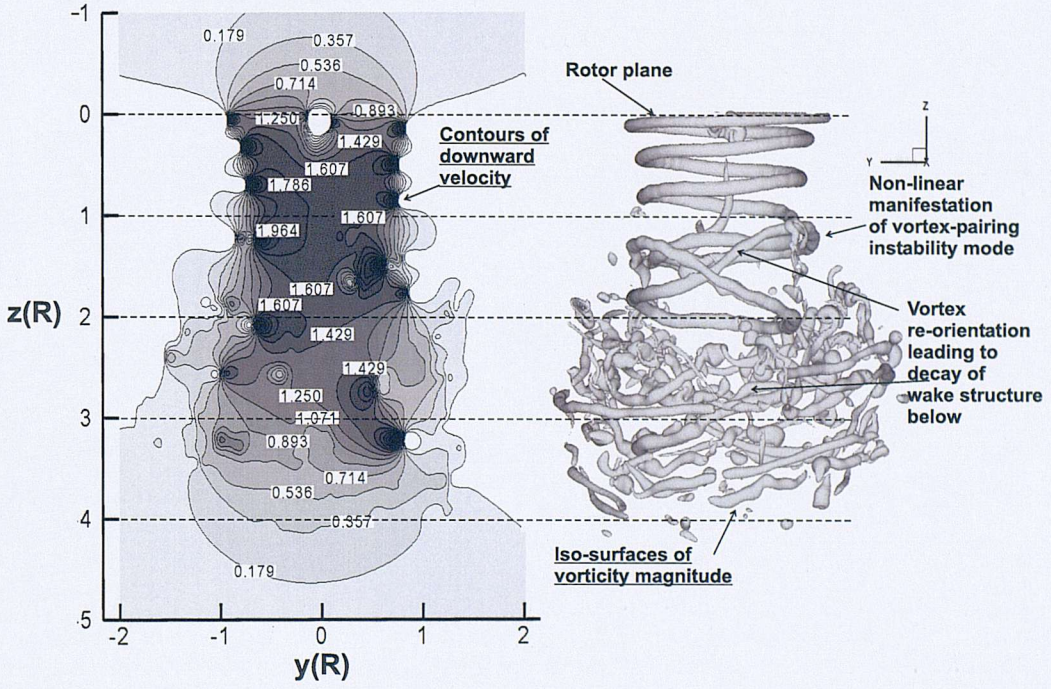



***Figure 4.1:*** *Iso-surface of the the instantaneous vorticity field (right) of a hovering, single-bladed rotor. The velocity field induced by the vorticity field is shown (left) as contours of downward flow velocity.*

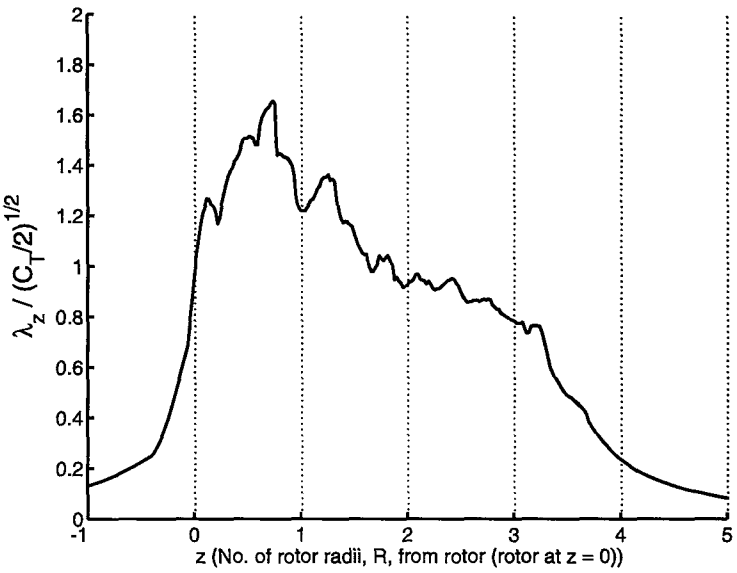



***Figure 4.2:*** *Distribution of instantaneous downward flow velocity along the rotor hub axis. The velocity data has been spatially averaged in the direction parallel to the disc at discrete vertical stations along the wake.*

have removed much of the vortical structure responsible for producing downwash in the wake. The result of this is low vorticity transport velocities and hence a congregation of disorganised, fragmented vortical structures.

If the vorticity in the wake decays along its length, then the profile of downward velocity within the truncated wake will not be symmetrical about a line that runs parallel to the rotor-disc through the centre of the wake, as it would be in a finite length wake of constant strength. Examples of such velocity profiles from constant strength wake tubes were computed by Perry *et al.* [21]. Instead, the peak velocity will be achieved closer to the rotor plane and will not reach the same magnitude as that achieved half way along the constant strength wake tube. At any instant, re-orientation of vortex filaments from a roughly horizontal orientation to a more vertical orientation, as has been discussed in the previous chapter of this thesis, will result in the reduction of induced inflow along the length of the wake. Figure 4.2 shows the result of spatially averaging the downwash velocity (of Fig. 4.1) in the direction parallel to the disc at discrete vertical stations along the wake. If the extent of the coherent region of the wake is assumed to start at $z = 0$ and to end at $z = 2$, then a lack of symmetry is clearly apparent and is thus evidence of the decay in the wake strength down the wake, even in this instantaneous case.

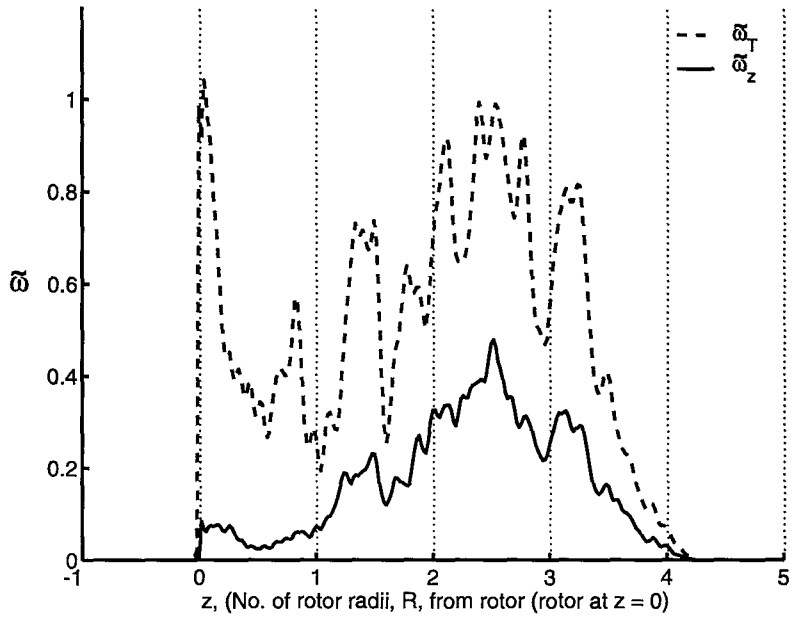



***Figure 4.3:*** *Normalised integrals of the total vorticity magnitude, $|\tilde{\omega}|$, and the magnitude of the vertically aligned vorticity $|\tilde{\omega}_z|$ in the instantaneous wake. The parameter values have been scaled by the magnitude of the total vorticity generated during one rotor revolution.*

The reduction in flow velocity down the wake can be associated with the wake's vortex kinematics by examining the total strength of the wake, at each vertical station used previously in Fig. 4.2, and comparing this with the strength of the vertically orientated vorticity that contributes to the total. This comparison is shown in Fig. 4.3, where the parameter values have been scaled by the strength of the vorticity generated by the rotor during one revolution. The figure shows how the total vorticity in the flow at first peaks near the rotor plane, as would be expected since the vorticity transport velocity is lower at this point than it is just a short distance further down the wake. The advection velocity of a newly generated turn of the helical tip-vortex system is relatively low until its radius reduces under the action of the flow induced by the wake beneath it whereby it then attains an increased transport velocity and moves away from the rotor at increased speed. The strength of the wake in the near-field of the rotor is lowest in the region of highest inflow velocity since the higher flow velocity allows for greater spacing of the trailed vorticity along the length of the wake. The strength of the wake is seen to increase further down the rotor axis, however. The collection of vorticity in this region ($2 \leq z \leq 3$) is observable in the vorticity iso-surface plot in Fig. 4.1. The strengthening of the wake does not appear

to be correlated with an increase in the span-wise averaged velocity, which it would likely engender if the vorticity here was were appropriately positioned and aligned. There are two factors at work here. The vorticity field spreads out under the action of the fluid instabilities thus decreasing the induced flow of any coherent turns of the helical wake tube. Secondly, the quantity of vertically aligned vorticity increases markedly, over the same region, from its initially low value near to the rotor. This is clearly evident from the curve of $\widetilde{\omega}_z$ also shown in Fig. 4.3. The implication of this result is that the unstable growth of small perturbations to the geometry or strength of the wake lead to a displacing and a re-orientation of the vortex filaments in the far wake from the attitudes they assumed nearer to the rotor. As a consequence, the wake is truncated and the instantaneous velocity profile through the wake tube is unlike that predicted by momentum theory for a steady flow. The ultimate fate of the structured helical vortices trailed from the rotor blades, then, is disorganisation in the far field, such that the number of structured turns of the helical vortex filament that constitutes the downwash producing part of the rotor wake are limited by the rate at which the flow becomes disorganised.

Thus far, this section has focused upon the properties of an instantaneous vorticity and velocity field generated by an idealised rotor in hover. To understand the wider implications of the instantaneous behaviour, the more general mean flow must be considered. The following discussion focuses on the influence that instantaneous wake properties have on the mean flow.

It has been shown how the instability mechanisms within the flow at a given instant lead to an effective decay of the wake downstream of the rotor. It was proposed by Wang [20] that, in the mean, the vortical rotor wake decays in a linear fashion along the length of the wake due to viscous diffusion of the vorticity. Since then, as has already been mentioned, Leishman and others have associated the wake truncation with the action of wake instabilities. More recently, Perry *et al.* [21] included the concept of truncation via the action of instabilities when arguing that the result of the pairing mode of instability is to remove, from the time-averaged mean wake, the vorticity that contributes to the generation of downwash, though it may well be present, instantaneously, in the flow field. They postulated that in the mean, the 'random' positions of the vortex filaments in the far field effectively cancels the instantaneous induced velocity contributions of those filaments from the mean flow field. What has been shown earlier in this section enhances the ideas

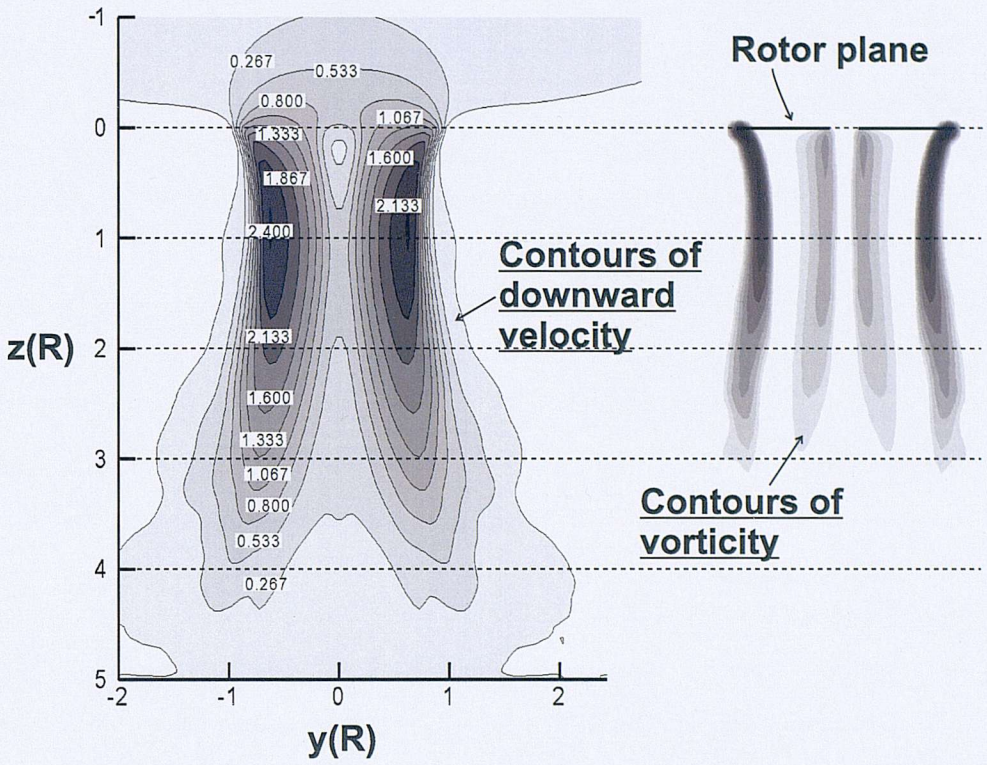



***Figure 4.4:*** *2D plots of mean contours of vorticity and the associated induced downward flow in the velocity field. The mean fields were constructed from 120 snapshots over 120 rotor revolutions. The velocity field has been scaled with the mean inflow at hover, $\lambda_h$.*

of Perry *et al.*: truncation of the mean wake does indeed occur due to the passive result of random motion, but also, it occurs because the instabilities in the wake actively remove from the flow the vortical structures that generate downwash. Figure 4.4 shows the result of averaging the vorticity and velocity fields of a hovering rotor over 120 revolutions. Since the mirror image of every available snapshot of the wake is as equally likely to occur as the actual image, given sufficient time, cylindrical symmetry has been imposed on the flow field. The image shows 2D slices of both the vorticity and the induced velocity fields. The slices coincide with the plane that passes through the hub of the rotor and is oriented parallel to the longitudinal axis of the rotor. It should be noted that due to the number of rotor revolutions required by this study of mean flow, it was necessary to use a large cell size ($\Delta_0 = 0.05$), relative to that which was used in the high resolution simulation discussed earlier, to reduce the cost of the simulation to an acceptable level. Ten contours are shown in each image, the darkest contour representing the strongest value of velocity

of vorticity. In the case of the vorticity contours, the lightest contour represents vorticity that is just one tenth of the strength of the strongest vortical structures occurring in the flow. The wake decaying effect of the irregular motion on the vertical distribution of the vorticity in the mean wake is clear: there is a definite, gradual reduction in the strength of the vorticity with distance from the rotor. At around $1R$ down from the rotor, the wake appears to have reached a minimum radius, and thereafter it expands. The reason for the expansion can be found in the image of the instantaneous vorticity field, shown in Fig. 4.1. In this case, the effective radius of the wake appears to increase in the region $1R \leq z \leq 2R$ and its apparent cause is the vortex pairing process that is so clearly evident. Thus, the smooth radial expansion of the mean wake is the result of the average of the vortex pairing processes that took place over 120 revolutions of the rotor.

Interestingly, the image of contours of mean downward flow velocity shows that the global aspects of the mean velocity field are very similar to those of the instantaneous velocity field shown earlier. Certainly the small regions of high velocity in the vicinity of discrete tip-vortices that are evident in the instantaneous velocity field are not present in the mean flow, since they have been smeared out in the time-averaging process. Even so, there is much commonality between the instantaneous and the mean velocity fields. For instance, and most importantly, both velocity fields exhibit a gradual decrease in the flow velocity in regions that roughly correspond to the vertical locations of effective expansion of their corresponding vorticity fields. The similarity between the instantaneous and the mean velocity fields strongly suggests that the decay in the flow velocity evident in each case is due to the same process - that of a reorientation of the tip-vortices and the ensuing general disorganisation of the wake in the far field.

The mean flow fields under discussion represent the general form of the flow field generated by a hovering rotor. It is seen that the vorticity in the wake is far from uniformly distributed along its length and that it is effectively truncated just a few rotor radii down from the rotor plane. The accompanying velocity field exhibits an initial region of flow acceleration, just below the rotor plane, as would be expected, but upon reaching the region of maximum velocity, the downward flow decelerates thereafter. These results show that the unstable nature of a rotor wake causes it to adopt a form that is largely at odds with the form assumed by the momentum theory for a hovering rotor flows. Momentum theory assumes that the wake stretches to infinity down from the rotor and that, once

reaching a maximum, at infinity, the velocity remains constant. The truncation of the actual mean rotor wake results in a further, very important, deviation from the momentum theory assumptions: momentum theory assumes that the topology of the hovering rotor's velocity field resembles a tube that contracts radially in the downward direction to infinity (See Johnson [71]). However, as is shown up by the particle paths in the mean flow field of a hovering rotor, in Fig. 4.5, the truncation of the vorticity field, evident in Fig. 4.4, actually engenders a recirculatory flow around the outside of the wake tube - whilst the vortical wake has the approximate geometry of helix of finite length, the topology of its induced velocity field is toroidal (in 3D). This finding has stemmed from a re-interpretation of the

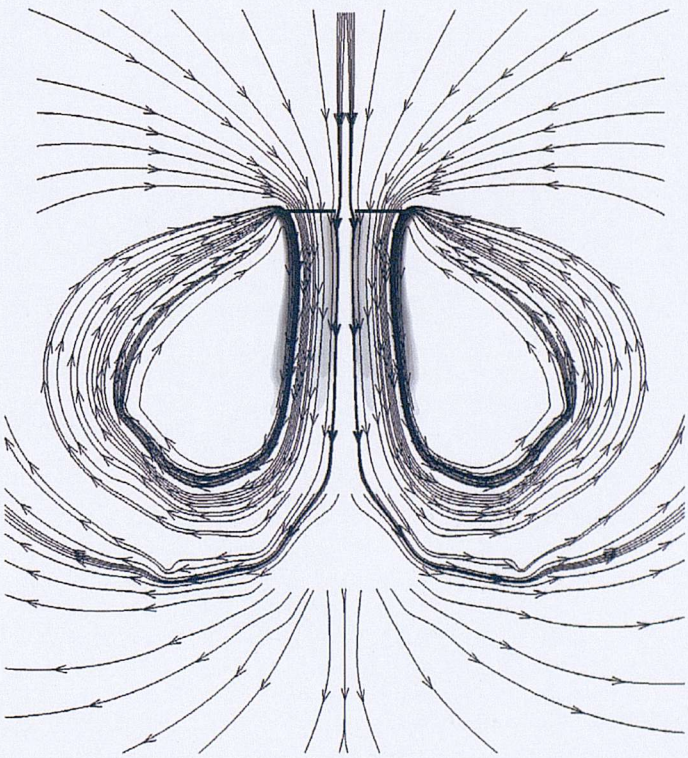


***Figure 4.5:*** *Particle paths in the mean flow field of a hovering rotor. The associated vorticity field is shown as contours beneath the particle paths.*

results of a study, using the VTM, that showed the recirculating flow field of a hovering rotor. The results were presented in the paper by Perry *et al.* [21].

This result raises an important point as it has long been assumed that the topology of the velocity field of a hovering rotor is very different to that of a rotor operating within the VRS. Indeed, the very fact that there is no momentum theory solution for the VRS flight regime supports this view*. In their paper describing PIV measurements of the of flow field of a rotor in hover and the VRS, Green *et al.* [13] constructed prototype flows for the VRS and low-speed descent conditions by time-averaging their velocity field data and applying cylindrical symmetry to the mean flow. They stated that the topologies of the two flow fields were different - a tubular topology corresponded to the low-speed descent condition and a toroidal topology was associated with the VRS condition. The result shown here in Fig 4.5 is at odds with their finding. The topologies of the velocity field of a rotor in hover, low speed descent and the VRS are the same - they are all toroidal. This is shown clearly in the sequence of velocity field images shown in Fig. 4.6 and Fig. 4.7. The images show the mean velocity fields of a rotor flying steadily at several descent speeds. The images are from simulations conducted by the VTM. The first condition of 'perturbed' hover represents a condition of very slow descent. It can be seen that there is recirculating flow in all cases, i.e. all of the topologies are toroidal. There are of course some geometric differences - the axis of the toroid expands and contracts and moves vertically about the rotor plane with change in axial flight speed. Saddle points are also evident in each of the flow fields though the positions in which these points arise also changes with the descent speed. Hence, if the flow fields are observed through too small a 'field of view', e.g. too small a PIV window, then the wake's topology appears as if it changes from cylindrical to toroidal.

It is likely that the flow topology will change, however, if the velocity of the upward flow recirculating around the outside of an ascending rotor is exceeded by the ascent speed and also when the velocity of the downward flow inside the full length of the wake of a descending rotor is exceeded by the descent speed. These conditions are represented by the velocity fields shown in Fig 4.8 which shows the mean velocity field of rotors operating in high speed ascent and high speed descent.

*There is no momentum theory for the VRS flight condition, since it is presumed that a definite stream-tube cannot be defined for the VRS flow as the flow direction over the whole flow field is not uniform.

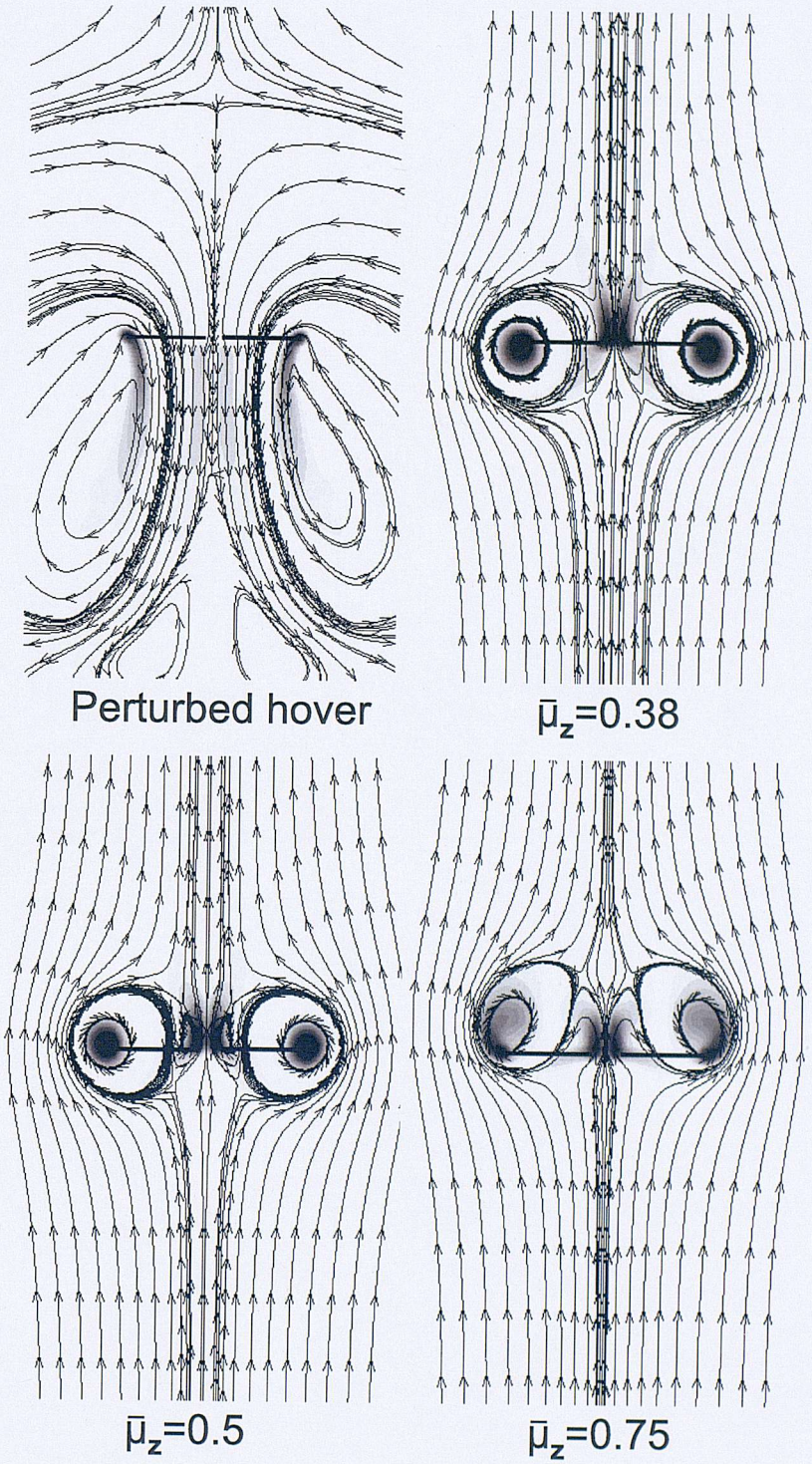



***Figure 4.6:*** *Particle paths in the mean flow field of a rotor flying steadily at various low descent speeds. The associated vorticity field is shown as contours beneath the particle paths.*

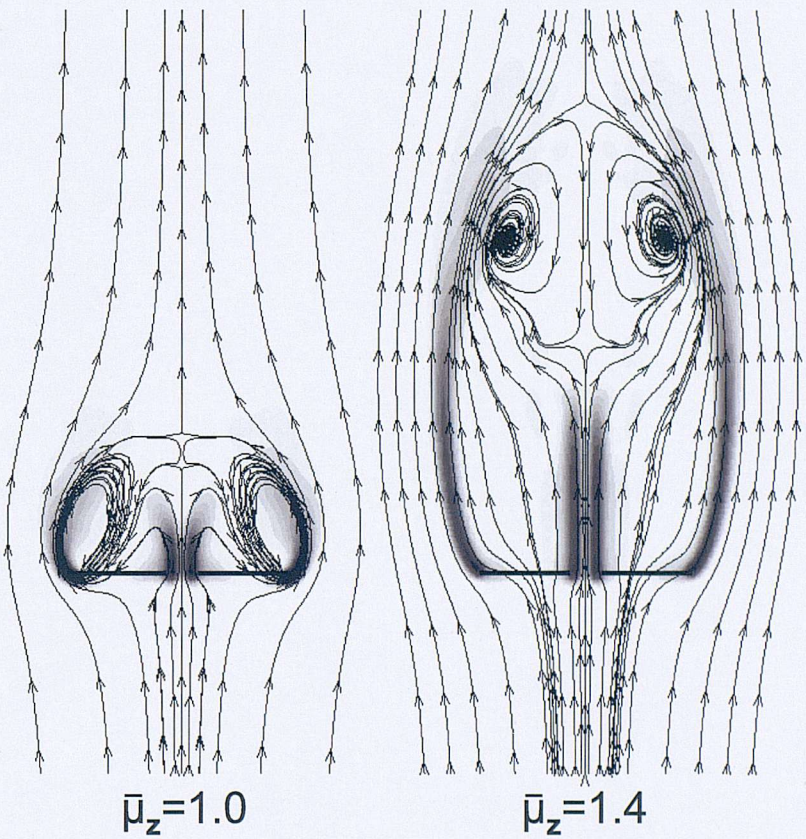



***Figure 4.7:*** *Particle paths in the mean flow field of a rotor flying steadily at various high descent speeds. The associated vorticity field is shown as contours beneath the particle paths.*

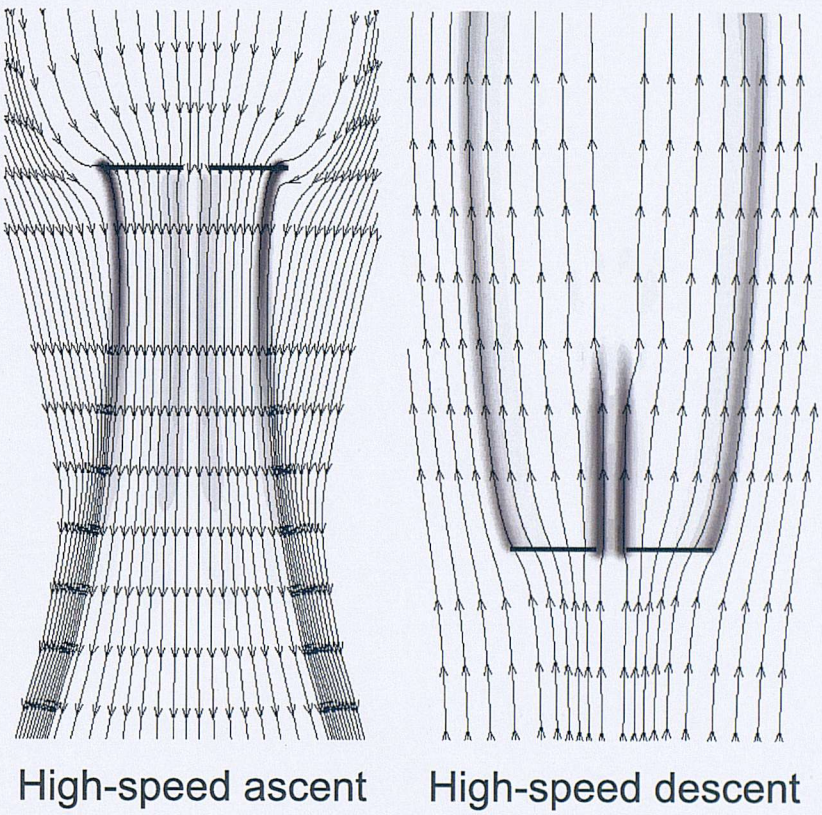



***Figure 4.8:*** *Particle paths in the mean flow field of a rotor flying steadily in ascent (left) and in the WBS (right). The associated vorticity field is shown as contours beneath the particle paths.*

## 4.3 Wake Geometry and Measures of Rotor Performance

Visualisations of the wake of a rotor operating in or near to the VRS flight regime have been achieved experimentally, by various methods, on several occasions (Refs. 13, 14, 15, 17 and 68 for instance), and to varying degrees of success by means of numerical simulations (e.g. Refs. 9, 21 and 30). From a global perspective, therefore, the geometry of the VRS wake is relatively well reported whilst the work of Chapter 3 in this thesis has aided the understanding of the fundamental vortex kinematics that are responsible for much of the known behaviour. In addition, several papers have presented the calculated mean disc inflow, rotor torque and thrust signals taken from VRS experiments. Rarely, though, has a correlation between the flow field and the rotor performance been made with the exception of Stack *et al.* [15] who linked the rise and fall of a periodic thrust signal to the various instantaneous positions of tip-vortices of a rotor oriented obliquely to the free-stream flow in a tow-tank.[†].

It is useful then, at this stage of the present work, to link the geometric state of the wake of a rotor with the performance of that rotor as it descends from hover through the VRS and into the windmill brake state. To show how the behaviour of the wake influences rotor performance, Gao's rotor (see Table 2.1) was simulated flying in a linearly accelerating axial descent. The trajectory of the rotor started from an initial period of hover which lasted some 40 revolutions - sufficient time for the start-up transients in both the flow field and the rotor thrust to decay to insignificance. The trajectory ended with the rotor operating well within the windmill brake state. Unlike the idealised rotor that was simulated for the work discussed in Chapter 3, the rotor used in the present simulation was coupled to the surrounding velocity field. In this case then, a nominally constant thrust coefficient of $C_T = 0.00724$ was maintained over the course of the rotor's flight. Since the trajectory of the rotor in this simulation would require a relatively large number of rotor revolutions to complete (up to 400), the flow was resolved using a relatively large cell size of $\Delta_0 = 0.05R$. The resulting moderately low resolution shows only the gross dynamics of the behaviour of the rotor's wake. The resolution is sufficient for the purposes of this

[†]During steeply angled descent, the shedding of large vortical structures away from the disc plane appears to be periodic [15] and as a consequence the rotor thrust fluctuation has been observed to also be periodic [22, 23]. Periodicity in the thrust signal of an axially descending rotor has not been detected however.

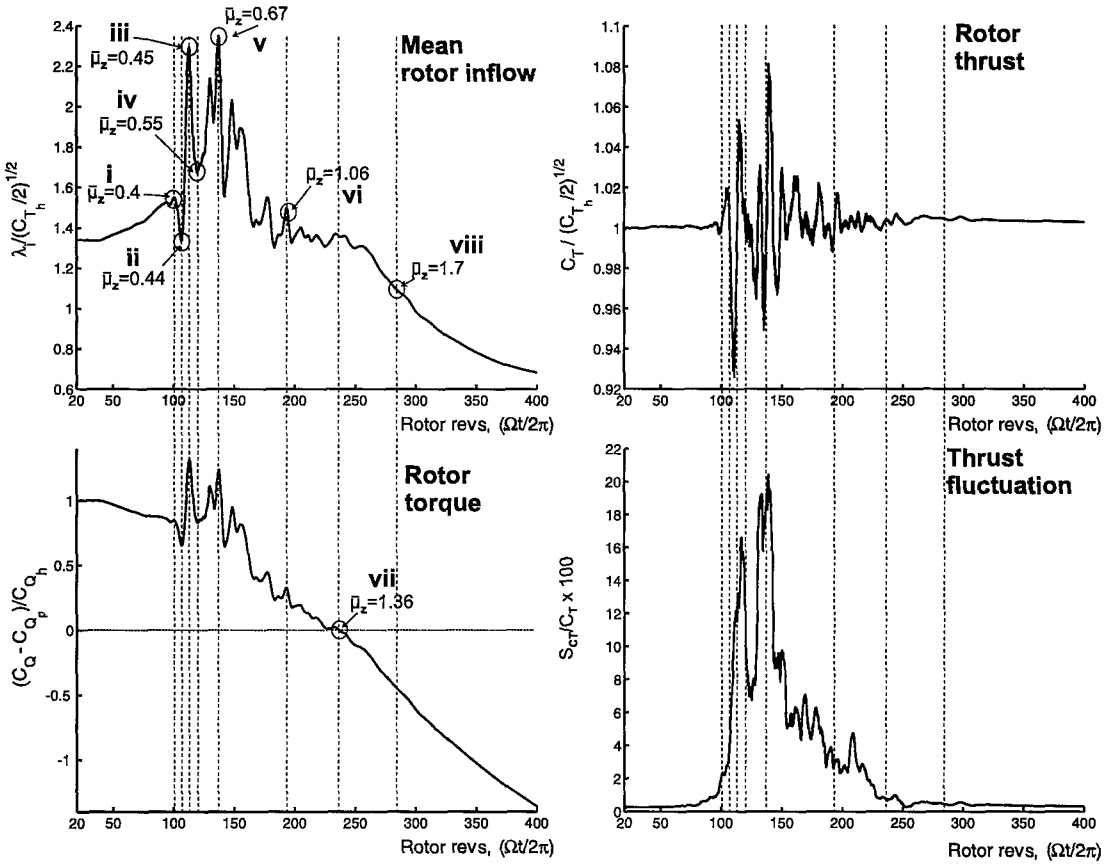



***Figure 4.9:*** *Measures of the performance of a rotor in a linearly accelerating axial descent. Measures shown are calculated mean rotor inflow, rotor torque, thrust and standard deviation about the mean thrust of the thrust fluctuations.*

investigation however.

Figure 4.9 shows the normalised disc inflow, calculated using Eq. 2.43, the rotor torque, $(C_Q - C_{Q_p})/(C_Q - C_{Q_p})_h$, where $C_{Q_p}$ is the instantaneous profile torque, the normalised thrust coefficient $C_T/C_{T_h}$ and the standard deviation about the mean thrust of the thrust fluctuations, $S_{C_T}$. All of these parameters are plotted as functions of time, or rather of rotor revolutions, $\Omega t/2\pi$.

Points of interest on the mean inflow and rotor torque curves have been highlighted. Figures 4.10 and 4.13 show the instantaneous vorticity fields that correspond to each highlighted feature. To provide further insight, the associated induced and induced plus free-stream velocity fields are plotted in Figs. 4.11, 4.12 and 4.14.

It should be noted that the flow field associated with the VRS is highly unsteady. Large spatial deviations of the vortical wake can occur [13, 14, 15, 36]. At some descent

speeds, when the flow is highly unsteady, the displacements of coherent wake structures are comparable in length to the rotor radius. It should be borne in mind, therefore, that over the course of around ten revolutions [13, 15] the wake and the measured rotor performance may have changed significantly and hence between each snapshot of the wake that is to be shown the flow field may have undergone several changes to its geometry.

Marker $i$, on the inflow graph in Fig. 4.9 highlights the stage in the descent which just precedes the first signs of VRS initiation. It can be seen from the wake image plotted at the top-left side of Fig. 4.10 that at this stage, the self induced advection against the free-stream of the trailed vortex systems was still able to admit the formation of an elongated cylindrical structure akin to that developed by the vortex system of a hovering rotor. However, the effects of fluid instability on the wake geometry can be seen to manifest at around $1R$ down from the rotor plane. The irregularity in the shape of the wake near its lower extreme is indicative of the action of growing perturbations to the ordered vorticity field. As has been shown in the preceding section, the instability engenders wake truncation. Also evident in this figure are fragmented vortical structures, including the starting vortex, that at an earlier time convected outwards from the rotor axis and thus away from the action of the downward induced flow. Due to the recirculating flow field that exists around a slowly descending rotor, as shown earlier in §4.2, it is evident that some of the fragmented vortical structures were convected upwards passed the rotor. The apparent unsteadiness near the end of the wake did not manifest as unsteadiness in the thrust generated by the rotor, as can be gleaned from the curves of thrust and standard deviation of thrust in Fig. 4.9. The induced and induced plus free-stream (i.e. $\lambda_i + \mu_z$), or net, velocity fields associated with this vorticity field are shown in Fig. 4.11. The images show the velocity fields on a two-dimensional plane than runs through the axis of the rotor and which is oriented parallel to the rotor's longitudinal axis. The shaded contours represent the strength of downward flow only. The shading grows heavier as the velocity increases, with the darkest contours representing downward flow which was ten times greater than the flow represented by the lightest shade. Accompanying the velocity contours in the plots of net velocity fields are the instantaneous velocity vectors, in the $x - z$ plane, to show the flow direction. The net velocity field arising at stage $i$ in the descent of the rotor strongly resembles that which surrounds a hovering rotor, as expected from the geometry of the vorticity field. Upward flow penetrates the region of slower

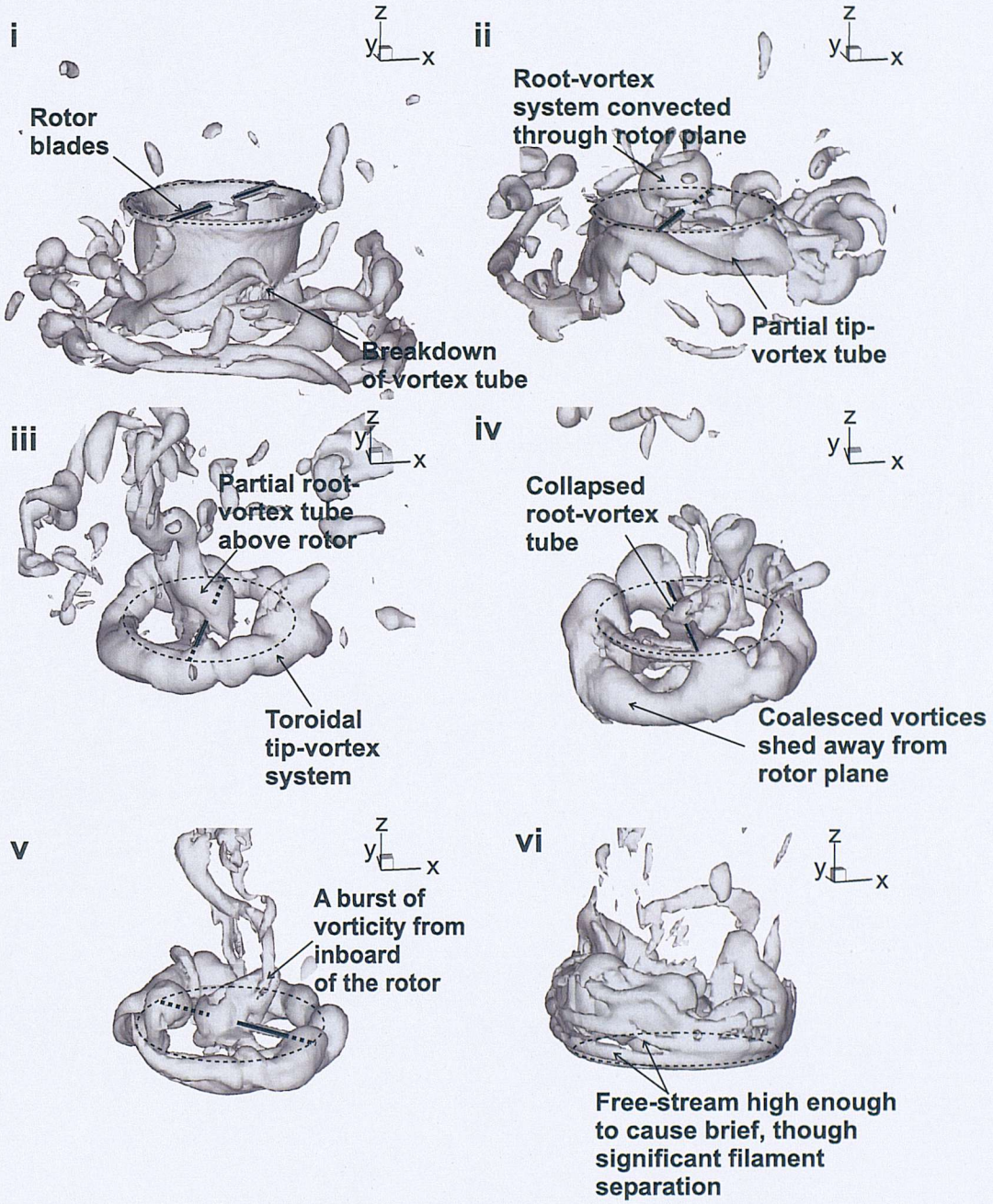



*Figure 4.10: Isosurfaces of vorticity showing the instantaneous geometry of a rotor wake at various descent speeds.*

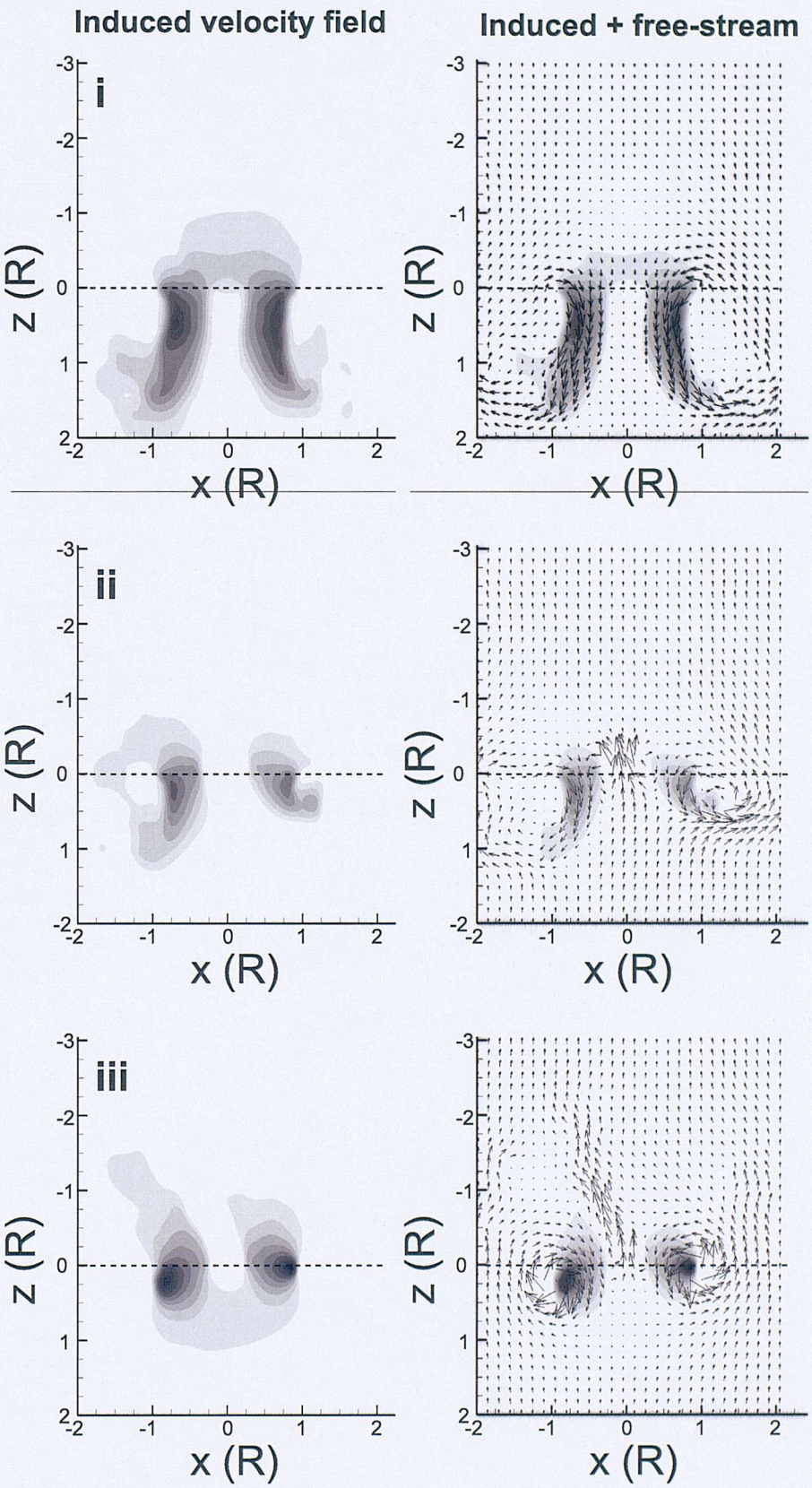



***Figure 4.11:*** *Contours of the instantaneous induced (left) and induced plus free stream* ($\lambda_i + \mu_z$)*, (right), velocity fields corresponding to markers i to iii. Net velocity fields also show the corresponding velocity vectors on top of the contours.*

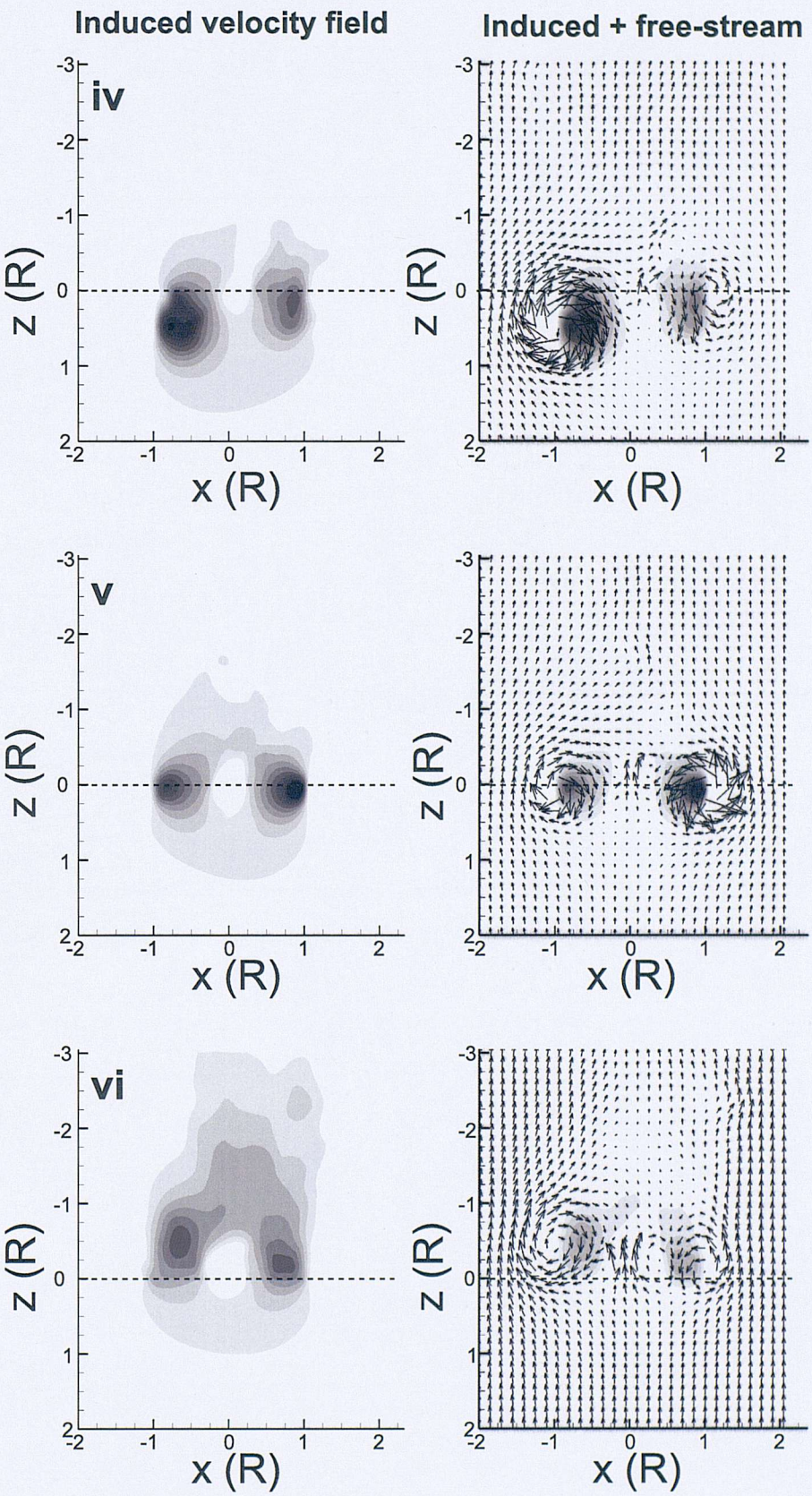



***Figure 4.12:*** *Contours of the instantaneous induced (left) and induced plus free stream* ($\lambda_i + \mu_z$)*, (right), velocity fields corresponding to markers iv to vi. Net velocity fields also show the corresponding velocity vectors on top of the contours.*

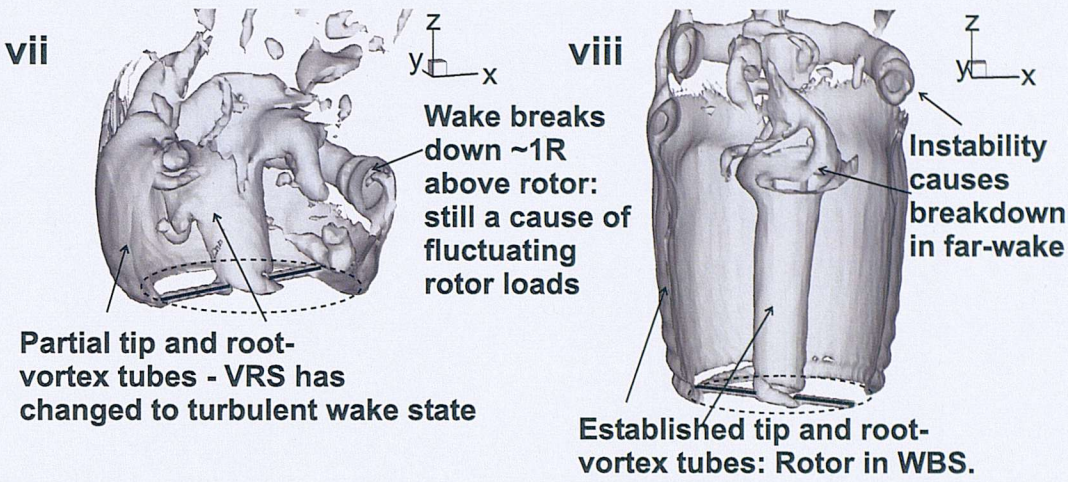



*Figure 4.13: Isosurfaces of vorticity showing the instantaneous geometry of a rotor wake corresponding to markers vii and viii.*

induced flow near the centre of the wake tube, though it does not quite breach the rotor plane, at least not in this particular snapshot.

Marker *ii* in Fig. 4.9 highlights a significant reduction of the inflow generated by the rotor. Inspection of the corresponding wake geometry shows that by this stage the once tubular structure had collapsed, though it had not yet transmuted into the toroidal geometry associated with the VRS. A large plume of vorticity trailed from the blade roots was convected though the root cut-out of the rotor. It appears that this image has captured a highly transient phase of the evolution of the wake - where it is changing from the elongated form seen in image *i* into the compact toroidal structure shown in image *iii*. During this process the vortical structures within the wake appear to have been severely disorganised and dispersed such that the inflow inducing capability of the wake was reduced to the levels seen at hover or post VRS, as suggested by the contours of induced velocity near the rotor which are lighter than in the previous instant, as shown in Fig. 4.11. In general, such a reduction of induced flow must serve to precipitate the transformation of the geometry of the wake, that is, it must hasten the onset of the VRS. The velocity vectors in the net velocity field reveal that the flow was highly nonuniform and that upward flow had by that stage penetrated the rotor plane near the root section which caused the upward convection of the root-vortex system above the rotor plane. It will be seen how the root vortex system governs the direction of the flow in this region. Note that the unsteadiness of the wake was by that stage inducing higher levels of thrust

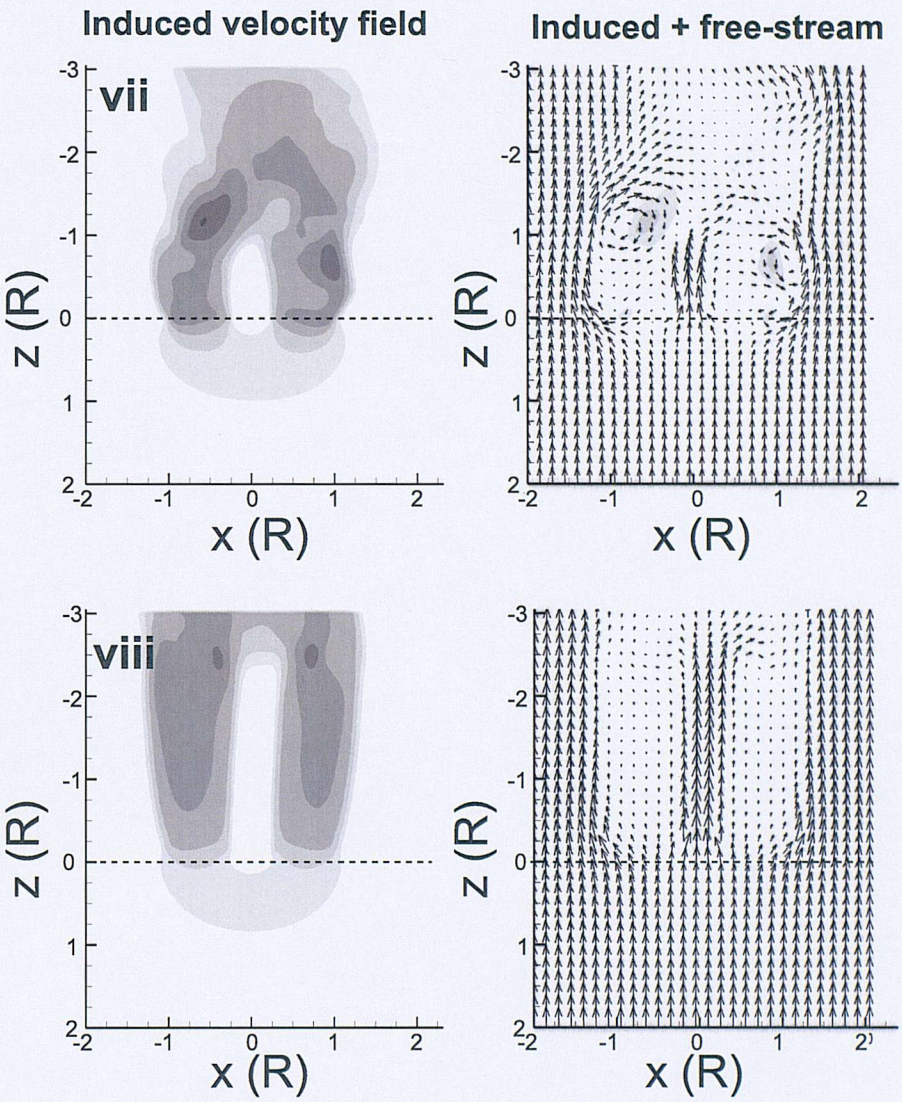



***Figure 4.14:*** *Contours of the instantaneous induced (left) and induced plus free stream* $(\lambda_i + \mu_z)$*, (right), velocity fields corresponding to markers vii and viii. Net velocity fields also show the corresponding velocity vectors on top of the contours.*

fluctuation than had occurred at the earlier stages in the descent of the rotor.

The third marker coincides with a high level of inflow production relative to that which was generated earlier in the descent. Image three in Fig. 4.10 shows that this sharp increase of inflow was induced by a coherent toroid of blade-tip vortices that circumscribed the rotor and sat approximately on the disc plane. The geometry of the wake and the corresponding high levels of thrust fluctuation and induced torque all suggest that the rotor was operating in a fully developed VRS by that stage. The images showing the associated velocity fields show that the toroid induced large regions of relatively rapid flow that recirculated about the edge of the rotor disc whilst at the same time the root-vortex system, evident above the rotor, generated considerable upward flow. It is interesting to note from the plot of the net velocity field, though, that this relatively rapid upward flow appears to have originated from around $0.25R$ below the root section of the rotor, and immediately below this area the flow velocity was much slower. The velocity vectors that immediately surround this region appear to diverge from each other which suggests that the region was a saddle point in the flow - in this zone the downward induced flow of the vortex toroid about the disc circumference is approximately equal to the sum of the free-stream and upward root-vortex flow. Beneath this region, the fluid appeared to turn sharply to flow either side of the rotor. In this particular phase of the VRS, then, the flow over the rotor blades was upwards on the inboard sections and downwards over the outboard sections. This feature of VRS flow was also generated by the single bladed, idealised rotor discussed in Chapter 3. This is an important observation since it supports the assumed generality of the results obtained from that somewhat unphysical rotor.

Image *iv* in Fig. 4.10 captures the shedding of a section of the strong vortex toroid. The associated marker indicates a reduction of induced inflow on the inflow graph of Fig. 4.9. This suggests that the overall inflow producing capability of a rotor might be reduced by the loss of a significant part of the vortex ring. However, close inspection of the corresponding plot of induced velocity contours suggests that it was on the other side of the rotor where the induced flow had reduced. Generally, the structure of the vorticity around the circumference of the rotor appears highly disorganised and it is thus most likely that it is this overall effect of the gross disorganisation of the wake in this instant that was responsible for the reduced inflow production. Stack *et al.* [15] made a related observation from their experiments - they suggested that large scale shedding of

vorticity led to an increase in thrust production. Such an increase in thrust would result from a decrease in the induced downwash through the rotor. However, the thrust in the present simulation does not seem to have responded in the manner observed by Stack *et al.*, possibly because the thrust was controlled to be nominally constant in this simulation. It is interesting to note that the large bundle of tip-vortices removed from the rotor was convected downwards by the locally induced velocity of the wake rather than upwards by the free-stream. This suggests that, local to the vortex bundle, the toroid as a whole, was momentarily able to build up sufficient strength, or rather, to comprise a sufficient number of coherent tip-vortices that its locally induced velocity was strong enough to overcome the free-stream in this region of the flow. The corresponding net velocity field shows the influence that the shed section of the vortex ring had on the rest of the flow. A zone of strong recirculation was induced below the rotor plane which engendered significant asymmetry in the flow as a result: large scale shedding of vorticity appears to be highly disruptive to the flow. With regard to the upward flow through the rotor, there appears to have been little flow through the root section in this instant and this is commensurate with a disorganised, collapsed, root-vortex system, as was suggested earlier.

The fifth marker highlights the maximum inflow that was induced during the descent of the rotor. This peak coincides with a peak in the rotor torque, though not the maximum torque, and also with the maximum level of thrust fluctuation. As in the case of the third point of interest, the peak in inflow seems to correspond to a coherent vortex toroid where much of the blade-tip vorticity near to the rotor helped to form the vortex ring in the plane of the disc. There appears to be little sustained tubular structure in the root-vortex system in this instance. The effect that this had on the corresponding velocity field is betrayed by the small zone of upward flow near the hub of the rotor which, importantly, is enclosed by downward flow coming from above it. This contrasts with the velocity field that arose in the instant highlighted by marker *iii*. In that instance the root-vortex system appeared as, relatively, a more coherent upwardly directed tube which induced an unimpeded upward flow above the root area of the rotor. This contrast in the two states highlights the importance of the root-vortex system in governing the flow through the inner part of the rotor. The velocity field also shows some semblance of symmetry in the outer recirculation zones and the centres of each appear to lie just beneath the plane of the rotor, as they have done in all the preceding instances that have been highlighted.

Marker *vi* highlights a stage in the descent of the rotor where the inflow and rotor torque had, in general, reduced from the elevated levels that where seen previously in the period between revolution number 120 and 170. Inspection of the corresponding vorticity field shows that much of the vorticity trailed from the tips of the rotor had been convected just above the rotor plane and that the tight, toroidal, structure evident in the preceding point of interest is less evident. Indeed, the wake had elongated sufficiently to render some individual tip-vortex filaments visible and a degree of filament re-orientation is also evident. So, the wake formed into a short, truncated, tube that was approximately half a rotor radius in height, above which the tube appears to have contracted radially and become disorganised. It seems as though the vortex ring dynamics, that were seen in § 3.3 to manifest in the wake of a rotor in high speed VRS, were driving the behaviour of the flow in the instant currently under discussion: the induced flow of the stack of approximate co-axial rings seems to have caused the slight contraction of the uppermost ring-like tip-vortex. Accompanying the relatively coherent wake structure just above the rotor in this instant is a region of downward velocity that is larger than at any other stage in the rotor's flight in the VRS that has been mentioned in this discussion. This region appears to have been induced by both the short wake tube formed by the tip-vortices above the rotor and by the apparent lack of a root-vortex system of similar height.

Marker *vii*, corresponds to the commencement of ideal auto-rotation, i.e. when $(C_Q - C_{Q_p}) = 0$. Figure 4.13, shows that the associated wake had regained, partially, the structure exhibited prior to VRS onset, except, of course, the wake in that instant was convected above the rotor rather than below it. Both the tip and root vortex systems were able to arrange themselves into tube-like structures that extended to approximately $1R$ above the rotor, though after this point the action of the instabilities in the flow appear to have manifested as a collapse of the upper extremities of the wake. The image of the net velocity field that this vortex wake induces, shown in Fig. 4.14, reveals that the zones of intense recirculation about the rotor plane that are engendered by the vortex toriod that forms at lower descent rates had moved up above the rotor to where the structured wake had broken down. Also apparent in the induced velocity field is a notable region of upward flow inside the structured tube formed by the root-vortex. This plot reveals, as does the the image of the vortex wake, that the flow field was still somewhat asymmetric, and this suggests that the flow was unsteady at that stage. However, the graphs showing

the thrust history and the magnitude of the thrust fluctuations indicate that the unsteadiness in the flow field above the rotor influenced the lift production on the rotor far less than when the rotor was in the VRS, though the fluctuation levels are still greater than those occurring at the stage highlighted by marker *viii*, i.e. when the rotor was in the WBS. The velocity vectors reveal that within the confines of the tip-vortex tube, the flow was non-uniform with regions of strong upward and downward flow: the wake that admits ideal auto-rotation, then, possesses some tubular structure near to the rotor, but the flow field is unsteady and irregular. At this stage in the descent the rotor had entered the turbulent wake state. Note also, that as predicted by momentum theory, the normalised induced flow was approximately equal to the normalised descent rate, or rather $\bar{\lambda}_i = \mu_z$.

Finally, the eighth marker highlights a point on the rotor performance curves where the behaviour appears to be steady. Inspection of the vorticity field reveals that the wake comprised ordered tip and root vortex tubes that extended up to about 2.5 radii from the disc plane. In the region above the rotor both vortex tubes exhibit signs of disorganisation signifying that even at such high descent speeds, i.e. at $\bar{\mu}_z = 1.7$, the action of the inherent fluid instabilities can still disorganise the wake, though only in the rotor far-field. The slight disorder in the velocity field that this disorganisation appears to have caused, as shown by the non-uniform direction of the velocity vectors in this region (in Fig. 4.14) seemed to have influenced little the rotor performance, as can be gleaned from the relatively steady thrust signal and the low standard deviation of the thrust fluctuations presented in Fig. 4.9. In the net velocity field there is evidence of small zones of recirculation and thus, even though the flow in the wake was generally upward, it is arguable that the overall topology of the flow was still toroidal.

The preceding discussion has illustrated how the various well known changes in the performance of a descending rotor is related to the geometry adopted by its wake. In essence, it has been shown that, prior to VRS onset, compression of the tubular wake increases the mean rotor inflow that it induces, but it is the vortex toroid of the VRS that induces the highest mean flow velocities through the rotor. The toroid is also highly unsteady, as borne out by the fact that the highest thrust fluctuations experienced by the rotor arose when the rotor was enveloped by a compact toroid of vorticity that has its locus just beneath the rotor plane. It has also been demonstrated that the flow up through the root section of the rotor, which has been previously observed in experiments by

Brinson and Ellenreider [68] and latterly by Green *et al.* [13], is governed by the geometry, coherence and position relative to the rotor plane at any given instant, of the root-vortex system - something which has not been explicitly shown before.

It was noted in Chapter 3, that the flow instabilities cause the wake to break down somewhere along its length, and so the influence of the free stream is to move the region of wake collapse closer to the rotor until it is sufficiently truncated that the predominant kinematics of the vortex filaments in the wake change from those associated with the kinematics of a helical vortex to those akin to vortex ring kinematics which thus gives rise to the VRS. Indeed, the observations made here are consistent with those of chapter 3 but the system simulated here was more like a real rotor and hence it is arguable that the conclusions of the previous chapter apply equally well to a more realistic, and from a numerical point of view, less well resolved, system.

## 4.4 The Aerodynamic Origin of Thrust-Settling

A well-known aspect of experimental measurements on rotors flown at constant collective pitch into the VRS is the decrease in mean thrust that accompanies the onset of large-amplitude thrust fluctuations on the rotor. This phenomenon, known as thrust settling, has been observed in numerous experiments (see Refs. 10 and 12 for instance) and most authors have associated its onset with the envelopment of the rotor in the recirculating, toroidal flow of the fully-developed VRS. When the thrust-level is being regulated, as in controlled flight conditions, a phenomenon described by pilots as 'settling-with-power' is a common precursor to the increased vibratory loads and loss of control effectiveness associated with developed VRS. Due to the similar normalised descent speeds at which these two phenomena arise, they have become interchangeable in the jargon used by the VRS research community. However, despite the various in-flight and experimental observations of this behaviour, the aerodynamic origin of thrust-settling remains obscure. The on-blade aerodynamics and associated wake dynamics have not been examined in sufficient detail in the published literature save for the aforementioned work of Azuma *et al.* [12], though they were unable to correlate the geometry of the wake with their rotor performance measurements. The aim of this section is to rectify this deficiency. To that end, the two-bladed, teetering rotor of Gao [16], defined in Table 2.1, was flown from a steady hover condition

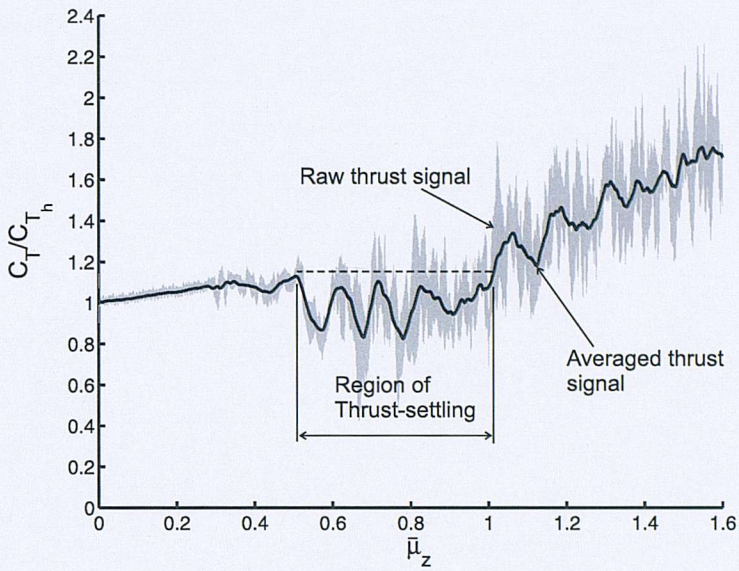



***Figure 4.15:*** *Filtered and raw $C_T$ signal as rotor descends. $C_{T_h}$ is the rotor thrust coefficient generated in steady hover. The descent rate is scaled by the inflow calculated from $C_{T_h}$. (Constant $\theta_0$ case.)*

on a slowly accelerating trajectory through VRS to the WBS condition. Two modes of rotor operation were simulated, individually. In the first simulation the constant collective pitch of the rotor blades were fixed at $\theta_0 = 10°$, where the nominal thrust coefficient, $C_T$, produced at hover was $C_T = 0.0073$. In the second simulation the thrust was held nominally constant throughout the descent of the rotor at a value of $C_T = 0.0073$. The first-order controller used to maintain the thrust in the latter case was able to maintain the desired mean thrust throughout the simulated flight, as will be shown later. However, the thrust changed significantly from that achieved in hover in the case when the collective pitch was fixed.

Figure 4.15 is a plot of the thrust coefficient generated by the simulated rotor with fixed collective pitch as it descended at gradually increasing speed. The graph is of mean $C_T$, scaled by the thrust coefficient achieved during steady hover, where the mean has been calculated by using the filtering technique described in § 2.7.2. The width of the averaging window was 10 rotor revolutions. The filtered thrust signal has been overlaid onto the raw thrust signal to provide an indication of the validity of the averaging process employed and also to highlight the highly fluctuating nature of the rotor operating conditions during the descent. The thrust data is plotted against descent rate scaled by the theoretical mean

inflow generated in hover, $\lambda_h$. Since the thrust varies during the descent when the collective pitch is fixed, it seems inappropriate to use this normalising method when comparing such data with results from a case where the thrust was held nominally constant. A detailed discussion on this matter is presented in Chapter 6 of this thesis. In the present study, though, the classical method is used to remain consistent with the standard practice.

The figure shows that the thrust increased in the early part of the descent. This is consistent with the relative free-stream flow causing an increase in the effective angle of attack of the blades. At a normalised descent rate of $\bar{\mu}_z \approx 0.5$, however, the thrust drops sharply and soon afterwards significant fluctuations in the thrust appear. Since an averaging window width of 10 rotor revolutions has not masked these fluctuations it can be deduced that they are of very low frequency relative to the blade passage frequency. The initiation of the thrust settling in this simulation occurs very close to the widely accepted [32, 34] analytical VRS onset boundary of Newman *et al.* [7] (at $\bar{\mu}_z \approx 0.52$). As was mentioned earlier, in previous literature this reduction in thrust has been linked, without strong supporting evidence, to the envelopment of the rotor in the fully developed VRS wake. Inspection of the vorticity field during the thrust-settling period reveals the qualitative behaviour of the wake that arises during the onset and early stages of the thrust reduction. Figure 4.16(a) shows the two-dimensional geometry of the vorticity locus plots (as described in §2.7.2) computed from 25 rotor revolutions during hover. The vertical 2D slice runs through the centre of the rotor hub. The purpose of presenting this figure is to provide a datum against which to make comparisons, in the figures that follow, of the rotor wake geometry that manifests at various stages in the descent of the rotor. Also shown in the figure are examples of the instantaneous vorticity contour geometry and the root-mean-square (RMS) of the fluctuation of the local strength of the vorticity in the flow. A note on the meaning of the RMS plots is required, since they were not discussed earlier in the section on data processing methods. The RMS plots were constructed in a similar fashion to the locus plots, though of course, the RMS of discrete values of vorticity was computed instead of the average of those values. Whilst the locus plots show regions of steady flow and also the existence of persistent though unsteady features, the relative level of unsteadiness of the flow cannot be ascertained. The RMS plots by definition, however, show up the regions of unsteadiness as well as indicate, by the inclusion of a range of contour levels, the relative magnitude of the fluctuations in the flow.

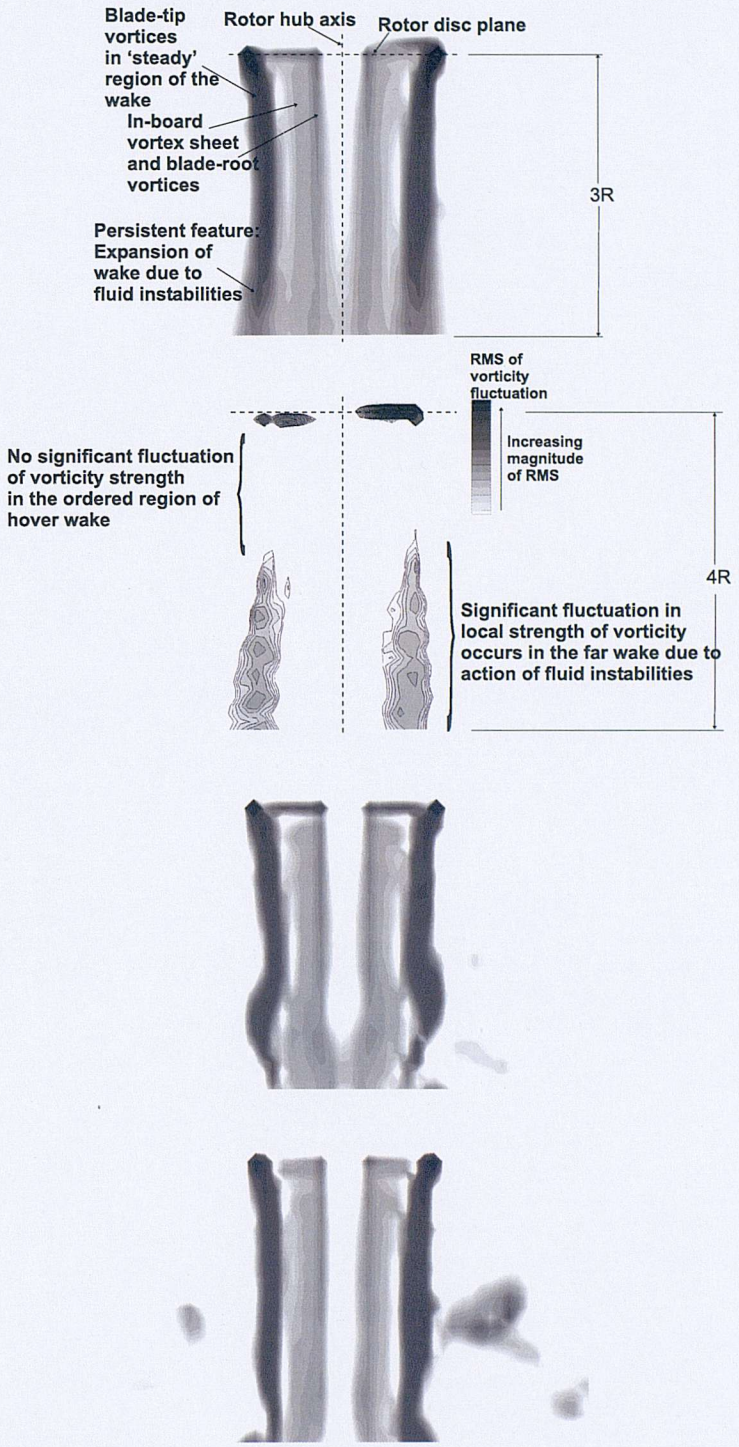



***Figure 4.16:*** *Various representations of wake geometry during hover: Top image: Locus plot; Image second from top: RMS of fluctuations; Bottom two images: instantaneous contours of vorticity. The highest RMS value (black contours) is 10 times higher than the weakest value (contours in lightest hue of grey.*

Figure 4.17 shows the locus plots of the wake, with accompanying instantaneous snapshots and contours of the RMS of fluctuations in the vorticity field as the descent rate increases from just prior to the onset of thrust-settling through to just after the thrust falls. Once again, the locus plots and the RMS contour plots were constructed from 25 rotor revolutions. Note that during 25 revolutions the descent rate changed by $\Delta\mu_z \approx 0.00672$ or in normalised terms, by $\Delta\bar{\mu}_z \approx 0.11$. The sequence of images shows the steady compression of the wake with increase in the descent rate, and, interestingly, how the fluctuating part of the wake moves upwards toward the rotor during the phase of the trajectory addressed in the figure. Note that in the wake of the hovering rotor, the RMS plots show no unsteadiness over a region of approximately 1R in length below the rotor. The increasing level of unsteadiness of the wake in the near-field is reflected in the thrust signal. The geometry of the mean wake in the early stage of thrust-settling shows clearly that the vorticity in the rotor wake is still convected below the rotor, and, indeed, that it retains qualitatively much of the structure of the hovering rotor wake - even though the coherent portion of the wake tube has been truncated significantly by the action of the free-stream flow and the dynamics of the disturbances in the wake. The accompanying instantaneous plots, in each case, have been selected because they represent the extremes of the variation of the wake's geometry during the particular interval of descent speed. In each case, they reveal how unsteady the instabilities in the flow field cause the wake to become. This behaviour is qualitatively very similar to the oscillating flow geometry in incipient VRS observed by Green *et al.* [13]. The important conclusion to draw from this set of images is that it appears *not* to be necessary for the wake to adopt a toroidal geometry to induce a velocity field that will engender thrust-settling.

The origin of thrust settling can be more clearly understood by examining the variation with descent rate of the mean span-wise distribution of loading along the rotor blades. The data used to generate the curves shown in this figure were filtered in the same method as was used to generate the plots of thrust coefficient. Fig. 4.18 shows clearly that thrust settling is associated with a considerable fall in the loading only on the outboard sections of the blade, only. The inboard sections of the blade play only a small role in the thrust settling phenomenon and the curves suggest that the loading on the inboard region of the blade actually increases slightly from just prior to the onset of thrust settling. The large amplitude, low frequency thrust fluctuations that occur during the thrust settling

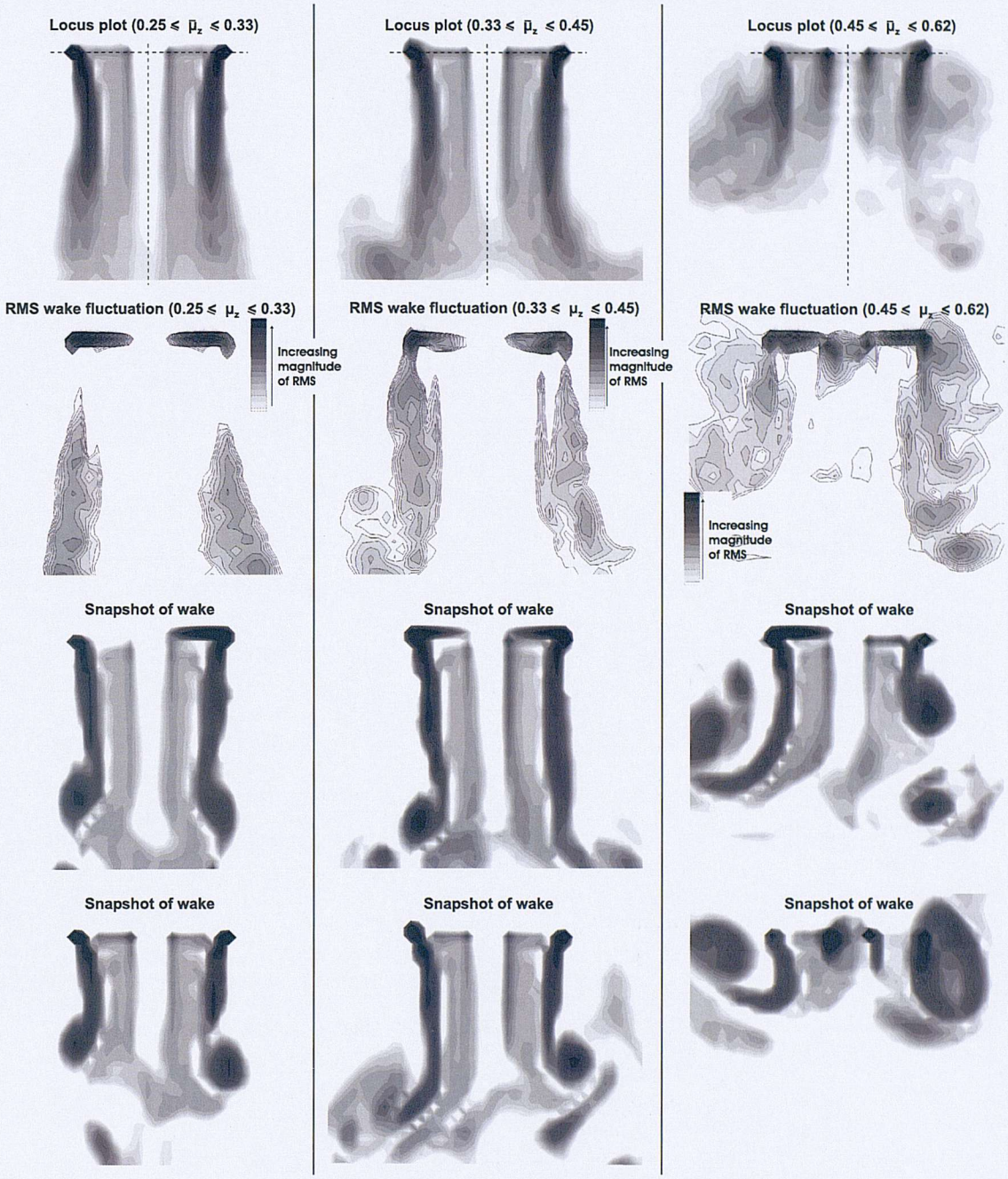



***Figure 4.17:*** *Two dimensional contour plots of the locus of vorticity and RMS of vorticity fluctuations both constructed from 25 rotor revolutions during various intervals of descent speed. Also shown are snapshots of the the corresponding instantaneous vorticity field. The contour plane passes through the hub of the rotor. The highest RMS value (black contours) is 10 times higher than the weakest value (contours in lightest hue of grey).*

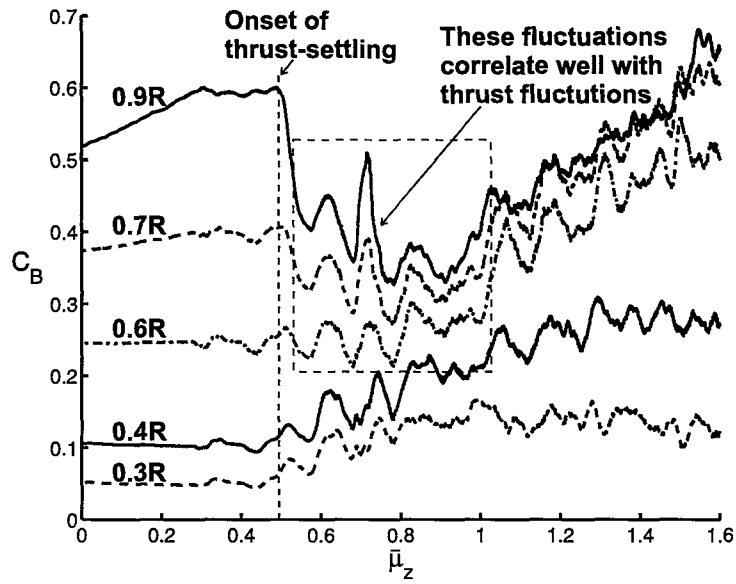



***Figure 4.18:*** *Sectional blade loading vs. descent rate scaled by mean thrust at hover, at various blade stations. Blade loading scaled with mean loading, $C_B/\sigma$. (Constant $\theta_0$).*

phase are apparent in this figure. The blade loading fluctuations, over the descent speed interval enclosed in the box overlaying some of the curves in the figure, correlate well with similar fluctuations in the thrust data. Interestingly, they occur over much of the blade. It appears, though, that the peaks and troughs in the thrust data correlate somewhat better with the fluctuations in blade loading that occur at the outboard sections of the blade than with those on the inboard sections. This suggests that the source of the fluctuations, i.e. the unsteadiness in the wake, occurs nearer to the outboard sections of the blade than it does to the inner sections. It is likely, therefore, that the fluctuations originate from the tip-vortex system.

Fig. 4.19 shows the variation with descent speed of the flow velocity normal to several stations on the blade. Comparison of Figs. 4.18 and 4.19 shows clearly that the reduction in loading on the blade tips is associated with an increase in the inflow over those section, only. A similar observation was made by Azuma and Obata [12], who were able to measure the inflow at several radial stations under their experimental rotor using small, responsive windmill type anemometers. In the absence of direct observations of the structure of the rotor wake, they postulated, however, that the increase in inflow resulted from the rotor being enveloped in the toroidal flow of the fully developed VRS. Of course, it was shown earlier in this section that thrust-settling arises before the toroid forms, however. The

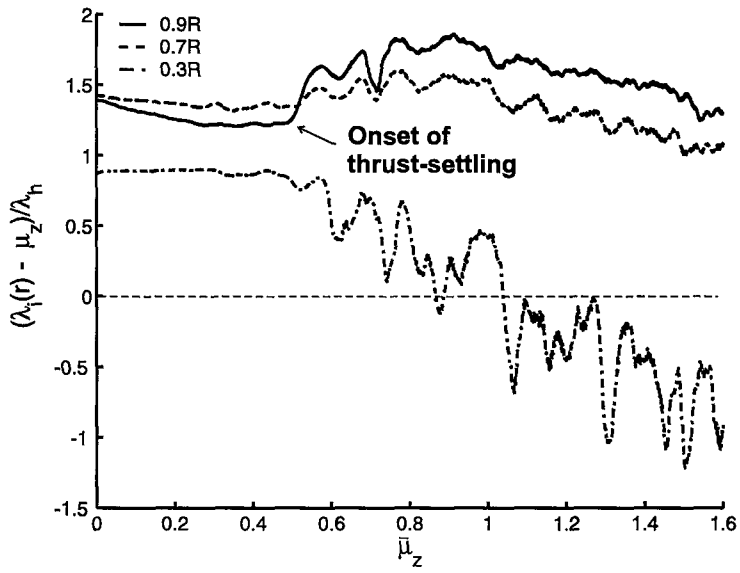



***Figure 4.19:*** *On-blade vertical flow velocity (scaled with the theoretical mean inflow at hover) vs. descent rate scaled by mean thrust at hover, at various blade stations. (Constant $\theta_0$).*

localised nature of the increase in sectional inflow, and thus blade loading decrement, associated with thrust settling suggests, however, that a much more local flow effect is responsible for the phenomenon than the large-scale flow disturbance associated with the fully-developed VRS. Indeed, in this simulation, the toroidal flow of the fully developed VRS was not fully established until a descent rate of $\bar{\mu}_z \approx 0.7$.

In trimmed flight, thrust settling is usually offset by an appropriate change to the collective pitch of the rotor blades. In this case, the flow dynamics associated with thrust settling appear instead as an increase in the torque required by the rotor to maintain constant angular velocity of the rotor, relative to the level of induced torque produced during hover. The total torque, $C_Q$, minus the profile torque, $C_{Q_0}$, (calculated using Eq. 2.40) is shown in Fig. 4.20 for a simulation of Gao's rotor, following an accelerating descent trajectory. In this case the rotor was trimmed throughout to a constant mean thrust coefficient of 0.0073. Figures. 4.21 and 4.22 show the blade loading and velocity normal to the blade, respectively, from the constant $C_T$ simulation. These figures reveal that the aerodynamic effect of the wake upon the rotor blades is similar to when the rotor is flown at constant collective pitch, with an important difference, however. The thrust on the rotor is maintained by a significant increase in the loading on the inboard sections of the blade brought about by the controller increasing the collective pitch of the blades

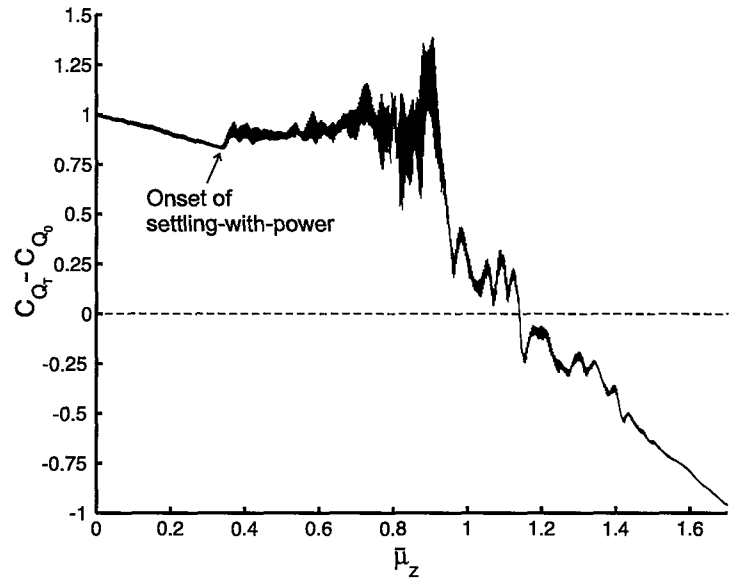



***Figure 4.20:*** *Estimated rotor torque (less constant profile torque $C_{Q_0}$) vs. descent rate scaled by mean thrust at hover. (Constant $C_T$).*

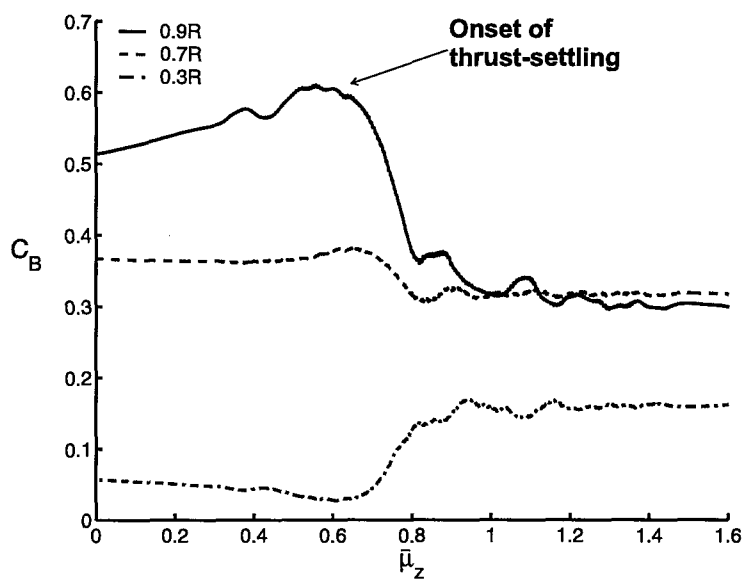



***Figure 4.21:*** *Blade loading vs. descent rate scaled by mean thrust at hover, at various blade stations. Blade loading scaled with mean loading, $C_B/\sigma$ (Constant $C_T$).*

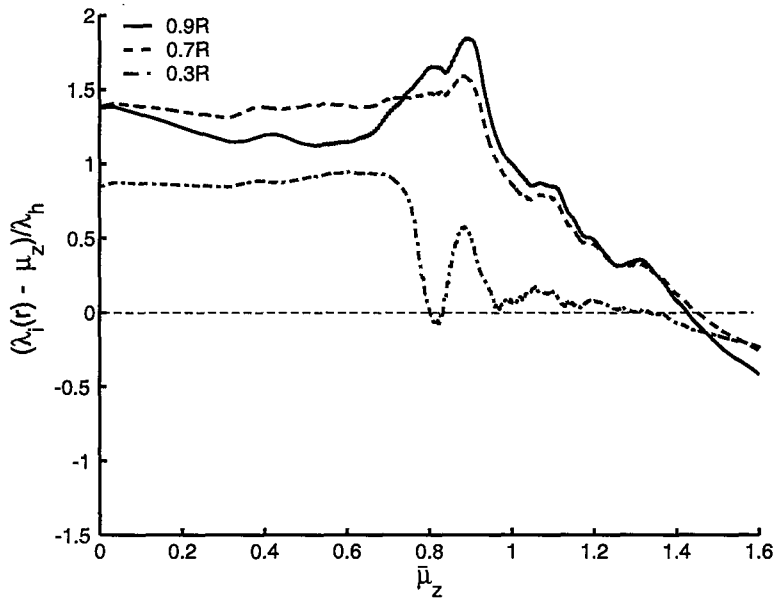



***Figure 4.22:*** *On-blade vertical flow velocity (scaled with the theoretical mean inflow at hover) vs. descent rate scaled by mean thrust at hover, at various blade stations. (Constant $C_T$)*

to compensate for the loss of lift on the outboard sections of the rotor.

It remains to relate the increase in inflow at the outer sections of the blades during the onset of thrust settling to changes in the structure of the wake. To this end, it is possible from the output of the VTM to measure the changes in the strength of the wake within specified regions of the flow field surrounding the rotor. This method was first used by Ahlin and Brown [8] where, as a direct measure of the fluid dynamics of the wake system, it proved to be a very useful indicator of significant changes in the wake behaviour such as the collapse of the wake into the VRS. For convenience, define the *wake intensity* $\Sigma$, as the integral of the vorticity magnitude over a specified volume of the flow. Fig. 4.23 compares the wake intensity, for Gao's rotor flown at constant collective pitch, in a box-shaped domain located just below the rotor to the wake intensity in a box-shaped domain enclosing the flow immediately above the rotor. The domains each had a width and depth of $2.4R$ and a height of $1R$ (this length lay parallel to the vertical axis of the rotor) and were aligned with the rotor such that the vertical axis of the rotor passed through the centre of the domains. In this figure, the wake intensities in each of the boxes have been scaled with the wake intensity in the union of the two domains under hovering conditions, $\Sigma_h$. During the initial stages of the descent, i.e. for $\bar{\mu}_z < 0.3$, the

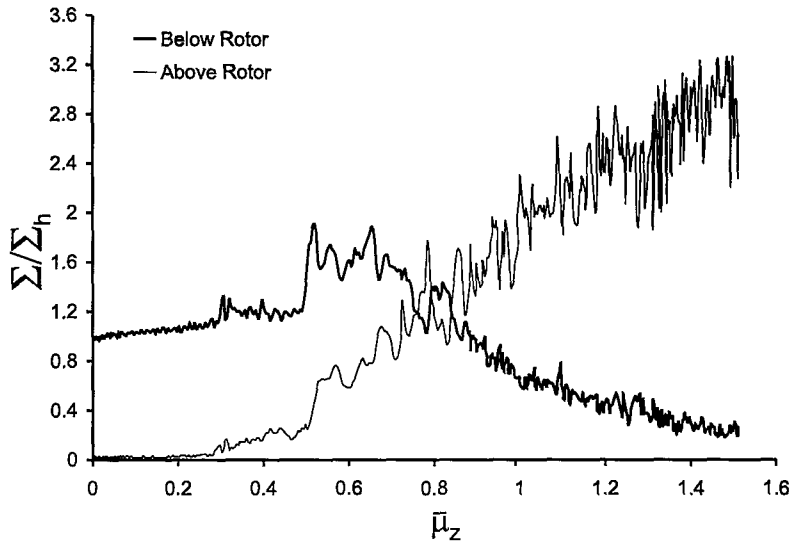



***Figure 4.23:*** *Comparison of wake intensity, $\Sigma$, above and below the rotor vs. descent rate scaled by mean thrust at hover. Wake intensities have been scaled with the wake intensity in the union of the two domains under hovering conditions, $\Sigma_h$. (Constant $\theta_0$)*

wake intensity beneath the rotor increased in approximately linear fashion, representing a smooth, uninhibited compression of the wake, or, in other words, a gradual bunching together of the vortex filaments immediately below the rotor. At $\bar{\mu}_z = 0.3$, the wake intensity below the rotor jumped suddenly, and at the same time, the first appearance of a significant level of vorticity above the rotor occurred. The wake intensity below the rotor remained roughly constant until $\bar{\mu}_z \approx 0.5$, but the appearance of fluctuations in the wake intensity of relatively large amplitude compared to the mean is consistent with the earliest appearance of significant disturbances in the structure of the wake near to the rotor, as shown earlier in Fig. 4.17. Comparing Fig. 4.23 and Fig. 4.15 shows that the change in character of the wake intensity below the rotor at $\bar{\mu}_z = 0.3$ marks also the earliest onset of notable unsteadiness in the thrust produced by the rotor. As the descent rate is increased beyond $\bar{\mu}_z = 0.5$, the wake intensity both above and below the rotor increases rapidly, and the fluctuations in the wake intensity become steadily more extreme. The onset of thrust settling coincides with the beginning of this regime. Fig. 4.24 compares the wake intensity in a domain that envelops the rotor from the mid-span outwards with the wake intensity in a volume that encloses the remaining internal sections of the near-rotor flow field. Again, the wake intensities shown in this figure are normalised by the wake intensity in the union of the two domains under hovering conditions. It is clear that the increase in

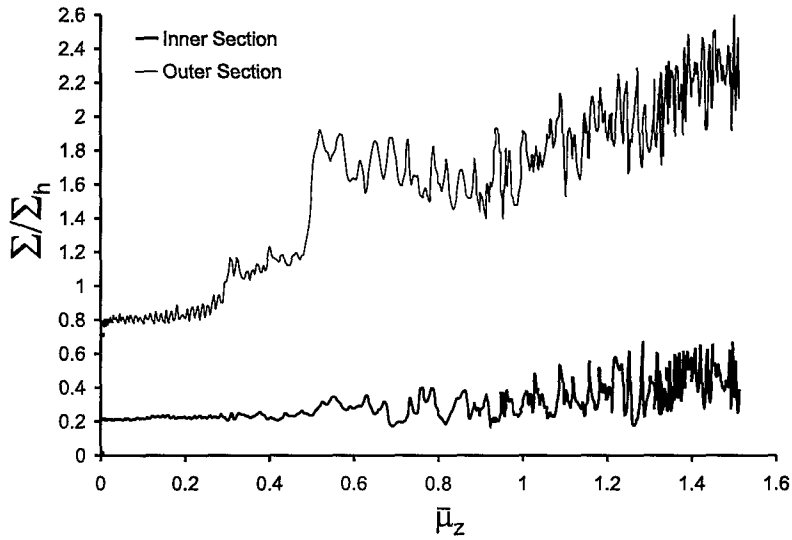



***Figure 4.24:*** *Comparison of wake intensity, $\Sigma$, inboard and outboard of the rotor vs. descent rate scaled by mean thrust at hover. Wake intensities have been scaled with the wake intensity in the union of the two domains under hovering conditions, $\Sigma_h$. (Constant $\theta_0$)*

the wake intensity between $\bar{\mu}_z \approx 0.45$ and $\bar{\mu}_z \approx 0.55$ is confined to the outboard parts of the rotor, suggesting that, when viewed in conjunction with the wake images of Fig. 4.17, the onset of thrust settling is caused by the increase in downwash velocity that is induced by the compression and slight outward convection of the tip vortices beneath the outboard part of the rotor, rather than by any gross change in the characteristics of the flow.

The rapid increase in the wake intensity both below and above the rotor as the descent rate is increased beyond $\bar{\mu}_z = 0.5$ occurs simultaneously with the breakdown of the orderly structure of the wake and the appearance of the toroidal flow that is characteristic of the fully-developed VRS. For descent rates greater than $\bar{\mu}_z \approx 0.7$, the wake intensity above the rotor increases at the expense of the wake intensity below the rotor, indicating a shift in the toroidal vortex structure from below to above the rotor. The crossover point at $\bar{\mu}_z \approx 0.8$ coincides with the maximum intensity of the thrust fluctuations experienced by the rotor and also with the maximum depth of the thrust settling regime. Thus, although thrust settling is brought about by the compression and slight displacement of the rotor wake while it is still in its low-speed, tubular form, it is certainly deepened and sustained by the collapse of the wake into the toroidal form found in the fully developed VRS. Figure 4.25 shows the locus plots of the vorticity field (method of locus plot calculation same as described earlier) arising over the descent speed ranges $0.75 \leq \bar{\mu}_z \leq 0.85$ and

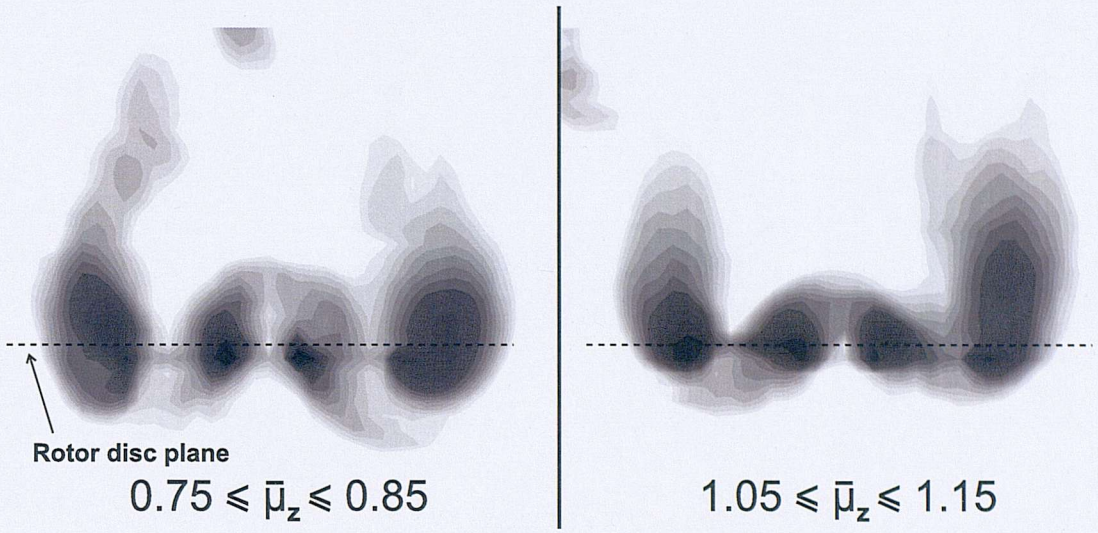



***Figure 4.25:*** *2D vorticity contour plots of the wake geometries during and just after the thrust-settling phenomenon. (Constant $\theta_0$)*

$1.05 \leq \bar{\mu}_z \leq 1.15$. Correlation of Fig. 4.15 with Fig. 4.25 shows that thrust recovery on the rotor begins once the toroidal VRS wake shown in the left image of the figure, is elongated upwards by the free-stream such that the majority of the wake within the rotor near-field resides above of the rotor, as in the image on the right side of the figure. This slight upward shift in the body of the wake is very subtle though and indeed the interpretation of the locus plots in this way has been guided by the trends shown in the wake intensity curves of Fig. 4.23. It is interesting to note then how seemingly very slight changes in the position and geometry of the VRS wake have an operationally significant influence on the rotor performance.

## 4.5 Effects of Acceleration on the Rotor and its Wake

In the past, most experimental (laboratory based) studies of the rotor vortex ring phenomenon involved capturing rotor performance or flow field data over a period of hundreds of rotor revolutions, and, importantly, whilst the free-stream flow (the rotor's trajectory) was held steady. In addition, analytical methods derived to predict the flow through a descending rotor, or to predict the onset of the VRS [7, 19, 20] omit any time dependency from the analysis. The descent speed and thrust production of the rotor is assumed constant by such methods and thus transients in the flow conditions are assumed to be neg-

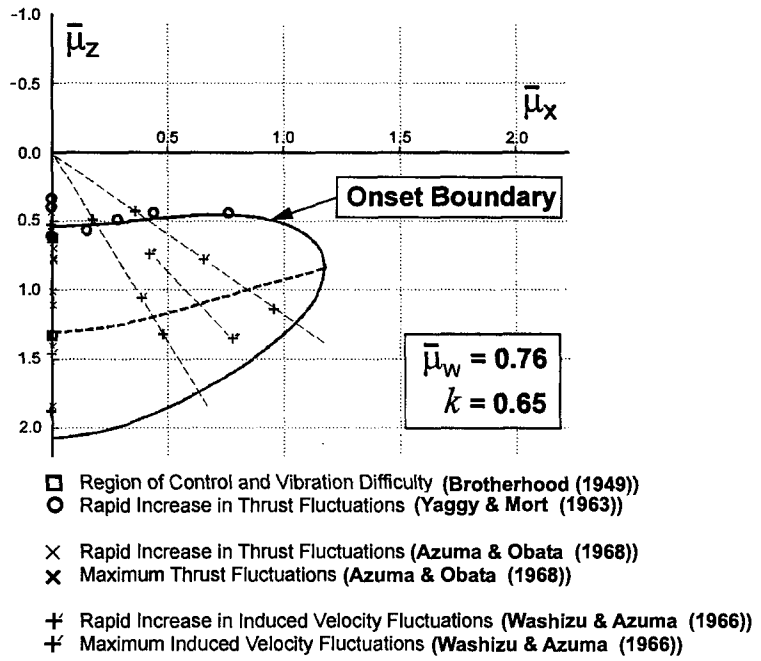



***Figure 4.26:*** *Analytical boundary for VRS onset of Newman* et al. *The boundary is compared with experimental VRS data from the literature. Image taken from Ref.[8].*

ligible; mean flow conditions are assumed. As an example of the steady-state treatments in the literature, Fig. 4.26 presents the flight envelope of the vortex ring state regime as predicted by Newman *et al.'s* [7] VRS steady-state onset prediction model. Nevertheless, this envelope has been accepted within the rotorcraft community (see Kisor [33]) as a reliable guide to VRS onset.

In numerical computations of the rotor VRS, the trajectory imposed on the rotor often includes an accelerated descent through the required range of velocities for reasons of computational tractability. Perhaps what is most important to the present discussion is the notion that the vortex ring phenomenon is unlikely to be encountered by a real rotorcraft under non-accelerating conditions. Indeed, in VRS flight tests, much care may be taken to achieve the steady conditions of laboratory experiments, but this is almost impossible to achieve in practice, such that only 'quasi-steady' conditions have been achieved at best [32]. Indeed, in 2004, Brand, Kisor and co-workers [32, 33] reported that during flight tests of the V-22 Osprey tilt-rotor the observable VRS onset descent-speed boundary was found to be dependent upon whether the regime was approached under quasi-steady or dynamic flight conditions.

Motivated by the papers of Brand and Kisor, Ahlin and Brown [8] presented an analytical and numerical study of the effects on VRS behaviour of accelerated flight conditions at the American Helicopter Society Annual Forum in 2005. A time-dependent prediction model was presented that represented both a re-interpretation and an extension (to include dynamic flight conditions) of Newman *et al.'s* VRS onset prediction model that was mentioned earlier. Newman *et al.'s* model accounted for both the axial and horizontal velocity components of the rotor's trajectory and predicted the onset of VRS when the transport velocity, $\bar{\mu}_W$, of a disturbance to the geometry or strength of the wake fell below some critical value. This disturbance was assumed to cause VRS when its convection speed reached the critical value and thus the boundary shown in Fig. 4.26 represents the combination of descent and forward speeds that admit the critical convection velocity of the disturbance. This approach was fundamentally different to many previously published onset prediction models since the earlier models relied on an evaluation of the rate of transport of vorticity away from the rotor and hence were fixated on a physical description of the VRS in terms of vorticity coalescence near the rotor plane. The VRS onset prediction model of Newman *et al.* is reproduced here in Eq. 4.1.

$$\bar{\mu}_W^2 = (k\bar{\mu}_x)^2 + (\bar{\mu}_z + \bar{\lambda}_i)^2 \tag{4.1}$$

where the over-bar denotes scaling by the inflow at hover. The value of $\bar{\mu}_W$ was established empirically where a value of 0.76 was found to give good agreement with a range of experimentally obtained data of VRS onset speeds, as shown in the aforementioned figure. The constant parameter $k$ is an empirical factor used to de-emphasize the role of the horizontal velocity of the rotor in the establishment of the critical disturbance transport velocity.

The inadequacy associated with this model is that it assumes that the strength or spatial extent of a disturbance in the wake is constant and that its rate of propagation through the flow is dependent only upon the inflow through, and the trajectory of, the rotor. The details of the wake, in terms of the strength and geometry of the vorticity field are in no way accounted for and nor is the history of the rotor's flight velocity. Taking inspiration from the work on the effect of instabilities within a spatially developing flow by Huerre and Monkewitz [72], Ahlin and Brown extended Newman *et al.'s* work by allowing that the propagation of a product of a flow field instability could be decomposed into two components - the disturbance assumed to trigger VRS must grow in spatial extent in

the flow and also convect through the flow. The rate of the growth in spatial extent, $c_d$, was made proportional to the local strength of the vortical wake, or, rather, to the thrust produced by the rotor at the time of the inception of the disturbance. The perturbation was assumed to have originated from the rotor. Thus, the locus of the perturbation's growth front, relative to the rotor, could be defined as

$$\int_{t^*-t_d}^{t^*} (c_d)\tau d\tau. \tag{4.2}$$

Where $t_d$ was originally conceived to represent the time taken for a disturbance to grow from inception to a strength sufficient to cause the onset of VRS. Location of the origin of the flow-field perturbation at the rotor was, of course, a simplifying assumption and thus the resulting model was said to represent just one of a possible spectrum of tractable theories. Defining time $t^*$ as the time at which a disturbance in the flow reaches the rotor and initiates the onset of the VRS, the disturbance will have originated from the rotor at time $t^* - t_d$, such that the distance convected by the disturbance by the time of VRS inception would be

$$\int_{t^*-t_d}^{t^*} (\mathbf{v}_d)\tau d\tau. \tag{4.3}$$

where $\mathbf{v}_d$ is the convection velocity of the disturbance, $\mathbf{v}_d/\Omega R = (\mu_W, \mu_x)$. By a simple geometric argument, time $t^*$ is the minimum value of time $t$ that satisfies the equality

$$|(\mathbf{x}_R)_t - (\mathbf{x}_d)_t| = |\int_{t-t_d}^{t} (c_d)_\tau d\tau| \tag{4.4}$$

subject, as mentioned earlier, to the condition that the disturbance that causes VRS originated at the rotor, or rather:

$$(\mathbf{x}_d)_t = (\mathbf{x}_R)_{t-t_d} + \int_{t-t_d}^{t} (\mathbf{v}_d)\tau d\tau \tag{4.5}$$

where $\mathbf{x}_d$ is the position of the disturbance and $\mathbf{x}_R$ is the position of the rotor and $\mathbf{x}_R/R = (x_R, z_R)$.

This extension to the original model allowed for some semblance of the unsteadiness of the behaviour of the rotor to be incorporated into the prediction of VRS onset by relating the growth parameter $c_d$ to the instantaneous thrust value. In addition, the model was made time dependent by requiring that the disturbance that triggered VRS had to have first grown by some predefined amount, which it would require some finite time to achieve. The critical disturbance velocity, $\mu_W$, was related to the instantaneous mean rotor inflow,

$\lambda_i$, as before though. Thus, onset of the VRS was predicted to occur at the minimum time $t = t^*$, for a prescribed rotor trajectory $\mathbf{x}_R/R$, for which the following equality holds:

$$\begin{aligned}[(x_R)_t - (x_R)_{t-t_d} - t_d(1-k)(\mu_x)_{t-t_d}]^2 \\ +[(z_R)_t - (z_R)_{t-t_d} + \int_{t-t_d}^{t} (\lambda_i)_\tau d\tau]^2 \\ = \frac{1}{2}\bar{\mu}_W^2 t_d^2 (C_T)_{t-t_d}\end{aligned} \tag{4.6}$$

The flight speed for VRS onset then followed from the relationship $\mu_x = (\dot{x}_R)_{t^*}$ and $\mu_z = (\dot{z}_R)_{t^*}$.

The major shortcoming of this model stemmed from the difficulty associated with the appropriate evaluation of the critical growth period $t_d$. Without a more complete idea of the form and dynamics of the disturbance that causes VRS, the identification and evaluation of a time constant in the flow field kinematics is practically impossible, though the findings of Chapter 3, and observations made later in this section, may provide guidance on this matter. Indeed, this time constant proved elusive in the data available from the supporting numerical simulations presented in the paper. Hence, it was not possible to use this model for anything other than the development of theories related to the VRS physics, via interpretation of the terms of the model. Later in this section, the interpretation of the parameters $t_d$ and $C_d$ will be modified on the basis of the evidence presented herein.

The numerical simulations of a rotor following various linearly accelerated flight conditions that accompanied the analytical work of Ahlin and Brown [8], showed clearly that the increase in thrust fluctuations associated with the VRS of a rotor was delayed by acceleration, in terms of the normalised descent speed at which the increase occurred. A quantitative view of the global wake behaviour was obtained via the integration, over a cuboid shaped domain that encompassed the rotor, of the magnitude of the vorticity that arose within the domain at discrete times during the computations. In much the same manner used in the analysis of the thrust settling phenomenon in the preceding section, this crude, though insightful, method of measuring the global strength of the wake allowed an effective means of identifying VRS onset, evolution and cessation. From this particular method of data reduction, the aforementioned delay in VRS onset could also be readily identified. It was also clear from this measure of the wake behaviour that the character of the rotor's experience of the VRS, through initiation to cessation, became more gradual

and perhaps less erratic as the descent acceleration increased. Three-dimensional visualisations of the vorticity field surrounding the rotor at pertinent times during the flight of the rotor showed that many of the large thrust fluctuations could be attributed to the rapid convection by the free-stream of significant quantities of vorticity away from the rotor. Although seemingly aperiodic, these large-scale breakaway events (as have been subsequently exposed and analysed in some detail in the work reported in Chapter 3 of this thesis) occurred approximately every 20 or so rotor revolutions. It was shown how some aspects of the change of character of the evolution of the VRS could be linked to the number of vortex 'agglomeration and breakaway' events experienced by the rotor - the number becoming fewer with increase in descent acceleration and, indeed, with increase in horizontal speed.

In their paper, Ahlin and Brown [8] postulated that the time allowed for instabilities in the flow field to influence the geometry of the wake became less as descent acceleration increased. The inference of this notion is that at a given descent speed prior to VRS onset, the wake of an accelerating rotor would be less disorganised than that of a rotor operating in steady-state conditions. So, at a speed that would cause the latter wake to break down into VRS the former wake would exhibit tubular geometry and less truncation than the latter and thus would be less likely to break down at that speed. The aim of the following work is to provide, through further numerical simulation, evidence that supports (or otherwise) the aforementioned postulation and its implications. In doing so, greater depth of understanding of how the behaviour of a rotor and its wake is influenced by an accelerated descent is obtained. The final aim is to inform the derivation of a further time-dependent, analytical, onset prediction model that is based upon a more accurate description of the dynamics of the disturbances with the rotor flow field.

For this investigation, simulations of the two-bladed rotor of Gao [16] (defined in table 2.1) were conducted. The rotor was flown in axial descent under controlled thrust conditions, where $C_T$ was held nominally constant at a value of 0.00724. The blade flap and lag dynamics were suppressed, such that the rotor was made rigid. The aerodynamic model of the rotor blades was arranged so that the blades would behave as idealised lifting-lines of finite aspect ratio, thereby preventing aerodynamic stall of the blades and so removing from the results a possible cause of ambiguity and obscuration of the important underlying wake dynamics. The effects of four different descent acceleration rates were

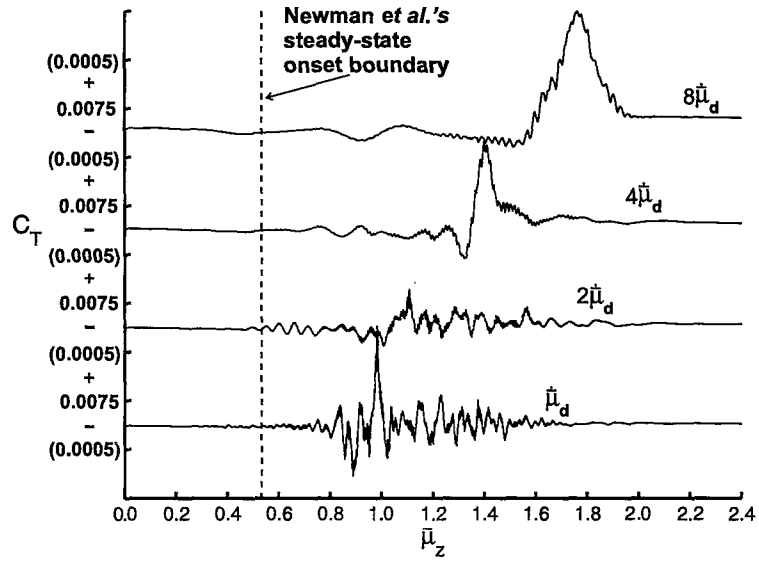



***Figure 4.27:*** *Comparison between the thrust histories of four descent acceleration cases, vs. descent speed scaled by the mean inflow of a rotor in hover. Thrust was controlled to be nominally constant at $C_T = 0.00724$. The thrust traces have been artificially separated in the vertical axis for clarity.*

compared. The accelerations were linear in each case and of the following magnitudes: $\dot{\bar{\mu}}_z = \dot{\bar{\mu}}_d - 0.007/\text{rev}$, where $\dot{\bar{\mu}}_d$ was the default acceleration and was relatively small, and then $\dot{\bar{\mu}}_z = 2\dot{\bar{\mu}}_d$, $\dot{\bar{\mu}}_z = 4\dot{\bar{\mu}}_d$ and $\dot{\bar{\mu}}_z = 8\dot{\bar{\mu}}_d$. These accelerations, especially the default rate, are quite small. To put them into context, if they are written in terms of gravitational acceleration, $g$, where $g = -9.81 m/s^2$, then the default descent acceleration is equivalent to a Blackhawk type helicopter, operating with maximum take off weight, descending with an acceleration of $0.066g$.

Figure 4.27 presents the thrust history versus descent rate, where the descent rate was scaled, as is conventional, with the inflow generated at hover, $\sqrt{C_{T_h}/2}$. As was mentioned earlier, the thrust was held nominally constant, and was the same in each simulation. In the figure, the four thrust traces have been artificially separated along the vertical axis. This was done simply for the sake of clarity.

The raw data was filtered using a moving averaging window with a period of just one rotor revolution. This filtering process was conducted in order to suppress the thrust fluctuations in the data that corresponded to the blade passing frequency, and any higher frequency content, usually due to blade-vortex interactions. The resulting thrust plot thus provides a good quantitative indication of the influence that the wake dynamics has on the

performance of the rotor. Most importantly in the context of this particular investigation, the effect of the various magnitudes of descent acceleration is also made more apparent by the suppression of the high frequency content of the thrust fluctuations. The steady-state onset boundary of Newman *et al.* [7] is included in the figure to highlight how acceleration causes the behaviour of the rotor in VRS to deviate from the steady-state condition.

It is clear that the initial occurrence of significant thrust fluctuations arises at higher and higher descent rates as the descent acceleration increases. In addition, an increase in the acceleration appears to delay the cessation of large thrust fluctuations and seems to modify the character and magnitude of the thrust variations. The magnitude of the thrust fluctuations are presented explicitly in Fig. 4.28, which shows the standard deviation about the mean thrust of the fluctuations in thrust as a percentage of the mean thrust at hover. Interestingly, the fluctuation magnitude does not appear to vary monotonically with acceleration. This indicates that the geometry and dynamics of the highly unsteady vorticity field with which the rotor interacts depends, non-linearly, on the rotor's trajectory.

It is very apparent then that the performance of the rotor is strongly influenced by acceleration of the rotor through the VRS regime. Evidence of how the gross inflow through the rotor is affected by the type of trajectory variation being examined here is provided by inspecting the variation of the rotor's induced power, $C_P$, with descent rate. $C_P$ is a function of the gross rotor inflow, since the thrust coefficient was maintained nominally constant. The data is set against results from classical momentum theory for an idealised rotor, a method of presentation proposed by Lock [73], to give an indirect indication of the deviation of the wake geometry from the classical tubular form below or above the rotor assumed by momentum theory. Such an indication is obtained because, as was seen in § 2.4.2, the inflow of the simulated rotor here adhered to the momentum theory result at low descent speeds, and because, as was seen in § 4.3, the initial large fluctuations in the induced inflow arise upon the onset of the VRS. Therefore, it can be concluded from these two results that in the simulations, large deviations in the induced inflow, and thus the induced power, from the momentum theory result for descending flight with the wake tube directed below the rotor, will arise upon the onset of VRS. A comparison of the effects of acceleration on the induced rotor power is presented in Fig. 4.29. Once again, the raw data has been filtered with a moving window, one rotor revolution in length.

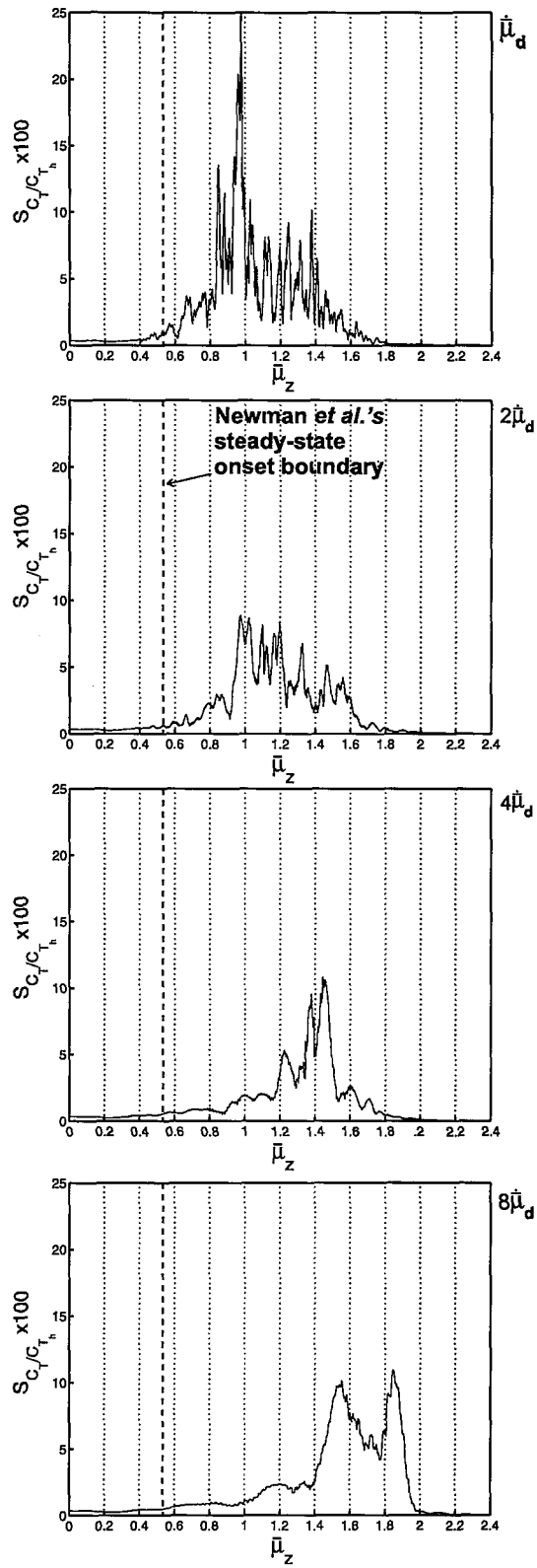



***Figure 4.28:*** *Comparison of standard deviation of the thrust fluctuation histories, $S_{C_T}$, of four descent acceleration cases, vs. descent speed scaled by the mean inflow of a rotor in hover.*

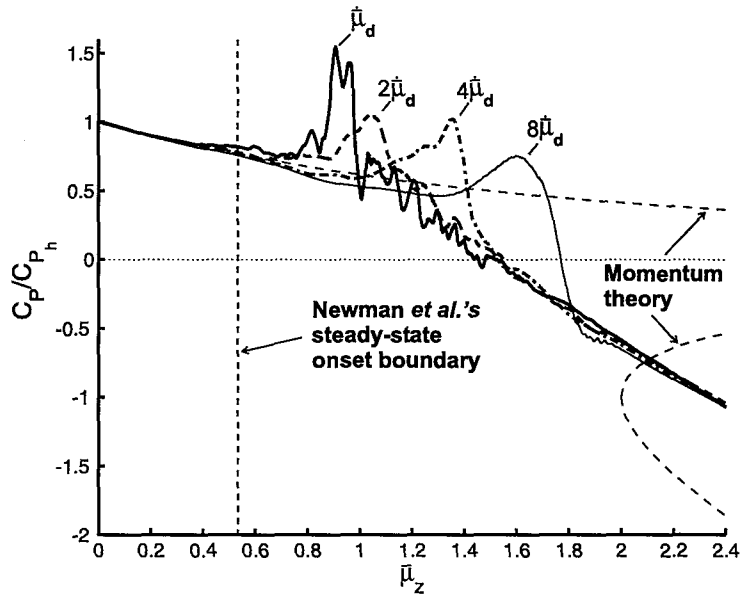



***Figure 4.29:*** *Comparison of the variation of the normalised induced rotor power, $C_P/C_{P_h}$, of four descent acceleration cases, vs. descent speed scaled by the mean inflow of a rotor in hover.*

In each case, the sudden increase in $C_P$ above the upper, unphysical, momentum theory result is representative of an increase in the mean rotor inflow brought about by the development of the VRS. Hence, the trend most worthy of note here is that the increase in induced power is delayed to higher normalised descent speeds as acceleration increases, and thus it can be inferred from this that the descent speed at which the wake of the rotor transitions from the tubular form found arising during hover into a geometry more associated with the VRS increases in some way with acceleration. Note though how the induced rotor power falls below the momentum theory result prior to increasing suddenly in the case of the two highest accelerations. This is indicative, perhaps, of the performance of a rotor with a wake of tubular geometry that induces a lower inflow than the constant strength, infinitely long wake envisaged in the momentum theory.

The relationship between the acceleration and the magnitude of the delay in VRS onset is very difficult to discern since VRS initiation becomes more gradual, and thus more difficult to define, as the rate of change of descent speed becomes relatively large. This topic will be returned to later on in this section.

Examination of visualisations of the flow fields at pertinent times during the four rotor trajectories reveals the underlying differences in the wake geometries arising at given times that engender the variations in the behaviour of the rotor when undergoing different

descent accelerations. Figure 4.30 shows three-dimensional iso-surfaces of the locus of vorticity overlaying two-dimensional contours of locus plots of vorticity that arise during a range of normalised descent speeds. The locus plots were constructed in the manner described in §2.7.2. The range of descent speeds is as follows: $0.5 \leq \bar{\mu}_z \leq 0.7$; $1.0 \leq \bar{\mu}_z \leq 1.1$; $1.3 \leq \bar{\mu}_z \leq 1.4$ and finally $1.5 \leq \bar{\mu}_z \leq 1.7$. The first speed interval coincides roughly with the first signs of unsteadiness in the thrust generated by the most slowly accelerating rotor. This speed interval has been included in the presentation to reveal how the pre-VRS rotor wake is influenced by acceleration. The last three of the speed ranges coincide approximately with the peaks in rotor induced power in each of the three highest acceleration cases. It is noteworthy that averaging the vorticity fields over the time interval covered by each of the speed ranges means that, of course, the number of rotor revolutions included in the averaging process decreases with acceleration rate. The result is that the wake visualisations of the higher acceleration cases will more closely resemble individual snap-shots of the highly unsteady wake and the transient features explained in §2.7.2 will appear stronger than if the locus plots were constructed from many more snap-shots. In spite of this, a very clear trend in the respective wake behaviours is observable, and this trend strongly supports the inference regarding the geometric state of the respective wakes that was made earlier from the induced power data. The onset of wake breakdown into the VRS, that causes the peak in the mean rotor inflow responsible for the peak in torque demand, is delayed to higher rates of descent with increase in acceleration rate.

In the speed range of $0.5 \leq \bar{\mu}_z \leq 0.7$ all of the wakes exhibit tubular geometry. Close inspection of the images reveals that the level of truncation diminishes slightly with increase in acceleration, however. In addition, there are definite signs in the image of the most slowly accelerated rotor of a more unsteady flow field (which is consistent with the unsteadiness in the corresponding thrust history shown earlier) as indicated by the asymmetry in the iso-surface plot and especially in the far-field of the vorticity contour plot. In the next speed interval, the most slowly accelerated rotor was operating within a fully developed VRS. During the same speed interval the wake of the second most slowly accelerated rotor was in the process of collapsing into the VRS toroid whilst the wakes of the higher acceleration cases reveal predominantly tubular, though disorganised, geometry. The wake in the lowest acceleration case was well established within the turbulent wake state when the most highly accelerated rotor had reached the descent speed range that

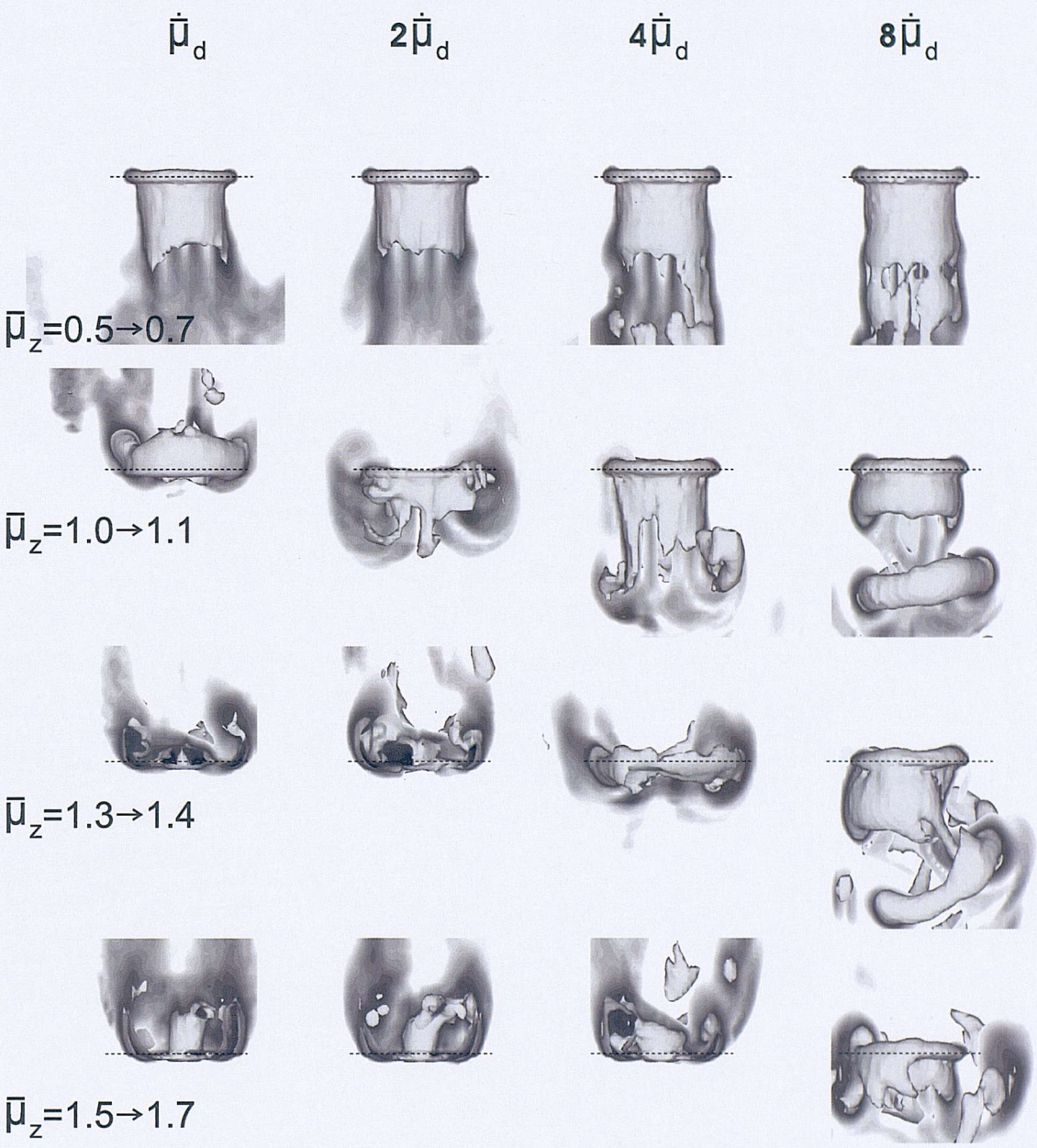



***Figure 4.30:*** *3D Iso-surfaces and 2D contour plots of locus plots of vorticity in the wake of a rotor undergoing accelerated trajectories. The mean wake from four linear accelerations are shown during four intervals of descent speed. A section of the foregrounds of some iso-surface images have been blanked to provide a view of the inner wake structure. The iso-surface and contour levels are the same in each image.*

induced the relatively broad peak in its induced power. Within the same range of descent speeds, the images of the two intermediate acceleration cases show that the rotors were near to the end of the VRS phase of their respective flight trajectories. This presentation has provided clear evidence that the kinematics of the wake of an axially descending rotor are sensitive to the time history of the rotor's descent since the kinematics of the wake are also time dependent: if the wake could adjust instantaneously to changes in the descent speed, however rapid those changes may be, there would be no sensitivity to acceleration. It is important to note though that all of the data on this subject presented up to now indicates that acceleration affects the speed of VRS onset more than it does the speed at which the subsequent cessation of VRS occurs. This trend suggests that the kinematics govern its truncation and collapse during descent are more strongly influenced by the time history of the rotor's descent than are the wake kinematics that maintain the wake in the toroid once it has collapsed. Indeed, there are similarities between this trend and the trend regarding the dependency of the computational solution on grid size. It can be seen from the thrust fluctuation data in Fig. 2.13, Chapter 2, for instance, that VRS onset speed is more greatly influenced by grid size, and thus the range of length scales in the flow and the energy contained within each scale, than is the cessation speed. These observations highlight, perhaps, how the roles played by the fluid instabilities in the wake change in the way that they govern the wake's evolution as the rotor's descent speed changes.

Re-orientation of vortex filaments out of the plane of the rotor disc was identified in Chapter 3 of this thesis to be a non-linear manifestation of the pairing and short-wave modes of fluid instability that are inherent to a helical vortex system. It was also noted in Chapter 3 that the mean contribution of the vertically aligned component of vorticity, $|\omega_z|$ to the total vorticity, $|\omega|$, in the flow field, where $\omega = (\omega_x^2+\omega_y^2+\omega_z^2)^{1/2}$, increased as a rotor approached and entered the vortex ring condition during an axial descent. This increase occurred when the VRS was approached via slowing from the windmill brake state and when approached from an initial hover condition. In the light of this observed behaviour it is instructive to examine how this aspect of the wake kinematics, being time-dependent in its nature, is influenced by an accelerated axial descent. Hence, this behaviour can be related to the effects on rotor performance that were highlighted earlier. Figure 4.31 shows the variation of the mean contribution of the three vectorial components of vorticity to the total vorticity within a region of the flow field that surrounds the rotor. The region of

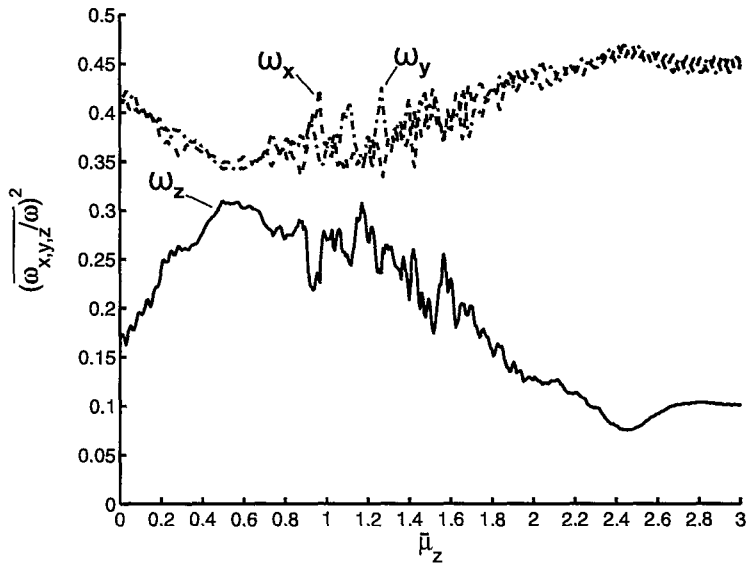



***Figure 4.31:*** *Variation of contribution to the total vorticity of the individual vector components of vorticity. Data from the default case,* $\dot{\bar{\mu}}_z = \dot{\bar{\mu}}_d$.

the flow domain over which the calculation of the mean contribution was performed had dimensions $3R \times 3R \times 7R$ with the upper part of its length reaching $2R$ above the disc plane and the lower end reaching $5R$ below the rotor. The domain was positioned such that the axis of the rotor passed along the centre-line of the domain. These dimensions were selected to ensure that the vorticity in the wake tube formed during hover and low speed descent prior to VRS onset and in the toroid arising during VRS was completely contained within the integration domain. The extension of the domain to just $2R$ above the rotor accounted for the VRS wake structure and its remnants only when the rotor was in or had just come out of the vortex ring condition; the fragments of vorticity that are ejected into the free-stream high above the rotor were not included in the integration. The data in Fig. 4.31 is taken from the case involving the lowest acceleration. As expected, the contribution of the vertically aligned component of vorticity, $\omega_z$, rises as the descent rate increases, at the expense of the strength of the horizontally aligned components of vorticity. Upon the onset of VRS, the contribution of the vertical component of vorticity reaches a maximum whilst the horizontally aligned components achieve a minimum level. Upon cessation of the VRS, at $\bar{\mu}_z \approx 1.8$, the reinstatement of an ordered helical wake is signalled by an increase of the mean strength of the horizontal vorticity components $\omega_x$ and $\omega_y$, and a consequent fall in the contribution of the vertical vorticity component,

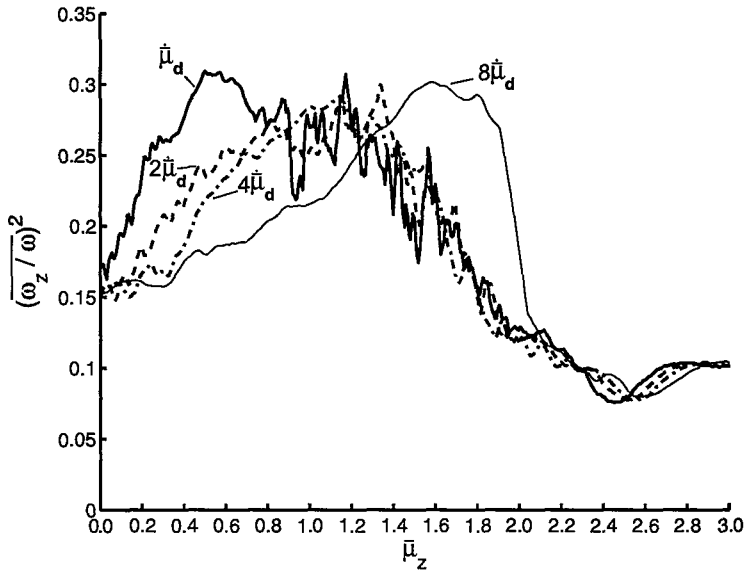



***Figure 4.32:*** *Variation of contribution to the total vorticity of the vertically aligned component of vorticity. Data from all four acceleration cases.*

relative to the levels achieved during the VRS. This figure is provided to illustrate the variation in the average alignment, relative to the rotor plane, of the vorticity within the flow field during a descent from hover through to the high speed windmill brake state. Such an illustration allows a more ready interpretation of the next figure, Fig. 4.32. This new figure shows the effects of descent acceleration on the variation of the mean ratio of the vertically aligned vorticity to the total vorticity in the flow, i.e. $\overline{(\omega_z/|\omega|)}^2$. The data was obtained by the method used to compute the data presented in the previous figure. It is clear that acceleration delays, to higher descent rates, the increase in the contribution of vertically aligned vorticity, $\omega_z$, to the total vorticity in the wake that arises at the onset of VRS. Put another way, acceleration delays the generation of vertically aligned vorticity. But it is interesting to note that there is an approximate agreement between the three lowest acceleration cases with respect to the speed at which the contribution of the vertical component of vorticity begins to fall and the rate at which it falls thereafter. It seems that acceleration affects only the production of vertical vorticity prior to VRS onset. Indeed, because the maximum level of vertical vorticity that was achieved in all four cases was roughly equal, it seems that these trends support the notion that a required amount of wake truncation is required to initiate the VRS.

The production of vertically aligned vorticity was earlier identified as a mechanism

of wake truncation, thus the logical extension of the trend shown in Fig.4.32 is that acceleration delays the truncation of the rotor wake to higher descent rates. It takes time for the vertically aligned vorticity to grow. Additionally, an increase in acceleration rate means that less time will elapse prior to the achievement of some given descent speed. It can, therefore, at the very least, be deduced that the delay in the growth of $\omega_z$ exhibited in the figure is due to the differentials in elapsed time. This effect seems too simplistic however, although it is likely to be a first-order effect. As has already been noted, the linear growth rate of small perturbations to the geometry or strength of the helical vortex system of a rotor is non-linearly dependent upon the pitch of the vortex helix. Thus, one can assume that as the vortex-filament separation distance is decreased by the relative upward free-stream flow during the descent of the rotor, the rate at which the wake is disordered increases, at least whilst the scale of the perturbations remain within the linear range. It can be postulated, therefore, that such dependence on the spatial intensity of the vorticity field does not only cause the evolution of the structure of the wake to lag in its response to an accelerating upward free-stream flow due to the first-order effect. But, in addition, so too does acceleration decrease the rate at which vortex filaments orientate away from the original ordered helical structure at a given descent speed.

It is perhaps noteworthy that in each case the ratio of vertically aligned vorticity to the total vorticity, $\overline{(\omega_z/|\omega|)}^2$, reaches a peak mean value of around 0.3, despite the differences in the time allowed for the respective peaks to develop. This is remarkable since it strengthens the assertion made in Chapter 3 that filament re-orientation, and the resulting repeating structure within the flow field, which was also seen in Chapter 3, is a fundamental aspect of the the vortex kinematics associated with the rotor VRS. It is also interesting to compare the time taken for these non-linear fluid processes occur in each case: in the highest acceleration case presented, the rotor made as few as approximately 28 revolutions from the start of its descent to reach the peak value of $\overline{(\omega_z/|\omega|)}^2$. This compares with a total of around 85 revolutions in the case of the lowest acceleration case; the time taken for VRS to initiate appears to be non-linearly dependent upon descent acceleration.

A feature of the data in all the figures presented in this section is the subtle change in character of the VRS-induced fluctuations of thrust and of induced power and, indeed of the value of $\overline{(\omega_z/|\omega|)}^2$ with increase in acceleration. The thrust signal, for instance,

becomes far less erratic. It was shown earlier in this chapter that the low frequency variability in the rotor performance is strongly associated with the gross motion of the wake. In addition, Stack *et al.* [15] showed that in fully developed VRS, there is a strong correlation between the agglomeration and subsequent breakaway of vorticity from the vortex toroid in the vicinity of the rotor with the fall and rise of rotor thrust levels. In Chapter 3 of this thesis the mechanism that governs this large scale process of vortex shedding from the VRS toroid was revealed to be associated with the local interaction of pairing vortex filaments. According to Stack *et al.* and also Green *et al.* [13] these processes appear to have a characteristic time-scale of around 10-30 rotor revolutions. It seems likely then, that since an increase in the descent acceleration of a rotor appears to reduce the length of the descent speed interval in which a rotor flies within the VRS, as discussed earlier, the rotor would be subjected to fewer disturbances caused by the ring build-up and breakaway process as the acceleration level is increased. The less erratic thrust signal is a product of the rotor having experienced less unsteadiness than the same rotor flying on a more slowly accelerated trajectory. This effect is clearly evident in Fig. 4.33. The figure shows, on the left side, the evolution of the wake of a rotor descending with an acceleration of $\dot{\bar{\mu}}_z = 2\dot{\bar{\mu}}_d$. A period of 20 rotor revolutions of rotor flight within the VRS is displayed. The uppermost image in the figure shows the wake just after the wake has collapsed into the VRS. The images are instantaneous snap-shots of the geometry of the wake and they have been visualised using a relatively low iso-surface value in order to expose the gross features of the wake. Over the period shown the wake is highly unsteady and several large-scale vortex shedding events are evident. The rotor remains within the VRS such that the states of the wake at the beginning and the end of this 20 rev period are qualitatively similar.

On the right of the figure is shown the evolution of the wake of a rotor descending with an acceleration of $\dot{\bar{\mu}}_z = 8\dot{\bar{\mu}}_d$, again over a period of 20 revolutions of the rotor but in this case, at the start of the period shown the rotor is flying within the incipient stage of the VRS. Note that the two 20 revolution intervals are by necessity not the same intervals in terms of descent speed. Such is the rate of acceleration, that the rotor passes through the entire VRS regime, i.e. from VRS onset to its cessation and into a fully developed windmill brake state. The rotor passes through the VRS regime so quickly that the timescale of VRS-related vortex shedding events is similar to the time taken

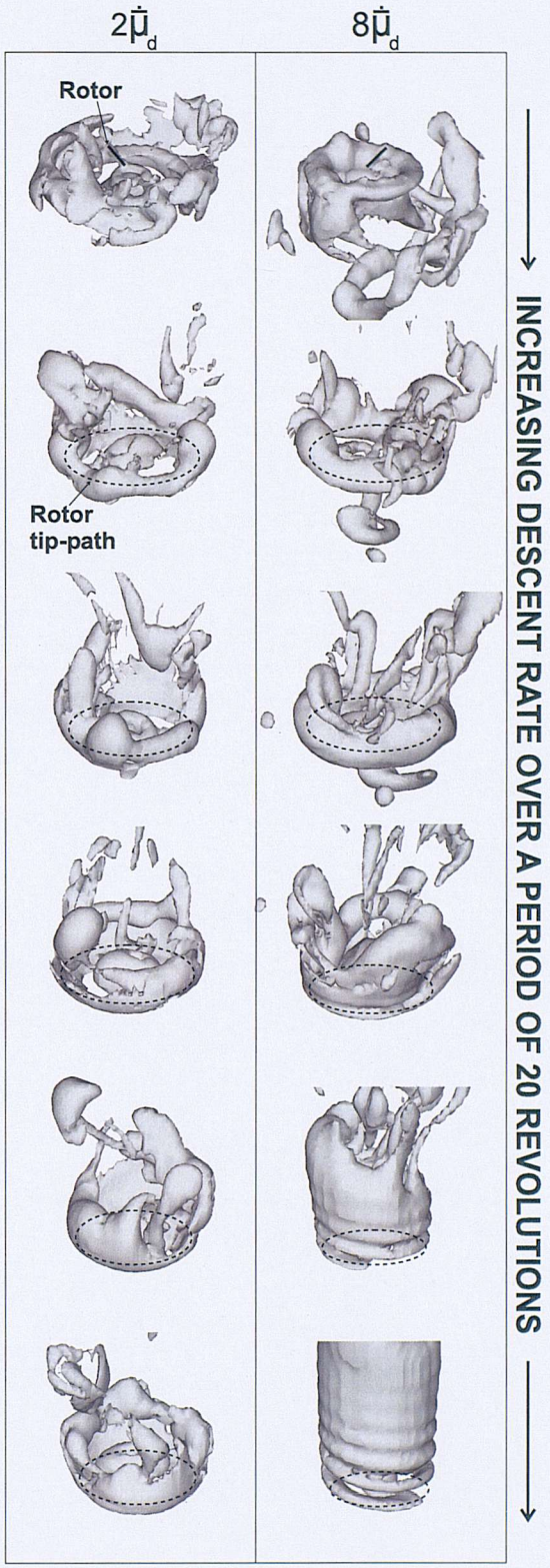



***Figure 4.33:*** *Visualisations of the vortical rotor wake as the rotor descends with increasing speed over a period of* 20 *revolutions. Two acceleration cases are shown:* $\dot{\bar{\mu}}_z = 2\dot{\bar{\mu}}_d$ *and* $\dot{\bar{\mu}}_z = 8\dot{\bar{\mu}}_d$*. The start points of the two 20 revolution intervals are necessarily different.*

by the rotor to pass right through the VRS regime, thus, the rotor experienced fewer large-scale vortex shedding events than the rotor that spent more time in the VRS. As a consequence, the lift generated on the rotor is disturbed less by the motion of the wake than at lower acceleration rates. Much of the vorticity seen streaming up over the more quickly accelerating rotor is that which has come up from far below the rotor and this is likely to have caused some thrust fluctuation. The large-scale vortex shedding event that is evident, however, is different in nature to that which occurred in the lower acceleration case featured here. It appears as if the entire agglomerated ring around the rotor is lifted off the rotor, all at once, (this phenomenon occurs simultaneously with the peak in the thrust signal) upon which the wake then transitions into the wake geometry associated with the WBS. Indeed, at high acceleration, perhaps the VRS regime is better regarded simply as a highly transient state through which the the rotor passes whilst the wake transitions from the downward flowing vortex tube associated with the hover condition to the upward streaming structure that forms in the windmill brake state.

### 4.5.1 Discussion

It has been demonstrated in the preceding work that the postponement of the onset of VRS until higher than expected descent rates, as measured by Kisor *et al.* [33], can be replicated in CFD calculations. The cause of such postponement is associated with the time dependent nature of vortex filament re-orientation out of a plane parallel to the rotor that is responsible for the disorganisation of the wake prior to VRS onset. The reduction in the elapsed time leading up to a given descent rate just prior to the onset of VRS, as the acceleration level increases, necessarily results in a reduction in the disorganisation and truncation of the wake in comparison to that which arises in the wake of a more gently accelerating rotor. The important consequence of this is that the less disordered wake is therefore able to maintain a tubular, hover-like, form at higher descent rates. It is important to bear in mind here, that as a rotor descends, the inflow that it generates increases up to the point where the VRS wake begins to convect above the rotor, as has been shown earlier in this chapter. It will be shown in Chapter 6 that scaling the descent rate, $\mu_z$, by the instantaneous mean inflow, $\lambda_i$, calculated using Washizu's method [22] as described in Chapter 2, is, arguably, a better normalising parameter than the more common hover inflow parameter, $\lambda_h$, at least in this context anyway, at least, since it

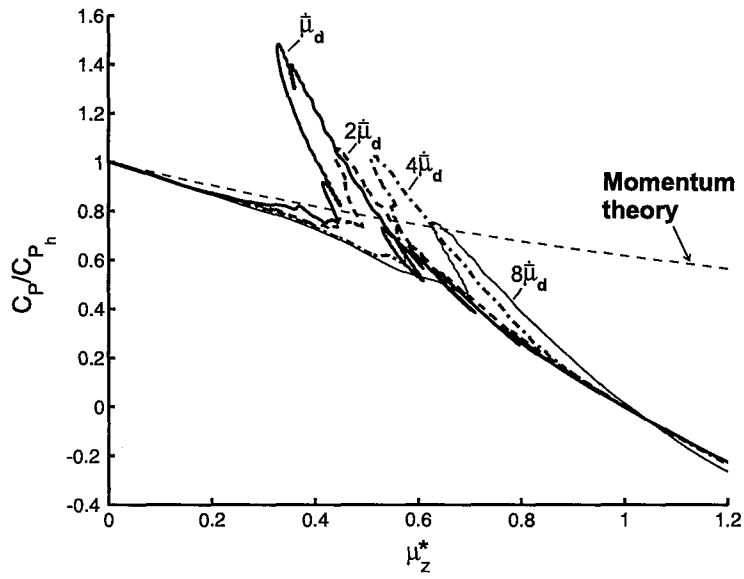



***Figure 4.34:*** *Figure shows mean $C_P/C_{P_h}$ vs. $\mu_z^*$ from the four acceleration cases. The upper branch of the theoretical induced power curves has been left on this graph to provide an indication of the scale of the deviation from the trend shown in the previous figure of induced power, Fig 4.29.*

gives a measure of the instantaneous difference between the inflow velocity and that of the free-stream at the onset of the VRS. It has been shown on numerous occasions in the past that VRS occurs at a descent speed that is considerably less that the mean induced inflow at hover, thus, since inflow increases with descent rate, up until the VRS phase, this means that the ratio between the descent speed and the actual mean inflow velocity that arises at the onset of VRS will be smaller than the ratio between descent rate and the inflow produced in hover. VRS arises well before the descent velocity equals the mean inflow velocity because of the instabilities in the flow that cause the wake to break down before the free-stream becomes sufficiently strong to completely prevent the downward transport of the tip-vortices of the rotor. Hence, as acceleration suppresses, temporally, the action of the fluid instabilities in the wake the difference between the descent velocity and the mean inflow that arises at VRS onset will be increased as a result. Fig. 4.34 shows the induced power, $C_P/C_{P_h}$, set against descent speed scaled with the instantaneous mean inflow, $\lambda_i$, such that $\mu_z^* = \mu_z/\lambda_i$. The curves representing the three highest acceleration cases were generated from the mean values of the normalised power coefficient, where the moving averaging window, as before, had a period of just one rotor revolution. The highly erratic nature of the thrust and torque from the rotor

descending with the default acceleration resulted in the calculated instantaneous mean inflow also being highly erratic. The resulting plot of normalised power in this instance was thus difficult to interpret. The curve representing this case, therefore, was generated from a moving averaging window of with a period of some sixteen rotor revolutions to remove much of the obscuring unsteadiness.

It is clear from this figure that acceleration does indeed modify the difference between the inflow and the descent speed required to initiate the VRS. In addition, the previous difference between the scaled descent speeds at which VRS onset arises, in the four acceleration cases, has been reduced. Consider the induced power curves from the three highest acceleration cases. If the peaks in the induced power are associated with VRS onset then the average of the descent speed interval between each of the peaks is $\Delta\mu_z^* \approx 0.1$. As can be seen in the previous figure showing induced power plotted against a conventionally scaled descent speed, in Fig. 4.29, the average of the descent speed interval between the corresponding peaks is $\Delta\bar{\mu}_z \approx 0.3$. This result implies that the effect of acceleration on ameliorating the wake truncating processes that lead to eventual wake breakdown is less than is suggested by the trends arising in the induced power curves when plotted against a descent speed scaled by the inflow induced during hover. However, this result, on the other hand, further highlights the fundamental role played by the inherent fluid instabilities in the wake in causing the wake to breakdown long before the velocity of the free-stream equals that of the mean rotor inflow.

The effects of an accelerated trajectory that have been shown here have implications for both flight tests and numerical computations of the vortex ring state. As has been suggested, during flight tests it is not possible to approach the VRS boundary in a perfectly steady manner and hence data collected to map out the VRS boundary for the particular rotorcraft used in the test should be viewed with caution - the 'steady-state' onset boundary for that vehicle may actually be at a lower descent rate than that recorded. In numerical computations of the rotor vortex ring phenomenon it is common [7, 34] for the prescribed trajectory of the rotor into the VRS to involve acceleration as mentioned previously. If such a method is implemented, then once again, any claims regarding the onset speed of the VRS for some particular rotor/rotor-fuselage configuration cannot be taken for granted. Hence, a comparison of one numerical study with another must be conducted in the knowledge that if the descent accelerations are markedly different, then

so will be the VRS onset speeds. Also, just as importantly, the character of the ensuing wake dynamics as the rotor descends will be different, as has been shown here. Indeed, since steady rather than dynamic entry into the VRS by a helicopter is not possible (it is only possible within the realms of the laboratory or numerical experiment), the notion of a unique VRS onset speed for a particular rotor is inappropriate, generally. It is more accurate to say then, that the static VRS onset boundary represents the lowest speed at which a rotor may enter into the VRS, in the absence of other factors, such as high levels of free-stream turbulence that may precipitate the action of the flow instabilities in the wake, perhaps.

It has been shown that the time-scales associated with vortex filament re-orientation affect the breakdown of the wake and also the number of the wake's violent fluctuations a rotor will experience as it passes though the VRS envelope. But, whether or not acceleration alters the perturbation growth rates associated with the fluid's modes of instability or indeed of the general time scales of the vortex kinematics is unclear.

In Chapter 3 of this thesis, a relatively high rate of acceleration was used to fly the simulated rotor from hover to a normalised descent speed of $\bar{\mu}_z = 0.45$. It was observed that up to the point of the cessation of the acceleration, the rotor wake had not developed the characteristic VRS geometry. Just a few rotor revolutions later, however, the wake had collapsed around the rotor into the toroidal form associated with the VRS. In contrast, in another simulation, at similar descent speeds, the initiation of the thrust-settling phenomenon was shown to be a product of a wake that exhibited a nominally tubular, rather than toroidal, geometry. The fundamental difference between these two cases lies in the trajectory - in the latter instance, the unabated acceleration of the rotor postponed the wake's collapse until a higher descent rate, to when the products of the fluid instabilities had reached sufficient strength and prevalence to transmute the structure of the vorticity field.

In the opening paragraphs of this section a model to predict the onset of the VRS under accelerated flight conditions was discussed. Incorporated within the model was the time parameter $t_d$ and the disturbance growth parameter $C_d$. These terms are worthy of discussion here. The first of these, $t_d$, was initially interpreted by Ahlin and Brown [8] as being the time required for a disturbance in the wake to grow to some critical strength for it to be able to initiate the breakdown of the wake. Results that suggested that the

onset of VRS was made more gradual with increasing acceleration, however, prompted a reinterpretation by the end of their paper. In the absence of an abrupt transition to the vortex ring condition $t_d$ was redefined to be simply "the age, and hence the strength," of the disturbance that precipitates VRS. This is subtly different to the original definition, since the latter definition implies that VRS onset does not occur when the disturbance reaches some critical strength after a discrete and fixed elapsed time $t_d$. But rather, it was said to be a measure of the duration of the interaction between the critical disturbance and the rotor, and hence that the measure was continuous. Some of the results of Chapter 3 suggest that a further re-interpretation is required. Firstly, since the coupling between rotor aerodynamics and the induced velocity of the wake was removed in the study presented in that chapter, any notion of a disturbance having to influence directly the rotor loading to induce VRS must be quashed. Thus $t_d$ cannot be a measure of the period of rotor-disturbance interaction. It was suggested in Chapter 3 that vortex filament re-orientation leads to a reduction in the induced downwash local to the re-orientating filament. In some instances this may engender truncation of the wake of a degree that subsequently admits a switch in the wake kinematics from those characteristic of helical vortex flow to those associated with co-planar vortex rings. Whilst, at other times in the evolution of the wake when the descent speed is not sufficient to maintain vortex ring kinematics, the wake breakdown will be local and short lived. If the parameter $t_d$ is continuous as was suggested, the implication is that the disturbance for which $t_d$ provides temporal representation, exists within the flow for all time and, importantly, that it continues to grow indefinitely. Whilst it may be acceptable, theoretically, that a disturbance will exist within the flow for all time, it is demonstrably inadmissible that the disturbance can grow without bound. The kinematics of the vorticity field causes the disorganisation of the wake's tubular structure, which in turn modifies the kinematics of the flow in the disorganised region. This must modify or even suppress the growth of the strength of a perturbation - the de-coherence of the wake modifies the stability characteristics of the flow. So, if $t_d$ is a continuous parameter, the foregoing argument raises the question of when in the descent does the timing of the disturbance growth commence.

The non-linearity of the disturbance growth rate, mentioned above, suggests that a modification to the form of the growth rate parameter, $C_d$, is also required. To recap, $C_d$ was defined as the rate at which the critical disturbance grew in spatial extent within the

flow, and the rate of growth was related to the the instantaneous rotor thrust. This is consistent with the findings of Widnall [5], and Bhagwat and Leishman [6], that the growth rate of a small, linear perturbation to the flow is dependent upon the strength of the vortex filaments in the wake. Widnall, and Bhagwat and Leishman also showed, though, that the aforementioned growth rate was *non-linearly* dependent upon the separation distance between the filaments - this property was not accounted for in the model. It is not clear how this non-linear relationship changes as the perturbations to the wake's geometry become very large, but, as it stands, the linear relationship with wake strength that was assumed in the derivation of $C_d$ will lead to erroneous predictions, though it is difficult to say without further quantitative knowledge of the kinematics of these growth modes whether the current form of $C_d$ will lead to an under or an over prediction of the VRS onset speed.

Finally, it is worth noting that in most VRS onset prediction models the transport velocity of a critical disturbance as in Newman *et al.'s* model, or of the wake itself as in Wolkovitch's model [29], is set equal to the relative mean flow velocity, i.e. $\lambda_i - \mu_z$. This assumption appears at odds with the observations made in Chapter 3, and with the mean velocity field image of Fig. 4.4 that shows a non-uniform span-wise and vertical velocity distribution throughout the wake. Indeed, it appears that the critical disturbance, whatever form it may have, travels most probably with the tip vortices from the rotor, and thus its convection speed is more closely correlated with the helical tip-vortex which it is distorting. This velocity is dependent upon the geometry of the rotor blades, and thus the distribution of the rotor inflow, as well as the rotor's operating condition and descent speed. Importantly, the transport velocity is also dependent upon the distance between the disturbance and its source, since as was suggested earlier, the speed of vortex filament transport, in the direction of the rotor axis, is not constant. The commonly assigned transport velocity is, therefore, too simplistic through being based upon the rotor inflow velocity, $\lambda_i$, which is not globally applicable to the convection speed of a tip-vortex filament and thus a disturbance within the rotor flow.

## 4.6 Summary

An examination of some of the effects that global and local wake kinematics have on both the velocity field that surrounds a descending rotor and on the near-blade aerodynamic environment has been presented.

It was demonstrated that the re-orientation of vortex filaments in the far wake of a hovering rotor lead to the truncation of the instantaneous and mean vorticity fields. As a consequence, the ability of the wake to produce downwash was shown to reduce with distance from the rotor. Importantly, it was shown that because the mean wake of a hovering rotor has a truncated tubular geometry, rather than being a semi-infinite tube as assumed in the momentum theory for rotor flows, it induces a vertically oriented, recirculating flow such that the topology of the velocity field resembles a toroid elongated parallel with its vertical axis. The important implication of this result is that the topology of the velocity field induced by the wake when in the VRS is the same as that induced by the hover condition - a finding that is contrary to the received wisdom on this matter [13]. Indeed, the toroidal topology of the velocity field of a rotor was shown to persist for a range of axial flights, from hover to a descent speed just below that which induces the windmill brake state. Additionally, a suggestion was made, supported by demonstration, that the velocity field only deviates from the toroidal topology, to form a cylindrical topology, at high descent and ascent speeds.

The discussion on the effects of wake kinematics on the velocity field of a rotor was extended with an examination of how the global geometric state of a rotor wake influences the performance of the rotor as well as the velocity field. The vortex toroid associated with the VRS was shown to produce an increase in the rotor torque and inflow above that which arises in hover or in the WBS. It was also demonstrated how large-scale shedding of vorticity from the vortex toroid of the VRS may result in a sharp decrease in the induced rotor inflow. A decrease in the large thrust fluctuations that arises when a rotor operates within the VRS was shown to arise when the vortex toroid is convected above the rotor plane by the free-stream flow. In addition, the auto-rotation condition was shown to occur once the rotor wake had formed a short vortex tube of approximately one rotor radius in height above the rotor plane. An examination of the associated velocity fields revealed that up-flow across the rotor plane in the vicinity of the blade roots that has been measured in experiments of a descending rotor [13, 68] was shown to be strongly correlated

with the geometry and position of the root-vortex system. An in depth assessment of the correlation between rotor wake geometry, its associated velocity field and the corresponding rotor performance has seldom been reported, but one of the main contributions of this section lies in its demonstration of how at least some of the aspects of the behaviour of an idealised, simplified rotor system are also applicable to the behaviour of a more complete representation of a real rotor system. For instance, the 'leap-frogging' process that was shown to occur in the simplified system was also evident in the simulation of a more comprehensively modelled, thus more realistic, rotor system.

An effect on the rotor thrust induced by a particular wake geometry, namely the thrust-settling phenomenon, was investigated in detail. It was shown that thrust-settling commences prior to the complete breakdown of the wake into the vortex toroid associated with the VRS, i.e. when the wake of the rotor is still essentially tubular. This finding is, again, contrary to previously held ideas on this subject [12]. The eventual collapse of the wake into a toroidal form only serves to exacerbate the reduction in the rotor thrust as it operates within the thrust-settling regime, whilst cessation of this regime commences as the vortex toroid is elongated and convected, mostly, above the rotor plane by the free-stream flow. An inspection of the on-blade aerodynamics revealed that the loss of thrust was restricted to the outer sections of the blade, only, as Azuma and Obata had also observed in their experiments [12]. In addition, however, it was shown that the settling-with-power phenomenon that arises when the rotor thrust is controlled to be nominally constant could be attributed to a similar loss of lift on the outboard sections of the blades. The thrust levels are maintained by an associated increase in the lift generated over the inboard sections of the rotor, which is achieved, of course, by an increase in the collective pitch. An assessment of the global geometry and strength of the wake that arises simultaneously with the thrust-settling regime showed that thrust settling must be initiated by the compression and thus intensification, and slight outward motion of the tip vortex system.

Simulations of a rotor undergoing different rates of linearly accelerated axial descent demonstrated that VRS onset and its subsequent cessation are postponed to higher descent speeds as the acceleration rate is increased. It was shown that, since the acceleration reduced the time that the rotor spent within the VRS regime, and since the truncation of the wake by vortex re-orientation takes some finite time to occur, the influence the wake

has on the rotor dynamics is significantly moderated. Examination of the ratio $\overline{(\omega_z/|\omega|)^2}$, which is the mean contribution made to the total vorticity in the wake by the vertically aligned vorticity, revealed that, in terms of descent speed, acceleration delays the growth of vertically aligned vorticity in the wake. That is, acceleration suppresses the action of the fluid instabilities in the wake and hence allows the wake to sustain its tubular structure at higher descent speeds. The final conclusion made on the basis of the results presented in that last section was that a successful VRS onset prediction model must account for the *non-linear* growth of the disturbances in the wake that engender wake breakdown and must also include a description for the transport velocity of the disturbances in the wake that allows for the variation, with vertical position, of the velocity of the flow over the entire length of the wake.

# Chapter 5

# Influence of Geometric Blade-Twist and Blade Stall on the Behaviour of the VRS

## 5.1 Introduction

The ideal rotor, in hover, would exhibit a uniform distribution of induced downwash over the blades such that the power lost by induced drag would be the minimum that was theoretically possible. According to momentum theory [17] such a distribution of inflow arises when the rotor blades incorporate the ideal distribution of geometric angle of attack, whereby, from the rotor hub, the pitch angle, $\theta(r)$, of the blade reduces along the blade span according to $\theta(r) = -\theta_{tip}/r$ (where $r = 0$ to $r = R$). In addition, it was found experimentally in the late 1940s that negative twist, $\theta_{tw}$, along the blade span could improve the performance of a rotor in forward flight. This was achieved through the partial amelioration of the profile drag incurred from blade stall on the retreating side of a rotor traveling at high advance ratios [74]. Perhaps as a consequence of these performance enhancing effects, the general trend emerging from the history of helicopter rotor design is one of an incorporation of some level of negative blade twist. Typically, however, blade designs have included only moderate levels of geometric twist, with a twist rate of around $-8°$ being typical, since at high advance ratios, large rates of twist ($\theta_{tw} < -15°$) have been found to reduce the efficiency of the rotor on the advancing side of the disc [17].

Accompanying the design trend of incorporating only moderate blade twist, there was an historical tendency to operate rotors at low levels of loading. In other words, in order to minimise mechanical stresses and the aerodynamic consequences of stalling of the blades, the ratio of integrated lift force to blade area was kept low in the past. Since the Figure of Merit, a measure of efficiency of the rotor, is proportional to $1/\sqrt{A}$, where A is the rotor-disc area, this means that a decrease in disc area increases the efficiency of the rotor due to an accompanying decrease in the viscous drag of the blades [17], though stall becomes the limiting factor as disc-loading increases. Hence, with advances in materials and aerofoil maximum lift coefficients, the more recent trend in rotor design has been toward highly loaded rotors.

As one would expect, such rotor design practices have been reflected in much of the laboratory work conducted to investigate the behaviour of a rotor when flying in the vortex ring condition. Between the years 1926 to 1999 ten individual experiments, from eight studies, using twisted blades have been reported [10, 11, 12, 16, 22, 23, 26, 75]. Of those ten rotors, eight had a twist level within the range $-5.5° \leq \theta_{tw} \leq -12°$. The other two rotors, tested by Yaggy and Mort [10] in 1962, had blades with considerably higher rates of twist of $-22.4°$ and $-46.6°$. The latter rotor was in fact a rigid propeller and so its geometry was quite different to other helicopter rotors of the time. The reason behind Yaggy's and Mort's investigation of the behaviour of far more highly twisted blades than had been tested before was not provided in Yaggy's and Mort's paper, though the test was likely aimed at tilt-rotor applications such as the Bell XV-3. Besides the aforementioned tests, other VRS experiments were conducted in the laboratory, during the aforementioned period, using rotors with untwisted blades [11, 12, 16, 76].

The rotor disc loading coefficient, $C_B$, where $C_B = C_T/\sigma$ and $\sigma$ is the non-dimensional rotor solidity, or rather, the ratio between blade area and rotor-disc area, provides an indication of the integrated lift forces on the rotor blades. Castles and Gray [11], Washizu [22, 23] and Azuma and Obata [12] have generally limited the maximum loading coefficient produced by their rotors when in hover to around $C_B = 0.1$. In contrast, Yaggy and Mort [10] conducted tests with their flapping rotor and rigid propeller generating relatively high blade loadings of $C_B = 0.55$ and $C_B = 1.4$ respectively. In the other cases of experiments investigating the effects of blade loading it is difficult to ascertain the value of $C_B$ that was used since it is either not stated explicitly or the absolute thrust

levels achieved during the tests are not quoted, though the normalised thrust coefficients ($C_T/C_{T_h}$) are usually available. Indeed, from all of these tests it is not possible to extract a coherent view of the effect that blade loading has on the behaviour of a rotor and its wake in descending flight. This is due either to missing data, or just a lack of consistency from one experiment to another. As a result it is not possible to ascertain how either of the two parameters in the expression for the blade loading coefficient, i.e. the thrust coefficient and the rotor solidity, influence VRS behaviour individually.

More recently, the trends in rotor design, with respect to blade twist and blade loading, have changed towards the use of much larger twist rates and blade loadings as materials and aerodynamic technologies have improved and, importantly, as operational requirements have changed. The Bell-Boeing Osprey V-22, developed for the US Marines over the last decade or so, is a tilt-rotor type rotorcraft conceived to meet the military's demands for faster transport of personnel or heavy loads into and out of environments unreachable by conventional helicopters or fixed wing aircraft. Such criteria led to the design of the V-22's rotors to feature blades with a non-linear (more akin to the $-\theta_{tip}/r$ type relationship of ideal rotor theory), negative twist rate of $\theta_{tw} \approx -41°$ and where the rotors were designed to operate when generating a thrust coefficient of around $C_T \approx 0.016$ which produced a disc loading of $C_B \approx 0.3$. This value is significantly higher than that associated with traditionally designed helicopter rotors. Such high levels of blade twist can be incorporated into the design of tilt-rotor aircraft as a means of optimizing their efficiency since the on-coming free-stream flow is most often roughly parallel to the rotor axis, and hence the inefficiencies that arise normally on the advancing side of a rotor rarely manifest.

In their VRS test on a tandem rotor configuration (rotors in fore/aft configuration), Washizu *et al.* [23] suggested that the speed range over which their model experienced VRS type flow behaviour was slightly larger than for their single rotor when tested under similar conditions [22]. In addition there was also some evidence in the literature that blade twist increased the severity of the thrust fluctuations encountered by a rotor operating in the VRS [11]. So, when, during flight tests, a V-22 experienced a crash that was later attributed to the rotorcraft having suffered from an encounter with the VRS [4], concerns were raised over the possible increased susceptibility of its highly twisted rotors to an encounter with the VRS, despite the evidence for such susceptibility being, in fact, somewhat scant or unsubstantiated.

In response to the heightened interest in VRS that the V-22 incident aroused, recent VRS research has featured studies of blades with high levels of twist. Betzina [24] used a model rotor with a non-linear twist rate of $-41°$, and relatively high thrust levels ($C_T \approx 0.014$, and $C_B \approx 0.12$) similar to those produced by tiltrotor aircraft. The experimental rig also incorporated a V-22 style wing beneath the rotor to replicate the tiltrotor configuration. Studies were conducted with the rotor in isolation, with the wing, and with the wing and an image plane parallel to the rotor axis to replicate the effects of the second tiltrotor on the opposite wing. The results of normalised inflow versus descent rate appear not to be markedly dissimilar to those of Castle and Gray [11] or Washizu [22], in terms of peak inflow and the descent rate coincident with the peak inflow. In addition to Betzina's experimental work, several numerical studies that investigated, among other things, the effects of blade twist, have also been published recently, by Leishman *et al.* [30, 77], Brown and Leishman *et al.* [34] and Ahlin and Brown [36].

As will be discussed in some detail in the following section, despite the numerous recent numerical studies on the effects of blade twist, and, in some ways, because of the somewhat vague and inconsistent nature of the experimental evidence, there is still much to discover about how varying blade twist and thrust levels, influence the rotor performance and associated wake dynamics when a rotor operates near to or within the vortex ring condition. In response to this lack of understanding, this chapter presents a study of the aerodynamic behaviour of three rotors differing only in the rates of twist of their blades. Connected to the issue of blade-twist effects is the issue of the influence of blade stall on the behaviour of a rotor in the VRS. It has been suggested by Brown and Leishman *et al.* [34] and Ahlin and Brown [36] that blade stall may play an important part in the performance of the rotor and the dynamics of the wake during an encounter with the vortex ring condition. A study offering further illumination of the effects of stall is included herein.

## 5.2 Blade Twist Effects on Rotor Aerodynamics in the VRS

Of the experimental work mentioned in the introduction to this chapter, only the works of Castles and Gray [11], Azuma and Obata [12] and Gao [16] allow a rigorously valid comparison between rotors of differently twisted blades that were otherwise of the same

geometry and operated under the same loading conditions. The rotors used in the experiments of Yaggy and Mort were too dissimilar to isolate any dependency in the results on blade twist [10]. Castles and Gray compared the performance of two three-bladed rigid rotors both exhibiting a rectangular planform and a solidity of $\sigma = 0.05$. The tests were conducted in a wind tunnel unlike the tests conducted by Azuma and Obata and by Gao. The blades of one of the rotors used by Castles and Gray was untwisted, whilst the other had a linear twist of $-12°$. From tests in which the mean thrust of the rotor was held constant, they found that the rotor with twisted blades produced the highest mean inflow velocity during the descent of the two rotors, and furthermore, that this peak value occurred at a higher descent speed than did the peak inflow generated by the untwisted rotor. The rotor with twisted blades also exhibited a higher auto-rotation speed than the rotor with untwisted blades. It was shown in Chapter 4 of this thesis that auto-rotation occurs once the rotor wake has convected above the rotor plane and shows signs of having moved from the VRS into the turbulent wake state. The implication, therefore, of the result reported by Castles and Gray is that the VRS extends to higher descent rates when the rotor blades are twisted. The twisted blades also generated significantly larger fluctuations of thrust and torque than the untwisted blades. In the experiment conducted by Azuma and Obata [12], two three-bladed rotors were tested. Both rotors incorporated flapping and lagging hinges, had a solidity of 0.0573, and a rectangular planform. The rotors, in turn, were mounted to a carriage which was towed along a track to generate the relative free-stream flow. One of the rotors was untwisted whilst the other had a linear twist rate of $-8°$. The collective pitch of the rotors was held constant for each pass through a set of discrete descent speeds that took the rotor from hover to the auto-rotative state. Although two rotors featured in the tests, little comparison between them was reported. However, it was noted that the rotor with *untwisted* blades induced the greatest fluctuations in torque of the two rotors tested, which was contrary to the findings of Castles and Gray described earlier. Gao [16] tested three different rotors. Unfortunately, only two of them were geometrically similar, aside from their respective blade twist rates, and thus only these two can be fairly compared in the context of this discussion. The two rotors were of the two-bladed teetering type. Their blades possessed a rectangular planform and the rotors had a solidity of 0.077. The blades of one of the rotors had a linear twist rate of $-5.5°$ whilst the blades of the second rotor were linearly twisted by $-9.2°$ from hub to

tip. The rotors were mounted to a whirling arm to generate the relative free-stream flow and the collective pitch was held constant throughout each test. The blades of each rotor were fixed at the same collective pitch, which was then held constant as the descent speed was varied. It was noted that, post the VRS phase, the torque generated by the rotor with the most highly twisted blade rose at a greater rate with change in descent speed than that of the other rotor, whilst the thrust of the former rotor was generally found to be the highest of the two cases over most of the rotor trajectory. Interestingly, the rotor with the most highly twisted blades generated the greatest fluctuations in rotor torque, which was contrary to the findings of Azuma and Obata [12] though such contradiction seems quite common in the VRS field. There was little difference between the magnitude of the thrust fluctuations experienced by the two rotors however and there appeared to be agreement in the speeds at which sudden changes in the mean thrust and torque occurred, suggesting that the VRS onset and cessation speeds experienced by these two rotors was the same. Note that few consistent trends have emerged from preceding review on the effects of blade twist and this is indicative of the complexity of the system being examined and the problems associated with a lack of consistency in the experimental set ups that have been adopted throughout the last eighty years or so.

In their numerical investigation into the effects of blade twist, Brown and Leishman *et al.* [34] used the Vorticity Transport Model of Brown [28] and the Free Vortex Model (FVM) of Leishman [6], to model two three-bladed articulated rotors that were geometrically identical, save that one had blades twisted linearly by $-8°$ from hub to blade tip and the other rotor possessed blades twisted linearly by $-35°$. The former rotor shared the same twist rate as the rotor tested by Azuma and Obata [12] and the latter rotor shared its rate of twist with the V-22 tilt-rotor, though the twist is non-linear in the tilt-rotor's case. The thrust was held nominally constant during the simulations at $C_T = 0.0036$, the same maximum value used, once again, by Azuma and Obata. In the simulations of Brown and Leishman *et al.*, the rotor had a varying component of forward speed in its trajectory, as well as a descent component, such that its glide slope was maintained at a constant $-65°$ since this was said to represent a realistic flight trajectory. Note that the rotors used by Castles and Gray and also Azuma and Obata were also subjected to angled flight paths, as well as to simple axial descents. Brown *et al.* noted that the rotor with the more highly twisted blades experienced the sudden occurrence of large thrust fluctuations, due to the

onset of VRS, at a higher descent rate (at $\bar{\mu}_z = 0.6$) than the other rotor ($\bar{\mu}_z = 0.4$). In addition, the large fluctuations caused by the VRS condition persisted to slightly higher descent speeds prior to the rotor entering the WBS than was the case for the rotor with the least twisted blades. In neither case was any reason for such behaviour given. In addition, a presentation of the variation of induced torque, $C_Q$, behaviour with descent rate was made. The VTM computations suggested that the descent speed at which $C_Q$ changed from positive to negative (the auto-rotation condition) occurred at somewhat lower descent rates for the rotor with more moderately twisted blades. This behavioural trend was in agreement with the experimental findings of Castles and Gray [11]. The results from the calculations conducted using the FVM suggested that the opposite behaviour should arise, however. It was thought likely by the authors, though, that this particular phenomenon, so highly dependent as it is upon blade loading distribution, would not have been modelled successfully by the FVM since the model trails vorticity only from the blade tips and thus cannot give a proper account of the vorticity distribution, and hence blade loading, near the inboard sections of each blade. It could be argued, therefore, that the FVM and other similar free-vortex methods are not appropriate tools with which to conduct comparative studies on what are essentially the effects of inflow distribution. In addition, Brown and Leishman *et al.* also found, contrary to experimental observations, that the results from the simulations of both models suggested that blade twist has little influence on the amplitude of the thrust fluctuations experienced by the rotors as they passed through the VRS regime.

The reasons behind the differences in behaviour of the two rotors that were observed by Brown and Leishman *et al.* were not researched in depth - a deficiency that the present study will rectify. In an accompanying section in their paper, however, they presented a linear stability analysis of the stability of rotor wakes. It was shown that the growth rate of small perturbations in the tip-vortex system of a hovering rotor increases with the rate of negative blade twist. The implication of this is that twist should decrease the VRS onset speed. The present study shall show that this result is misleading, however. The growth rates that were presented were scaled with the strengths of the rotor-tip vortices, (the strength reduces as twist increases), and hence it was deduced that the increase in growth rate was a result of the decreased spacing between tip vortices that arises because of the reduction in the tip vortex transport velocity.

At the 31st European Rotorcraft Forum, Ahlin and Brown [36] presented a paper that included work on the effects of blade twist on the behaviour of a rotor in VRS. The VTM of Brown and Line [35] was used to simulate three of the two-bladed teetering rotors used by Gao [16]. The blade twist rates examined in the investigation were: 0°, −5.5° and −9.2°. The rotors were flown axially; the trajectory started in hover and ended at a descent speed sufficient to put the rotors into the WBS. The descent speed was increased slowly and continuously at a rate of $\dot{\bar{\mu}}_z = -0.0035$/rev. Throughout the trajectory the collective pitch of the blades of each rotor was held constant. The thrust generated by each rotor when in hover was $C_T = 0.0074$ (producing a blade loading of $C_T/\sigma = 0.097$). Save for the blade twist, the three rotors were identical, unlike in Gao's experiments. The results of Ahlin and Brown showed that there was no significant difference in the descent speeds at which both the thrust-settling regime and the onset of significant thrust fluctuations were encountered by the three rotors. Gao also observed these two trends. However, it was noteworthy that there seemed to be a reasonably significant influence of twist on the breadth of the thrust settling regime. The rotor with untwisted blades appeared to recover the thrust level achieved prior to thrust-settling at a lower descent rate than the other two rotors, the last rotor to recover being the one with the most highly twisted blades. It was also shown that the amplitude of the peak thrust fluctuation was marginally higher in the case of the rotor with untwisted blades, and that the rotor with the most highly twisted blades experienced its peak thrust fluctuation at somewhat higher descent rates than the other two rotors. It was pointed out, though, that the effects were rather subtle, as in Gao's tests, such that it was debatable whether the differences in behaviour between the rotors would be operationally significant. Also presented in their paper was the sectional blade loading behaviour, $C_B(r)$, of the three rotors. The data was plotted against normalised descent speed, $\bar{\mu}_z$. The blade loading was normalised by $C_T/\sigma$, i.e. the mean blade loading coefficient, to allow any spanwise redistribution in blade loading with descent rate to be visualised more clearly. The earlier thrust recovery of the rotor with untwisted blades was associated with a much more rapid increase of the blade loading in the region around $0.7R$ out from the rotor hub, than in the other two cases. Interestingly, unlike in the region around $0.7R$, at the other blade locations presented, at $0.2R$ and $0.9R$, the three rotors exhibited qualitatively similar behaviourial trends for blade loading.

In an attempt to correlate the blade loading behaviour with the kinematics of the wake,

the magnitude of the vorticity in a volume immediately above the rotor was integrated and compared with the integral of the magnitude of the vorticity in a region of equal volume immediately below the rotor (in a similar manner to that presented in § 4.4). This analysis showed the relative division of wake intensity between the flow above and below the rotors and illustrated quite clearly that, in the case of the rotor with untwisted blades, the wake moved more suddenly from below to above the rotor - this effect arose at a descent speed that was closely correlated to the cessation of the thrust-settling regime for that rotor. It was not possible however to discern why this apparently blade-twist dependent behaviour should manifest, though. But, it was postulated that the small differences in blade loading, and hence inflow distribution along the blades, could yield a subtly different trajectory of the toroidal VRS flow as it moves from below the rotor to above. It was concluded, finally, that at least for moderately twisted blades, the influence of twist on the behaviour of the rotor, both in terms of its mean thrust performance and in terms of the levels of unsteady loading generated by the system when in the VRS, is relatively minor, as can be gleaned from the results of Gao, also. Whilst this conclusion should provide some confidence to the designers of conventional rotorcraft, the trend in modern rotor designs is to use somewhat higher levels of blade twist than those analysed by Ahlin and Brown and the majority of those rotors that have been tested experimentally. The following study was motivated by this modern design trend.

### 5.2.1 Aims of The Investigation

The foregoing review has highlighted that there is a general lack of understanding of how varying the twist geometry of a rotor blade influences the rotor's behaviour within the VRS. Trends related to the effects of blade twist on the thrust behaviour and inflow generation of rotors in descending flight have been shown by several workers, though some of the experimental results are contradictory. The aim of the following work is to follow on from the findings of Ahlin and Brown, just described, by investigating the effect that high blade twist has on the behaviour of rotors and their wakes when they operate within the VRS. Due to the current fashion within the helicopter industry to install rotors with highly twisted blades ($\theta_{tw} < -15°$) on their rotorcraft, any additional understanding gained from this work would be particularly useful. By careful examination of both the rotor-blade aerodynamics and the rotor wake behaviour the goal is to obtain an in-depth

| | |
|---|---|
| Blade number, $N$ | 2 |
| Rotor solidity, $\sigma$ | 0.077 |
| Blade twist, $\theta_{tw}$ | $-15°$; $-25°$; $-35°$ (linear) |
| blade chord, $c$ | $0.12R$ (constant) |
| root-cut-out | $0.2R$ |
| Constant thrust | 0.00724 |

***Table 5.1:*** *Rotor definition.*

comprehension of the physics at work which could then be used to inform future rotor design.

### 5.2.2 Description of the Numerical Experiment

The VTM of Brown and Line [35] was used to conduct three simulations of a rotor, as defined in table 5.1. The blade twist rate was different in each simulation, thus the three twist rates examined in this study are also defined in the table. The flight trajectory of each rotor comprised an initial period in hover lasting 40 rotor revolutions, which was sufficient to allow any transient effects from the start-up of the rotor to be convected into the far field thus allowing the rotor to start its descent in an initially 'quasi'-steady near field. The hover period was followed by a descent with linearly increasing speed through the VRS to the WBS. The descent acceleration was $\dot{\mu}_z = -0.007$/rev. The flap and lag dynamics of the rotors were suppressed, effectively making the rotors rigid, to remove the aerodynamic fluctuations and unsteadiness in the wake that such motions induce. This simplification had the added benefit of reducing the computational time required by the simulations. 20 collocation points set along the blades in a cosine distribution were used to resolve the blade aerodynamics, and the size of the computational cells on the finest grid level was $0.05R$ - an intermediate to low level of computational resolution. This level of resolution was deemed adequate for the reasons offered in Chapter 2 of this thesis.

Importantly, the aerodynamic blade-stall model was removed such that the lift-curve slope of the blades varied as predicted by a classical lifting line model of a finite aspect ratio wing. This simplification of the fluid dynamics was made in order to remove a very complex, though probably secondary, non-linear aspect of the physics from the calculation in the hope of exposing the fundamental differences that arise in the fluid dynamics

engendered by the geometrical differences of the rotors. The important influence of stall is considered separately later on in this chapter.

### 5.2.3 Results

The geometric twist of the blades of a rotor has a significant influence on the distribution of the strength of the vorticity trailed from the blades, and hence on the magnitude and distribution of the velocity of the induced downwash along the blades. These parameters are non-linearly coupled, of course. Figures 5.1 and 5.2 show the mean spanwise distribution of these parameters, along the length of one of the rotor blades when the rotor was in a 'steady' hover condition. The absolute values of the sectional induced downwash velocities were normalised by the mean value occurring over the disc: the momentum theory result for mean inflow velocity at hover, or $\sqrt{C_{T_h}/2}$.

Of significance to the analysis to follow is the relative difference in the strength of the root and tip vortices from each of the rotors, and the difference in the strength of those vortex systems that exists between each of the rotors, as shown in Fig. 5.1. The tip vortex strength, which is one of the primary factors influencing the growth rate of perturbations in the flow [5], weakens as twist levels increase, whilst the root-vortex becomes stronger. Indeed, when the blades have twist $\theta_{tw} = -35°$, the tip vortex strength, $\omega_{tip}$, is only marginally stronger than the root vortex strength, $\omega_{root}$, or rather $\omega_{tip} \approx 1.23\omega_{root}$, compared to $\omega_{tip} \approx 3.2\omega_{root}$ when the blade twist is $\theta_{tw} = -15°$. This suggests that the root vortex system of rotors with more highly twisted blades may play a much bigger role in the dynamics of the rotor wake than those trailed from only moderately twisted blades. This has very important implications for the modelling of wakes of highly twisted rotor-blades when only the tip-vortex system is represented, as is common practice in the field of so-called 'free-wake' methods.

The other primary factor that influences the growth rate of perturbations is the spacing of the helical vortex filaments. The growth rate increases non-linearly with decrease in separation distance [6]. Since, as can be seen in Fig. 5.2, the inflow over the outer parts of the blades falls with increasingly negative blade twist, this will result in closer tip-vortex spacing. However, as has just been suggested, the root vortex system of the more highly twisted blades may have more influence on the global behaviour of the wake than when the blade twist is moderate. Thus, the increase in linear perturbation growth rate

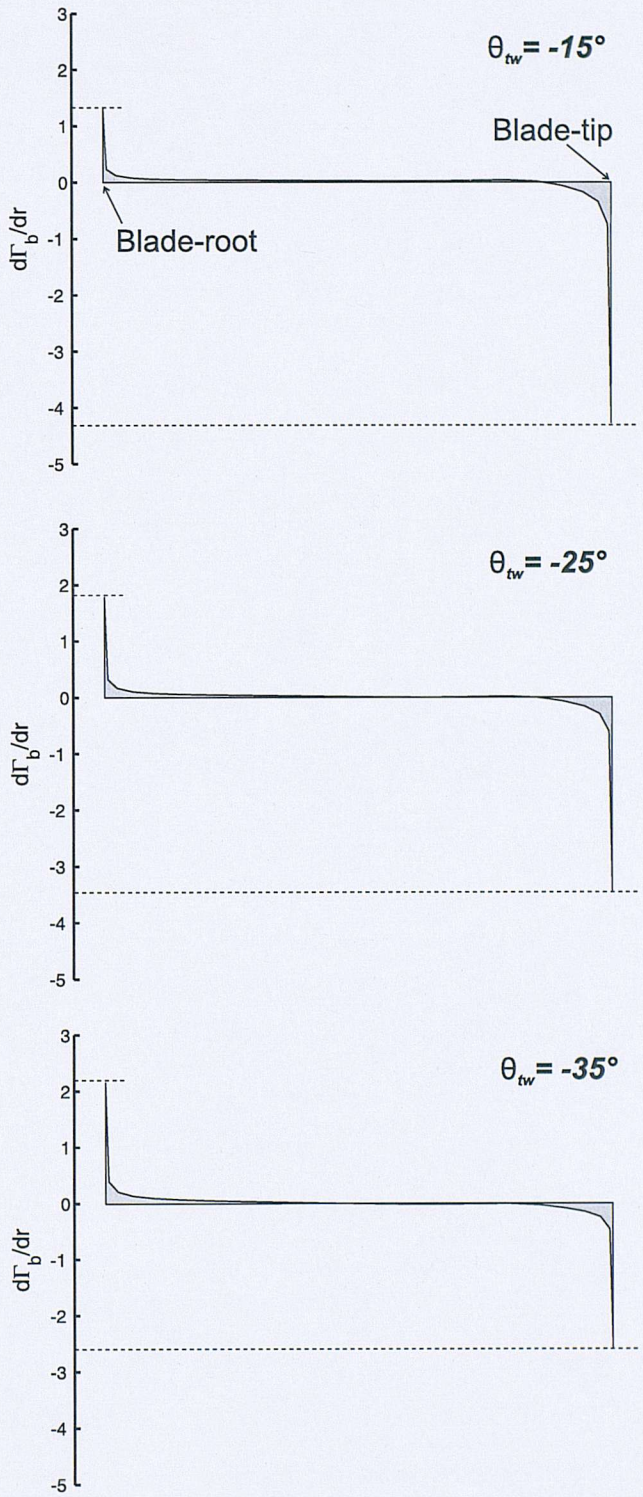



***Figure 5.1:*** *Graphs show the variation in the strength, per unit length, of the trailed vortex system caused by variation in blade twist*

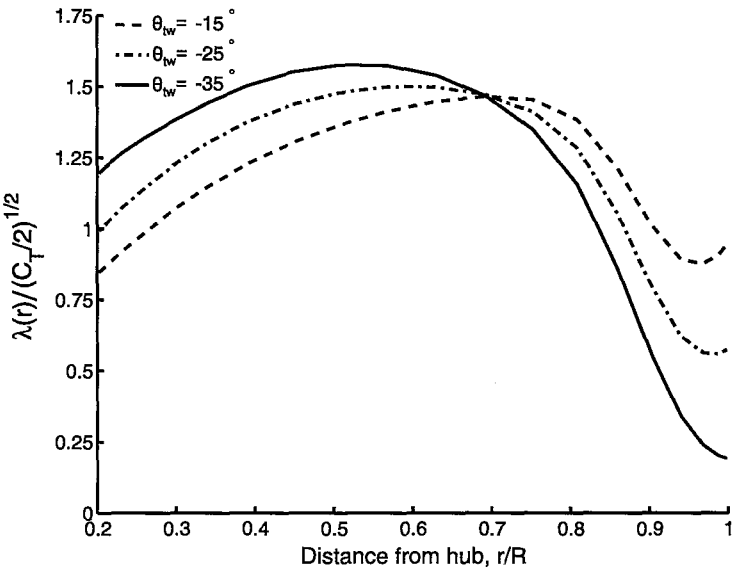



***Figure 5.2:*** *Graph shows spanwise distribution of inflow velocity on rotor blades of varying twist rates during hover.*

arising in the tip-vortex system of highly twisted blades as calculated by Leishman [30] may be of less importance, or rather, may be negated somewhat by the change in the stability characteristics of the root-vortex. It is very likely, though, that there is significant interplay between these two systems. Indeed, to achieve a better understanding of how blade-twist influences the linear stability of rotor wakes, the root-vortex system must also be accounted for in such an analysis. The consequences of omitting the root vortex system from computations will become clear later in this work. In relation to the inflow distribution, it is noteworthy that the spanwise variation of induced downwash shown in Fig. 5.2 for the most highly twisted blade appears less evenly distributed than that of its lesser twisted counterparts. This is contrary to the design intention of incorporating large negative twist. This result, though, is merely an artefact of the simple linear variation of twist assigned to the rotor blades. The optimum twist rate for a rotor blade is dependent upon thrust. On a real rotor it is common for the blade twist distribution to be non-linear such that the tip of the blade would be pitched down far less than in the linear-twist case.

The thrust histories and the standard deviation about the mean of the fluctuations of the thrust, that were generated by the three different rotors are shown in Fig. 5.3 and Fig. 5.4 respectively. To produce the thrust traces shown in the former figure, a moving averaging window with a width of one revolution was used to suppress the high frequency

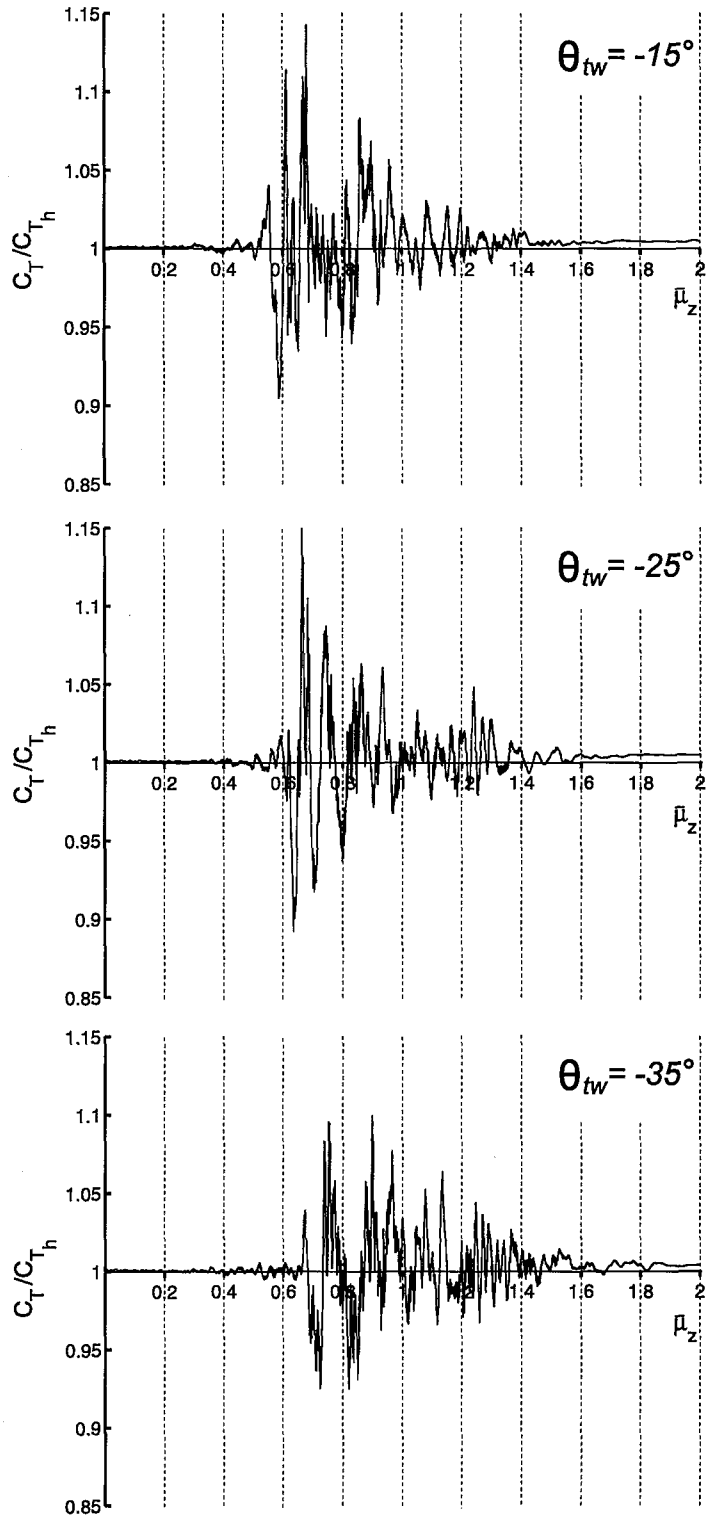



***Figure 5.3:*** *Mean thrust history of rotors descending through VRS to WBS from hover. Averaging window has width of 1 rev.*

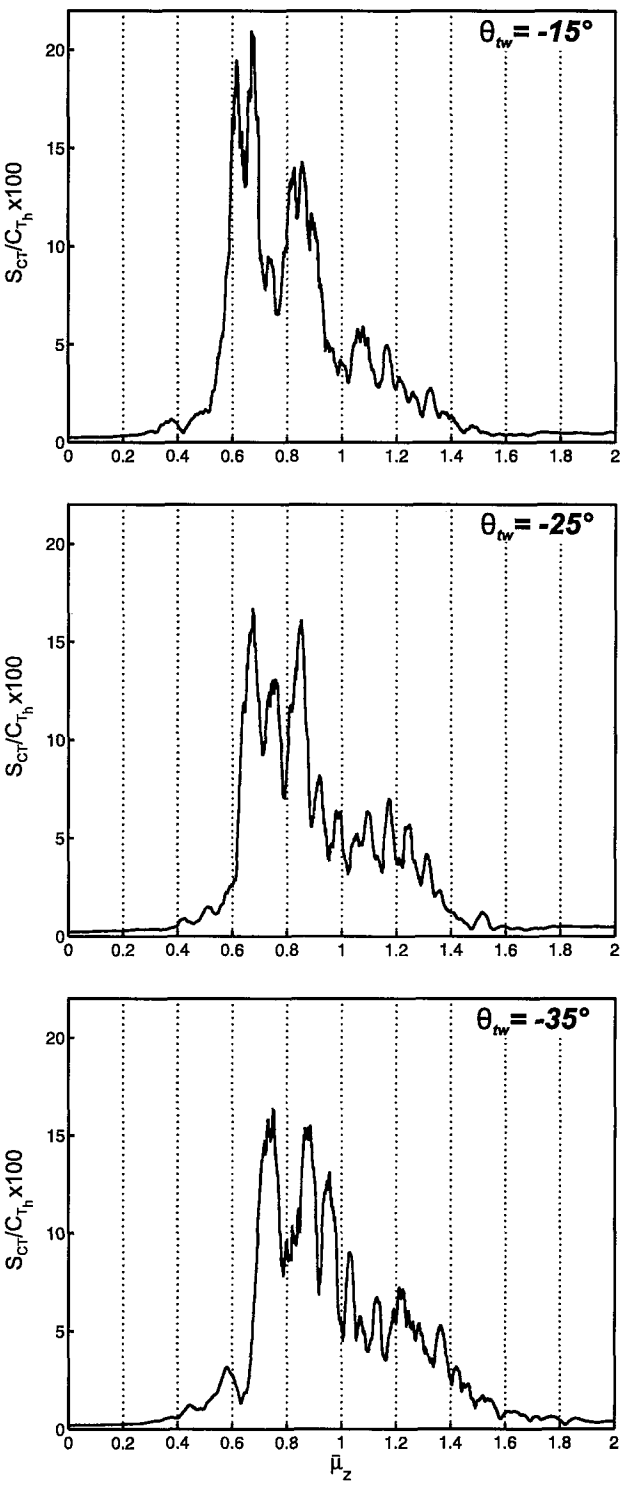



*Figure 5.4: Standard deviation about the mean, of thrust fluctuations as a percentage of the mean thrust at hover, of rotors descending through VRS to WBS from hover. Averaging window has width of 4 revs.*

$N$/rev BVI related vibrations for the reasons discussed earlier in § 2.7.2. The width of the averaging window was selected to qualitatively expose any interesting changes in the unsteady nature of the thrust production that may have occurred. In the case of the latter figure, the standard deviation of the thrust fluctuations was filtered using a moving window with a width of four revolutions. A larger filtering window was used in this case to extract the gross trends in the thrust fluctuation amplitudes arising from each simulation since filtering with the narrower window obscured the important, more slowly varying behaviour in each case. It should be noted that this larger processing window caused a slight clipping, by just a few percent, of the fluctuation levels. The general trend that arises remains unchanged, however.

Figure 5.3 shows that there is a qualitative similarity, at least, in the character of the thrust signals produced by the three rotors. The onset of large fluctuations in the thrust, however, seems to be postponed until higher descent rates by greater blade twist - a trend that this is very clearly evident in the graphs of the standard deviation of the fluctuations shown in Fig. 5.4. Similarly, the significant fluctuations in thrust persist to greater descent rates with increase in twist rate. Note that, a 'significant' fluctuation amplitude is taken to be that which is greater than the amplitude of the thrust fluctuation that arises when the rotors are in the WBS, i.e. when $\bar{\mu}_z = 2$. The peak amplitude of the fluctuations is largest in the case of the rotor with $-15°$ of twist, though the peak amplitudes of the standard deviations of the other two rotors are similar. It is difficult to ascertain the nature of the twist related effect on the severity of the thrust fluctuations, therefore.

The gross geometry of the wake of a rotor descending with nominally constant thrust can be inferred approximately from the behaviour of the rotor torque, $C_Q$, as can the speed at which the maximum inflow through the rotor arises. The speed at which the auto-rotative state occurs can be determined directly, of course. Figure 5.5 presents a comparison of the mean total torque, versus descent rate, of the three rotors. The profile torque component has been removed from the torque data presented herein. The total torque, therefore, is the induced torque plus the component of torque arising from the axial translation of the rotor, given by $\mu_z C_T$, which is negative in descending flight. From hereon, the total torque will be referred to only as the 'torque' and designated as $C_Q$.

As with the thrust, the mean of the induced torque was calculated via a moving averaging window with a period of one revolution. In the figure, the torque, $C_Q$, has

been scaled by the induced torque generated at hover, $C_{Q_h}$. As was inferred in § 4.4 the settling-with-power phenomenon is quickly followed by the collapse of the wake into the toroidal structure of the VRS, and, as was shown in § 4.3, the collapse of the wake is closely correlated with the first appearance of large peaks in the torque $C_Q$ of the rotor. The results shown in Fig 5.5 suggest, therefore, that settling-with-power and the ensuing collapse of the wake occurs at higher descent speeds with increased blade twist. In addition, since the disc inflow is closely related to the torque, the trends displayed appear to be in qualitative agreement with the observations of Castles and Gray [11] - increasing the amount of twist causes the peak inflow that arises during descent to occur at higher descent rates. When the rotors enter into ideal auto-rotation (i.e. when $C_Q = 0$) there is still a significant level of unsteadiness apparent in the inflow, as implied by the fluctuating torque within this region on each of the curves. It is clear, though, that the rotor with the most highly twisted blades entered auto-rotation at the highest descent speed, whilst the torque of the rotor with the least twisted blades became steady at a lower descent rate than occurred in the other two cases. In conclusion then, the results suggest that the cessation of the VRS and entry into the auto-rotative condition is postponed to higher descent rates with increasing blade twist. The reasons for this will be discussed later in this section.

It remains to examine the flow field and blade aerodynamics in more detail in order to expose the flow physics behind the observed gross behaviours of the rotors. Figure 5.6 compares the geometry of the locus of the vorticity fields and a two-dimensional, vertical slice through the rotor hub of the root-mean-square (RMS) of the fluctuations of the vorticity fields produced by the three simulated rotors during the normalised descent speed range of $0.2 \leq \bar{\mu}_z \leq 0.3$. These plots were calculated from 14 snap-shots of the wake from the 14 contiguous rotor revolutions that corresponded to the aforementioned speed interval. The locus plots were calculated by the method described in § 2.7.2, and the plots of the RMS of the vorticity fields were calculated in a similar manner, only the RMS rather than the average of the 14 snap-shots was computed, of course.

The portion (where $x > 0$) of the foreground of the three-dimensional locus plots of the vorticity field has been removed in each case so that the inner structure of the wake can be exposed. It will be shown later that the internal structure of the wake plays an important role in the global dynamics of the vortical wake. In addition, to provide an

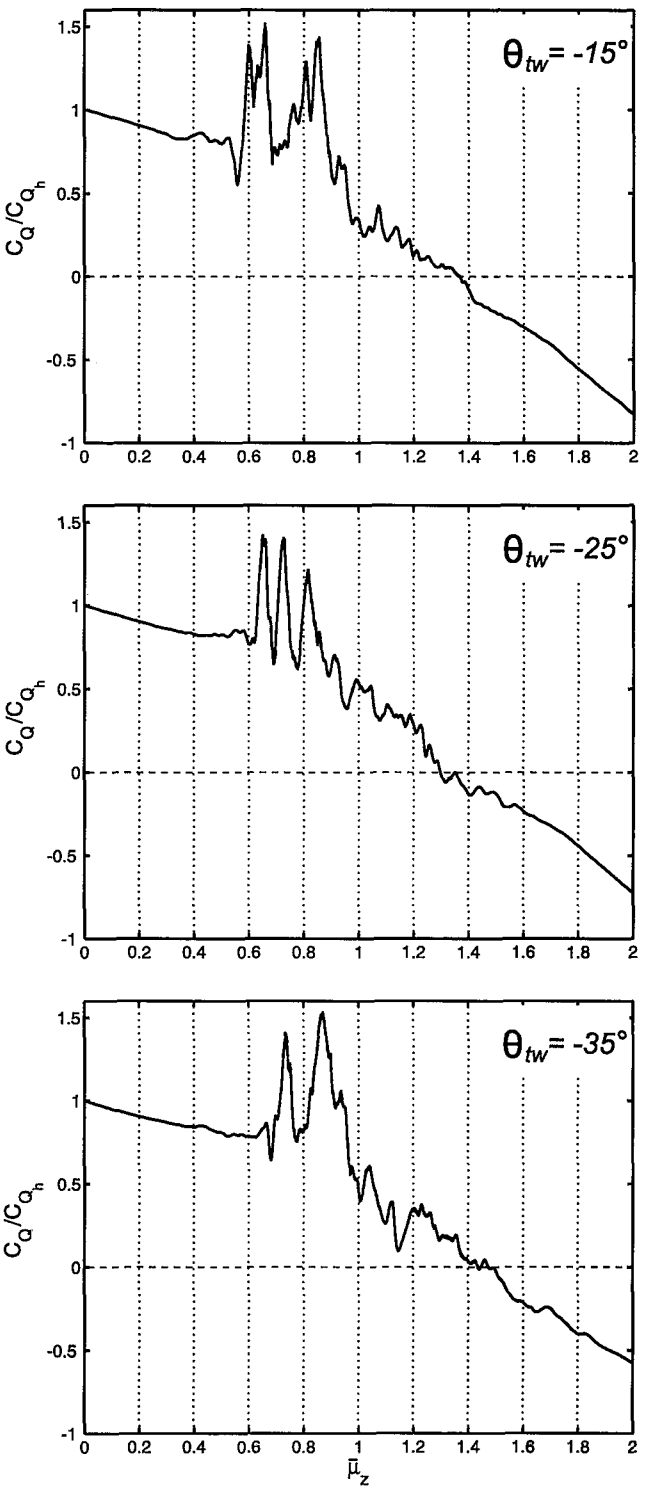



***Figure 5.5:*** *Normalised total torque, $(C_Q - C_{Q_p})/C_{Q_h}$, versus $\bar{\mu}_z$ for three rotors each with different blade twist to the other. Width of averaging window is 1 rev.*

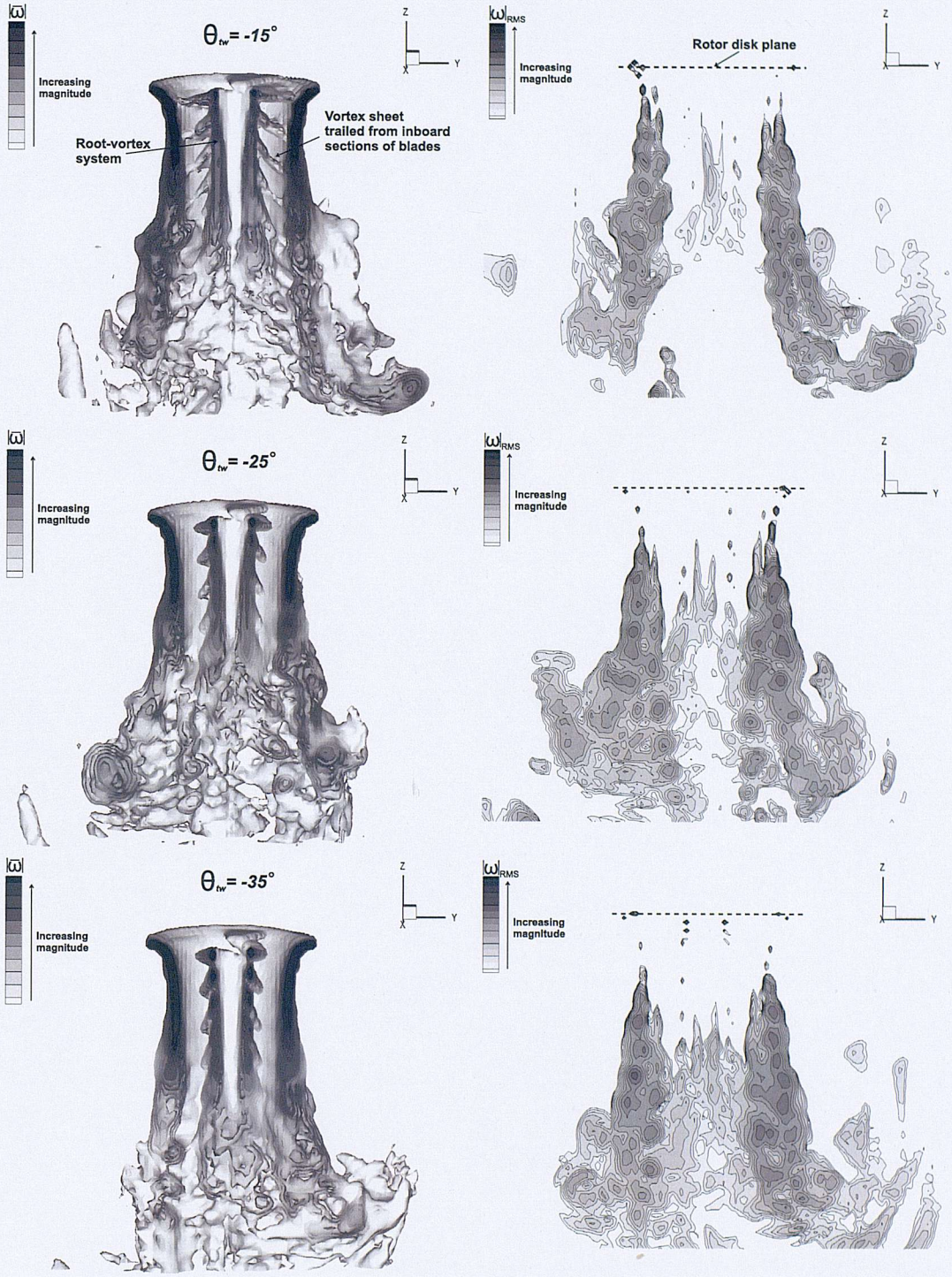



***Figure 5.6:*** *Locus plots of the geometry of the vorticity field and 2D RMS contour plots of the vorticity field for the three rotors. The 2D plots run vertically through the rotor hub. Plots were computed from 14 snap-shots from 14 contiguous rotor revolutions corresponding to the speed interval:* $0.2 \leq \bar{\mu}_z \leq 0.3$.

indication of the relative strength of the wake stuctures, several iso-surfaces of vorticity have been included in the plots to expose the distribution of the strength of the wake. The darker the surface the stronger is the vorticity.

In this speed range the wake, in all three cases, exhibits the tubular structure most commonly associated with the wake of a hovering rotor. The tip and root vortex systems exhibit definite structure as do the sheet vortices that spiral down and around the root-vortex system. Since in each case, these features appear as coherent, well defined structures in the region starting from the rotor plane to around $1.5R$ down from the rotor, it can be assumed that the flow is relatively steady in this region, using the definition of this term given in § 2.7.2. Below the steady region the features are somewhat smeared and incoherent, thus, from $1.5R$ to around $3R$ from the rotor the features in the wake can be assumed to be persistent, again, according to the definition of this term given in § 2.7.2. The marked difference in the relative strengths of the inboard sheets that are produced by each of the three rotors reflects the very different bound circulation distributions generated on the blades. There is little of significance with which to differentiate the geometries of the three vorticity locus plots shown in this figure, save for the subtly increased strength of the root vortex system produced by the more highly twisted rotor blades. The RMS contour plots, however, show that an increase in blade twist strongly increases the unsteadiness in the region around the root-vortex system in the lower parts of the wake - the RMS contour plot of the wake of the rotor with the least twisted blades exhibits little unsteadiness in this region compared to that of the rotor with the most highly twisted blades. This feature of the flow is, perhaps, a result of higher rate of growth of the perturbations in the flow of the rotor with the most highly twisted blades. The higher growth rate being a consequence of the stronger root-vortex filaments produced by this rotor. But, this interpretation of the results does not seem to be consistent with the findings of Leishman *et al.* [30] regarding the effects of blade twist on the stability characteristics of a wake. Argued another way though, perhaps the increased unsteadiness in the inner region of the far wake is induced by the theoretically faster growing disturbances of, and thus greater unsteadiness in, the tip-vortex system of the rotor with the most highly twisted blades. This interpretation of the observations would at least be consistent with the analysis of Leishman *et al.*. However, it is difficult to establish whether or not this is likely to be the case since there is little variation between the three cases in the values of the RMS contours in the outer

locations of the wake that correspond to the location of the tip-vortex system.

The next sequence of images, displayed in Fig. 5.7, shows the locus plots and RMS contour plots of the vorticity fields generated by the three rotors during the speed interval of $0.4 \leq \bar{\mu}_z \leq 0.5$: the descent speed interval during which a significant increase in sustained unsteadiness of the thrust produced by the three rotors occurred. Note that the VRS had not initiated within this descent interval in any of the cases. The locus plots of the wake and the RMS contour plots of the two rotors with the least twisted blades show significant recirculation of what was originally far field vorticity back up into the the rotor plane. This is especially so in the case of the rotor with the least twisted blades where the recirculation of a vortex filament back into the rotor is clearly evident. The increased unsteadiness of the flow fields in each case, as indicated by the corresponding fiuctuations in the rotor thrusts shown in Fig. 5.4, is evident from the increase of the RMS of the wake fluctuations along the tip-vortex paths immediately beneath the rotors, over what was shown in the previous figure. Although the root-vortex system of the first rotor in the figure appears to have maintained its tubular form, the corresponding RMS plot displays an increase in the unsteadiness in this region of the fiow at this range of higher descent speeds. Such an increase is not so apparent in the RMS plots from the other two cases, however. It is noteworthy that the wake produced by the rotor with the most highly twisted blades appears to have deviated far less from the geometry that arises at the lower descent speeds shown in the previous figure, than in the other two cases.

An inspection of the locus plots and RMS contour plots of the three vorticity fields, occurring over the next, higher, range of descent speeds as featured in Fig. 5.8 reveals a marked change in the geometry of the flow field around the rotor with the least twisted blades - much of the wake has collapsed. Significantly, the root-vortex system of this rotor appears to have collapsed more than the tube formed by the tip-vortices, and part of it has, in fact, convected above the rotor plane. Indeed, the tracks of the root-vortices above the rotor plane are more clearly exposed in the RMS plot for this rotor. The reason for the earlier collapse of the wake of the rotor with the least twisted blades will be discussed in more detail later but it is most likely due to the lower downward induced velocities in the region of the root-vortex tube resulting from the lower blade twist. Such wake behaviour contrasts with that exhibited by the other two rotors. The wake structures in these latter cases continue to display a relatively ordered tubular form, though increased

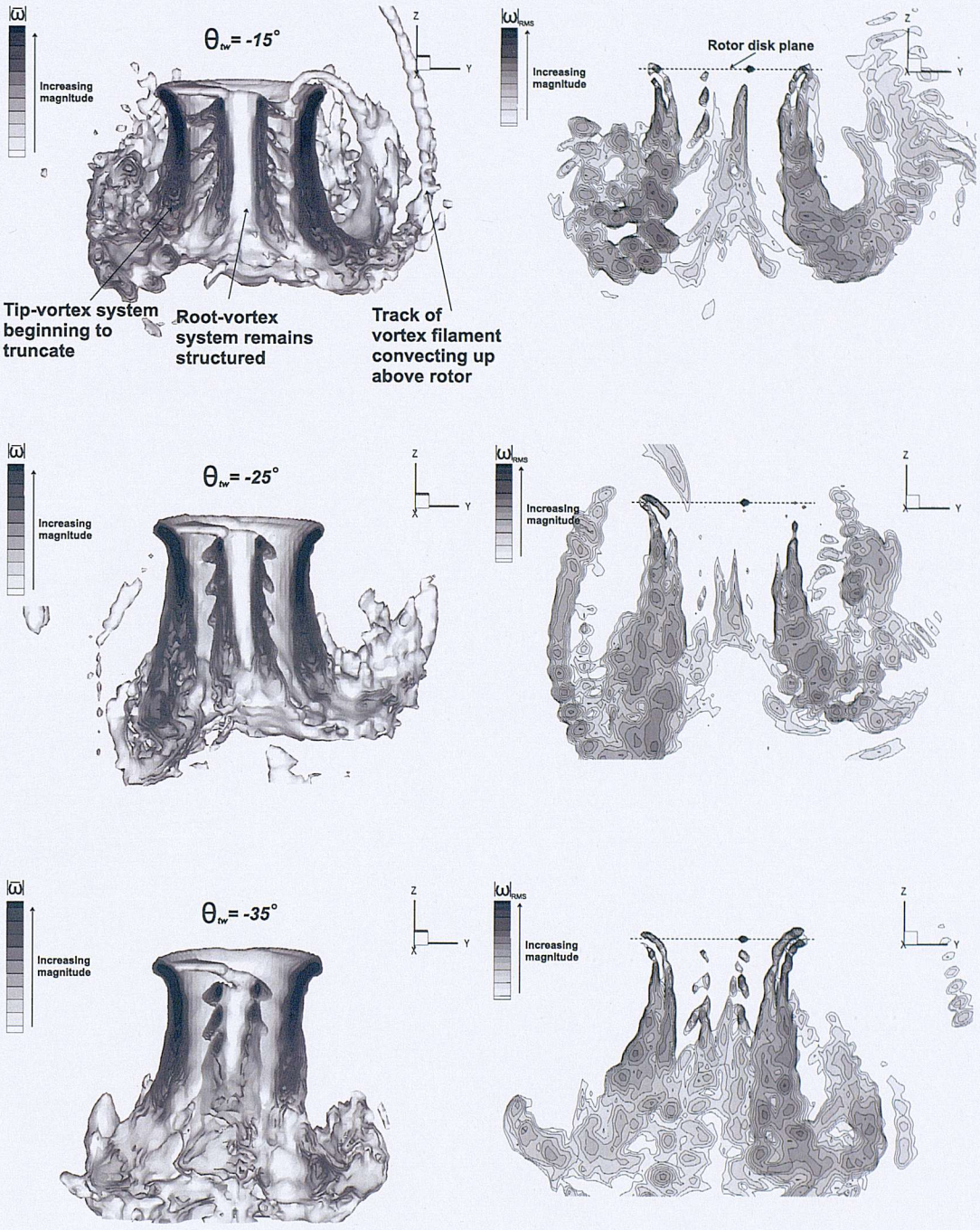



***Figure 5.7:*** *Locus plots of the geometry of the vorticity field and RMS contour plots of the vorticity field for the three rotors. The 2D RMS plots run vertically through the rotor hub. Plots were computed from 14 snap-shots from 14 contiguous rotor revolutions corresponding to the speed interval:* $0.4 \leq \bar{\mu}_z \leq 0.5$.

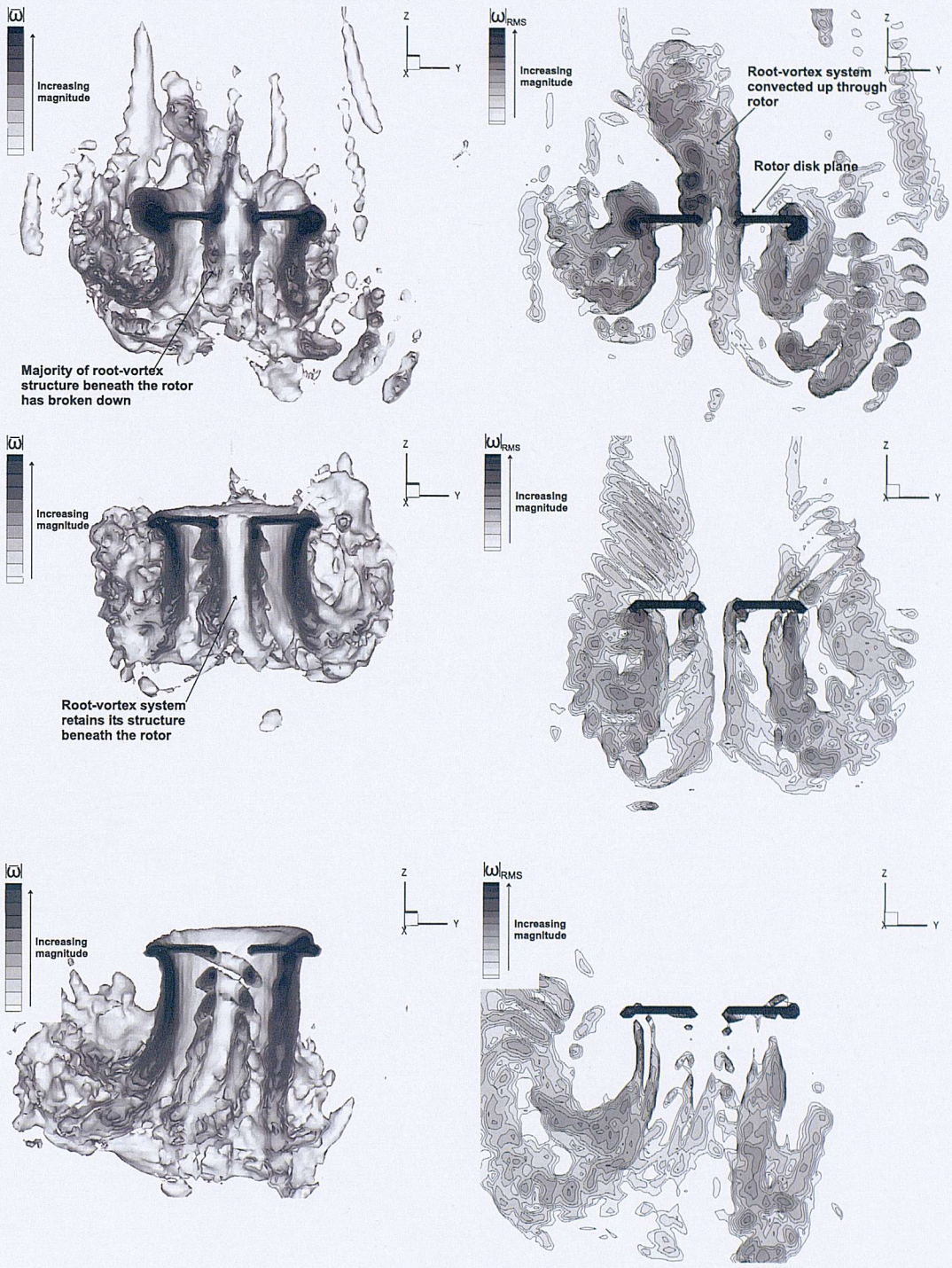



***Figure 5.8:*** *Locus plots of the geometry of the vorticity field and RMS contour plots of the vorticity field for the three rotors. The 2D plots run vertically through the rotor hub. Plots were computed from 14 snap-shots from 14 contiguous rotor revolutions corresponding to the speed interval:* $0.5 \leq \bar{\mu}_z \leq 0.6$.

levels of recirculation and reingestion of the vortical wake from the rotor with $\theta_{tw} = -25°$ above the situation shown in the preceding figure are evident. Again, it is noteworthy that, whilst much greater wake excursions than seen before are now evident, the rotor with the most highly twisted blades was able to maintain much of its tubular structure. Indeed, the difference in behaviour between this and the rotor with the least twisted blades is striking.

The locus plots of vorticity and the RMS contour plots that show the early stages of the collapse of the wake of the rotor with the least twisted blades suggest that the breakdown of the root-vortex system precedes, slightly, that of the stronger tip-vortex tube. To emphasise this inferred kinematical behaviour, a sequence of three-dimensional iso-surface plots of the instantaneous vorticity field that shows the collapse of the wake structure is presented in Fig. 5.9. Arguably, the root vortex system collapses just before that of the tip-vortex system, though the effect is subtle. This is interesting since such an observation has not been reported before, and, such a phenomenon may indicate that the onset speed of the VRS may be strongly influenced by the dynamics of the root vortex in addition to the supposedly more dominant tip-vortex dynamics. It is conjectured that the root-vortex system provides 'support' to the tip-vortex system in helping to oppose the free-stream flow through its contribution to the total induced downwash within the annulus between the root and tip vortex systems. Without this contribution from the root-vortex system, which is removed upon its collapse, the transport velocity of the tip-vortex system is reduced which thus decreases the separation distance between the tip-vortex filaments. The effect of reducing the separation distance is to increase the rate of disorganisation in the wake as a result. The collapse of the tubular geometry of the tip-vortex system thus quickly follows that of the root vortex system to form a toroid around the rotor.

Inspection of the distribution of the velocity of the downwash over the blades reveals, in a quantitative fashion, the detail differences in the aerodynamic environments in which each rotor operated during their descents. Figure 5.10 shows the total speed, $(\lambda_i(r) + \mu_z)$, of the flow normal to the rotor disc at several stations along the blade. The outboard sections of the rotor included in the figure are at: 0.98R (just inboard of the blade tips), 0.9R, 0.8R and 0.7R from the rotor hub, and the inboard sections of the rotor included are at: 0.5R, 0.4R, 0.3R and 0.22R (just outboard of the blade roots). This data is shown for each rotor. In each case, the downwash velocities over the outboard stations are shown

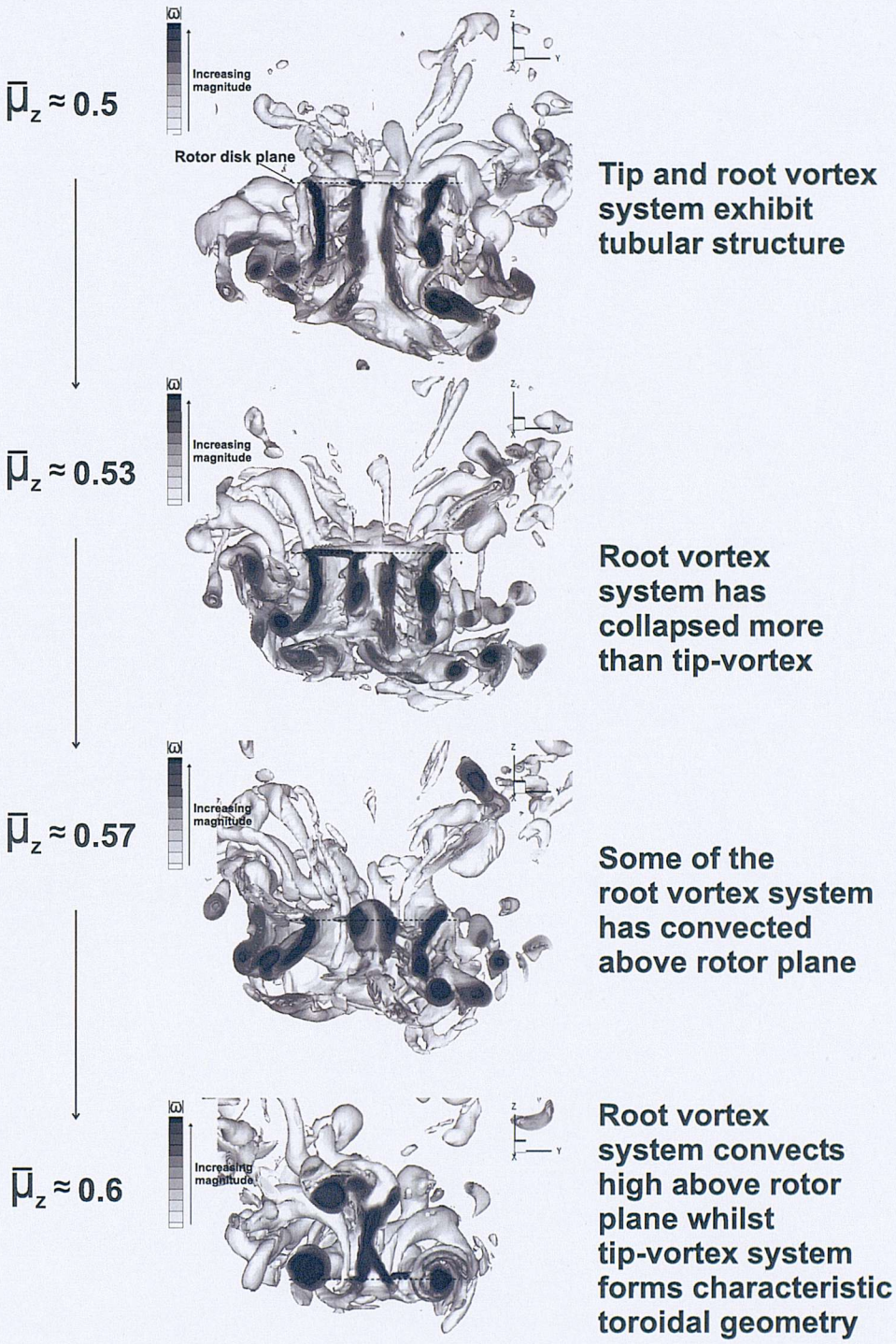



***Figure 5.9:*** *Iso-surfaces of the instantaneous geometry of the vorticity field produced by a rotor with blade twist of* $\theta_{tw} = -15°$. *The figure shows the convection of the root and tip vortex systems.*

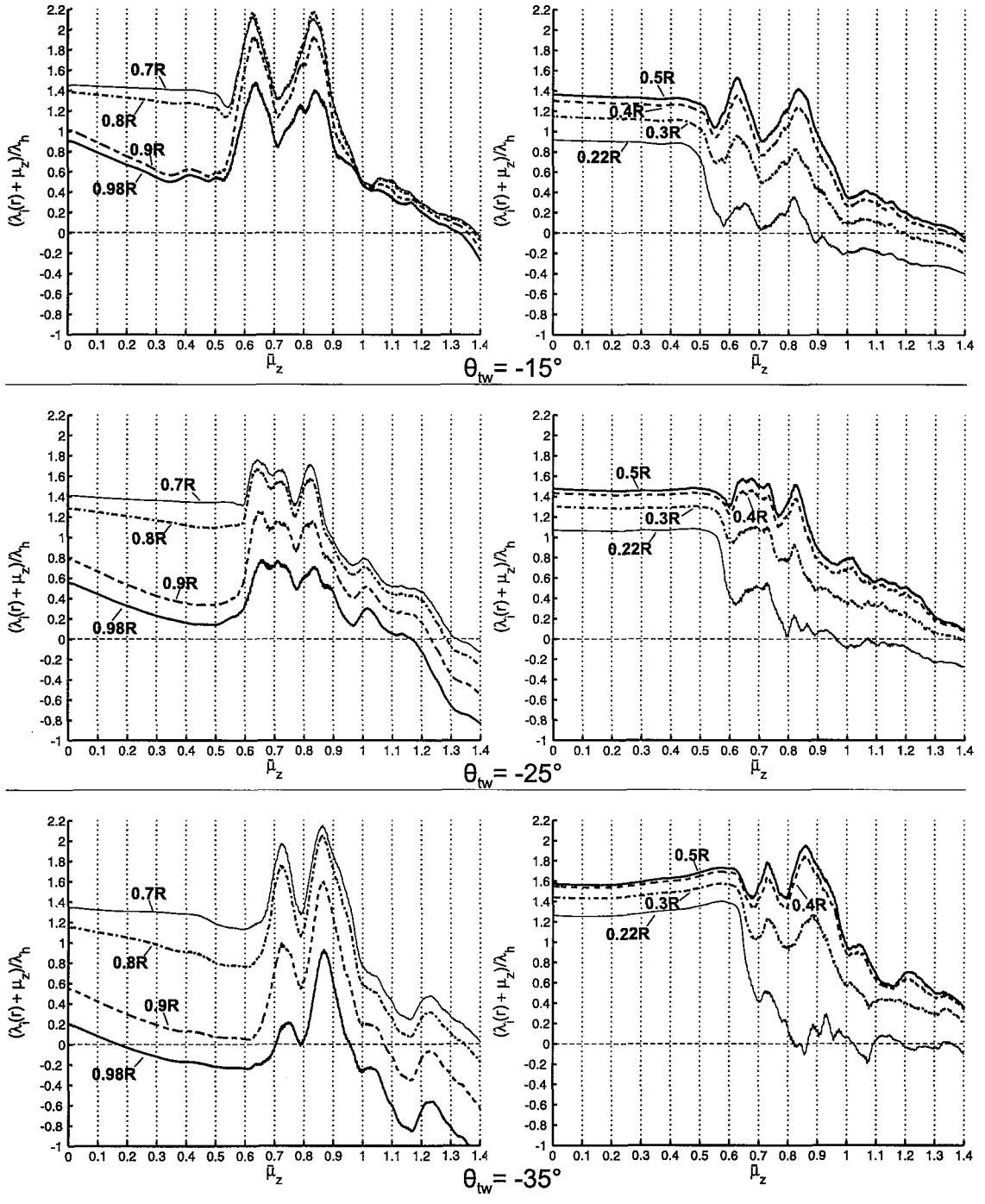



***Figure 5.10:*** *Total speed, $(\lambda_i + \mu_z)$ of the flow normal to the rotor disc at several stations along the blade. The data is taken from rotors with twist of $\theta_{tw} = -15°$, $-25°$ and $-35°$.*

on the left side of the figure. The downwash velocities over the remaining stations are shown on the right side. The data has been filtered, in the manner described in § 2.7.2 using a moving averaging window with a width of 10 rotor revolutions. This window was sufficiently small to avoid obscuration of important flow features whilst just large enough to remove many of the higher frequency fluctuations that serve only to diminish the clarity of the plots.

Consider first the downwash distribution over the rotor blades with a twist of $\theta_{tw} = -15°$. The graphs show a gradual reduction in the magnitude of the downward flow speed on the blades, over the whole length of the blade, up to a descent speed of $\bar{\mu}_z \approx 0.35$. The rate of reduction of the flow speed is more pronounced at the two most outboard sections included in the figure. At a descent speed of $\bar{\mu}_z \approx 0.45$, however, the rate of reduction of the downwash speed increases over the inboard sections, especially in the region very close to the blade roots at 0.22R and 0.3R. The downwash over the outboard sections, however, do not replicate this behaviour. Indeed, the rate of change of reduction in the flow speed at stations 0.8R and 0.7R appears unchanged from that arising at lower descent speeds at this stage. This differential in the trends of the downwash velocity between the outboard and inboard sections is suggestive that a change in the geometry of the wake somewhere has diminished the velocity of the induced flow near to the root-vortex system. This change is very subtle, however, since it is not evident from a comparison of the corresponding locus plots of the vorticity shown in Figs. 5.6 and 5.7.

Between descent speeds of $\bar{\mu}_z \approx 0.51$ and $\bar{\mu}_z \approx 0.55$ the downwash speed drops suddenly over much of the blades, from stations 0.22R to 0.8R, though the extent of the drop and the range of speeds over which the drop occurs decreases with increase in distance from the rotor hub. At the outermost sections of the the blades though, the character of the behaviour of the downwash is different to that on the inboard sections. Indeed, at 0.9R, the downwash speed begins to *increase* over the same range of descent speeds indicating that this part of the rotor was subject to a different aspect of the wake behaviour to that which influenced the flow over the inboard sections. This is indicative of the onset of the thrust-settling phenomenon (actually 'settling-with-power' in this controlled thrust scenario) that was discussed in Chapter 5. Indeed, the increase in downwash velocity and the fluctuating behaviour that arises over the descent speed range of $\bar{\mu}_z \approx 0.55$ to $\bar{\mu}_z \approx 0.85$ are closely correlated with the general increase and accompanying fluctuations

in rotor torque that were shown earlier in Fig. 5.5. The sudden drop, at $\bar{\mu}_z \approx 0.5$, in the downwash speed at a distance of 0.22R from the rotor hub is steeper and occurs over a larger range of descent speeds than that which arises at the other inboard blade stations featured in the graph. This behaviour is consistent with the breakdown of the nearby root-vortex system and the decrease in the velocity of the induced flow that such a collapse would engender. Indeed, this drop in downwash velocity arises over the same range of descent speeds that show the collapse of the root-vortex in Fig. 5.9 and are also consistent with the appearance of upward flow in the central part of the wake tube shown in the instantaneous velocity contours of marker *ii* in Fig.4.11 shown in the previous chapter.

A comparison of the graphs showing downwash data from the rotor with the least twisted blades with the graphs of similar data from the other two rotors reveals that the general trends behaviour seen in the former data are also evident in the latter two cases, but with some exceptions. The velocity of the downwash over the outboard sections of the rotors with the more highly twisted blades decreases as it does in the former case. In the case where $\theta_{tw} = -25°$ the velocity of the downwash over the inboard sections of the blades, from blade stations 0.5R to 0.22R remains approximately constant until the rotor reaches a descent speed of $\bar{\mu} \approx 0.5$ (there is actually a very slight fall and then rise in the downwash speeds prior to this point), after which it begins to decrease rapidly. In the case of the rotor with the most highly twisted blades the inboard downwash velocities begin to rise after having been approximately constant from $\bar{\mu} = 0.0$ to $\bar{\mu} \approx 0.2$. The rise in downwash velocity continues to a descent speed of $\bar{\mu} \approx 0.56$. This difference in behaviour of the downwash over the inboard sections of the blades between the three rotors is consistent with the increase in strength of the root vortex system and the accompanying decrease in strength of the tip-vortex system, induced by an increase in the blade twist rate. The observation regarding the difference in the behaviour of the downwash over the inboard and outboard sections of the blades is illuminating. Even though the velocity of the downwash in the vicinity of the tip-vortex system decreases with an increase in twist rate, which should increase the susceptibility of the tip-vortex system to collapse during descent, the same increase in twist rate actually postpones VRS onset to higher descent speeds, as has been shown. This behaviour strongly suggests, then, that it is the increased downwash velocity over the inboard sections of the rotor, engendered by an increase in blade twist, that is responsible for the higher VRS onset speeds. Therefore, this supports

the idea that the root-vortex system plays an important role in the dynamics of the wake prior to wake breakdown. The effect that the difference in the distribution of the velocity of the downwash over the blades, at various pertinent descent speeds is discussed later in this chapter.

Further comparison of the data in this figure shows that increasing the blade twist rate increases the descent speed at which the onset of settling-with-power occurs - the sudden rise in the velocity of the downwash over the outboard sections of the blades occurs at higher descent speeds with increase in twist rate, as does the sudden decrease in the downwash velocity over the inboard sections. It may be inferred from this that the descent speed at which the tip and root vortex systems of a rotor collapse increases with an increase in twist rate. This inference is, of course, consistent with the behaviours shown by locus plots of the vorticity fields shown earlier in this chapter. Note also how the disparity between the downwash velocities over each of the outboard blade stations during the first large fluctuation, that is associated with the settling-with-power phenomenon, increases with blade twist rate. This is suggestive that increasing in the twist rate moves the origin of the phenomenon towards the rotor hub or at least smears the effect out over a larger portion of the rotor blades. In the case of the rotor with the least twisted blades is was noted that there was a slight difference between the descent speeds at which the sudden increase in downwash velocity over the outboard sections of the blades occurred and at which the sudden decrease in downward velocity over the inboard sections occurred. This difference is also evident in the downwash velocity data from the other two rotors. The difference in descent speeds at which these sudden changes occur is subtle in each case, though.

A change in blade twist appears to influence the timescales associated with the dynamics of the rotor wake. The second of the two large peaks in downwash velocity that occurs at a descent speed of $\bar{\mu}_z \approx 0.82$ in the case of the rotor with blades with a twist of $\theta_{tw} = -15°$ occurs at a similar descent speed as that experienced by the rotor with blades exhibiting a twist of $\theta_{tw} = -25°$, even though the onset of the settling-with-power phenomenon, occurred later in the latter case. In addition, in the case of the rotor with the most highly twisted blades, although the corresponding second peak in downwash velocity arises at the slightly higher descent rate of $\bar{\mu}_z \approx 0.87$, the difference between the speed at which this peak occurs and the speed at which it occurs in the case of the rotor with the

least twisted blades, is approximately half that of the difference in the speed at which the settling-with-power phenomenon first occurs between these two rotors. Indeed, the range of descent speeds that is flown through between the occurrence of the first and second peaks in the downwash velocity decreases with increase in blade twist. This indicates that the timescales of the dominant wake dynamics are altered subtly by a change in the relative strengths of the tip and root vortex systems. This presentation of the data has allowed only a rather low resolution, and indirect realisation of the dynamics of the rotor wakes, however, and the fundamental aspects of rotor flows that govern the time constants associated with the gross dynamics of the vortical wakes in the VRS is something that is yet to be fully established.

In the present aerodynamic analysis it has been suggested that there is perhaps a precursor to the large, oscillatory, increase in downwash velocity over the tip region of the blades that signals the start of the 'settling-with-power' regime i.e. the precursor is an earlier change in the downwash velocity over the inboard sections of the blades than at the outboard sections. In general, the evidence suggests that an increase in twist rate allows a rotor wake to maintain a tubular form at higher speeds. Inspection of the two-dimensional mean velocity fields that arise at low speeds of descent, before wake breakdown occurs, provides further insight into why blade twist is able to influence the wake behaviour so significantly. Figure 5.11 shows contours of the average downward vertical velocity induced by the wake of the three rotors. The average velocity fields were calculated from the instantaneous flow fields that arose during the descent speed interval of $0.2 \leq \bar{\mu}_z \leq 0.3$ - a duration of 14 revolutions. Some 14 snapshots of the 3D *vorticity* field were available to generate the corresponding instantaneous velocity fields. For each snapshot, the velocity fields induced in two orthogonal vertical planes that pass through the rotor hub axis and lie parallel to lines running through the 90° and 270°, and the 0° and 180° positions on the rotor was calculated and included in the overall mean flow computation. This method of calculating the mean flow was implemented in order to increase the number of data points used, thus giving a more reliable representation of the mean flow. The speed intervals over which the mean velocity fields were computed were selected because they allow a comparison of the respective wake behaviours whilst the structures of the vorticity fields still exhibit largely tubular geometry, especially in the near-field. The unsteadiness of the wake is thus low relative to that which arises in the VRS, and hence a fair comparison of

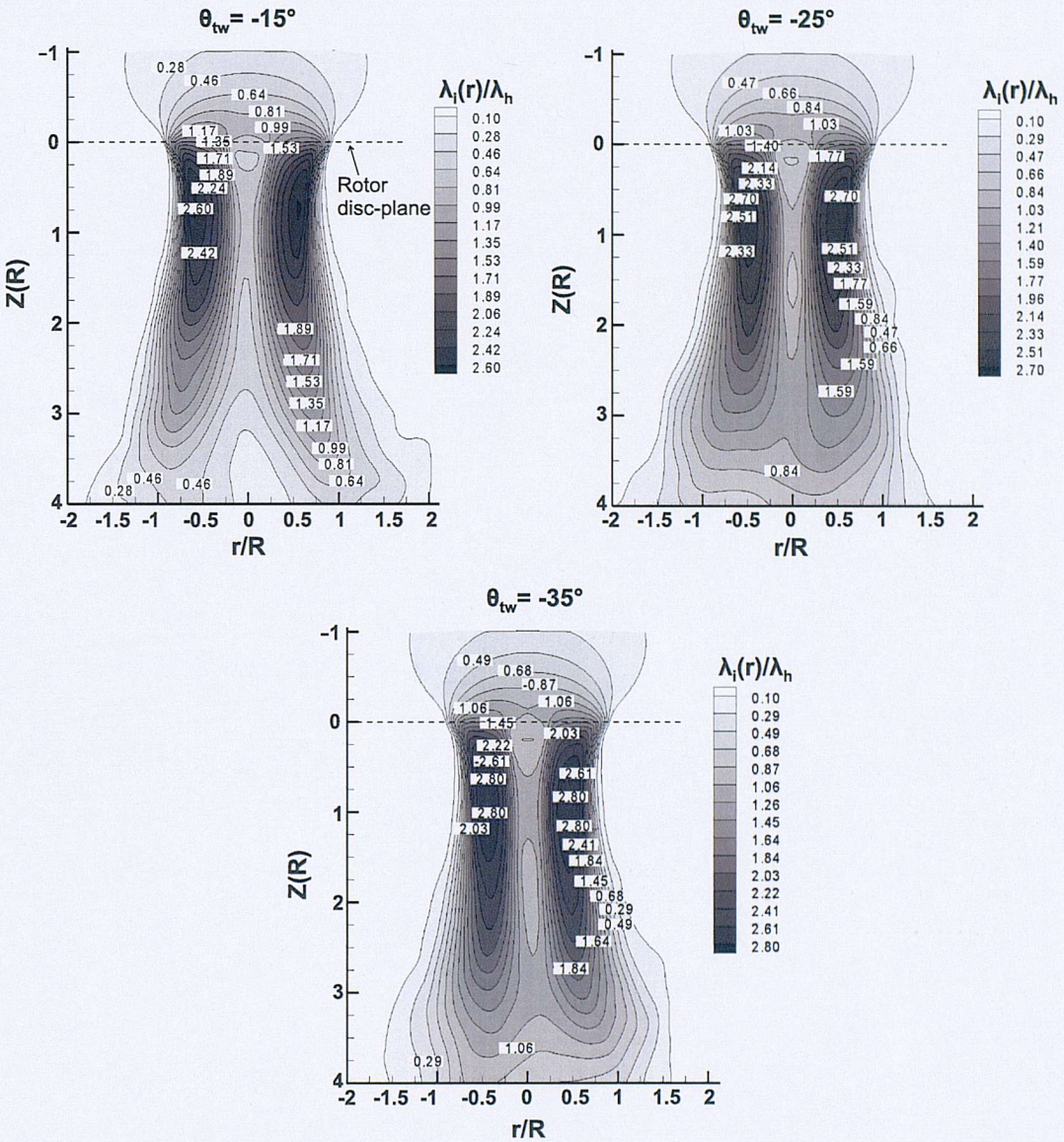


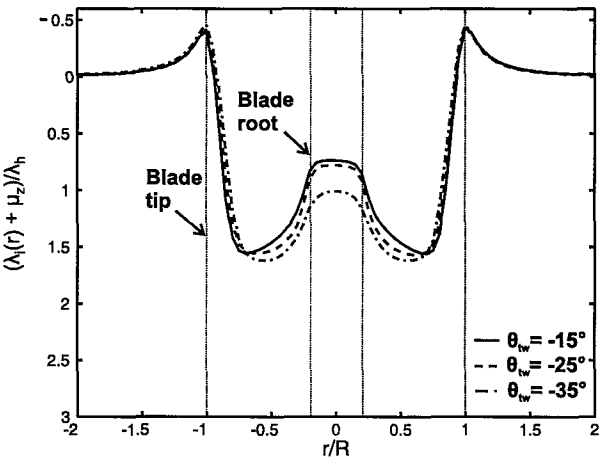

***Figure 5.11:*** *Mean velocity field produced by rotors with blade twist of* $\theta_{tw} = -15°$, $\theta_{tw} = -25°$ *and* $\theta_{tw} = -35°$. *Mean field arises during the speed interval* $0.2 \leq \bar{\mu}_z \leq 0.3$ *(14 rotor revolutions). Direction of free-stream is upwards.*

the velocity fields can be made. In all cases, the downward velocity, $\lambda_i(r)$, is normalised by the theoretical hover induced inflow, $\sqrt{C_{T_h}/2}$.

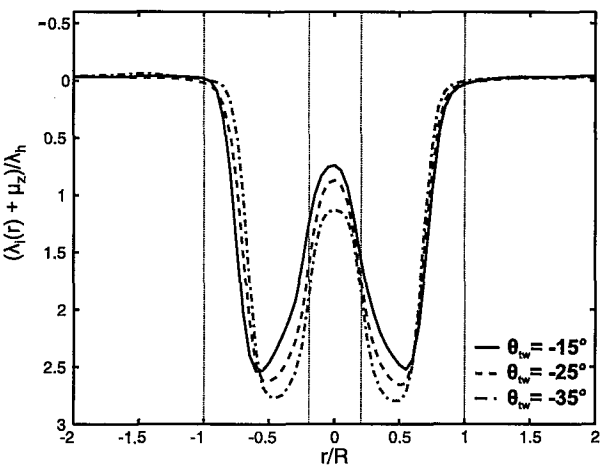
Comparison of the velocity fields shown in the three images reveals that, consistent with data presented earlier, the region within the wake where the peak velocities arise, at approximately $1R$ from the rotor, move further inboard as the twist rate increases, although the effect is subtle. This effect alone could arguably assist in maintaining the tubular structure of the root-vortex system to higher speeds as blade twist rate is increased. In addition to this, the peak velocities within the wake tube are shown to increase with blade twist rate. These higher velocities are maintained through much of the wake downstream of the rotor such that even at distances of $4R$ from the disc-plane the rotor with the most highly twisted blades generates the highest flow speeds. These trends, and others, can be seen with greater clarity in the graphs showing the profiles of velocity $\lambda_i(r)$ arising at vertical stations $0R$ (the disc-plane), $1R$ and $2R$ down from the rotor in each of the three cases, as presented in Fig. 5.12 (a), (b) and (c) respectively. The distinct asymmetry apparent in the profiles of Fig. 5.12 (c) arises from the unsteadiness in the far wakes of the rotors. At each of the three vertical stations, the rotor with the least twisted blades appears to generate the highest flow velocities within the outer portions of the rotor blade and wake tube. An increase in twist rate produces increased velocities between the mid-span and the root of the blades, but, interestingly, the downward velocities within the region that corresponds to the inside of the root-vortex tube, are also increased. It can be inferred from the presence of the increased flow velocities near to the root-vortex system that higher descent rates may be required to produce sufficient disorganisation in the root-vortex system to cause it to collapse, as twist rate is increased. The collapse of the root-vortex system appears then to quickly lead on to the global collapse of the wake, as suggested by the data presented earlier.

Such trends can be seen to continue at higher descent speeds also, as revealed by an examination of the mean velocity fields arising within the descent speed interval of $0.4 \leq \bar{\mu}_z \leq 0.5$ shown in Fig. 5.13. Note that the rotor with the least twisted blades enters the VRS just after this interval. As before, these figures show the contours of induced downward velocity $\lambda_i(r)$, normalised by the mean hover inflow, that arise in each of the three rotor cases.

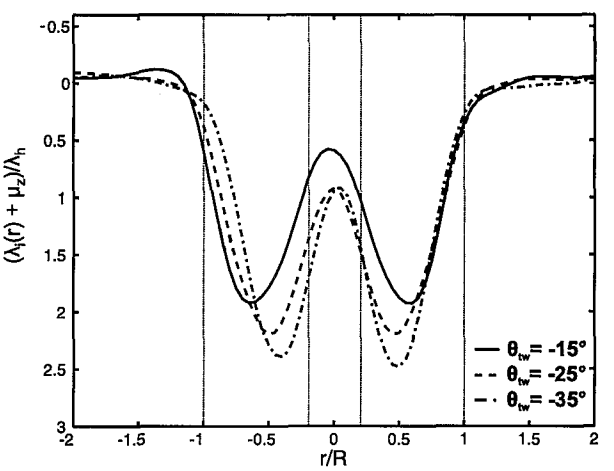
As expected, the peak induced velocities are larger compared to those generated at




(a) At disc plane $r/R = 0$




(b) 1R from disc plane $r/R = 1$




(c) 2R from disc plane $r/R = 2$

***Figure 5.12:*** *Profiles of mean flow velocity in a plane passing vertically through the rotor hub, arising over descent speed interval* $0.2 \leq \bar{\mu}_z \leq 0.3$. *Direction of free-stream is upwards.*

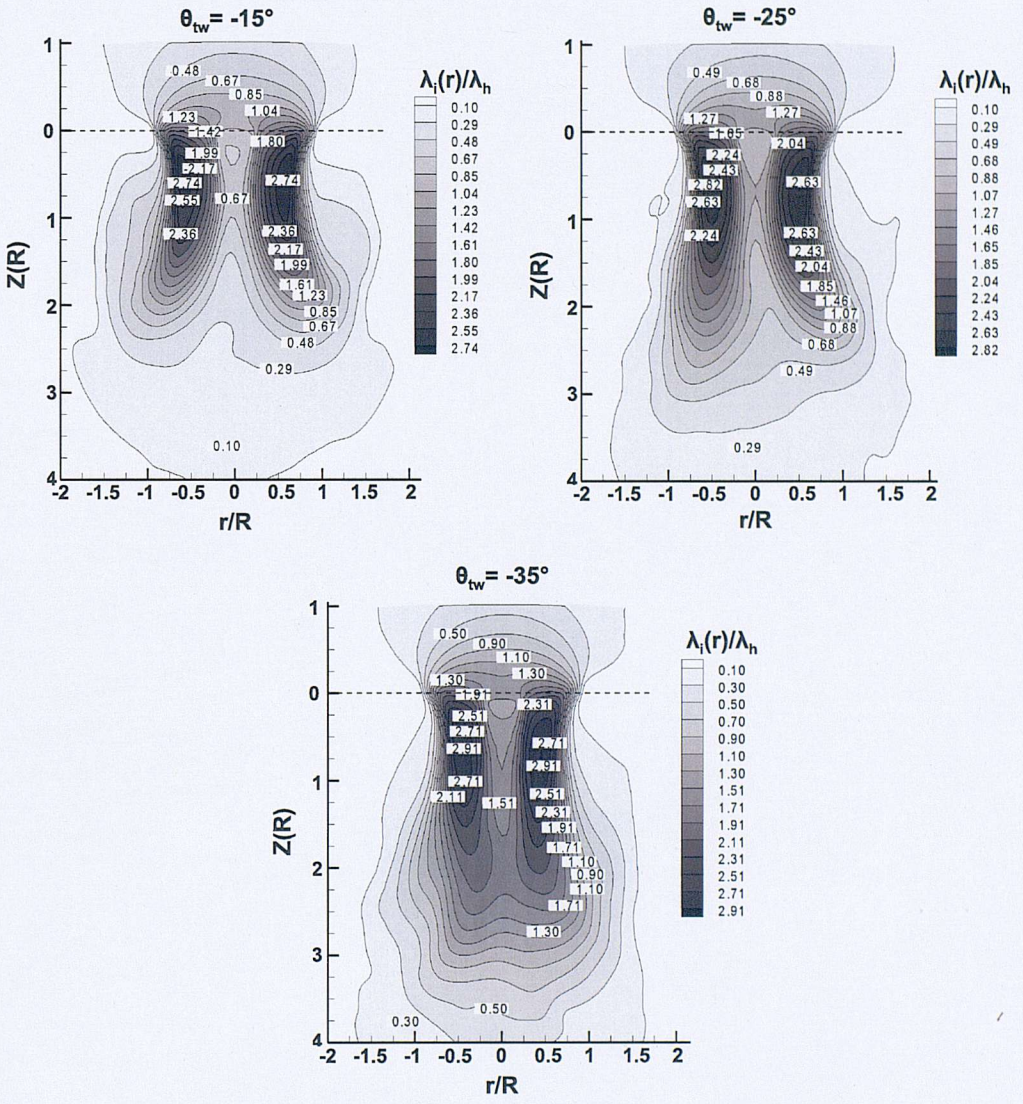
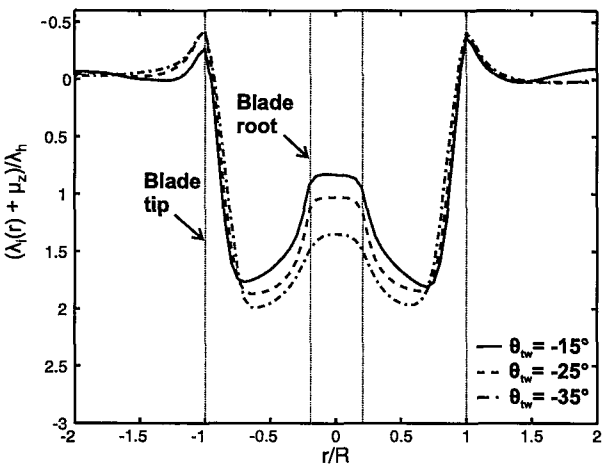
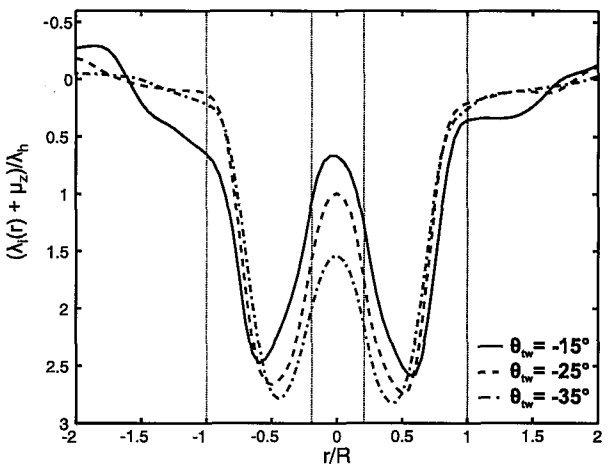


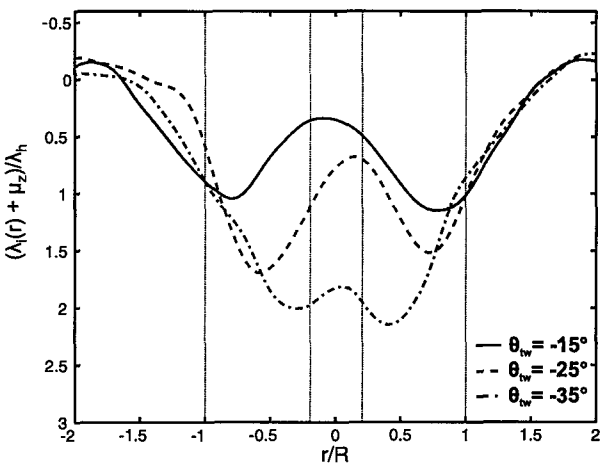

***Figure 5.13:*** *Mean velocity field produced by rotors with blade twist of* $\theta_{tw} = -15°$, $\theta_{tw} = -25°$ *and* $\theta_{tw} = -35°$. *Mean field arises during the speed interval* $0.4 \leq \bar{\mu}_z \leq 0.5$ *(14 rotor revolutions). Direction of free-stream is upwards.*




(a) At disc plane $r/R = 0$




(b) 1R from disc plane $r/R = 1$




(c) 2R from disc plane $r/R = 2$

***Figure 5.14:*** *Profiles of mean flow velocity in a plane passing vertically through the rotor hub, arising over descent speed interval* $0.4 \leq \bar{\mu}_z \leq 0.5$. *Direction of free-stream is upwards.*

lower descent speeds since the higher free-stream flow increases the spatial intensity of the vorticity capable of inducing downwash in the near field. The rotor with the most highly twisted blades induces the highest velocities. A consequence of this is that the region of the flow field below the rotor that exhibits a downward flow with a velocity greater than $|\lambda_i(r)/\lambda_h| = 0.1$ (the cut off value applied to the contours) appears to stretch farther down from the rotor than it does in either of the other two cases. This rotor is able to maintain the longest wake at these descent speeds. Once again, the velocity profiles are presented, in Figs. 5.14 (a), (b) and (c), to provide greater clarity to the comparison. As in the profiles shown in the preceding figure, the rotor with the least twisted blades still produced the highest velocities at the outer portions of the wake (within the confines of the rotor diameter) but the inboard flow velocities increase significantly with blade twist, which, as suggested before is likely to be the factor that allows the the collapse of the wake to be postponed to higher descent speeds. This is so, perhaps, because the higher velocities may decrease the rate of disorganisation of the root vortex structures that results from the action of the instabilities in the flow, in accordance with the findings of Bhagwat and Leishman [6].

The preceding discussion dealt with the effects of blade twist on the speed at which a rotor enters the VRS. What remains is to consider how blade twist influences the descent speed at which a rotor moves out of the VRS. In Fig. 5.4, which shows the behaviour of the fluctuations of thrust incurred by each rotor, it could be seen that from a descent speed of around $\bar{\mu}_z = 1.2$ the rotor with the least twisted blades experienced a slightly more rapid decrease in the magnitude of its thrust fluctuations back to pre-VRS levels than was experienced by the other two rotors, especially when compared to the rotor with the most highly twisted blades. Although the effect is subtle, it is suggestive that not only does blade twist appear to increase the VRS onset speed, but it also postpones the cessation of VRS until higher descent speeds. Such a notion is easily verified by inspection of locus plots of the vorticity field that are constructed from pertinent intervals of high speed descent. Therefore, to assess whether or not twist prolongs the VRS to higher descent speeds, locus plots of vorticity were constructed from a sequence of snap-shots that arose during the following intervals of descent speed: $1.3 \leq \bar{\mu}_z \leq 1.4$; $1.4 \leq \bar{\mu}_z \leq 1.5$ and $1.5 \leq \bar{\mu}_z \leq 1.6$ and are presented in Fig. 5.15. The locus plots were generated in the same manner as that described earlier in this chapter. Only the wakes generated by

rotors with blade twists of $\theta_{tw} = -15°$ and $\theta_{tw} = -35°$ are shown in order to juxtapose only the most widely differing geometries, since the differences are subtle. During the descent speed interval of $1.3 \leq \bar{\mu}_z \leq 1.4$ the wake of the rotor with the least twisted blades exhibits a tip-vortex and a root-vortex tube that both extend approximately half a rotor radius above the disc plane. Persistent features within the flow, as defined in § 2.7.2, appear at the top of these truncated tubes and are spread over the inboard of the rotor. These features represent flow that is highly unsteady relative to the vortical structures that formed the tip and root vortex tubes below. As was seen in Chapters 3 and 4, this region of the flow contains re-circulating, structured vortex filaments, as well as unstructured vortex fragments of course. Significantly, the averaging process used to generate the locus plots reveals approximate cylindrical symmetry in the flow just above this rotor which is indicative of steady axial rotor flow, though this symmetry is lost from the flow field after an approximate distance of 1R above the disc plane. In contrast, the wake of the rotor with the more highly twisted blades appears to exhibit less order in the vicinity of the rotor, and no cylindrical symmetry, can be detected from this qualitative assessment; the tip and root vortex systems shows little sign of having formed a coherent tube above the disc plane, unlike in the former case. A further, telling, difference between the two wake geometries is that the wake produced by the rotor with the more highly twisted blades shows distinct regions of vorticity lying beneath the rotor plane. This is suggestive of the presence of a net downward flow through the inboard parts of the rotor, outside of the blade root cut-out, that convects the inboard sheet and the collapsing root vortex system down beneath the rotor before it is drawn into the recirculating tip-vortices. The process of recirculation of vorticity was discussed in Chapter 3. The velocity of the flow over the rotor blades at the high VRS speeds on which the present argument is based is discussed in detail later in this chapter.

The next two sets of locus plots in the figure show the wake during the descent speed intervals of $1.4 \leq \bar{\mu}_z \leq 1.5$ and $1.5 \leq \bar{\mu}_z \leq 1.6$. These images show that the wakes of both rotors are lifted clear of the rotor plane and the formation of more coherent, and longer, tip and root vortex tubes. Again, in each set of images, the wake from the rotor with the least twisted blades appears to exhibit the more coherent and the longer root and tip vortex tubes of the two wakes shown. Additionally, and importantly, the recirculation of strong vorticity appears to occur closer to the plane of the rotor in the higher twist case

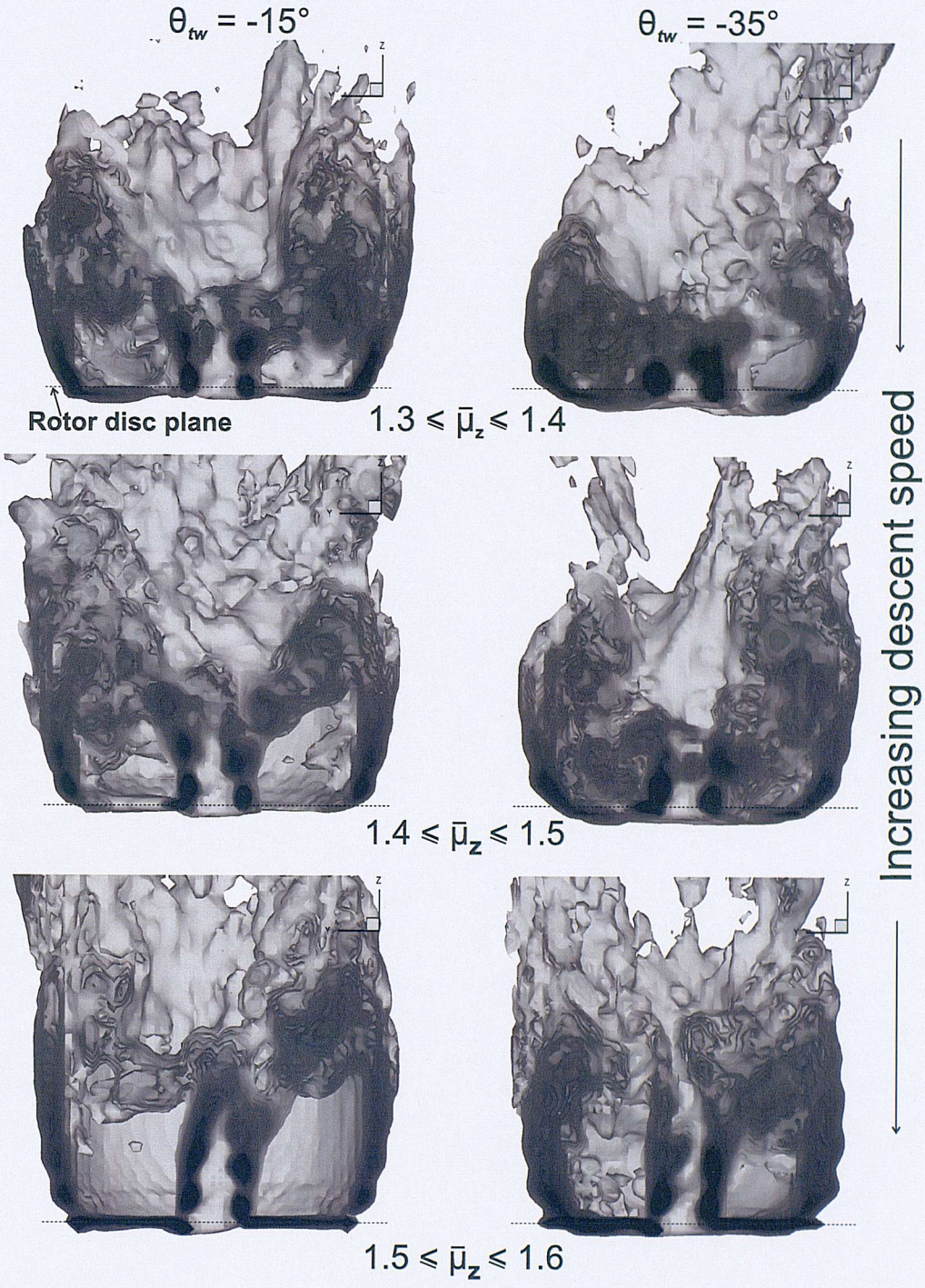



***Figure 5.15:*** *Iso-surfaces of the locus of vorticity in rotor wakes in high-speed VRS. Rotors featured have blade twist of* $\theta_{tw} = -15°$ *and* $\theta_{tw} = -35°$. The darker the surface, the stronger the vorticity.

though it now occurs at at a greater distance above the disc than seen earlier. In addition, in the speed interval of $1.4 \leq \bar{\mu}_z \leq 1.5$ there persists signs of net downward flow over the inner sections of this rotor. Within the speed interval of $1.5 \leq \bar{\mu}_z \leq 1.6$, it could be argued that both of the rotors had exited the VRS and had entered the turbulent wake state.

The visualisations of the wake have demonstrated that twist postpones the cessation of the VRS to higher descent speeds. The reasons behind this phenomenon can be gleaned, in part, from an analysis of the local velocity field. Figure 5.16 shows the spanwise distribution of total speed of the vertical flow over the blades, i.e. $\lambda_i(r) + \mu_z$, during the same descent speed intervals as were featured in the locus plots shown in the previous figure. Data from all three of the rotors in the present study have been included in order to expose and confirm the emerging trends. Consider first the graph showing the net average vertical velocities arising during the speed interval $1.3 \leq \bar{\mu}_z \leq 1.4$. At first glance the results appear counter-intuitive. That is, although the downward induced flow of the rotor with the least twisted blades causes the lowest net *upward* velocity over the blade tips, of the three types of rotor blades considered, it was shown earlier that this rotor escaped the VRS at the lowest descent speed of the three rotors. This result might be unexpected if it is assumed that the convection speed of the tip-vortices, which can be loosely inferred from the flow velocity over the tips of the blades, is seen as the primary factor influencing the wake dynamics when a rotor is in VRS. That is, the lower the upward convection speed of the tip vortices, the higher would be the assumed the VRS cessation speed. The importance of the convection speed of the tip-vortex system in governing the global dynamics of the wake when in descending flight has been postulated previously, by Wolkovitch for instance [29]. The results presented here, though, directly contradict what was envisioned in the past. It is apparent from the data shown in Fig 5.16 that upward flow over the entire rotor is required to convect the wake out of the VRS. This implies, then, that as twist rate increases, the velocity of the flow over the inboard sections of the rotor blades becomes increasingly dominant in governing the cessation speed of the VRS. Put another way, higher upward velocities in the blade tip regions do not appear to correlate with the earlier development of a coherent tube of tip-vortices (which leads to the cessation of the VRS). It seems though that higher upward velocities near to the blade *roots* can be correlated with the earlier development of a coherent tube consisting of *root*-vortices and it is this that leads to the earlier cessation of the VRS. Thus the VRS

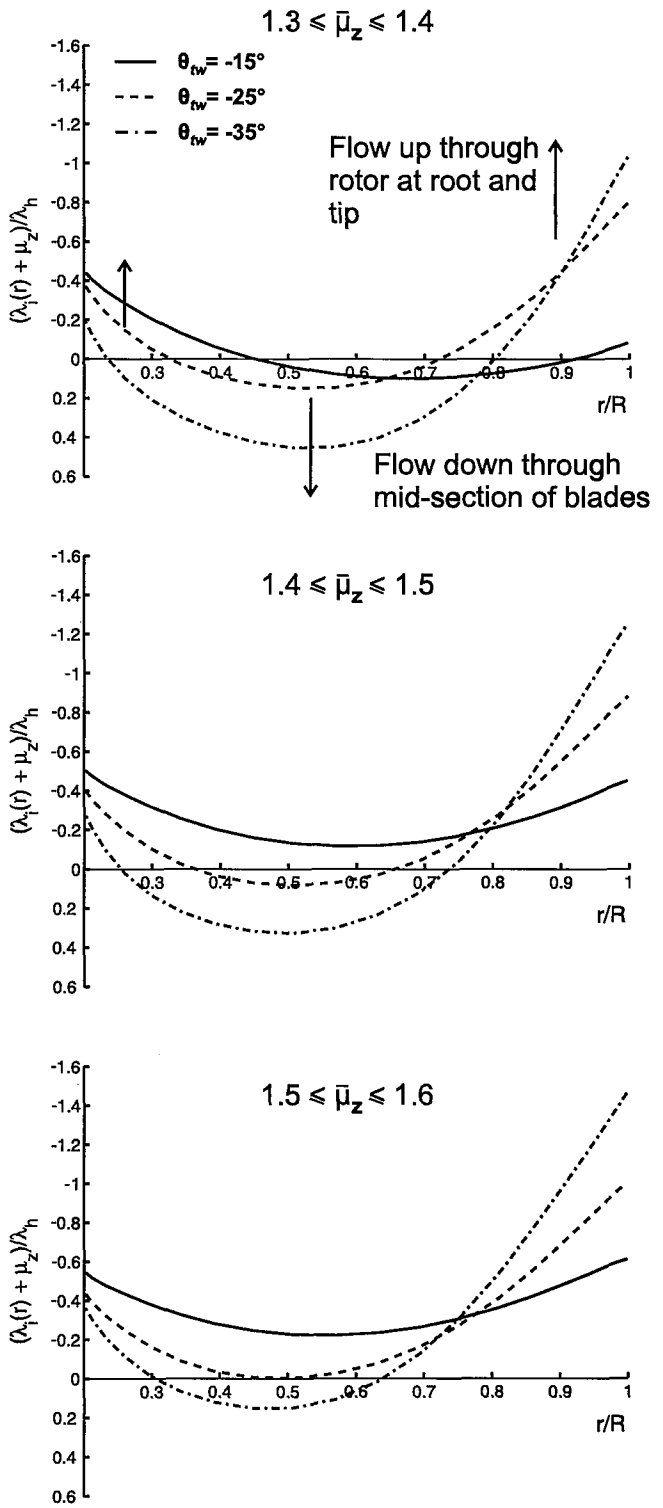



*Figure 5.16: Distribution of net speed of vertical flow, $\lambda_i(r) + \mu_z$, over rotor blades with different levels of twist. Negative velocities are upward.*

cessation speed decreases with a decrease in blade twist rate because the upward flow velocity at the blade root *increases* as blade twist *decreases*. In addition, the reason for the apparent downward convection of vorticity through the plane of the rotor with the most highly twisted blades, again in the centre sections of the blades, that was highlighted earlier lies in the relatively strong downward flow velocity that was generated by this rotor.

The trends in net vertical flow velocity occurring during the speed interval of $1.3 \leq \bar{\mu}_z \leq 1.4$, the lowest in the range of VRS speeds that are featured in the present figure, are replicated during the other two speed intervals shown. Interestingly, over the full range of descent speeds covered in this figure, the total velocity of the flow near to the roots of the rotors changed little relative to change in the speeds of the flow near the tips of the rotors. This is indicative, perhaps, of the trend in the changes in strength of the tip and root vortex systems, as discussed later in this chapter. As the descent speed increases though, the region of up-flow over the blades of each of the rotors becomes larger such that within the highest speed interval there exists an entirely upward flow through the two rotors with the least twisted blades. In the case of the rotor with the most highly twisted blades, however, a small region of downward flow existed within the highest range of descent speeds, and this is reflected in the higher level of disorder in the wake near to the rotor plane that can be seen in the corresponding wake image in Fig. 5.15.

The fact that there are differences in the net speed of the vertical flow over the blades of the three rotors can be inferred from the differences in the strengths of the blade tip and root vortices that are trailed from each rotor during their descents. Figure 5.17 shows the variation with normalised descent speed of the strengths of the root and tip vortices occurring on the blades of the rotors with twists of $\theta_{tw} = -15°$ and $\theta_{tw} = -35°$. The data has been filtered, using a moving averaging window with a width of ten rotor revolutions. The strengths of the root and tip vortices of the two rotors follow approximately the same corresponding trends over the whole range of descent speeds shown. The effect of the 'settling-with-power' phenomenon (indicated by the sudden weakening of the tip vortex and the strengthening of the root vortex of each rotor) can be seen to influence the rotor with the least twisted blades at a lower descent speed than it does the rotor with more highly twisted blades. This result is commensurate with observations made earlier that the speed at which the settling-with-power phenomenon arises decreases with decrease in blade twist. The most relevant feature of the data presented here is the difference,

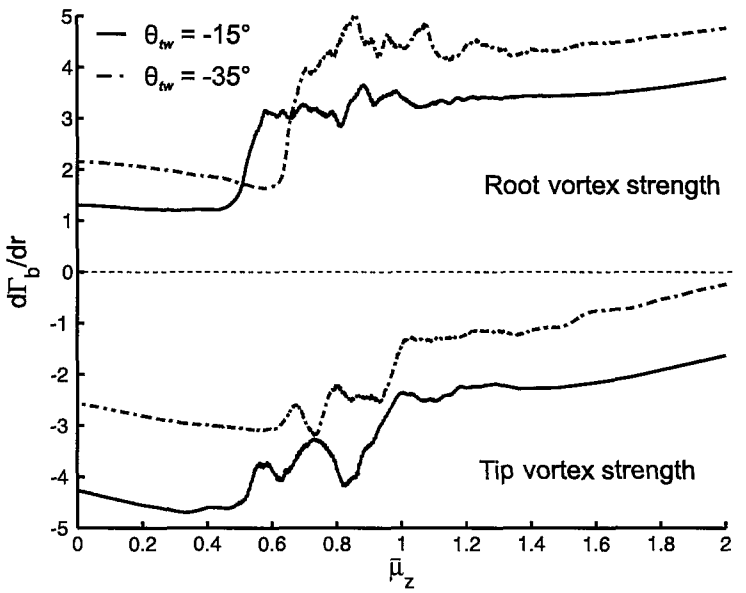



***Figure 5.17:*** *Variation with normalised descent speed of the strengths of the blade tip and root vortices that are trailed from a rotor with blade twist of $\theta_{tw} = -15°$ and a rotor with blade twist of $\theta_{tw} = -35°$. The data has been filtered using a moving averaging window with a width of 10 rotor revolutions.*

between the two rotors, in the strengths of their trailed tip and root vortices: As expected the tip-vortex strength increases as twist decreases and root-vortex strength behaves in the opposite manner. That the rotor with the least twisted blades experiences the slowest upward flow over its tips during VRS and post VRS is due to the higher downward flow velocity induced by its stronger tip vortices, relative to the tip vortices generated by the other two rotors. The opposite effect arises at the blade roots. Note that the behaviour of the tip and root vortices of the rotor with blades with a twist of $\theta_{tw} = -25°$ has been inferred from the trends shown earlier.

The net velocities of the vertical flow over the blades do not provide sufficient information to fully explain why the speed of VRS cessation is increased by an increase in blade twist. A more complete picture is provided by examination of the velocity field at and near to the rotor. Therefore, as was done earlier, profiles of net vertical velocity, on a plane passing through the rotor hub, have been calculated from the temporal average of the flow field that occurred over fourteen rotor revolutions. The associated descent speed intervals were $1.3 \leq \bar{\mu}_z \leq 1.4$, shown in Fig. 5.18 and $1.5 \leq \bar{\mu}_z \leq 1.6$, shown in Fig. 5.19. In each figure, sub-figures (a) to (c) show the velocity profiles that arise at vertical stations

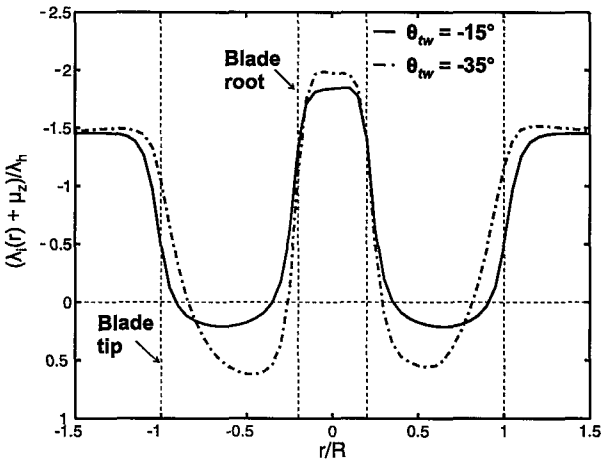
$r/R = 0$ (on the disc plane), $r/R = -0.5$ and $r/R = -1$ above the disc plane, respectively.

Consider first image (a) in Fig. 5.18. The trends revealed by the examination of the net speed of the vertical flow over the blades shown in Fig. 5.16 are, of course, replicated. In addition though, it can be seen that the velocity of the up-flow inside the root-vortex system induced by the root vortices of the rotor with the most highly twisted blades is the highest of the two cases shown, though the difference is small. However, inspection of the velocity profiles half a rotor radius above the disc shows that this trend reverses - the flow velocity up along the rotor centre-line is higher in the case of the rotor with the least twisted blades. It is not clear why the trend reverses. It is likely, though, that the higher upward velocities induced at a distance of $0.5R$ from the rotor plane by the rotor with the least twisted blades is due to the taller and more coherent root-vortex tube that was generated by this rotor. The root-vortex system of the rotor with the more highly twisted blades was less well structured at this stage of the descent. It is however, extremely difficult to determine exactly why the velocity profiles take the form that is shown here from a global examination of the vorticity field, such as has been conducted here.

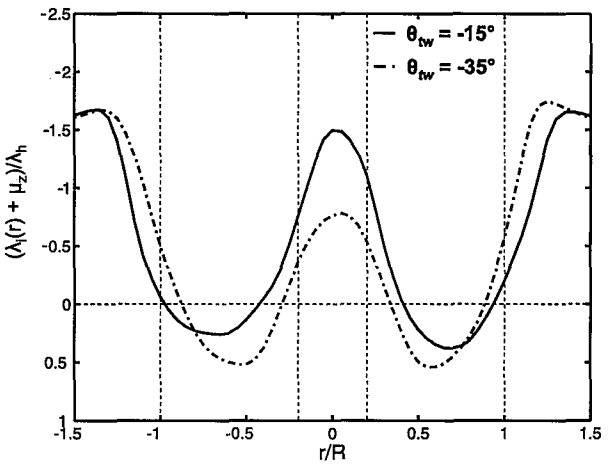
Interestingly, at a distance of $1R$ above the rotor plane the up-wash inducing effect of a root-vortex system has almost disappeared, which suggests that in both cases there is no coherent root vortex structure this high above the rotor, as it appears from the corresponding wake images of Fig. 5.15.

The velocity profiles at the same vertical stations in the field, but which arise in the higher descent speed interval of $1.5 \leq \bar{\mu}_z \leq 1.6$ are presented in Fig. 5.19. At these higher speeds the trends seen earlier are maintained, although, there is no downward velocity at the rotor disc generated by the rotor with the least twisted blades - the wake is convected only upwards here. A further difference is the appearance of some influence of a root-vortex system at a distance of $1R$ above this particular rotor - as suggested by the peaks in upward velocity that occur near the rotor centre line. There is large difference in the velocities of the up-flow in this region that were generated by the two rotors which indicates a significant variation in the coherence of the two root vortex systems, though this was not readily evident in the wake images shown earlier in Fig. 5.15. In addition, note the asymmetry in the two velocity profiles at this distance above the rotor - this is likely to be due to the very unsteady nature of the wake at this distance from the rotor.

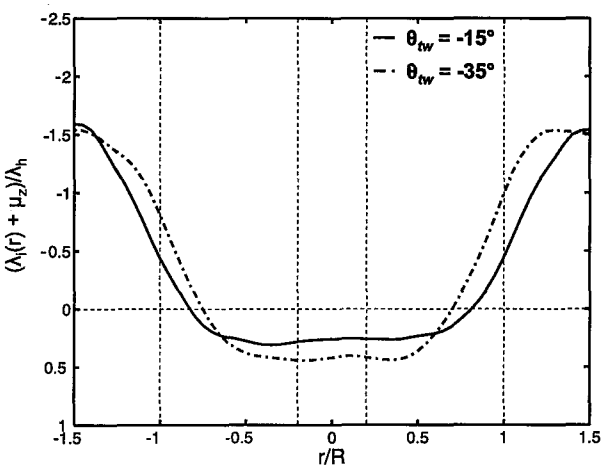
From these velocity profiles, it appears that the postponement to higher descent speeds




(a) At disc plane $r/R = 0$

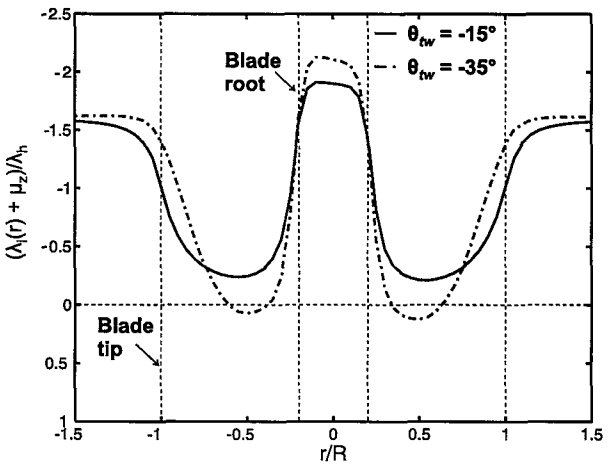



(b) 0.5R above disc plane $r/R = -0.5$

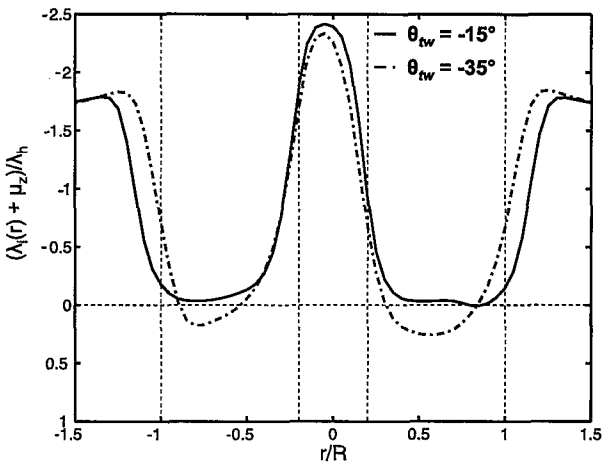



(c) 1R above disc plane $r/R = -1$

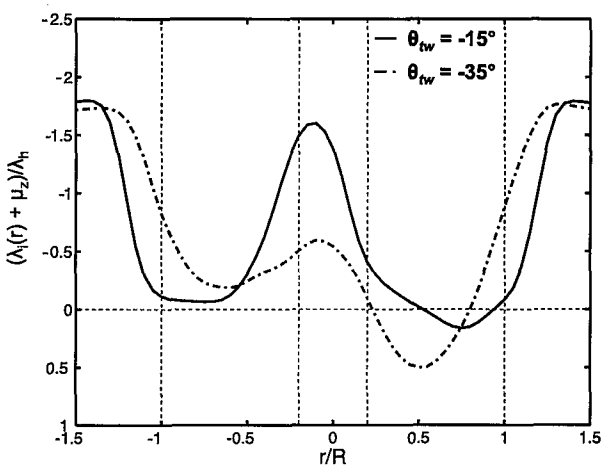
***Figure 5.18:*** *Profiles of mean flow velocity in a plane passing vertically through the rotor hub, arising over descent speed interval of* $1.3 \leq \bar{\mu}_z \leq 1.4$, *for rotor with blade twists of* $\theta_{tw} = -15°$ *and* $\theta_{tw} = -35°$.




(a) At disc plane $r/R = 0$




(b) 1R from disc plane $r/R = -0.5$




(c) 2R from disc plane $r/R = -1$

***Figure 5.19:*** *Profiles of mean flow velocity in a plane passing vertically through the rotor hub, arising over descent speed interval of* $1.5 \leq \bar{\mu}_z \leq 1.6$*, for rotor with blade twists of* $\theta_{tw} = -15°$ *and* $\theta_{tw} = -35°$.

of VRS cessation caused by blade twist (at least when the twist levels are high) can be associated with the increase in the velocity of downward flow over much of the inner section of the rotor blades that is engendered by an increase in blade twist rate. That the, inferred, higher tip-vortex convection speed of the rotor with greater blade twist, that is seen in these velocity profiles does not lead to the development of a longer and more coherent tip-vortex tube before such development occurs in the case of the rotor with the least twisted blades is not expected. However, if the wake dynamics associated with high-speed VRS that was discussed in detail in Chapter 3 are taken into account, then a postulation for why blade twist increases the VRS cessation speed can be constructed, as follows: It was shown in Chapter 3 that the vortex toroid that lies above the rotor plane is made up of a number of coherent ring-like vortex filaments that are trailed from the blade tips. As a ring is formed it is convected upwards away from the disc plane and expands radially as it does so. There comes a stage in the trajectory of the ring where it approaches the top of the small stack of vortex rings that form the toroid. Remember that the number of rings in the stack is limited by the rate of re-orientation and subsequent de-coherence of the vortex filaments that make up the toroid. As a tip-vortex reaches the top of the stack it begins to contract, radially, and the action of this contraction must then increase the self induced velocity of that ring-like filament, as it would if it behaved like a pure vortex ring. In addition, because the action of the radial contraction of the filament moves the vortex into the region of flow with generally higher downward velocity that was evident in the recently presented velocity profiles, the filament begins to move back down towards the rotor plane, inside of the stack of ring-like filaments. This recirculatory motion of the tip-vortex filaments is what generates the smeared, persistent features that lie just above the rotor plane in the locus plots of the wakes in VRS that correspond to the descent speed interval of $1.3 \leq \bar{\mu}_z \leq 1.4$ in Fig. 5.15. So, the postulation is, then, that if the velocity of the flow in the relatively high downward-speed region is reduced, by a decrease in blade twist, the convection of the top vortex ring in the stack down towards the rotor plane will be slower. If it is slower, then this will allow more time for local vortex pairing, rather than global ring recirculation, to take place and thus the recirculation of vortex filaments will occur further away from the rotor plane, than if the inner-disc velocities were higher, so allowing a longer, more coherent vortex tube to develop. So, the faster inboard downwash velocities induced by rotors with more highly twisted blades

prolong VRS cessation to higher descent rates because these higher velocities are able to maintain tip-vortex-filament recirculation close to the rotor plane at higher descent rates. This postulation remains to be tested but it is, nonetheless, supported by all the relevant evidence presented in this thesis.

This result is interesting since it is not clear as to whether it is in agreement with or contrary to what might be extrapolated from Leishman's analysis of the linear stability of rotor wakes [30]. That is to say, Leishman's results showed that the linear growth rate of small perturbations, to the strength or geometry of the flow field, increases with vortex strength and with decrease in the perpendicular separation distance between vortex filaments. The tip vortices of rotors with low rates of blade twist, as has been shown in the present work, are stronger than the tip-vortices trailed from rotors with relatively highly twisted blades and thus they convect upward from the rotor plane in high speed VRS conditions more slowly than those from more highly twisted blades and so should be closer together. It could be assumed from Leishman's results, or rather extrapolated from his results since Leishman did not consider the case high-speed VRS post its onset from lower speeds, that decreasing blade twist would make blade tip-vortices more susceptible to the actions of instabilities in the flow, and hence would break down more rapidly than the tip-vortices from rotors with more highly twisted blades. The effect of this is not clear, however. It could be that more rapid breakdown of the wake reduces its ability to generate downwash and hence such a wake would be lifted clear from the rotor plane at lower descent speeds than if the perturbation growth rates were smaller. This could explain the observations made herein but such an effect would be largely independent of the velocity field inboard of the blade tips. On the contrary, however, more rapid breakdown of individual filaments could lead to a more persistent vortex toroid that would require a higher descent speed to convect it above the rotor plane. But, this particular aspect of the flow physics could be countered by the faster upward, inboard, flow that is produced by rotors with lesser twisted blades. This higher flow velocity then suppresses the non-linear wake breakdown mechanism, discussed in Chapter 3, by preventing the ring-like vortices from evolving as they would naturally in a flow field without a free-stream. The result of this would be a recirculation of the ring-like vortices that takes place further away from the rotor plane and the consequent admittance of the earlier establishment of a structured tip-vortex tube, much as has been observed in the analysis presented in this chapter. The

unresolved nature of the foregoing argument suggests that there is interesting work still to do in this area. Indeed, it is a problem that perhaps further high resolution simulations and more complete stability analyses can resolve.

## 5.3 Comments on the effects of blade-stall on the VRS

The aerofoil model used in the foregoing simulations exhibited the $C_L - \alpha_e$ dependency shown in Fig. 5.20.

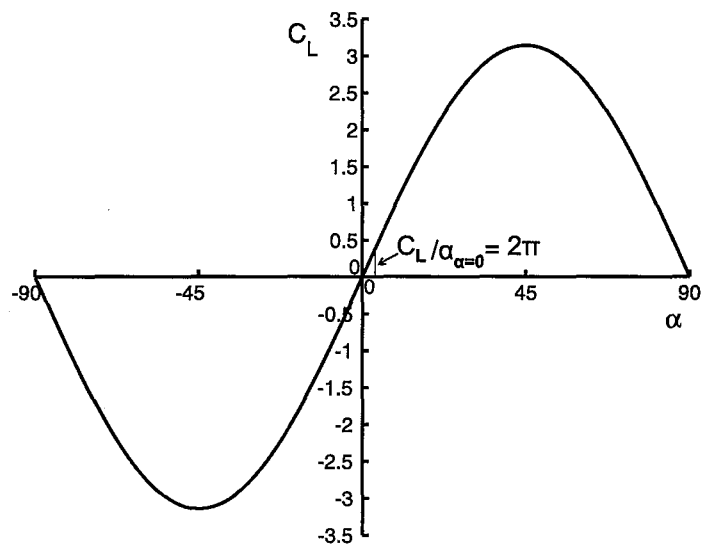



***Figure 5.20:*** *$C_L - \alpha$ relationship of a high aspect ratio ($AR = 30$) wing without viscous stall representation.*

The relationship shown in the figure is that predicted by the rotor aerodynamic model of the VTM for the mid-span of a wing with an aspect ratio of 30, i.e. the prediction is for an effectively two-dimensional aerofoil. Note that the prediction is different to that produced by standard lifting line theory: such an approach incorrectly predicts a non-zero force normal to the free-stream when the angle of attack of the aerofoil is 90°. This is due to the requirement of the method to ensure zero through-flow at the 3/4 chord line which is achieved by setting the appropriate non-zero value for the bound circulation at the 1/4 chord line. Clearly, in an inviscid flow, the streamlines around a flat plate oriented normal to the free-stream will be symmetrical about the centreline of the plate and thus the net lifting force applied to the plate will be zero. The modification to the prediction

of the $C_L - \alpha_e$ dependency of the standard lifting line method that has been applied in the VTM has been done so specifically to account for this discrepancy - the correction to the lifting line model ensures that the aerofoil generates zero lift when its angle of attack is 90°. Therefore, as was stated at the beginning of this chapter, viscous stall effects were omitted from the flow physics in this investigation - the lift coefficient would only fall with increase in angle of attack due to inviscid effects, but only at very high values of $\alpha$. The implication of such simplification of the governing fluid mechanics is that the effects of aerodynamic stall cannot be fully ascertained - the results just presented represent the pure case, they show what might happen if, somehow, stall could be avoided. Since flow separation from a lifting surface is sensitive to a considerable number of flow parameters such as the local free-stream turbulence, wing surface roughness, the recent history of the flow field, and, on rotating wings, spanwise flow, it is conceivable that the degree of stall and the character of the effects that stall will have on the behaviour of a rotor operating within the VRS will vary from test to test. The changes in behaviour of the rotor and its wake caused by stall are likely to be difficult to isolate from non-stall related effects in the results of the small number of experiments and flight tests that were discussed earlier. Therefore, stall may well be one of the causes of the sometimes conflicting findings that have been reported.

In their paper on the effects of blade twist, Brown and Leishman *et al.* [34] discussed the kind of effects that blade stall may have on the VRS behaviour of a rotor. They reported that an examination of data from FVM simulations of rotors with differently twisted rotor blades ($\theta_{tw} = -8°$ and $\theta_{tw} = -35°$), but both producing a high thrust coefficient of $C_T = 0.00966$ (to increase the likelihood of the occurrence of stall during the simulated descent of the rotors), provided some evidence that stall was more pronounced on the rotor with the most highly twisted blades. They also observed from these simulations that the effects of stall, at high descent rates, was to reduce the level of thrust fluctuations experienced by that rotor compared to the rotor with more moderate blade twist. Although careful inspection of their data, in isolation, certainly supports this claim, it appears that similar trends are apparent in the results from the FVM simulations of the same two rotors undergoing the same descent trajectory but when producing a much lower thrust coefficient of $C_T = 0.00362$ (and so were much less likely to experience blade stall). The reason given for the reduction of the thrust fluctuations was unsubstantiated though logical: flow

separation reduces the sensitivity of the aerofoils to local changes in flow velocity, hence the stalled blades responded to the highly unsteady VRS flow field by generating smaller increments in lift than they otherwise would if the flow remained fully attached to the blades. In addition, the thrust fluctuations experienced by both rotors in the high thrust simulations were significantly higher than those arising when the thrust was approximately three times lower. This is an interesting result in itself and suggests that either stall or blade loading can effect the severity of thrust fluctuations induced by a VRS encounter. Although, if stall were responsible for this result it would contradict the authors' ideas on stall effects. As an extension to their work on stall the authors made an interesting and partially successful attempt to isolate the influence of stall from the experimental VRS data of Yaggy and Mort [10] and Azuma and Obata [12]. Since high twist and low blade loading appeared to produce much higher thrust fluctuations at high rates of descent than the same rotor when producing high blade loads (contrary to the results from the FVM simulations) it was concluded from Yaggy and Mort's data that stall was responsible for the observed difference in the thrust fluctuations. Indeed, both sets of tests exhibited, to varying degrees, trends to this effect and so the authors' conclusions seemed viable.

The influence of stall has been addressed more recently by Ahlin and Brown [36] via numerical simulations using the VTM of rotors operating with constant collective pitch. Only moderate blade twist rates, ranging from 0° to −9.2°, were investigated. It was found that on the blades with the highest twist rate stall did indeed occur but only near the blade root at $r/R = 0.2$, just after the onset of VRS. The region of stall on the blades spread out to around $r/R = 0.44$ at the later stages of VRS, at $\bar{\mu}_z = 1.2$. An examination of the thrust and local blade loading fluctuations from the three rotors that were examined did not reveal any significant differences and thus it was concluded from this small set of tests that the presence of stall on rotors having blades with only slightly differing twist rates, produced no important effects.

Only the two-dimensional aerofoil characteristics are accounted for in the aerofoil model currently employed in the VTM, and therefore the effect of flow along the blade span on the $C_L - \alpha$ relationship of the aerofoils is not captured. Blade rotation modifies the velocity profile in the boundary layer on rotor blades which results in the postponement of blade stall to higher angles of attack [60]. Since stall becomes more likely as blade twist increases, it seems particularly important to account for these effects when simulating rotors with

highly twisted blades by using a suitable model. Such models have been developed by Du and Selig [78] or Corten [79], for instance. If the simulations of rotors with highly twisted blades featured in this chapter were to be conducted again, but with a standard 2D $C_L - \alpha$ relationship assigned to the aerofoils, any differences in behaviour that arises between the rotors that could be associated purely with stall may be misleading, or at least may be exaggerated. This is because the partial amelioration of flow separation afforded by the spanwise flow would not be accounted for. Arguably then, such computations should not be made until such time as an appropriate stall model has been implemented into the VTM.

Nonetheless, it is interesting and useful to examine the extent to which stall would have occurred on the blades of each the three rotors that were examined earlier in this chapter. For this exercise, then, allow that the aerofoil sections were of the NACA 0012 variety. It is assumed therefore that stall on a given section of the blades arises when the maximum lift coefficient of $C_{L_{max}} \approx 1.6$ is reached on the corresponding section. This assignation of aerofoil section is arbitrary but since it is commonly found on helicopters, especially on tail rotors, it provides a valid reference point. Figures 5.21, 5.22 and 5.23 show, as contour plots, the variation of the spanwise distribution of effective angle of attack, $\alpha_e$, and the corresponding lift coefficient $C_L$, with normalised descent rate, $\bar{\mu}_z$ for rotors exhibiting blades with twist $\theta_{tw} = -15°$, $\theta_{tw} = -25°$ and $\theta_{tw} = -35°$, respectively. In order to remove much of the obscuring high frequency fluctuation in the data that results from the highly unsteady VRS flow field, each data set has been filtered using a moving averaging window with a width of ten rotor revolutions. In addition, for the sake of clarity the regions in which either the angle of attack or the lift coefficient reach or exceed the stall values ($C_{L_{max}} \approx 1.6$, $\alpha_{e_{stall}} \approx 16°$), the contour patches were made entirely black such that the areas on the blade that would likely have suffered stall are clearly identified. It is important to bear in mind, though, that the extent to which stall occurs on the blades can only be validly considered at the descent rate at which stall first occurs. This is because the effects of stall on blade loading, and the way in which the thrust controller will vary the collective pitch of the blade to account for the ensuing loss of loading due to stall, are somewhat non-linear and are coupled to the non-linear response of the wake to the change in loading distribution. Thus the effects of stall on the behaviour of the rotors and their wakes, post the onset of stall, cannot be extrapolated from the results of these 'stall-free'

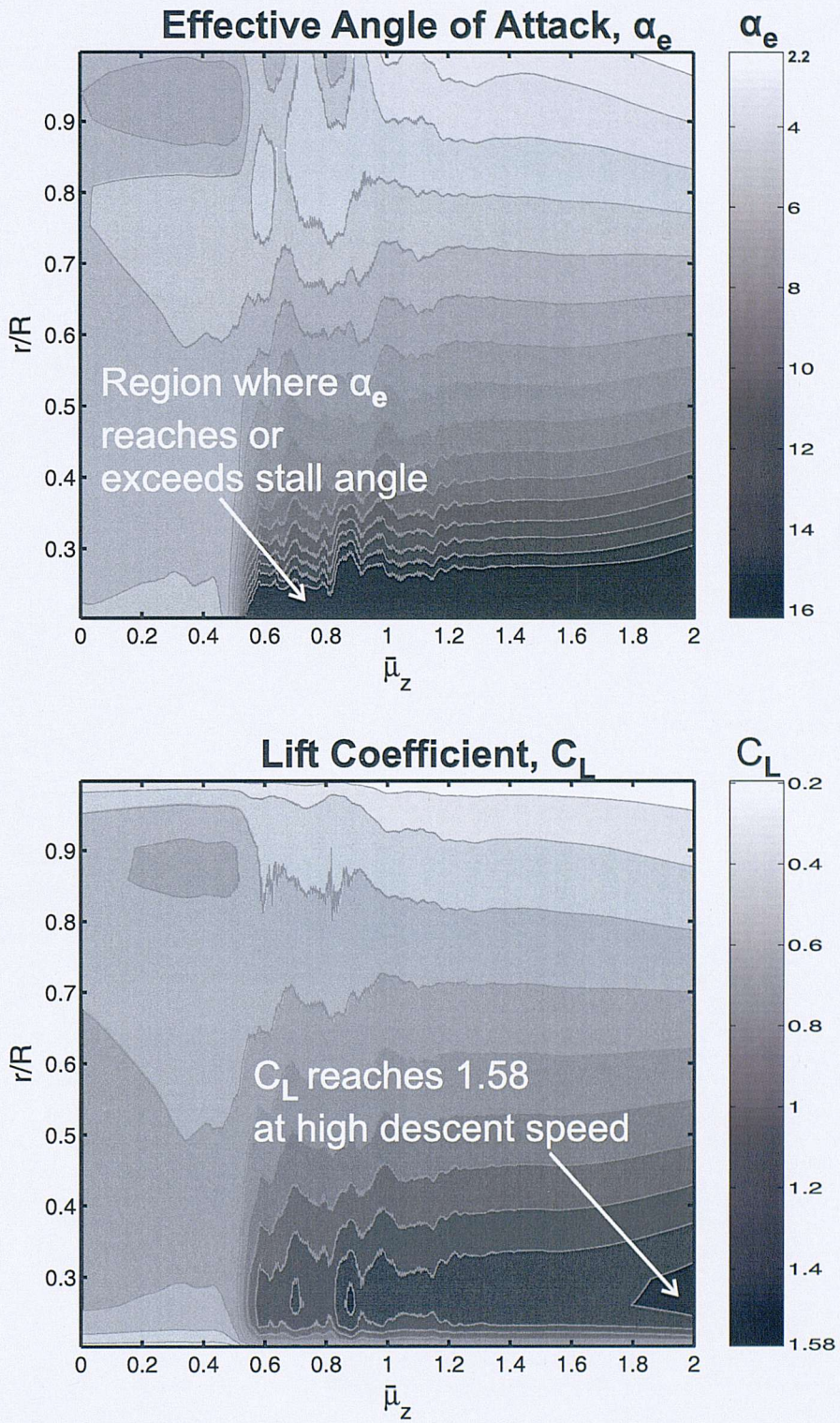



***Figure 5.21:*** *Spanwise distribution of effective angle of attack vs. normalised descent rate for the rotor comprising blades with* $-15°$ *of twist. Denoted stall characteristics assumed to be those of NACA 0012 aerofoil:* $C_{L_{max}} \approx 1.6$, $\alpha_{e_{stall}} \approx 16°$ .

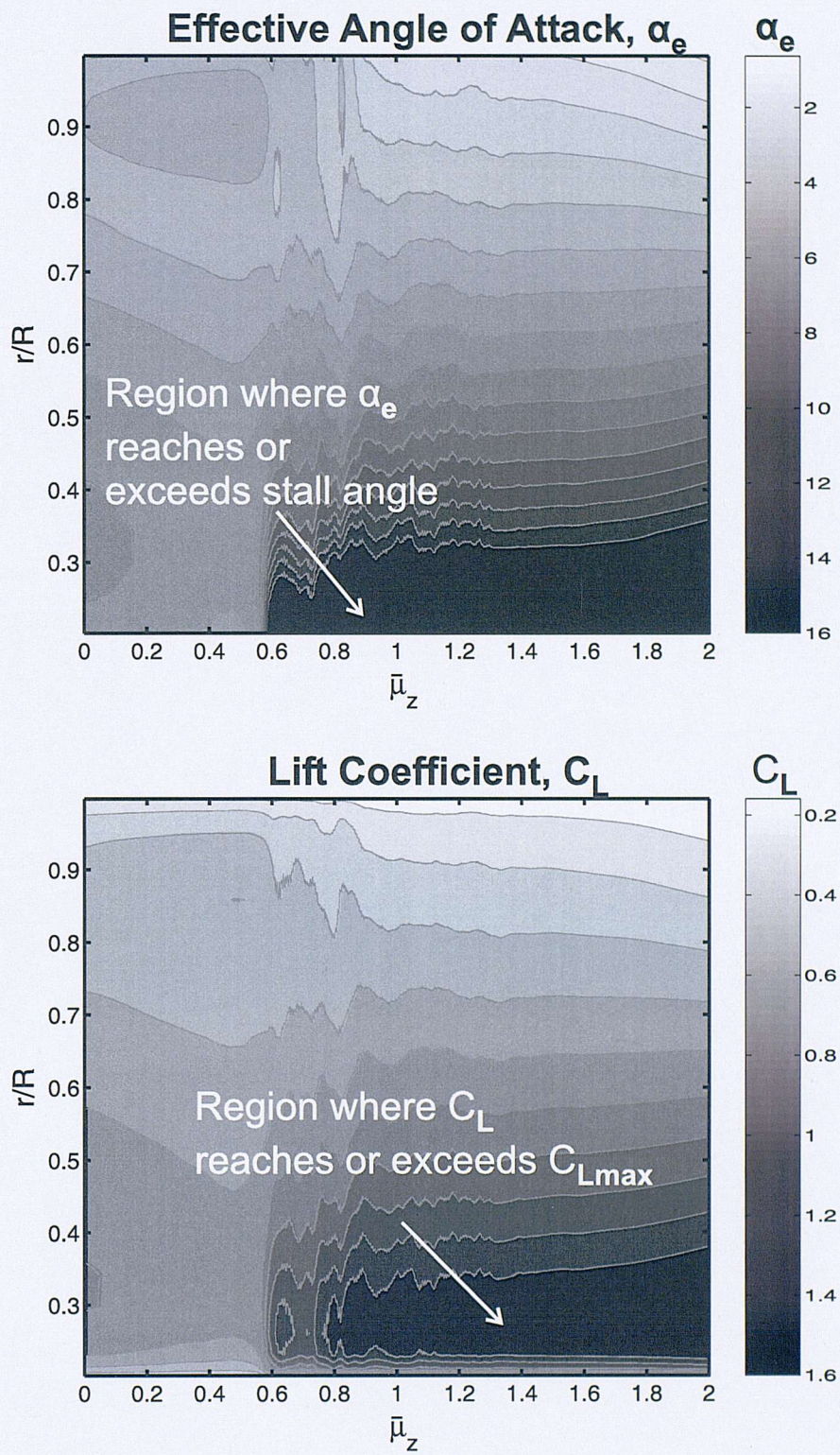



***Figure 5.22:*** *Spanwise distribution of effective angle of attack vs. normalised descent rate for the rotor comprising blades with* $-25°$ *of twist. Denoted stall characteristics assumed to be those of NACA 0012 aerofoil:* $C_{L_{max}} \approx 1.6$, $\alpha_{e_{stall}} \approx 16°$.

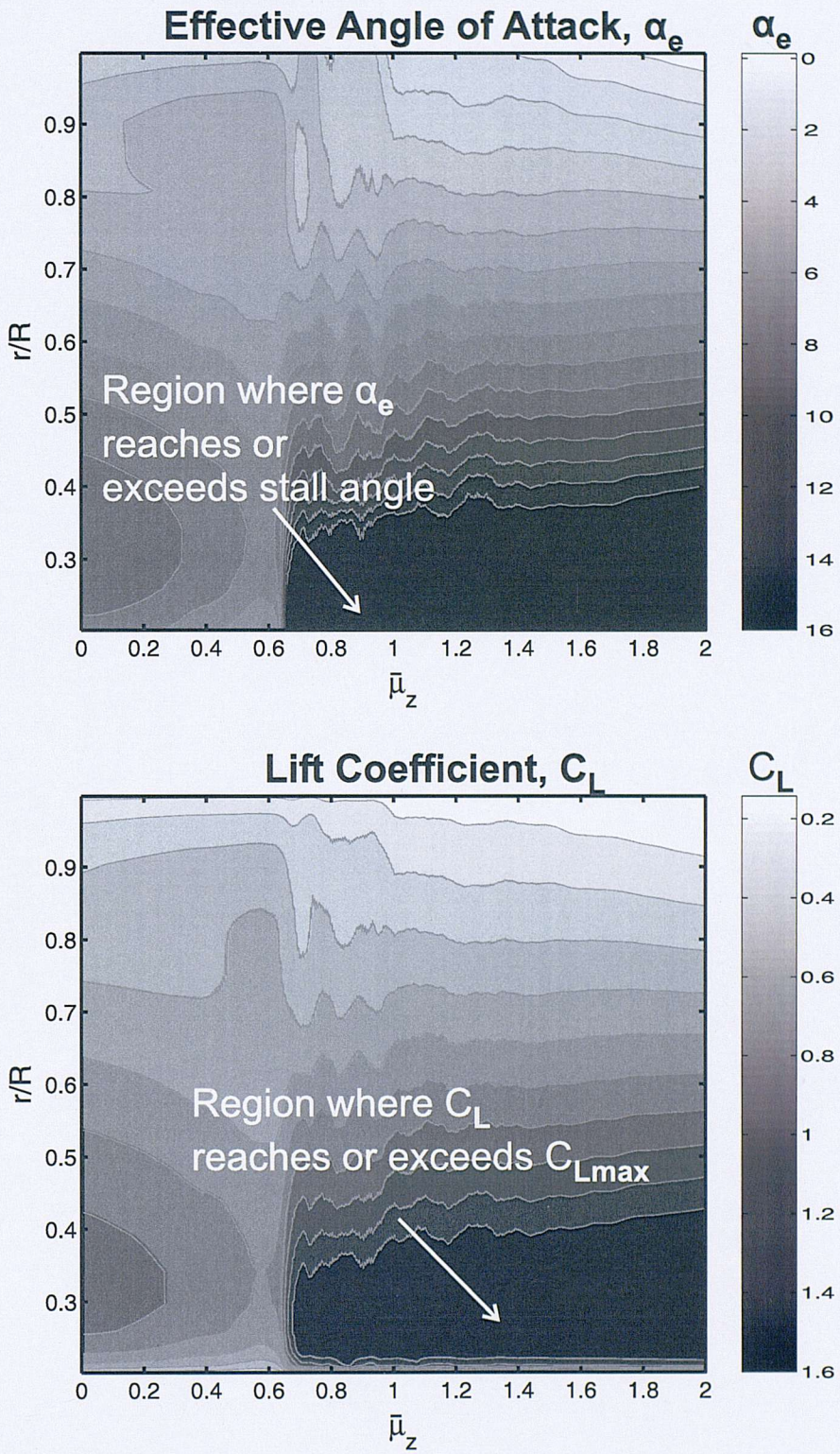



***Figure 5.23:*** *Spanwise distribution of effective angle of attack vs. normalised descent rate for the rotor comprising blades with $-35°$ of twist. Denoted stall characteristics assumed to be those of NACA 0012 aerofoil: $C_{L_{max}} \approx 1.6$, $\alpha_{e_{stall}} \approx 16°$.*

simulations. It is expected that regions of separated flow that occurs on blades, modelled to have a standard, non-linear $C_L - \alpha$ relationship, during high speed descent will be larger than those indicated in the present figures since the geometric angle of attack of the blades would normally be increased if stall arose in order to maintain the thrust at its prescribed value.

Figure 5.21 shows the variation of the distribution of $C_L$ and $\alpha_e$ on the blades with twist $\theta_{tw} = -15°$. It can be seen that the stall angle is first achieved only very near to the root of the blade and occurs at the descent speed $\bar{\mu}_z \approx 0.55$. But, since the effective angle of attack output from the VTM is only the angle predicted by the lift model algorithm it can vary from the correct value by a small amount, however, especially when there are large changes in the flow velocity between the 1/4 chord line and the 3/4 chord line of the blade. The lift coefficient, however, is the value that corresponds to the value of bound circulation that gives a zero blade-normal velocity at the 3/4 chord line and is therefore the more reliable of the two measures. The angle of attack measure is needed, though, to provide a basis of rationale for the observed variations in the lift coefficient. It can be seen from the contour plot of $C_L$ that the maximum lift coefficient is not quite achieved during the descent speed range presented. A peak value of $C_L = 1.58$ is achieved at a descent speed of $\bar{\mu}_z \approx 1.8$, i.e. when the rotor is in the windmill brake state, and occurs close to the blade root, only. Stall is very much in evidence, in that $C_{L_{max}}$ was reached or exceeded, on the other two rotors, however. In the case of the rotor with blades exhibiting a twist of $\theta_{tw} = -25°$, in Fig. 5.22, the maximum lift coefficient for the NACA 0012 aerofoil is reached at a descent speed of $\bar{\mu}_z \approx 0.8$, but, once again, the stall is confined to the inboard sections of the blades only (from $0.22 < r/R < 0.32$). As can be seen, the stall region spreads slowly from inboard towards the mid-span as descent speed increases. But as was discussed earlier, the spreading of the stall region is unlikely to be representative of the real case, though it may give a vague indication of what might happen in reality. Stall on the most highly twisted rotor blades first occurs at a descent speed of $\bar{\mu}_z \approx 0.65$ and spans the region $0.22 < r/R < 0.35$, approximately.

As expected then, the region of the blades on which stall occurs increases with blade twist rate, though stall barely manifests on the least twisted of the rotors featured here. In addition, the descent speed at which stall first occurs decreases with increase in blade twist. It is extremely important to note however, that on the two rotors with the least

twisted blades, stall first initiates post VRS-onset (if the onset speed is defined as that speed where a sharp increase in thrust fluctuations is observed to occur). In the case of the rotor with the most twisted blades, however, stall appears to coincide with the onset of VRS. Using the behaviour of the lift coefficient, once again, as the marker for stall approach and onset, it can be seen that on the inboard sections of the blades with twists of $\theta_{tw} = -15°$ and $\theta_{tw} = -25°$ the lift coefficient increases steadily, just prior to a short region of slightly more rapid rate of change of $C_L$, until $C_{L_{max}}$ is reached. That is, the onset of stall is quite gradual in these two cases. However, on the rotor with the most highly twisted blades, stall initiation is abrupt and follows a region of relatively low and slowly varying lift coefficient. This markedly different behaviour suggests that in this latter case, stall followed, or was caused by, the collapse of the rotor wake, i.e., VRS onset initiated blade stall in this case. In the former two cases, stall more likely occurred due to the more gradual increase in the velocity of the upward flow over the inboard sections of the two rotors that occurs once the VRS has developed. This interpretation of the results is highly significant - it suggests that, just like when the level of blade twist is moderate, stall does not affect VRS onset even at the high levels of blade twist featured in the present work. It may, however, affect the speed at which a rotor exits from the VRS, though it was not possible to examine this aspect of the vortex ring phenomenon with the present simulations.

## 5.4 Summary

An investigation into the effects of blade twist on the behaviour of a rotor and its wake as the rotor descends into, within and out of the VRS has been presented. The blade aerofoil model used in the study did not include a representation of viscous stall, thus stall was prevented by allowing the blades to behave only as idealised lifting lines in an inviscid fluid. The onset of aerodynamic stall is partly dependent upon the magnitude of the blade twist, thus the amount of blade twist would influence the descent speed at which stall occurred. Allowing stall to occur, therefore, would obscure the manner in which the inflow distribution, which is a function of the blade twist, influences VRS behaviour. Omitting blade stall thus allowed the importance of inflow distribution to be readily exposed.

An examination of thrust fluctuations and rotor torque revealed that the sudden increase and subsequent reduction in both the amplitude of thrust fluctuations and the levels of rotor torque that are brought about by the onset and cessation of the VRS, respectively, are postponed to higher descent rates by an increase in blade twist. It was also shown that blade twist has only a small, but ambiguous influence on the severity of the fluctuations of the thrust produced by the rotor. Averaging instantaneous snap-shots of the vorticity field that arose over various pertinent ranges of descent speeds allowed the geometry of the resulting locus plots of the vorticity in the flow during those speed ranges to be examined. The geometry of the vorticity loci showed that as twist rate increases, the corresponding rotor wakes maintain their initial hover-like tubular geometry to higher descent rates, prior to the onset of VRS. In addition, inspection of the changing wake geometries during the process of the collapse of the rotor wake, revealed signs that a precursor to the total collapse of the wake as the rotor enters the VRS regime is the initial breakdown of the root vortex system. Further evidence to support this claim was gleaned from the variation with descent speed of the spanwise distribution of the downwash velocities over the rotor blades. It appears that the downwash velocity in the region of the blade roots decreases suddenly at a lower descent rate than the downwash velocity increases over the outboard sections of the blades, though the difference is very subtle. It is postulated that these observations indicate, since the root vortex system provides a component to the total downwash in the wake, that even a partial collapse of the root vortex system will remove part of this component of the downwash which then leads quickly to a corresponding collapse of the tip-vortex system.

Inspection of the velocity fields produced by each rotor showed that there is a link between the speed at which VRS occurs and the inflow velocities over the inboard sections of the rotor - the higher the inboard downwash velocity the higher the speed of VRS onset. The velocity of the downwash in the vicinity of the root vortex system governs the transport velocity of the helical root-vortex filaments. Thus, the higher these velocities the larger will be the pitch of the root-vortex helix, and hence the lower the rate of disorganisation of the helix due to the action of its inherent instabilities [30]. It was shown in Chapter 3 that disorganisation of the far wake leads to truncation of the wake. Ultimate collapse of the wake of a descending rotor follows the truncation once the descent speed becomes high enough to initiate VRS. This observation implies, then, that if the

rate of disorganisation of the root-vortex helix is dependent upon the transport velocity of the vortex filaments in that helix, then the descent speed at which the collapse of the helix occurs is also dependent upon this transport velocity. It is suggested then, that the delay of initiation of the VRS afforded by rotors with more highly twisted blades results from the higher transport velocities of their root-vortices and the consequent postponement to higher descent speeds of the collapse of their root vortex systems.

Inspection of the wake geometries arising at speeds around which the rotors exited the VRS revealed that increasing blade twist increases the cessation speed of the VRS. Inspection of the local velocity fields showed that the velocity of the upward flow near to the rotor tips decreases with decrease in twist rate, as a result of the stronger tip vortices generated by such rotors. That the rotor with the least twisted blades exited from the VRS at a lower speed than the rotors with more highly twisted blades, is at odds with the received wisdom regarding the importance of the transport velocity of the tip-vortex system. As in the case of low speed descent, prior to VRS, the induced flow over the inboard sections of the rotors during high speed descent increases with negative twist rate, and thus it appears that it is the higher inboard induced flows generated by rotors with more highly twisted blades that prolongs VRS cessation to higher descent speeds. It was postulated that this behaviour arises because the recirculation close to the rotor plane of the tip-vortices in the vortex toroid of the VRS is maintained to higher descent rates by the higher inboard downwash velocities induced by rotors with more highly twisted blades.

An examination of where on the blades and at what descent speeds the maximum lift coefficient of an arbitrarily chosen aerofoil, the NACA 0012, would occur was presented. It was shown that on none of the rotors examined here would stall have occurred prior to the initiation of VRS. Therefore, even in the cases of the high rates of blade twist considered in this work, blade stall does not influence the VRS onset speed of a rotor. The onset of VRS caused the max lift coefficient of the NACA 0012 aerofoil to be reached abruptly on the rotor with the most highly twisted blades considered in this study. It was argued this was due to the large and sudden increase in up-flow over the blade root sections that occurs during VRS onset. Stall arose more gradually, post VRS onset, on the rotors with less twisted blades. It can be concluded, therefore, that whilst stall does not effect the onset of the VRS of rotors with blades twisted by at least $-35°$, stall will

certainly occur at some stage during the VRS on rotors with highly twisted blades and will thus influence the character of the VRS experienced by these rotors, in some manner. The effect of stall of the behaviour of the VRS is postulated as follows: The presence of stall, which first occurs over the inboard sections of the blades, after the onset of the VRS, will reduce the magnitude of the lift generated by this region of the blades and thus the strength of the root-vortex system will be reduced as a consequence. In trimmed flight, the collective pitch will be adjusted to maintain the thrust at a constant level with the likely result being the production of a stronger tip-vortex system. As stall occurs at lower descent speeds and over a larger region of the blade as twist is increased, the influence of stall on the strength of the root and tip-vortex systems will be more pronounced on rotors with more highly twisted blades. Therefore, the influence of blade twist on the descent speed at which VRS cessation occurs will be at least partially negated by the presence of stall. Indeed, based on this postulation, it is conceivable that the effects of blade twist that have been exposed in this chapter could even be reversed by stall, if the behaviour of a rotor with blades of zero of very low twist were compared with that of a rotor with very highly twisted blades. This is merely conjecture however, and the effects of viscous stall on the behaviour of rotors in descending flight have yet to be systematically investigated.

As stall effects were not included in the present investigation the findings reported in this chapter can be generalised. This work has not only exposed the influence of blade twist on the behaviour of a rotor flying within the VRS, but more than that, it has provided guidance on how, generally, the distribution of the velocity of vertical flow over the rotor affects the flight of a descending rotor. This is important because the distribution of vertical flow velocity is modified by several different rotor parameters, such as spanwise variation of blade planform, the root cut-out length, and the spanwise variation of aerofoil section.

The findings of this work have implications for the modelling of the VRS and of rotor wakes generally. As was mentioned earlier, Bhagwat's and Leishman's analysis of the effects of blade twist on the linear stability of the tip vortex system of a rotor wake [6] showed that increasing the twist rate causes small perturbations in the flow to grow faster due to the reduction in tip vortex spacing that higher twist rates engender. It was implied, therefore, that the onset speed of the VRS is *decreased* by an increase in blade twist. This conclusion is in direct opposition to the findings presented in the present work. It

is suggested that the heart of this disagreement lies in the omission of the root vortex system from Bhagwat's and Leishman's analysis. A further, related implication then, is that confidence in the results of free-wake simulations that address the onset and cessation points of the VRS for any given rotor can only be obtained if the wake model includes a full representation of the root-vortex system in addition to the tip-vortex. Currently, such an inclusion is not common practice. This is especially important since this work has shown that the contribution to the induced downwash of the wake of the root vortex system is arguably the prime driver of twist-related changes to the behaviour of a rotor and its wake in descending flight.

# Chapter 6

# Effect of the Mode of Operation of the Rotor on VRS Behaviour

## 6.1 Introduction

The axial flight speed of a rotor has in the past been scaled, for purposes of generality, by the mean induced flow velocity that occurs when the rotor is in hover, $\lambda_h$, as calculated by $\sqrt{(C_{T_h}/2)}$. Often, workers in the field of VRS research present graphs that show the inflow vs. descent speed (scaled with $\lambda_h$) relationships of rotors from past experimental investigations into VRS. On occasion, the graphs presented show the inflow of just one rotor that was used in a past experiment, though these are juxtaposed with results from other experiments in separate graphs (see Johnson [80] for instance). Whilst on other occasions, results from several experiments are set on the same graph [30]. Such comparisons, implied or otherwise, are generally acceptable if the aim is to identify trends in the effects of blade twist, or blade loading, for instance. An important difficulty arises from such comparisons, however, when the rotors involved in the various experiments were flown under different modes of operation. Some experiments involved flying the rotor at varying descent speeds whilst the collective pitch of the rotor was held constant [10, 12, 16, 22, 23, 24] whilst in other experiments, including flight tests, the operational aim was to hold the thrust nominally constant by adjusting the collective pitch when the descent speed was altered [1, 11, 19, 81]. A possible source of concern, in terms of the validity of the comparisons that have previously been made between two or more data sets that differ in this

way, stems from the fact that descent under the conditions of the former operational mode causes the thrust, in general, to rise significantly with increase in descent rate. This effect occurs due to the increase in the effective angle of attack, $\alpha_e$ of the rotor blades caused by the accompanying reduction in net velocity, $(\lambda_i + \mu_z)$, of the flow over the blades. If the descent speed against which the induced inflow, or any other rotor performance measure, is normalised by the inflow generated at hover, it is clear that such universal application of this scaling will modify the resulting trends. Despite the transparency of this potential perversion of the observed behaviours and the subsequent invalidation of any comparisons that may have been made, this matter has received little attention in the literature, though Ahlin and Brown have remarked upon it recently [36].

The aim of this chapter is to explore the differences in behaviour that arise when rotors are flown through the VRS under the conditions of the two aforementioned modes of operation. Furthermore an alternative method of scaling the descent speed, thrust and power, is suggested, in order to allow fairer comparisons between the inflow results obtained from unrelated experiments, flight tests and numerical investigations into the rotors in descending flight.

## 6.2 Results

Two simulations of Gao's [16] rotor in descending flight were conducted for this study. The rotor is defined in Table 2.1. In both simulations, the rotor, flying axially, underwent a linearly accelerated descent, where the acceleration rate was $\dot{\mu}_z = 0.007/\text{rev}$. The trajectory of the rotor commenced in hover and passed through the VRS and finished in the WBS. In the first simulation, the thrust generated by the rotor was controlled to remain nominally constant at $C_T = 0.00737$. In the second simulation, the collective pitch, $\theta_0$, of the rotor blades was held constant, throughout the rotor's descent, at an angle that allowed the rotor to produce the aforementioned thrust coefficient when in hover. The flap and lag dynamics of the rotor were suppressed. In addition, viscous stall effects were omitted from the aerofoil model so that the lift-angle of attack relationship was as defined in Fig. 5.20. This simplification was made in order to allow the differences in VRS behaviour caused by the two modes of operation to be exposed without the behavioural variations being obscured by the effects of stall.

Figure 6.1 shows the variation in thrust with descent speed scaled with the inflow at hover, $\lambda_h$, that was generated by the rotor when operating under the operational modes of constant collective pitch and constant thrust. The raw data from the computation has been filtered using a moving averaging window with a width of ten rotor revolutions to expose only the low frequency variations in the thrust signals that are the most significant symptoms of the vortex ring state. As expected, when the collective pitch of the rotor is held fixed the thrust is seen to rise considerably, aside from a very noticeable drop in the thrust generated by the rotor that commenced when the descent speed $\bar{\mu}_z \approx 0.6$. The sudden drop in thrust is due to the thrust settling phenomenon that was discussed in detail in Chapter 4 of this thesis. After an abrupt recovery of the thrust level at $\bar{\mu}_z \approx 0.9$ the thrust then rises, in general, with descent speed. Such a rise in thrust would not continue indefinitely, however, since the theoretical lift coefficient, $C_L$, of the idealised aerofoil modelled in this investigation reduces post an angle of attack of 45° and in reality, viscous stall would limit the ultimate thrust produced by the rotor.

When the thrust level is controlled to be nominally constant the sharp reduction in the thrust that is evident when the collective pitch is held constant is prevented by an increase in the collective pitch by the thrust controller though low frequency fluctuations do, nonetheless, manifest at a descent speed similar to when the thrust reduction occurs in the fixed $\theta_0$ case. The large, low-frequency thrust oscillations that arise at this stage in the descent of the trimmed rotor are different in character to those that occur when $\theta_0$ is fixed. That fluctuations occur at all when the thrust is being controlled might be attributed to the response rate of the first-order controller used to maintain the desired thrust level. The rate constants in the controller model are set specifically not to suppress these oscillations. The thrust fluctuations appear to subside at a descent rate $\bar{\mu}_z \approx 1.6$, after which the thrust generation of the rotor becomes steady.

The magnitude of the thrust fluctuations represents more clearly, though still indirectly, the unsteadiness of the flow field in which the rotor operates in each of the two cases. Figure 6.2 presents the standard deviations about the mean of the thrust fluctuations that were generated in each of the two cases. As before, the data has been filtered using a moving window with a width of ten rotor revolutions. The onset of significant thrust variability occurs at approximately the same descent speed in each of the two cases, though the subsequent rate of increase in the fluctuations is slightly higher in the controlled case.

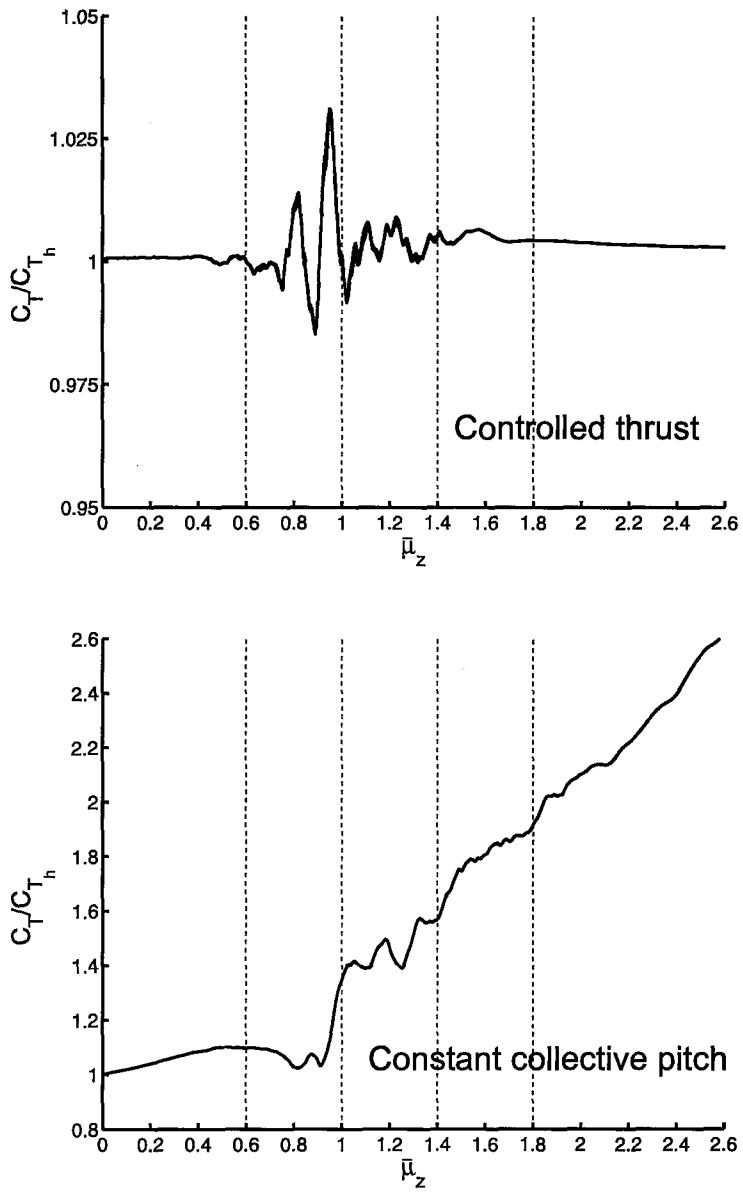



***Figure 6.1:*** *Thrust coefficient, normalised by thrust coefficient arising in hover, from simulations of a rotor operating with either constant collective pitch, $\theta_0$, or nominally constant thrust, undergoing an axial descent through the VRS to the WBS from an initial hover.*

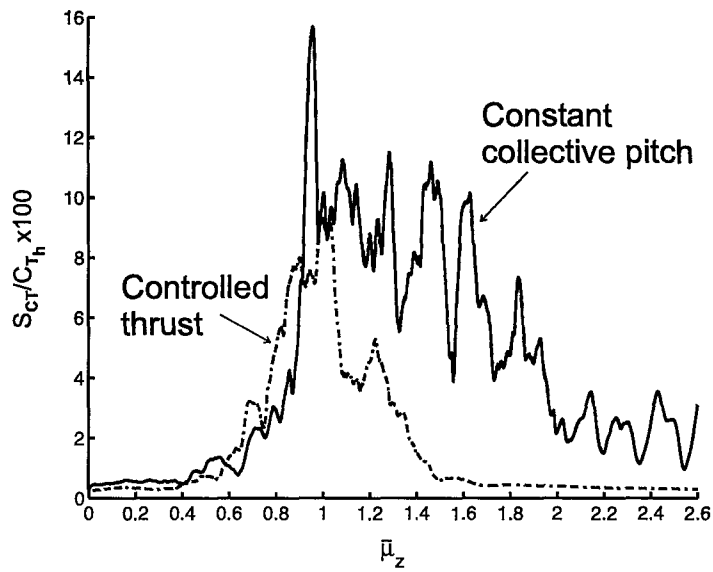



***Figure 6.2:*** *Standard deviation of fluctuations of thrust, as a percentage of the mean thrust, from simulations of a rotor operating with either constant collective pitch, $\theta_0$, or nominally constant thrust, undergoing an axial descent through the VRS to the WBS from an initial hover.*

As has been discussed before in this thesis, the initiation of large thrust fluctuations indicates the appearance of the incipient phase of the VRS. The differences between the two modes of operation, then, have only subtle manifestations prior to the full development of the VRS. Upon the occurrence of the largest fluctuations in thrust, in both cases, the nature of the thrust signal then differs greatly. The peak thrust fluctuation that arises when the collective pitch is held constant is approximately 16% of the mean thrust, compared to an amplitude of around 10% when the thrust is controlled. It should be noted though, that since the rotors are in a constantly accelerating descent the geometry of the wake is constantly changing. Therefore the short lived peak in thrust fluctuation of the constant $\theta_0$ case that arises at $\bar{\mu}_z \approx 0.95$ may actually be smeared out if the standard deviation were to be taken from a simulation of a rotor operating at a similar constant descent speed. More importantly, though, is the persistence of thrust fluctuations above around 4%, from $\bar{\mu}_z \approx 0.95$ to $\bar{\mu}_z \approx 2$ that occurs when the the collective pitch is held constant. This contrasts strongly with the behaviour of the controlled rotor since in that case the fluctuations of the thrust fall to amplitudes similar to those that arose prior to the onset of VRS (at around 0.5%), at a desent speed of only $\bar{\mu}_z \approx 1.5$. It appears from this figure, then, that the range of descent speeds over which the rotor remains within

the VRS is very much larger when the collective pitch is held constant. It is clear, then, that VRS behaviour is sensitive to the mode of rotor operation, or appears to be be so, at least, when the performance and flight parameters are scaled in the standard fashion.

Inspection of the wake geometries generated by the rotor in each of its two operating conditions provides evidence that supports the inferences related to the behaviour of the wake made in the preceding paragraph. Figure 6.3 shows the locus of the vortex wake produced by the rotor during descent intervals: $0.2 \leq \bar{\mu}_z \leq 0.3$; $0.5 \leq \bar{\mu}_z \leq 0.6$ and $0.7 \leq \bar{\mu}_z \leq 0.8$. The iso-surfaces used to realise these 3D plots were set to the same value in each case. Each locus plot was constructed from the average of a sequence of 14 instantaneous snap-shots of the rotor wake. At some of the descent intervals featured the wake is highly unsteady thus the effect of the averaging process is to highlight the strong and most persistent structures, in terms of position, and to smear out the weaker, or more spatially fluctuating regions of the flow field, as discussed in § 2.7.2. Within the intervals $0.2 \leq \bar{\mu}_z \leq 0.3$ and $0.5 \leq \bar{\mu}_z \leq 0.6$ there is little of significance to distinguish the geometries of the wakes from the two cases that arose during these descent speed intervals. It may be argued, though, that during the descent speed range of $0.5 \leq \bar{\mu}_z \leq 0.6$ the wake produced by the rotor with fixed collective pitch exhibited a more structured root-vortex system than is apparent in the wake produced by the rotor producing a nominally constant thrust. In the interval $0.7 \leq \bar{\mu}_z \leq 0.8$ it can be adjudged that the degree of wake breakdown is greatest, and hence occurs earlier, when the thrust is held constant. These results are consistent with the effects inferred from the thrust fluctuation data shown earlier.

Figure 6.4 shows locus plots of the wake that arose from four different descent speed intervals that cover four stages of high-speed descent within the VRS. In the first two descent speed intervals featured in this figure, i.e. during the speed ranges $0.9 \leq \bar{\mu}_z \leq 1.0$ and $1.1 \leq \bar{\mu}_z \leq 1.2$ both rotors were in a fully developed vortex-ring-state and the overall geometries of the wakes are quite similar. That said, though, there does appear to be a greater level of disorder in the fixed $\theta_0$ case. In addition, since each case used the same iso-surface level to realise the locus plots, the quantity of vorticity that persisted below the rotor plane can be seen to be greater when the collective pitch was held constant, signifying that a higher mean inflow was generated by that particular vortical wake. In the speed interval $1.2 \leq \bar{\mu}_z \leq 1.3$ the rotor with fixed collective pitch remained in the VRS whilst the wake of the trimmed rotor shows signs that it was exiting the VRS by that stage

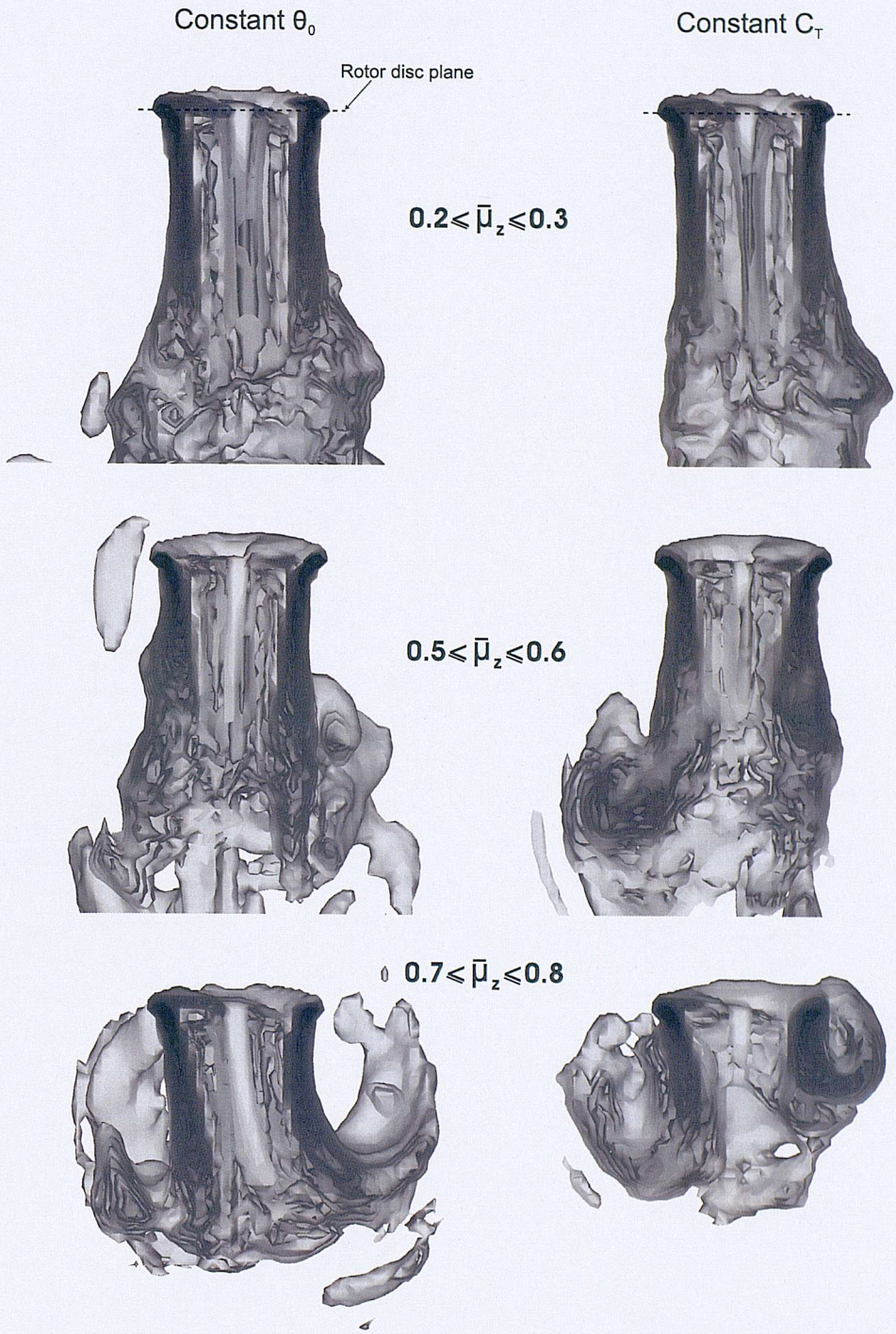



***Figure 6.3:*** *Iso-surfaces of the locus of the vorticity field arising over three, pre-VRS, descent speed intervals. The highest (darkest) vorticity level shown is 5 times greater than the lowest level.*

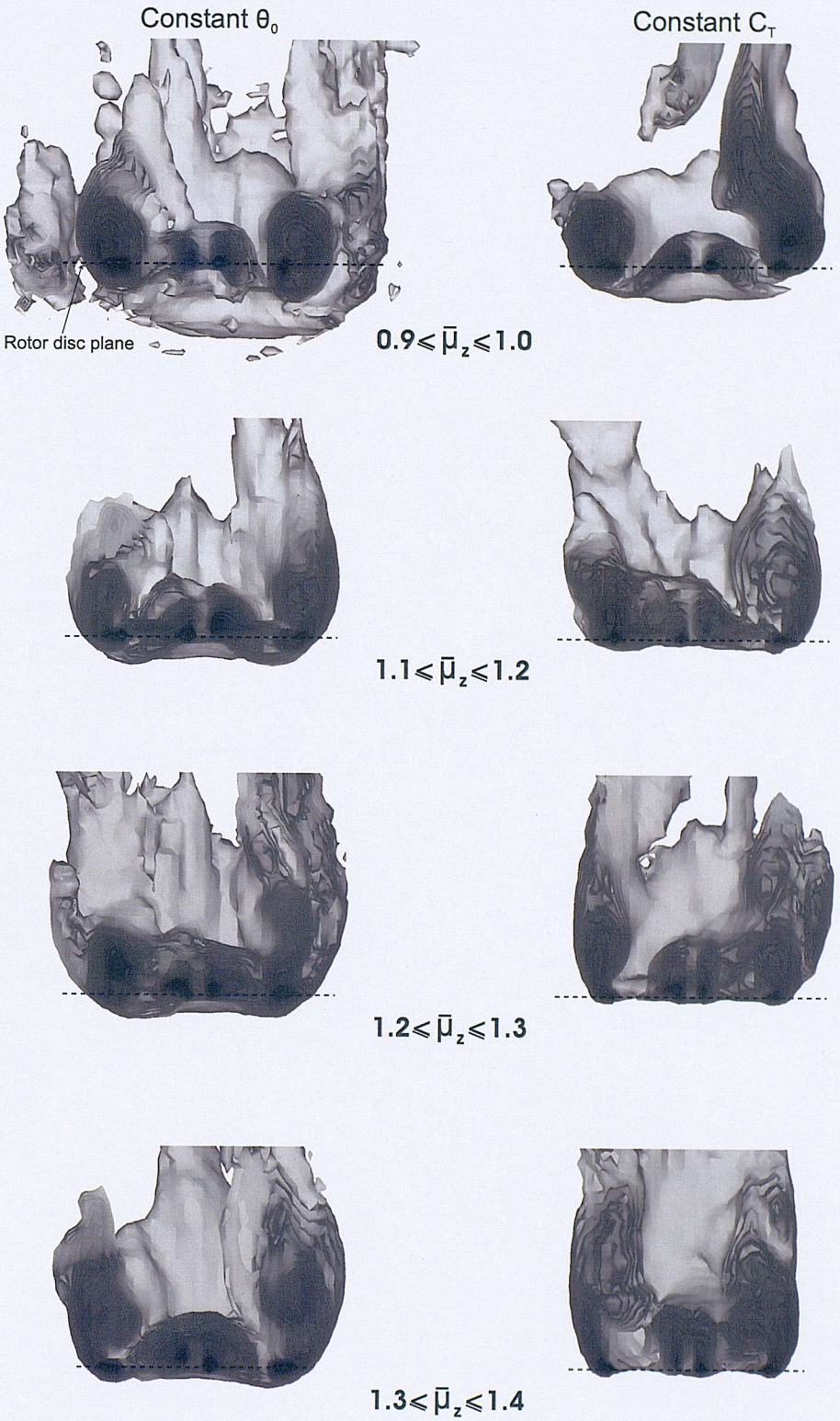



*Figure 6.4: Iso-surfaces of the locus of the vorticity fields arising over four, in-VRS, descent speed intervals. The highest (darkest) vorticity level shown is 5 times greater than the lowest level.*

of its descent. In the higher speed interval of $1.3 \leq \bar{\mu}_z \leq 1.4$ the wake produced by the trimmed rotor had lifted just off the rotor plane and a truncated tubular structure had formed from the tip-vortices. The root-vortex system also exhibits a truncated tubular structure, though, in both cases, these structures break down less than a rotor radius in distance above the rotor. In contrast, part of the wake produced by the rotor with fixed collective pitch was advected below the disc plane during this range of descent speeds. Furthermore, the tip and root-vortex systems exhibit signs of recirculation and possess a geometry that is more toroidal than tubular.

Figure 6.5 shows the locus of the wakes, from each case, that arose during the higher descent speed intervals of $1.4 \leq \bar{\mu}_z \leq 1.5$ and $1.6 \leq \bar{\mu}_z \leq 1.7$. It is at these higher descent speeds where the wake geometries are the most dissimilar. Whilst the rotor with fixed collective pitch was flying very much within the VRS, during both descent speed intervals, it appears however that operating with controlled thrust engenders definite cessation of VRS and entry into the WBS over the interval $1.6 \leq \bar{\mu}_z \leq 1.7$, as was suggested by the thrust data presented earlier. This is strong evidence to support the notion that a steady

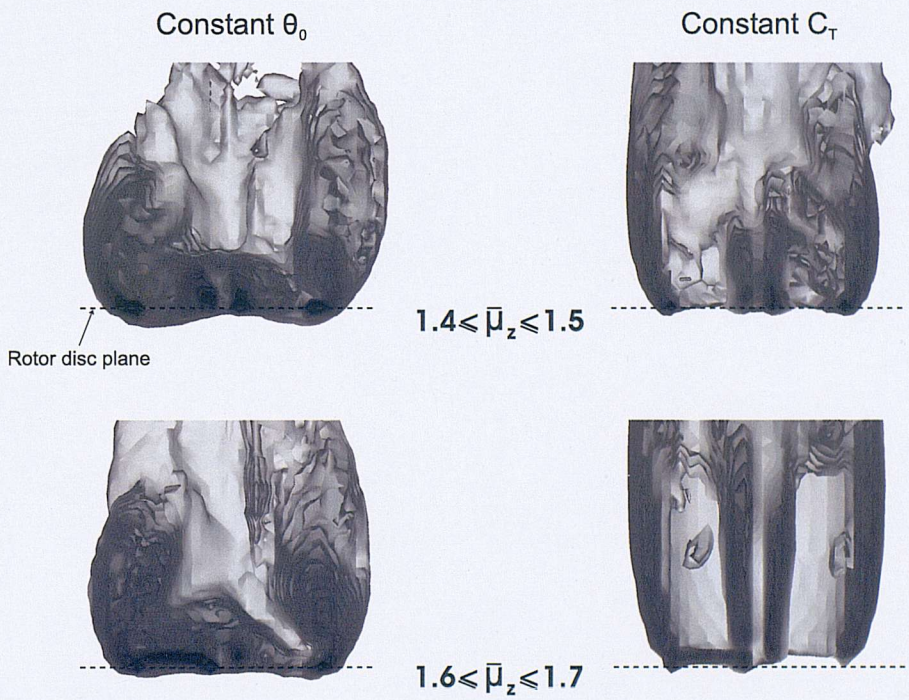



***Figure 6.5:*** *Iso-surfaces of the locus of the vorticity field arising over a descent speed interval of* $\Delta\bar{\mu}_z = 0.1$. *The highest (darkest) vorticity level shown is 5 times greater than the lowest level.*

increase in rotor thrust with descent rate increases the area of the flight envelope over which the VRS occurs. This has important consequences for the assessment of a rotor's behaviour in the VRS - the mode of operation of the rotor must be accounted for when scaling the descent speed.

The magnitude and the distribution of the rotor inflow are important factors governing the onset and cessation speeds of the VRS, as was demonstrated in Chapter 5. To understand the reasons behind the differences in the observed wake behaviour and in the VRS cessation speeds in particular, in the present work, the magnitude of the net velocities of the vertical flow $\lambda_z(r) = \lambda_i(r) + \mu_z$ over various stations along the rotor blades was evaluated. Figure 6.6 shows $\lambda_z(r)$ over the blades of the rotors, where the data has been filtered using a moving averaging window with a width of ten rotor revolutions. The net vertical velocity, $\lambda_z(r)$, is positive downwards.

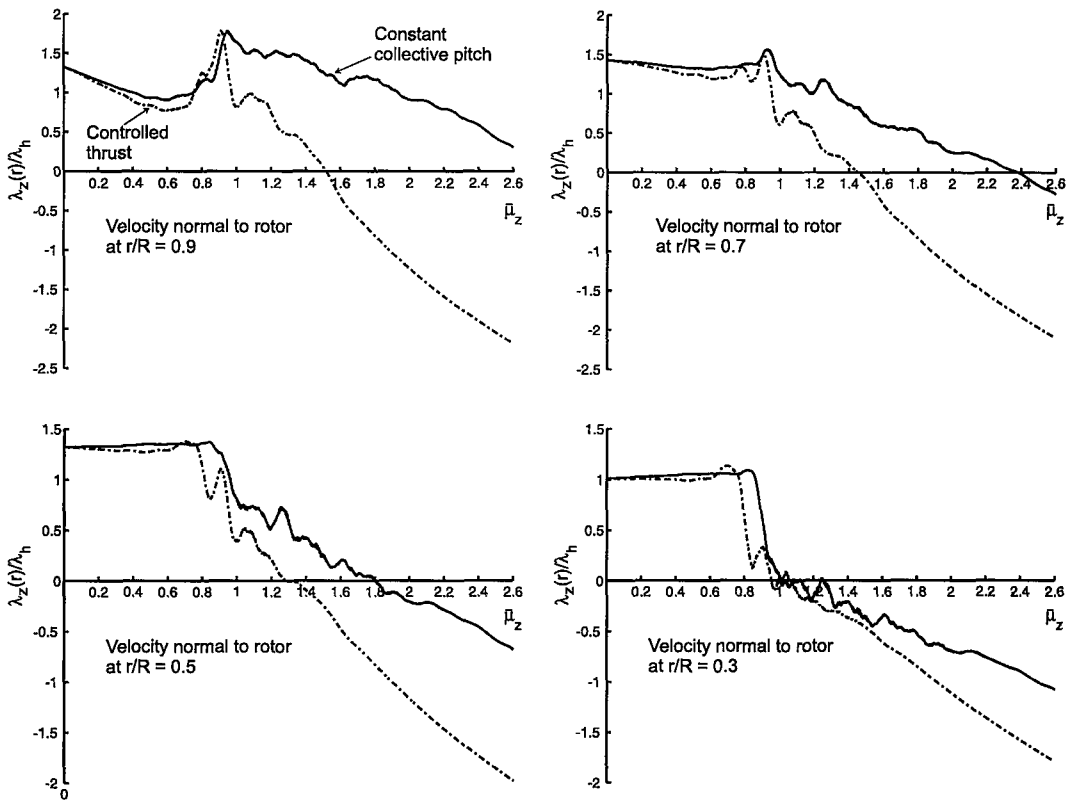



***Figure 6.6:*** *Resultant vertical velocities, $\lambda_z(r) = \lambda_i(r) + \mu_z$, scaled by the mean inflow at hover, at four blade stations, 0.9R, 0.7R, 0.5R and 0.3R. The results are from the two cases of rotor operational modes.*

Up to a descent speed of $\bar{\mu}_z \approx 0.6$ the total velocity of the flow at the outboard sections of the blades ($0.9R$ and $0.7R$) reduced due to the increasing free-stream velocity in both cases. Although up to this stage of the descent the two rotor modes engendered similar behaviour, $\lambda_z(r)$ fell more quickly when the thrust was controlled: when the collective pitch was held constant the increasing thrust generated an increase in the induced inflow which opposed, though did not exceed, the on-coming free-stream. Between descent rates $\bar{\mu}_z \approx 0.6$ and $\bar{\mu}_z \approx 0.8$ the sudden rise in $\lambda_z(r)$ at the outboard sections is indicative of the occurrence of the thrust-settling phenomenon, as discussed in Chapter 4, though perhaps the onset of thrust-settling, or settling with power rather, occurred earlier and a little more abruptly when the thrust was controlled. It is suggested that this is because the lower total velocities of the flow down over the blades, of the controlled rotor, transports disturbances down through the wake more slowly down the wake and as a result the disorganisation of the wake caused by the growing disturbances occurs closer to the rotor. The wake of the controlled rotor may have been more truncated when $\bar{\mu}_z \approx 0.6$ than in the case when the collective pitch was held constant which led to the collapse of the wake at a lower descent speed. From hover to a descent speed $\bar{\mu}_z \approx 0.6$, the magnitudes of the velocities of the flow, in the two cases, over the inboard sections of the blades ($0.5R$ and $0.3R$) only deviated slightly from each other - the velocity of the flow increased slightly, above the velocity at hover, by around 4% over this speed range when the collective pitch was fixed, whilst the velocity of the flow over the same sections of the controlled rotor fell by a similar amount. These trends suggest that the inflow at the roots of the rotor with fixed collective pitch increases faster than the descent speed, whilst the free-stream velocity exceeds slightly the inboard downwash velocity induced the controlled rotor. The net velocity over the inboard sections of the controlled rotor drops suddenly at a descent speed of $\bar{\mu}_z \approx 0.75$ probably as a result of the collapse of the root vortex system, as was discussed in the previous chapter. A similar drop in the flow velocity over the inboard sections of the rotor with fixed collective pitch occurs, but not until a descent speed of $\bar{\mu}_z \approx 0.85$. Note that between the descent speeds $\bar{\mu}_z \approx 0.6$ and $\bar{\mu}_z \approx 0.9$, i.e. between incipient VRS and the full development of the VRS as seen in Figs. 6.3 and 6.4, it appears that the behaviour of the flow over the inboard sections of the rotor is more sensitive to the mode of operation than is the flow over the outboard sections of the rotor. That is to say, the difference in the descent speeds between the two modes of operation at which

the root-vortex systems collapse is significantly larger than the difference in the descent speeds between the two modes of operation at which the thrust-settling effect manifests on the outboard sections of the blade.

Once VRS has been initiated at $\bar{\mu}_z \approx 0.9$, the sectional vertical velocities betray the most significant aerodynamic variances between rotors operating under the two different modes. The general trend is the same at all blade stations, and in both cases of operational mode - the vertical velocity reduced and eventually went negative. That is, a net downward flow changed into an overall upward flow through the rotor. When the trust was controlled, the rate at which $\lambda_z(r)$ decreased was higher than when the collective pitch was fixed, with the difference in the rates being larger at the outboard sections of the rotor than at the inboard sections. Indeed, it is from this behaviour that the cause of the earlier cessation, in terms of a descent rate scaled by the mean inflow velocity induced in hover, of the VRS brought about when the thrust is held constant can be inferred. The wake of the rotor with fixed collective pitch generated the greater sectional downwash velocities of the two cases, once the VRS had developed. The lower descent rates at which $\lambda_z(r)$ went negative, when the thrust was held constant, indicates that the recirculating, toroidal wake was convected upwards and away from the rotor by this upward flow at around that stage of the descent. That is, a formation of a tubular structure, rather than a toroidal one, appears to correspond to a decrease in the mean inflow through the disc, as shown in Chapter 5, since it reduces the intensity of downwash producing vorticity in the vicinity of the rotor plane. In contrast, whilst a structured vortex tube formed at descent speeds of $\bar{\mu}_z \approx 1.4$ when the thrust was held constant, the thrust, and thus the induced inflow, produced by the rotor with fixed collective pitch was increasing at this stage in the descent. The result was the lower rate of change of sectional net speed of the vertical flow and the prolonging of the rotor's flight within its own collapsed wake.

The behaviour of the wake, revealed in the flow-field visualisations shown earlier, suggests that at the higher descent speeds the strength of the wake was higher when the collective pitch was fixed (this would have also been the case at the lower descent speeds but the effect was negated by the thrust-settling phenomenon). This notion can be tested by evaluating the strengths per unit length of the tip and root vortex systems by taking the spanwise derivative of the bound circulation on the blade, i.e. $d\Gamma/dr$. The result of this exercise for each operational mode case is shown in Fig. 6.7. The data was filtered

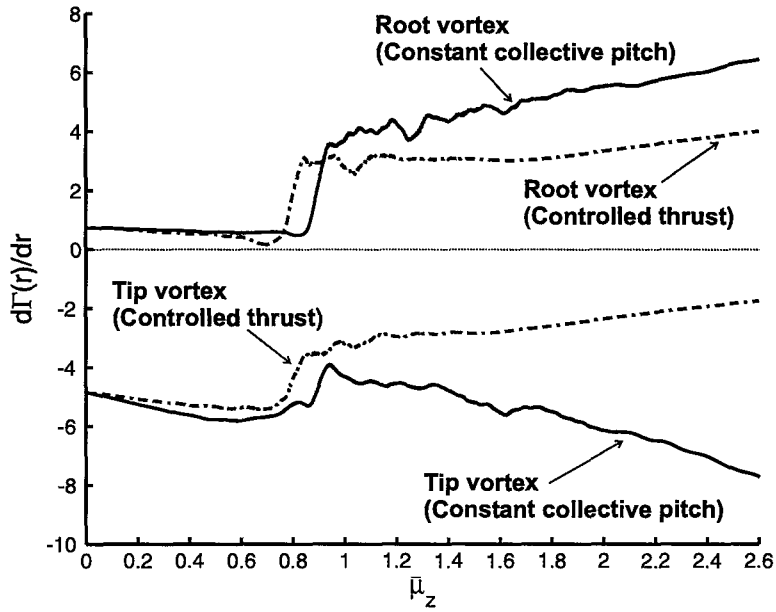



***Figure 6.7:*** *Graph of the variation of the strength per unit length of the tip and root vortex systems trailed from the rotor blades with increasing descent rate for two operational mode cases.*

using a moving averaging window with a width of ten rotor revolutions in order to remove some of the obscuring, high frequency content from the data such that only the gross, slowly varying trends are exposed. This is a very revealing plot. Up to a descent speed of $\bar{\mu}_z \approx 0.9$ the behavioural trends of both the tip and root vortex systems from the two operational mode cases are similar. The strength of the tip vortex systems in both cases increased due to the increase the effective angle of attack engendered by the net decrease in the velocity of the vertical flow over that region of the rotor, as shown in Fig. 6.6. In contrast, the strength of the root-vortex systems, when the collective pitch was fixed and when the rotor was controlled, decreased during aforementioned range of descent speeds. The reason behind this behaviour is dependent upon the operational mode. When the collective pitch was fixed, the net velocity of the flow over the inboard sections of the rotor was shown earlier to increase slightly, with the consequent reduction in the effective angle of attack, and thus lift, over the inboard regions of the rotor. When the thrust was controlled the total velocity of the flow over the inboard sections of the rotor was shown to decrease slightly, which would have lessened the downwash-induced reduction in angle of attack. But, it was shown in Fig. 4.21 of Chapter 4 that the blade loading near to the root section of a similar rotor falls as descent speed increases, prior to VRS onset, whilst

the blade loading increases at the outboard sections. Therefore, in order for the rotor thrust to remain constant the controller decreased the collective pitch and therefore it can be deduced from this that the net change in effective angle of attack inboard of the rotor was negative, hence the decreasing trend of the strength of the root-vortex system.

The effects that thrust-settling has on the strengths of the trailed vortices is clearly evident between the descent speeds $\bar{\mu}_z \approx 0.7$ and $\bar{\mu}_z \approx 0.9$ . The strengths of the tip vortices, in both cases, were reduced by the increase in inflow over the outboard sections of the blades. To counter these effects, a sudden increase in the strength of the root vortex system of the controlled rotor occurred at the initiation of thrust settling. The strength of the root vortex system of the rotor with fixed collective pitch remained relatively unperturbed, however, during the early stages of the thrust-settling effect, which indicates how, initially, the thrust settling phenomenon influences only the outer parts of the rotor.

It is after the thrust-settling period of the descent has passed, and once the vortex toroid that is characteristic of the VRS sits atop the rotor plane (rather than beneath it) as shown in the locus plots of Fig. 6.4, that the fundamental differences in behaviour brought about by the two operational modes arises. That is, it is during the cessation of the VRS and the ensuing flight into the WBS where the behaviour of the rotor and its wake are the most sensitive to the rotor's mode of operation. At the blade root, the strength of the trailed vortices rise with descent rate in both cases. It is at the blade tips, however, where the difference lies - whilst the increasing speed of the free-stream increases the effective angle of attack and thus strengthens the tip vortices of the rotor with fixed collective pitch, the opposite effect occurs when the thrust is held constant. That is, the collective pitch of the controlled rotor is reduced to maintain a nominally constant thrust which reduces the strength of the tip-vortex, although at the same time, the root vortex gets stronger due to the net increase in effective angle of attack over the inboard sections of the blades owing to the relatively high upward flow velocities there. This variance in behaviour is the key factor that governs the difference between the VRS cessation speeds of a rotor operating with fixed collective pitch and a rotor operating under controlled thrust conditions.

When flying within the VRS, the strengthening tip-vortices of the rotor with fixed collective pitch generate an increasingly strong downwash (as demonstrated later in this section) that appears to maintain the tip-vortices in the toroidal form of the VRS to higher

descent rates than can be achieved when the rotor thrust is controlled to be nominally constant. As was shown in Chapter 3, when the wake exhibits toroidal geometry and is positioned largely just above the rotor disc plane, the gross kinematics of the wake resembles the kinematics of a stack of co-axial vortex rings, i.e. the tip-vortices adopt a behaviour that is approximately akin to the 'leap-frogging' of vortex rings. It is plausible, then, since the wake is constrained by the free-stream to evolve only just above the disc plane, that strengthening the tip-vortex filaments will maintain the leap-frogging tendency to higher free-stream speeds, i.e. the toroidal form of the wake is prolonged by strengthening the leap-frogging tendency of the tip-vortices. Contrarily, since the tip-vortex system generated by the controlled rotor is progressively weakened with descent rate, upon the onset of VRS, its ability to generate a downwash able sustain the vortex toroid of the VRS is gradually lessened. In addition, when the thrust is controlled to be constant the leap-frogging tendency of the tip vortex filaments will likely be weakened as the tip-vortex strength falls with increasing descent speed. All of these factors culminate in the earlier transition of the vortex toroid of the VRS into the tubular wake structure of the WBS than when the transition occurs if the collective pitch is fixed.

It has been demonstrated, then, that the lift generation on the blades of a rotor controlling its thrust appears to be coupled to the local velocity field in a fundamentally different way to that of a rotor with fixed collective pitch. The major differences seem to surface only once the VRS has developed fully and the thrust-settling phenomenon has subsided, though. But, it could be argued that perhaps the diametrically opposed tip-vortex-strength/velocity field coupling must always be present, since the different coupling is perhaps masked somewhat by the effects of the increased downwash induced over the outer sections of the rotor disc during the early phase of VRS onset.

Since it has been shown that the relative strengths between tip and root vortices differ between the two operational modes, it might be determined from this that the spanwise lift distributions are also very different. Indeed, as Fig. 6.8 shows, this is indeed the case when the sectional blade loading, $C_B(r)$ is normalised by the mean blade loading, $C_B$, arising at hover in each of the two cases, where $C_B = C_{T_h}/\sigma$. The data has been filtered as described before in this chapter. Also presented in the figure are the sectional blade loadings from the fixed pitch rotor when they have been scaled by the instantaneous mean blade loading, i.e. $C_T/\sigma$, where $C_T$ is the instantaneous thrust arising for a given

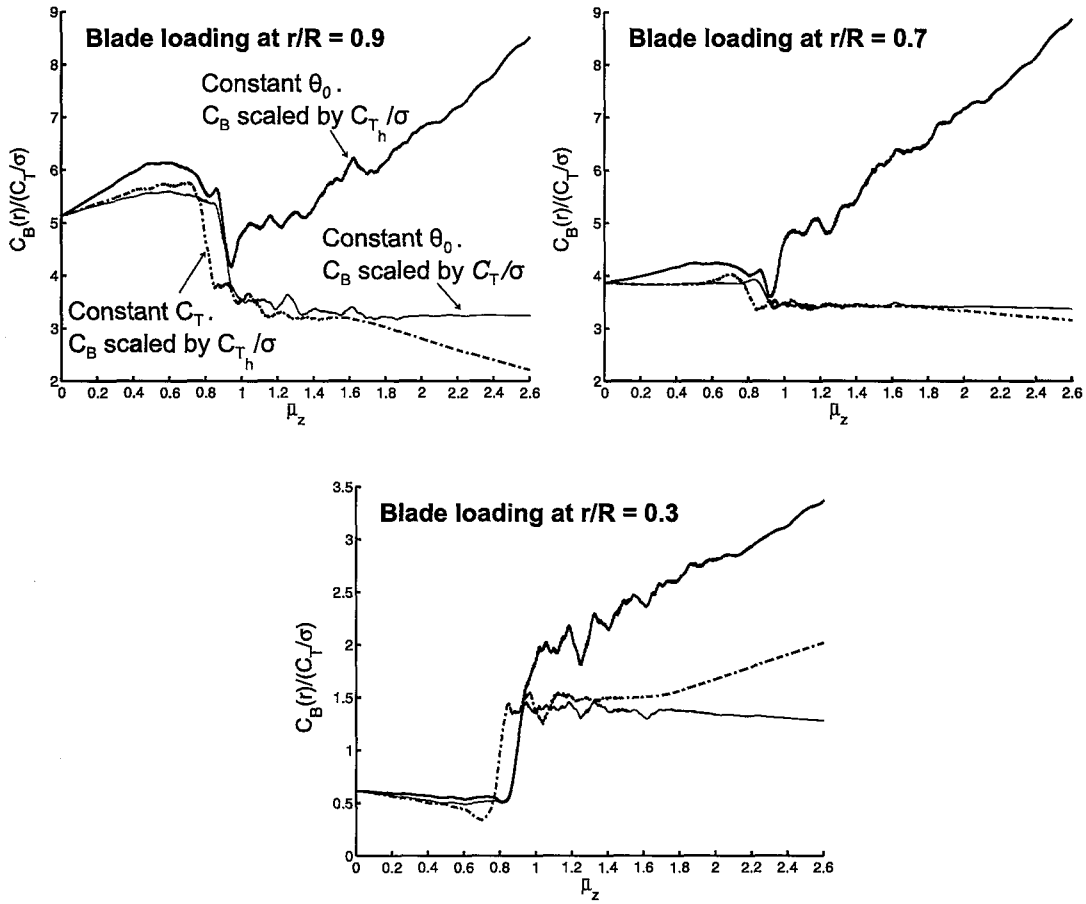



***Figure 6.8:*** *Comparison of the variation of sectional blade loading with descent rate arising on rotors operating under different operational modes.*

descent rate. It should be noted that scaling the data from the controlled thrust case in this way barely changes the results shown and thus for clarity these particular results have been omitted. When the sectional blade loadings are normalised by the fixed, mean blade loading, the sectional lift forces each behave in a manner that is consistent with the behaviour of the net speed of the sectional vertical flow, $\lambda_z(r)$, and of the trailed vortex strengths. That is, similar differences in the blade loading histories, arise between the two operational mode cases. Scaling the data from the rotor with fixed collective pitch with the instantaneous mean blade loading moves the curves very much closer to those of the controlled thrust case, although the curves don't collapse together entirely. The influence of this rescaling is most apparent after the cessation of the thrust-settling. That is, using the the mean blade loading from hover to scale the sectional blade loading of the rotor with fixed collective pitch shows how the blade loadings increase significantly, post

thrust settling, with increase in descent rate. This is unlike the loading on the blades of the controlled rotor which changes little until a descent rate of $\bar{\mu}_z \approx 1.6$ which roughly coincides with the cessation of VRS in that case. However, normalisation of the sectional blade loading of the rotor with fixed collective pitch by the *instantaneous* mean blade loading parameter shows very clearly how the loading behaviour, or rather, the variation of loading distribution with descent rate, actually matches very closely the distribution of the loading on the blades of the controlled rotor from a descent speed $\bar{\mu}_z = 1.0$ to $\bar{\mu}_z = 1.6$. The absolute values of the sectional blade loadings between the two operational cases differ greatly though, during this speed range. Once the controlled rotor has entered the windmill brake state, however, the blade loading distributions exhibited by the two cases, diverge (when the sectional loading is scaled with the instantaneous mean loading). In the controlled case the lift generation moves away from the outboard section of the rotor in favour of the inboard sections. Contrarily, the scaling method using the instantaneous mean blade loading reveals that, on the rotor with fixed pitch, the outboard sections very gradually assume an increasing fraction of the lift generated by the rotor as the descent speed increases.

Another way of viewing the blade loading distributions, and the changes brought about by the two scaling methods discussed above, is achieved by plotting the mean of the normalised blade loading as a function of spanwise position $r/R$. Fig. 6.9 shows the spanwise loading distributions at several pertinent descent speeds. These plots show clearly how, in both operational mode cases, the loading distribution changes as the rotors descend from hover, through VRS and into the WBS. The figure also shows the very significant effect that rescaling the fixed collective pitch data has on the evaluation of the differences that arise between the two cases: scaling the sectional loading with the instantaneous mean blade loading parameter shows that the distribution of the lift generated over the rotor blades is only weakly influenced by the mode of operation, even though the absolute values are very different.

## 6.3 Discussion

The preceding presentation has highlighted the sensitivities of the rotor and its wake to the rotor's operational mode whilst in descending flight. Not only do the thrust and the

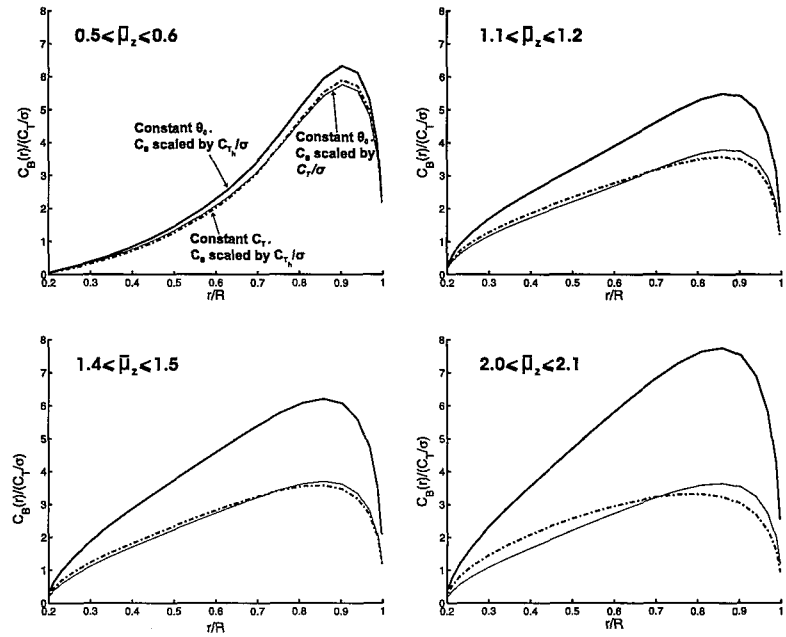



***Figure 6.9:*** *Comparison of the spanwise distribution of blade loadings at several descent speeds arising on rotors operating under different operational modes.*

absolute local blade loading differ, at a given descent rate, when the descent rate is scaled with the inflow generated by the rotor in hover, but differences of more fundamental importance have been exposed. At a given descent rate, after the onset of VRS, the geometry of the wake of a rotor that operates with fixed collective pitch is quite different to that of a rotor controlled to descend with nominally constant thrust. More importantly still, the fundamental reason behind the differences between the wake conditions, at a given descent rate, that results from the two operational modes lies in the fact that the coupling of the rotor with fixed collective pitch to the local flow field is diametrically opposed to that of a controlled rotor, though only at the outermost sections of the blades, or so it appears at least.

Hitherto in the present work, much has been made about how the rotor's performance and the geometric state of its wake at a given normalised descent rate, $\bar{\mu}_z$, depends upon the operational mode under which it is flying. The consequence of this is that a fair assessment of the effects of other parameters that may influence the behaviour of the rotor and its wake during descending flight, such as rotor geometry, cannot be made if the data which are being compared are from tests or simulations that operated their respective rotors in different modes. There is a clear need, particularly, for a more appropriate

method of scaling the descent velocity. Additionally, as suggested by the revealing results obtained by re-scaling the sectional blade loading, there is a benefit in establishing a more appropriate method for scaling the rotor performance parameters, such as rotor torque, as will be discussed later in this section.

The problem with the classical method of scaling the descent speed is that the inflow value used is calculated from the thrust generated during hover, which is of course a fixed value for a given rotor. It seems reasonable that a scaling parameter that allows like for like comparison of two rotor systems operated in different modes must account for the instantaneous state of the rotor and its wake. This can be very simply achieved by scaling the descent rate, $\mu_z$ with the instantaneous mean inflow, $\lambda_i$, calculated from a modified version of Washizu's method [22], given in Eq. 2.43, to yield a new normalised descent rate: $\mu_z^* = \mu_z/\lambda_i$. Furthermore, the estimated profile torque used by Washizu, $C_{Q_0}$ is found by taking the momentum theory result for the induced torque produced in hover, i.e. $C_{T_h}\sqrt{C_{T_h}/2}$, from the total torque, $C_Q$. This estimated profile torque value is then assumed to be constant for the entire descent of the rotor. The assumption of constant profile torque is clearly inadequate, when the blade pitch is fixed, especially: the profile torque depends upon the effective angle of attack of the rotor blades which certainly does not remain constant when the collective pitch is fixed, as can be inferred from the fact that thrust varies significantly with descent rate. The model employed to represent the profile drag of the blades in this investigation took the form $C_D = 1.03 - 1.02\cos(2\alpha_e)$ and is given by Prouty [82]. This expression for $C_D$ describes a curve, fit through the profile drag data of a NACA 0012 aerofoil. Figure 6.10 shows the total torque minus the constant profile torque, $C_{Q_0}$, estimated using Eq. 2.40, and also the total torque minus the instantaneous profile torque, $C_{Q_p}$, calculated using the profile drag model. Note that the assistance to the rotation of the rotor provided by the on-coming free stream, given by the term $\mu_z C_T$, has not been extracted from the torque data. It is clear from this figure that as a consequence of the assumption that the profile torque remains constant throughout the rotor's descent that there is a large overestimation of the torque when the collective pitch is held fixed and an underestimation when the thrust is controlled. In each case these discrepancies grow post the onset of a fully developed VRS wake - from a descent speed of $\bar{\mu}_z = 0.9$. This figure also serves to highlight the considerable difference in the behaviour of the rotor torque that is engendered by a change in the operational mode of

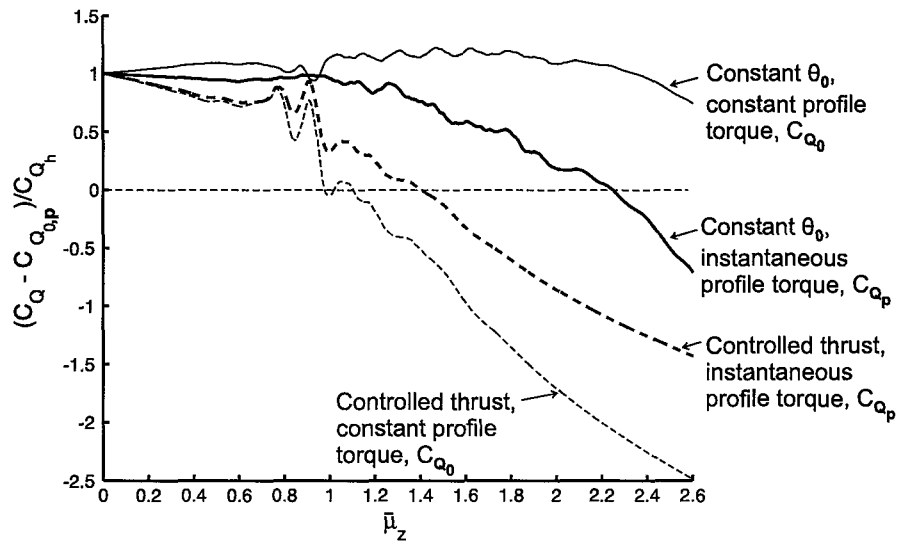



***Figure 6.10:*** *Total torque coefficient minus profile torque coefficient, normalised by induced torque coefficient arising in hover, from simulations of a rotor operating with either constant collective pitch, $\theta_0$, or controlled thrust. The rotor is undergoing an axial descent through the VRS to the WBS from an initial hover condition.*

the rotor. Inspection of the curves representing the total torque minus the instantaneous profile torque, generated by flying the rotor with fixed collective pitch or in a controlled condition, shows the dependence of the auto-rotation speed of the rotor upon the mode of operation. This is an obvious result, since the auto-rotative condition is dependent upon thrust magnitude, but nonetheless, it serves to highlight the invalidity of making a direct comparison of the performance of descending rotors from past experiments without accounting first for their operating conditions. The consequence of using the standard method (Washizu's method) to compute the mean rotor inflow through a rotor operating with fixed collective pitch whilst incorporating the assumption that profile torque remains constant throughout the descent of the rotor is shown at the top of Fig. 6.11. The lower graph in the figure is the inflow through a rotor controlled to have nominally constant thrust. The difference in the two results is striking. Indeed, the estimated inflow for the case of constant collective pitch appears to be unphysical - it climbs approximately parallel with the momentum theory result for the inflow generated by a rotor in descent when its tubular wake extends to infinity below the rotor disc plane. This particular momentum theory result is strictly invalid of course. That the wake deviates from this theoretical result is evident in Fig. 6.4, though, where it is seen that the wake does indeed adopt the

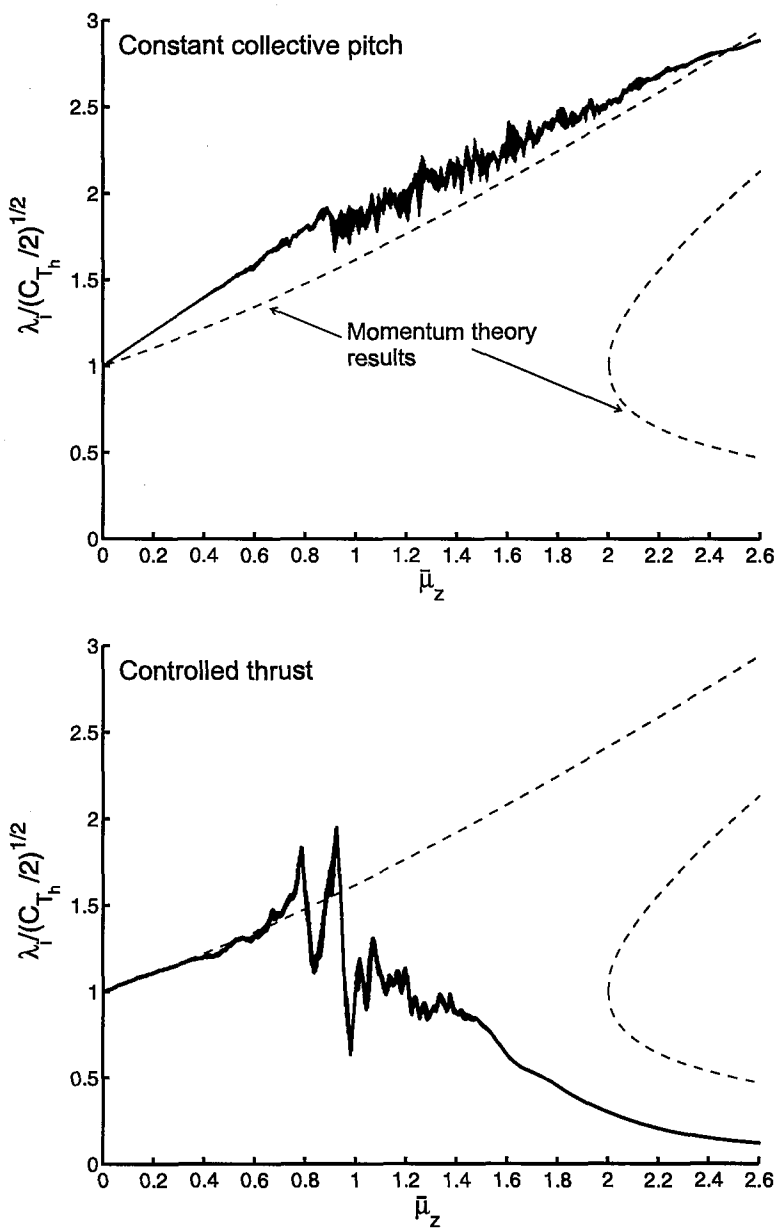



***Figure 6.11:*** *Comparison of induced inflow calculated using Washizu's method (Eq. 2.43. Inflow generated by a rotor descending through to the WBS from hover when the thrust is being controlled to be nominally constant or when the collective pitch is being held constant.*

toroidal structure characteristic to the VRS.

The discrepancy between the two sets of inflow data presented here is not readily evident when Washizu's method is used to compute rotor inflow from the results of experimental test, however. The disparity between the simulation results, where aerodynamic stall has been omitted, and those of experiment suggests perhaps that stall plays a significant role in suppressing the lift generation on the blades of a real rotor operating with fixed collective pitch. The consequence being that the thrust and hence rotor inflow cannot rise so steeply when stall has occurred on the blades. Calculation of the inflow from such data would thus give the appearance, erroneously, that the inflow estimations for real fixed pitch rotors give better agreement with the inflow generated by a real rotor operating under controlled thrust conditions than is evident in Fig. 6.11. This is because stall on controlled rotors with moderately twisted blades would not be as pronounced as it would be on fixed pitch rotors since the geometric angle of attack is reduced, generally, as descent rate is increased.

The effect on the calculation of rotor inflow of assuming constant profile torque can be shown by calculating the inflow by Washizu's method, but by replacing the constant profile torque with the instantaneous value, $C_{Q_p}$. A further modification is required, however. Washizu's expression for inflow was derived with the underlying assumption that the mean inflow across the disc was uniformly distributed. Since this is certainly not the case in the present instance, tip-loss effects must be accounted for if the method of inflow calculation is to work appropriately with profile torque data computed from the integral of the sectional profile torque, as is done in the VTM. Johnson [71] suggests that the tip-loss factor, $k$, can be assumed to be constant over the whole of the rotor trajectory, though this is likely to be valid only to a first approximation. Thus, this correction factor can be written simply as $k = (C_{T_h}\sqrt{C_{T_h}/2})/(C_Q - C_{Q_p})_h$, where subscript $h$ denotes that the values are taken from the hover condition only. Hence, the mean disc inflow is calculated as follows:

$$C_P = (C_Q - C_{Q_p}) + \mu_z C_T \tag{6.1}$$

$$\lambda_i = kC_P/C_T \tag{6.2}$$

The effect of using the more appropriate instantaneous value for profile torque in the inflow calculation is shown in Fig 6.12. When the rotor operates with fixed collective pitch the effect of using instantaneous profile torque data in the inflow calculation is to

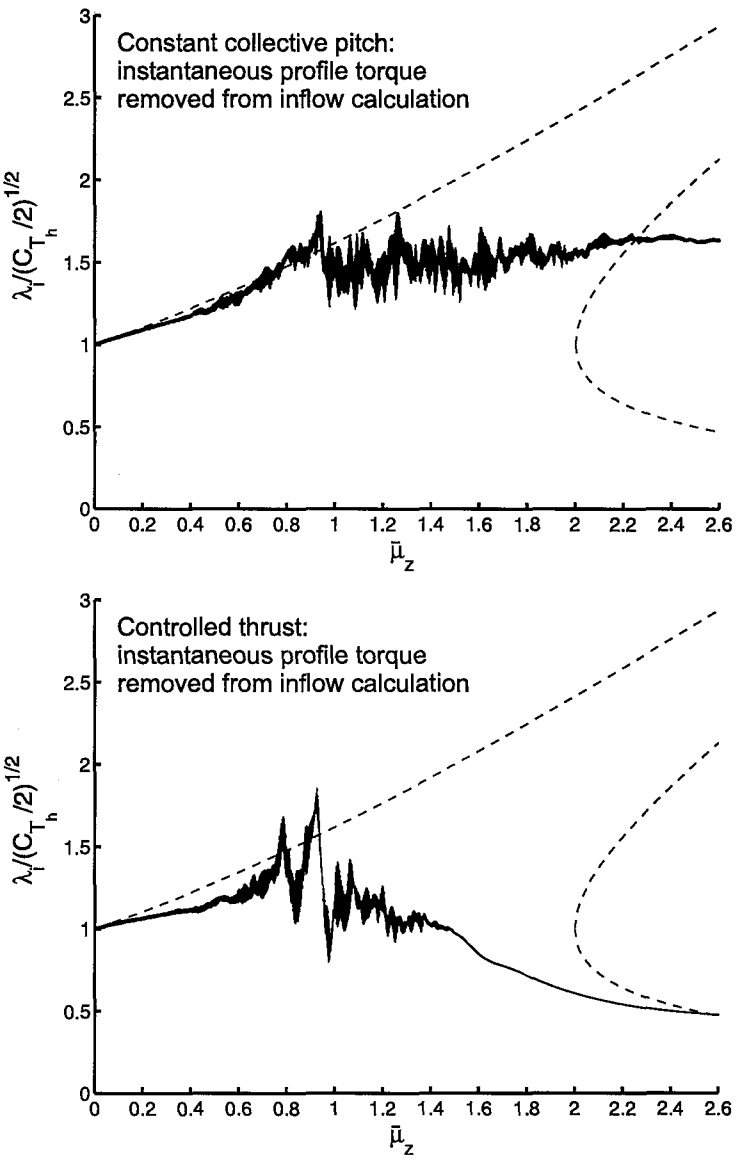



***Figure 6.12:*** *Comparison of induced inflow computed using Washizu's method but with the constant profile torque value replaced with the instantaneous value of profile torque, $C_{Q_p}$. Inflow generated by a rotor descending through to the WBS from hover when the thrust is being controlled to be nominally constant or when the collective pitch is being held constant.*

reduce the rate of increase in the mean inflow from that seen when the profile torque was assumed to be constant, in Fig. 6.11. Note though that the inflow doesn't begin to fall, post the onset of VRS, as it does in the lower graph in the figure of the mean inflow generated by the controlled rotor. The effect of the increasing thrust with descent speed in the constant collective case is to increase the inflow at descent speeds which take the controlled thrust case into the WBS. This provides further indication, if it were needed, of the inappropriate nature of the standard method of scaling the descent speed. The instantaneous profile torque must therefore be incorporated into the calculation of the mean rotor inflow such that a more accurate result for the mean inflow can be used in the calculation of $\mu_z^*$ - the proposed, alternatively scaled descent rate.

Figure 6.13 shows the combined result of using the instantaneous profile torque in the inflow calculation and of plotting the inflow data against the descent rate scaled with the instantaneous mean inflow. It is clear that employing the instantaneous profile torque in

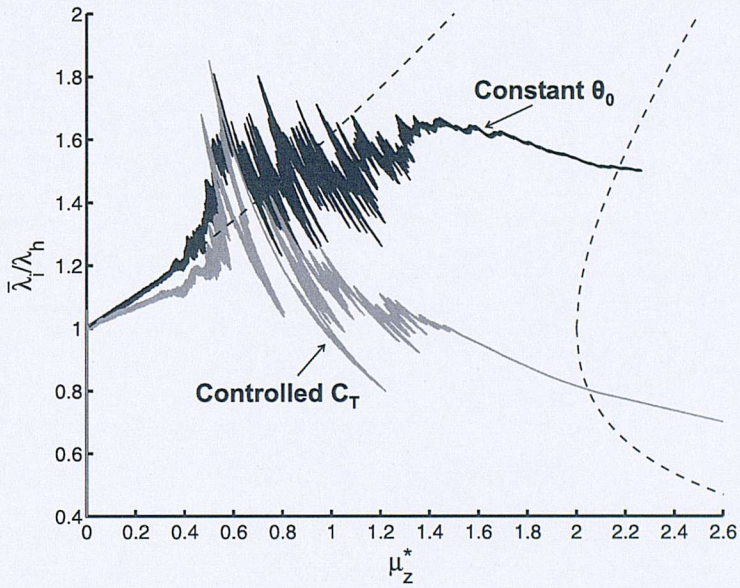



***Figure 6.13:*** *Estimated mean disc inflow using actual profile torque and a descent rate scaled with the instantaneous mean inflow $\lambda_i$. Inflow generated by a rotor descending through to the WBS from hover when the thrust is being controlled to be nominally constant or when the collective pitch is being held constant.*

the inflow calculation and using the alternative scaling for the descent speed modifies the result from than shown in Fig. 6.12, especially in the case of constant $\theta_0$. Indeed, this latter result shows some signs that the mean induced inflow actually falls post the VRS, as

would be expected, as the vortex tube above the rotor is stretched out by the quickening free-stream. Secondly, it is also clear how the alternative scaling for the descent speed has resulted in far better agreement between the two operational mode cases. That is, there is now good agreement on the descent speeds at which the significant fluctuations in the data begin and end and also on the speeds at which the significant changes in the character of those fluctuations occur. Before further evidence of the success of this scaling method is presented it is necessary to discuss what could be perceived as a potential drawback of the method - the 'zig-zagging' of the data in the horizontal plane. This horizontal fluctuation occurs, of course, because of the considerable unsteadiness of the rotor inflow. Whilst it makes any trends in the data slightly less accessible, it does, however, provide some insight into the behaviour of the system: when in the VRS, a particular state of the rotor and its wake may arise at several descent speeds, $\mu_z$ (for a given value of $\mu_z^*$). This indicates the non-linearity of the response of the wake to the increasing free-stream flow - it does not move up towards and over the rotor monotonically. The horizontally 'zig-zagging' data should not be seen as a drawback however, since, after all, it is an honest representation of the system in action and does not actually obscure the system's behaviour. Moreover, because the instantaneous inflow is a representation of the instantaneous geometric state of the rotor wake, scaling the descent rate with the instantaneous inflow results in the various significant VRS events that manifest in the data to occur at approximately the same values of $\mu_z^*$. This is readily evident in Figs. 6.14, 6.15 and 6.16, which show the standard deviation about the mean thrust of the thrust fluctuations, the sectional blade loading (normalised using instantaneous mean blade loading) and the rotor torque, respectively. That is to say, the appropriate scaling factor for the descent speed of rotors operating under different modes of control is their instantaneous mean inflow, rather than the mean induced inflow generated at hover.

Figure 6.14 shows that the sudden increase in thrust fluctuations, that result from the rotor being enveloped by its own highly unsteady toroidal wake, occurs at almost the same alternatively normalised descent speed. Additionally, the cessation of the VRS in the two cases, which manifests as a decrease in fluctuation amplitude, also occurs approximately at the same value of $\mu_z^*$. Remember that this was not the case when the fluctuation data was set against the standard normalised descent rate, $\bar{\mu}_z$. Likewise, the rapid changes in the local blade loading, $C_B(r)$, that occurred at slightly different values of $\bar{\mu}_z$ now occur at

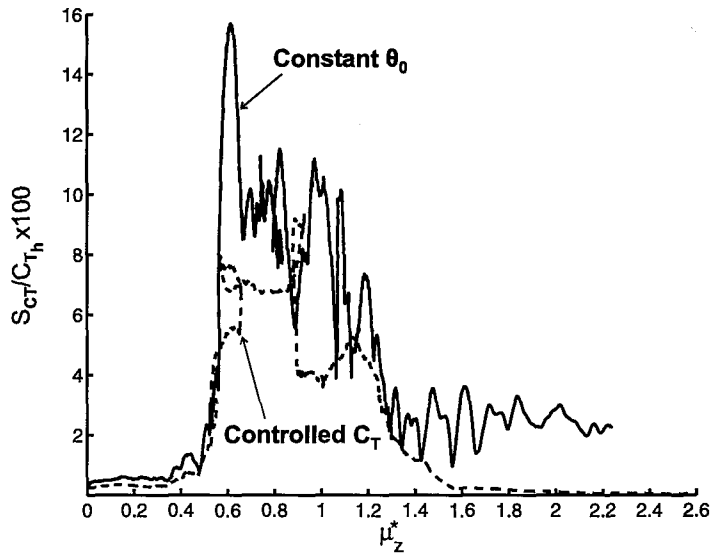



***Figure 6.14:*** *Standard deviation about the mean thrust of the thrust fluctuations vs. descent rate scaled with the instantaneous mean inflow. The thrust was generated by a rotor descending through to the WBS from hover when the thrust is being controlled to be nominally constant or when the collective pitch is being held constant.*

almost the same value of $\mu_z^*$, as shown in Fig. 6.15. As a final example of the the success of this alternative method for scaling the descent speed, the torque, $C_Q - C_{Q_p}$, is plotted against $\mu_z^*$ in Fig. 6.16. Rescaling the descent speed with a parameter that represents the instantaneous geometric state of the wake means that the auto-rotation speeds now coincide, whereas they were somewhat disparate when the standard scaling method was used. That the curves diverge quickly, post the start of auto-rotation, is indicative of the fact that at the descent speed ratio coinciding with auto-rotation, the thrusts and the unscaled descent rates of the two cases were significantly different. In the fixed pitch case the thrust and the unscaled descent rate was significantly larger than in the other case at the start of auto-rotation, therefore, the assistance provided by the free-stream to the rotation of the rotor, given by $\mu_z C_T$, is much larger than that which occurs when the rotor thrust is controlled at the same value of $\mu_z^*$.

It has been shown that the various behaviours associated with the VRS occur at the same ratios of the free-stream velocity to instantaneous mean induced inflow velocity, and this has indicated that the ratio represents a particular state of the rotor wake. But, this agreement on the magnitude of the ratios required for a particular behaviour to occur,

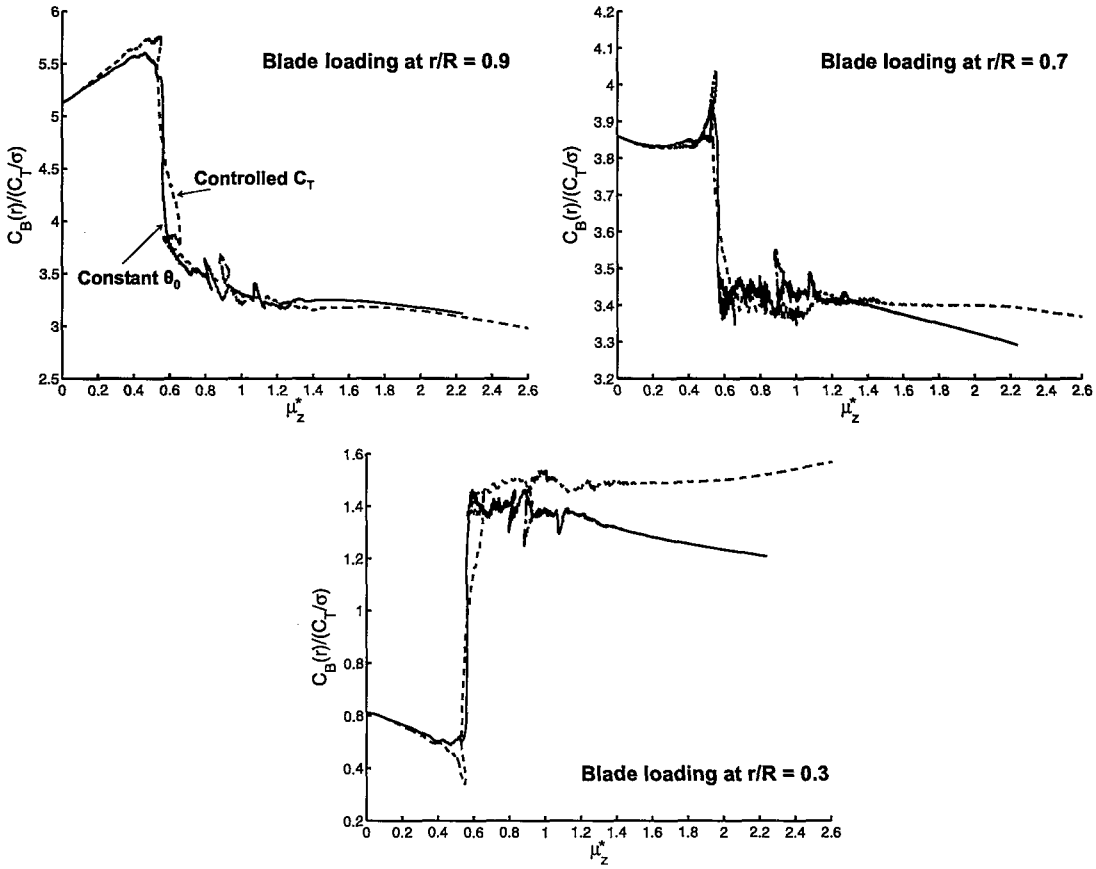



***Figure 6.15:*** *Variation of sectional blade loadings, scaled with the instantaneous mean blade loading with descent rate scaled with the instantaneous mean inflow. Blade loadings are from a rotor descending through to the WBS from hover when the thrust is being controlled to be nominally constant or when the collective pitch is being held constant.*

during the descent of the rotor, is achieved whilst the actual value of thrust, or inflow, or blade loading, etc, are very different. Indeed, it appears that it is possible to normalise the rotor performance data too, such that data from two or more different rotor tests may be collapsed onto similar curves, so that any variances arising in the curves may highlight the common dependencies of the behaviours under scrutiny. As an example then, the torque, $C_Q - C_{Q_p}$, is scaled by twice the cube of the estimated inflow, thus: $\bar{C}_Q = (C_Q - C_{Q_p})/2k\lambda_i^3$, where $k$ is the constant factor accounting for tip-losses and other deviations caused by non-uniform inflow distribution, as used previously. The result of this method of normalising of the rotor torque, generated when the rotor operated with constant collective pitch and also when it operated with nominally constant thrust, is shown in Fig. 6.17. As can be seen, using the instantaneous inflow to scale the torque

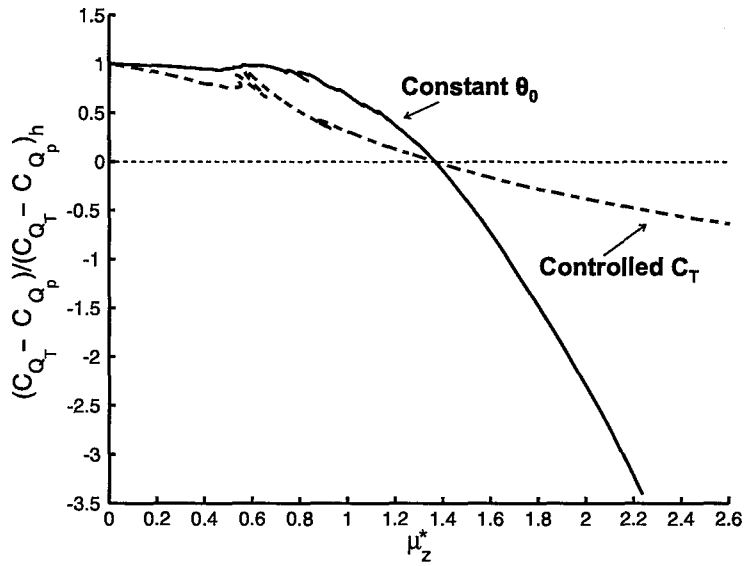



***Figure 6.16:*** *Variation of rotor torque with descent rate scaled with the instantaneous mean inflow. The torque was generated by a rotor descending through to the WBS from hover when the thrust is being controlled to be nominally constant and when the collective pitch is being held constant.*

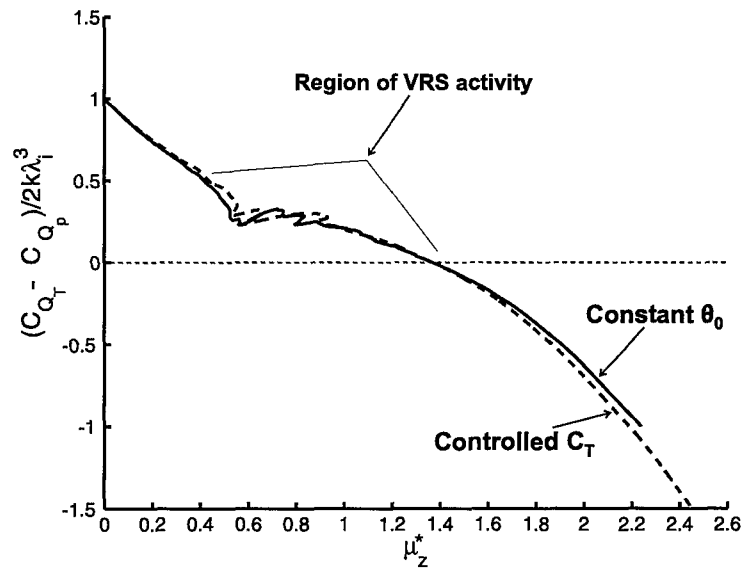



***Figure 6.17:*** *Variation of rotor torque scaled with* $2k\lambda_i^3$ vs. *descent rate scaled with the instantaneous mean inflow. The torque was generated by a rotor descending through to the WBS from hover when the thrust is being controlled to be nominally constant and when the collective pitch is being held constant.*

collapses the two data sets onto one another, even in the region of VRS activity.

## 6.4 Summary

The differences in gross rotor performance, local blade aerodynamics and in the wake behaviour that exist between a rotor descending with constant collective pitch and a rotor descending with nominally constant thrust have been investigated. In the past it has been common practice to group data sets from tests of rotors operating under each of these conditions together and compare them as if their behaviours should be fundamentally the same. The present work has shown clearly that significant differences in rotor thrust, torque, estimated inflow, local on-blade velocities and blade loading arise between the two cases, even when the rotors and their trajectories are otherwise identical. These differences arise, though, primarily when the descent speed at which the state of the rotor and its wake are assessed is scaled with the inflow generated by the rotors when hovering. The fundamental difference in the behaviour of the two systems was shown to be due to the reversal in the sense of the coupling between the rotor and the local velocity field, but only at the blade tip. That the tip vortices from the fixed pitch rotor get stronger with increase in descent rate whilst those of the controlled thrust case get progressively weaker, post thrust-settling, or rather, upon the arrival of a fully developed VRS, is of great significance. The increasing strength, with descent rate, of the wake of the rotor with constant collective pitch prolongs the VRS to higher descent rates since the increasing wake strength increases the rotor inflow velocity and thus sustains the vortex toroid at higher descent speeds, whilst the opposite occurs when the thrust is controlled. In addition, it was postulated that the increasing strength of the tip-vortices of the rotor with fixed pitch also strengthens the leap-frogging tendency of the tip vortices when in the vortex toroid of the VRS. This behaviour would further help to maintain the VRS wake at higher descent speeds than when the rotor thrust is controlled to be constant, since, again, the opposite effect would arise in this latter case.

The lesson learned from this work is that such a comparison of rotor performance on the basis of the standard method of scaling the descent velocity is not valid. Furthermore, since the 2D aerodynamic behaviour of the blade was simplified by neglecting stall due to viscous effects, it seems reasonable to presume that the highlighted differences between

the two cases considered are larger than has been seen in past VRS research. The possible implication of this is that in the literature, the variations arising from using different rotor operational modes are hidden somewhat by the effects of stall at high descent speeds, and so, as a consequence any dependencies of the rotor performance in VRS on blade geometry, etc, may have also been hidden. In addition, the standard method of calculating the rotor inflow, which employs a constant profile torque estimation, has been shown to have a considerable negative influence on the reliability of the result. This was demonstrated by re-calculating the inflow using the instantaneous value of the profile torque derived from the sectional profile drag computed during the simulations. Whilst no validation with experimental data was included in this study, the significant difference between the two results suggests that the consequences of assuming that using a constant value for the profile torque in the calculation of inflow will provide reasonable accuracy, are perhaps more severe than have been thought in the past. The results of the comparison suggest strongly, then, that such a simplistic assumption should not be employed in the computation of mean induced inflow when actual profile torque data, along with a correction factor for tip-losses, can be obtained.

In an attempt to show that the mode of operation of the rotor does not, in fact, influence the state adopted by the rotor and its wake when any particular relative balance between mean induced inflow and descent speed has been reached, an alternative method of scaling the descent speed, $\mu_z$, was proposed and tested. The instantaneous mean inflow $\lambda_i$ was used as the scaling parameter. It was shown that with this approach, the sudden changes to rotor performance or local on-blade aerodynamic environment, of the rotor in the two operational mode cases, that are engendered by the sudden collapse of the wake of the rotor as the rotor descends into the VRS, occurred at the same, or approximately the same values of normalised descent rate, $\mu_z^*$. This results implies, then, that the instantaneous mean inflow is a more appropriate normaliser of rotor descent speed than the standard method that is adopted in the literature. It was also shown, briefly, that the torque and local blade loading, and thus potentially any other rotor performance measure, could be scaled by instantaneous functions of mean inflow and mean blade-loading, respectively. This means that data from similar descending rotors, flying under the two different operational conditions, can be collapsed, approximately, onto one curve. Further indication was provided, therefore, that it is the instantaneous measures of the state of

the rotor and its wake that should be used to normalise data in a VRS study since the states of a rotor, and its wake, in descending flight are universal to all rotors, whilst the thrust and inflow that they generate are not, necessarily. The utility of this alternative scaling method, then, is that it provides a more valid means of comparing the behaviours of different rotors flying under different modes of operation: If employed in a comparison, the observed variations in trends, and in the descent speed ratios at which trends change, will be due to the properties of the rotors being compared and not to the way in which they were operated.

# Chapter 7

# Conclusions

Computational simulations of rotors in axial descent have been conducted to remedy some of the deficiencies in the understanding of the fluid dynamics of the helicopter vortex ring phenomenon. These simulations, performed by Brown's Vorticity Transport Model [28, 35], were designed to allow detail examination of the vortex kinematics that are responsible for the onset and ensuing evolution of the VRS, to highlight the influence of the gross wake geometry on the associated topology of the velocity field of rotors in axial flight, and also, to expose the physics behind the sensitivity of the VRS dynamics to rotor-blade geometry and to the rotor's operational mode.

In an initial validation exercise conducted to ensure that the VTM was a suitable tool with which to perform the analyses required by this research, the VTM was shown to be capable of reasonable quantitative and qualitative prediction of the rotorcraft vortex ring phenomenon. In addition, the dependency of the computational solution to the grid resolution used to perform a VRS simulation was assessed. Simulations of a rotor in descending flight from hover through the VRS and into the WBS, using different grid resolutions, showed that the results had a strong dependency on the computational cell size, though only when the rotor operated in the VRS. Indeed, no significant sensitivity of the results was found in the rotor performance prediction for a rotor in hover, low speed descent or in the WBS. It was shown that the onset speed of the simulated VRS is dependent upon the grid size, the implication being that the stability characteristics of the computed flow field are modified by a change in the size of the computational cell. An assessment of the turbulent kinetic energy in the flow field of a decaying rotor wake

showed that the cell size acted as the limit to the size of the flow scales that could be resolved. Additionally, the distribution of kinetic energy through the range of resolved scales was also found to be grid dependent. It appears then, that perhaps the sensitivity of the simulated wake's stability characteristics arises because the range of small-scale flow features that manifest as disturbances in the flow, and which cause disorganisation in the wake, depend upon the grid size. Further research into the emergent properties of the numerical schemes employed within the VTM is certainly required to understand better how the dissipation of energy at the grid scale influences the simulated behaviour of dissipative systems such as the VRS. Nonetheless, the vorticity conserving properties of the VTM allows the gross features and large-scale dynamics of the VRS to be examined, even when the computational resolution is low. A flow field computed at low resolution still possesses the unstable flow processes that admit VRS-like behaviour, as was suggested by the low resolution validation simulations.

A series of high resolution simulations of an idealised single-bladed rotor were performed to expose the detail kinematics of the vorticity field of the rotor as it entered the vortex ring state from the windmill brake state and from hover. The rotor loading was de-coupled aerodynamically from the surrounding velocity field by prescribing the bound circulation on the blade to remain constant throughout each descent of the rotor. The wake of the rotor in both descent scenarios collapsed into the VRS despite the omission of the non-linear aerodynamic feedback between the rotor and its wake. This result contradicts several suggestions in the existing literature that VRS onset is a result of the interaction between the rotor loading and the local velocity field. The aerodynamic feedback in real systems is thus only a modifying feature of the flow phenomenon - VRS arises fundamentally because of the dynamics of the wake in response to the action of its inherent fluid instabilities and the oncoming free-stream flow.

In the same study it was found that the vorticity field of a rotor operating within the unsteady VRS flow field possesses significant coherent structure. In high-speed VRS, when the VRS toroid generally sits atop the rotor disc plane, the wake comprises a small number of ring-like tip-vortex filaments that are part of a compacted helix of tip vortices. The vortical helix is compacted by its induced convection against the free-stream flow and the resulting global geometry gives the VRS its characteristic gross toroidal form. The dominant kinematics of the vortex filaments within the toroid are akin to the 'leap-frogging'

kinematics of individual vortex rings within a stack of coaxial vortex rings. A difference arises, though, due to the geometric constraints imposed on the vortex filaments by the essentially helical nature of the wake, as a whole, and by the action of the fluid instabilities within the wake. Perturbations in the geometry of the vortex filaments evolve under the action of the fluid instabilities to manifest as large scale, longitudinal re-orientation of the filaments out of a plane parallel to the rotor. The re-orientation process was shown to be ultimately responsible for the breakdown of the coherence of individual vortex filaments within the toroid and is thus the primary mechanism that limits the number of coherent tip-vortex filaments within it. Short-wave disturbances were shown to facilitate and expedite the re-orientation process.

In low speed VRS, when the vortex toroid of the VRS generally lies beneath the rotor, the aforementioned 'leap-frogging' motions are still evident. Fewer coherent rings exist in this scenario however, and this is probably because of the upward direction of the flow of disturbances into the toroid which expedite the de-coherence of the tip vortex filaments. Large-scale re-orientation is mostly suppressed by the compacting nature of the free stream and thus the non-linear growth of short-wave disturbances in the wake is the dominant cause of the breakdown of the tip vortex filaments within the toroid.

The most common orientation of vortex filaments within the wake of a rotor in hover or in the WBS was shown to be nearly co-planar with the rotor. As the VRS was approached, however, it was shown that the contribution of vertically aligned vorticity to the total vorticity in the flow increased such that the contribution of vertically aligned vorticity equalled, approximately, the contribution of each of the two horizontal components. This result confirmed in a quantitative fashion the observations made from the visualisations of the rotor wake. There is a statistical tendency for the vortex filaments, in both high and low speed VRS, to adopt a range of preferred orientations, rather than be randomly orientated by the highly unsteady flow field. By far the majority of filaments in a VRS wake are oriented non-planar with the rotor.

In the wake of a hovering or slowly descending rotor the non-linear continuation of the linear pairing instability mode identified by Widnall [5] and by Bhagwat and Leishman [6] has been shown to be large-scale longitudinal re-orientation of pairing filaments out of the plane of the rotor. The re-orientation locally reduces the ability of the filaments to advect down through the flow thus the re-orientation of vortex filaments is implicated as

the primary mechanism driving the truncation of the wake that was observed to occur in the study and which has been reported in the literature.

The onset of the VRS, from an initial hover, is not caused by the gradual convection up to the disc plane of bundles of pairing vortex filaments, as has been suggested in the past. Instead, it arises due to a process whereby the wake, truncated by the free-stream flow and the action of the re-orientation process, causes the dominant helical vortex kinematics of the tubular wake to switch to a kinematic mode that is characterised by the leap-frogging of individual vortex filaments in a stack of coaxial vortex rings. It is postulated here that this switch in kinematics arises when the wake is truncated to some critical length, i.e. when the wake's lowermost coherent tip-vortex filaments reach some critical distance below the rotor plane. Once the critical length is reached, the leap-frogging kinematics of coaxial rings is admitted. Thus the descent speed required to initiate the VRS is the descent speed required to cause the instabilities in the flow to truncate the wake tube to the critical length. The author recommends further research to test this 'critical length' hypothesis, perhaps by simulating the evolution of stacks of vortex rings, where the number of rings or the overall length of the stack are varied, to determine whether there is dependency of the global kinematics of the stack on the length of the stack and/or on the number of rings within the stack.

As was mentioned, the rotor used for this high-resolution investigation was single-bladed. It is believed that the fundamental kinematics of the wake, and the form of the non-linear growth of disturbances in the wake, that have been exposed by this study are common to VRS flows generated by any type of rotor. But, it is thought that the VRS wake of a multi-bladed rotor operating under the same flight conditions may well comprise a different number of coherent tip-vortex filaments than that of a single rotor. Further research in this area is needed to improve the understanding of the timescales related to the non-linear growth of disturbances within the VRS wake. This might be especially important if the number of coherent tip vortices that are sustained in the toroid influences the timescales of the fluctuations of the thrust generated by a rotor operating in the VRS.

The re-orientation out of the rotor plane of vortex filaments in the far wake of hovering rotor were shown to be associated with the truncation of the vorticity field at any given time. The truncation of the instantaneous vorticity field reduces, as a consequence, the ability of the far wake to produce downwash, thus the instantaneous velocity field is also

truncated. The truncation processes evident in snap-shots of the vorticity field were linked to the truncation of the *mean* vorticity field which was previously thought to be simply due to the spatial cancellation, in an ensemble average, of vortical structures in the far wake due to their erratic motion. It has been shown that the consequence of the truncation of the mean vorticity field is the induction of a vertical, recirculating flow field such that the topology of the mean velocity field resembles a toroid elongated parallel to its vertical axis. This is contrary to previous statements made in the literature that the topology of the velocity field of a hovering rotor is different to that of a rotor operating within the VRS. Indeed, a sequence of images of the mean velocity field of a rotor in hover, at low-speed descent, in the VRS and in high-speed descent just prior to the establishment of the WBS, showed that the rotor's velocity field is always toroidal, at least within the range of axial flight speeds considered. It is tentatively conjectured that the momentum theory for axial rotor flow might be modified to model toroidal flow, rather than a tubular slip stream, and thus that it might then be possible for the momentum theory to admit the prediction of VRS flow.

The discussion on the effects of wake kinematics on the velocity field of a rotor was extended with an examination of how the global geometry of a rotor wake influences the performance of the rotor as well as the velocity field. A study of the velocity fields associated with the wake of a rotor near to or in the VRS revealed that the upward flow in the vicinity of the blade roots that has been observed in previous experiments was shown to be strongly correlated with the geometry and position of the root-vortex system. This study of the various geometric states adopted by the rotor wake during descent through the VRS demonstrated how some of the aspects of the aerodynamic behaviour of the idealised, simplified rotor featured in Chapter 3 of this thesis are also applicable to the behaviour of a more complete representation of a real rotor system.

The role played by the wake in the well reported VRS related effect known as thrust-settling was investigated in order to establish the aerodynamic origin of this phenomenon. It was shown that thrust-settling is initiated by the compression and radially outward motion of the wake rather than by the complete collapse into the toroid of the VRS as was previously thought. The complete collapse was shown to exacerbate the effect, however. The compressed wake induces an increase in the speed of the downward flow over the blades, particularly over their outer regions. The same flow behaviour was shown

to be responsible, also, for the problematic settling-with-power phenomenon experienced by pilots flying rotorcraft in the VRS. Thrust-settling was shown to end when the VRS toroid was elongated upwards and convected, mostly, above the rotor disc plane.

Simulations of a rotor undergoing different rates of linearly accelerated axial descent were conducted to demonstrate that the descent speeds at which the rotor wake adopts its various geometric states is dependent upon the time history of the descent. The results showed that VRS onset and, to a lesser extent, its subsequent cessation are postponed to higher descent speeds as the acceleration rate is increased because the wake breakdown processes, i.e. longitudinal filament re-orientation, take time to manifest. The result of this is that acceleration reduces the amount of re-orientated filaments, and thus the amount of disorganisation, that arises in the wake at any given descent speed. In addition, it was shown that since the acceleration reduced the time that a rotor spends within the VRS regime, the influence the wake has on the rotor performance is significantly moderated. These results lead the author to believe that future efforts to formulate analytical models for the prediction of the speed of VRS onset, that are based upon the evolution of disturbances in the flow, should not only include a means to account for the time history of the rotors descent but should also model the non-linear growth of vertically aligned vorticity within the wake, since this is ultimately responsible for the collapse of the wake. In addition, any description of the transport velocity of the disturbances in the wake, that is employed in the analytical VRS onset prediction model, should allow for the variation, with vertical position, of the velocity of the flow over the entire length of the wake. Rather, that is, than simply relating the transport velocity to the speed of the inflow through the rotor as has been done in the past.

The effect of high levels of blade twist on the behaviour of a rotor and its wake in descending flight was assessed by simulating three descending rotors each possessing a different level of blade twist from the other. To prevent the effects of stall from obscuring the influence of blade twist on the flow behaviour, a representation of viscous stall was omitted from the aerodynamic model of the blades. It was found that the onset and subsequent cessation of the VRS are postponed to higher descent rates as blade twist increases. A link was made between the stability of the root-vortex system of the rotor and the induced downwash velocities in the vicinity of the root vortex. It was observed that there is a subtle difference in the speed at which the root and tip vortex systems of a

rotor wake collapse into the toroidal flow of the VRS; it appears that the collapse of the root vortex system is the pre-cursor to complete wake breakdown. The increase in the velocity of the induced downwash near to the root vortex system with increase in blade twist leads to higher transport velocities of the root-vortices. It was suggested that this higher transport velocity of the root vortices decreases the rate of disorganisation of the root-vortex system as a whole. This serves, therefore, to maintain the tubular form of the root vortex system at higher descent speeds, thus the total collapse of the wake also occurs at higher descent speeds. Further studies specifically designed to highlight any differences in the speeds at which the root and tip vortex systems collapse are required, however, to confirm the suggestion made herein.

The finding that twist increases the VRS onset speed is at odds with the implication made by Brown and Leishman *et al.* [34] that an increase in blade twist would lead to wake collapse at lower descent speeds because of the increase in the growth rate of perturbations to the flow field found to be induced by an increase in twist rate. The stability analysis alluded to was performed on a wake that consisted of only a tip-vortex system, however. The findings of this thesis suggest that a further stability analysis of a rotor wake in descending flight should be conducted but with a representation of the rotor's root vortex system included in addition to the tip-vortex system. Such an analysis would provide insight into the results of the blade twist effects study reported in this thesis.

An increase in blade twist was shown to postpone the cessation of the VRS to higher descent speeds. It was observed that a net downward flow over the inboard sections of the rotor was sustained to higher descent rates by an increase in twist whilst visualisations of the rotor wake showed that the wake remained in a toroidal form at higher descent rates as twist increased. Based upon these results it was concluded that cessation is postponed by increasing twist rate because the downward motion *inside* the VRS toroid of the vertically recirculating, coherent tip vortex filaments is sustained to higher descent rates by the higher inboard downwash produced as twist is increased.

An assessment of the occurrence of blade stall was made by examining where on the blades and at what descent speed did the lift coefficient exceed the maximum lift coefficient of a common aerofoil. This analysis showed that stall does not influence the descent speed at which VRS arises. It is possible though the onset of the VRS may be influenced by stall when rotors have blades exhibiting greater twist than the rotors featured in this

study. Therefore, further research would be required to confirm this finding if twist rates of greater than $\theta_{tw} = -35°$ were of interest. In addition, though stall was not present prior to VRS onset, it was shown that it would have appeared at some stage during the flight of the rotors through the VRS. The effects of viscous stall on the behaviour of rotors in descending flight has yet to be systematically investigated though, and it is thought crucial to the rotorcraft community's full understanding of the VRS that this ultimately unavoidable aspect of descending flight be properly assessed. This is especially important since it is plausible that the influence of stall could reverse the trends in blade twist effects that have been exposed herein.

Since stall was not included in the study on the effects of blade twist in this thesis, the influences of twist on the behaviour of a rotor operating in the VRS can be generalised. That is, what has actually been shown is the influence on the dynamics of the VRS wake of varying the distribution of inflow through the rotor. Inflow distribution is not only influenced by blade twist, of course. Therefore, the results of this study can be used to inform on the likely effect on VRS behaviour of changes in blade planform and of the distribution of aerofoil section along the blade.

The study on the effects of blade twist has highlighted the importance of the role played by the root vortex system in governing the overall dynamics of the wake of a descending rotor. In past computational investigations, such as in typical rotor simulations using the 'free wake' method, the root vortex has been considered so inferior to the tip-vortex system in its influence on the wake dynamics that it was omitted from the wake representation altogether. However, the findings of the study herein suggest strongly that the role of the root vortex system is highly influential in the behaviour of the rotor wake, and this role will grow in importance as the strength of the root vortex increases relative to that of the tip-vortex. Therefore, future computations of the behaviour of a rotor in descending flight must include a representation of the root-vortex system, as well as that of the tip-vortex system, in order for confidence to be obtained in the results of studies on the effects of changes to rotor geometry.

An investigation into the differences in VRS behaviour induced by trimmed descent and uncontrolled, fixed pitch descent was conducted. Whilst VRS does not need feedback between the rotor and its wake for VRS to occur, as has been shown in this thesis, the way in which the rotor is operated, i.e. whether its thrust production is controlled to

be constant or whether the collective pitch is held fixed during a descent, was shown to fundamentally alter the rotor-wake coupling. Little difference arises between the behaviour of the two systems prior to the onset of VRS, though the speeds at which VRS occurs differs slightly when the descent speed is normalised in the traditional way, i.e. by using the inflow generated at hover. Upon the onset of the VRS, however, a significant difference between the two systems manifests - as the descent rate increases, after VRS onset, the strength of the tip-vortices of the fixed pitch rotor increases whilst the opposite occurs when the rotor thrust is controlled to be nominally constant. The strengths of the root vortices from the two systems vary similarly, however. A large difference between the VRS cessation speeds experienced by the two systems results, again when the descent speed is scaled in the traditional way. The conclusion then, is that rotor behaviour, such as the variation with descent speed of mean rotor inflow velocity, computed from the thrust and torque data taken from two such systems, cannot be fairly compared using traditional scaling methods for the descent speed, as has been done on several occasions in literature.

An alternative method of scaling the descent rate using the instantaneous rotor inflow velocity is proposed. The method was demonstrated to be successful in collapsing together, along the descent speed axis, the rotor performance data taken from two rotors, one flying with fixed collective pitch and the other flying with controlled, nominally constant thrust. That is, using the instantaneous rotor inflow velocity to scale the descent rate, the onset and cessation speeds of the two systems were in excellent agreement. The success of the alternative scaling method arises because the ratio between the descent speed and the velocity of the instantaneous rotor inflow represents a geometric state of the wake. It is the ratio that is important, and not the absolute values of rotor inflow (and thus also thrust) and descent rate. This finding provides much insight into the flow physics of a descending rotor. It appears that, for a given rotor, the ratios of descent speed to inflow speed required to obtain any given geometric state of the wake are universal, whilst the absolute values of mean inflow and descent rate might not be. The work on the effects of acceleration, discussed earlier, suggest that the trajectory of the rotors must be the same to obtain such universality, however. Furthermore, it was shown that the sectional blade loading or the rotor torque curves from the two systems could also be collapsed together, along the blade loading or torque axis, if those parameters were scaled using instantaneous, rather than hover based, measures of mean loading and functions of rotor

inflow, respectively. This analysis suggested how the results from different rotors that were flown in experiments using different modes of operation can be fairly compared. Additionally, and importantly, the analysis suggests that the differences in performance that arise due to variations in rotor geometry can be exposed, rather than be obscured by the variations in the results induced by any difference in the operational modes of the rotors. This conclusion must be tested of course on a range of experimental VRS data.

Finally, this thesis has provided insight into the flow physics that govern the collapse and subsequent evolution of the wake of a rotor flying in the VRS. The thesis has also shown some of the sensitivities of the behaviour of the VRS to the rotor's trajectory and also to the distribution of the velocity of the inflow within the wake and also to the way in which the rotor is operated. There are many aspects of the VRS that are yet to be properly understood, however. For instance, it is not yet known exactly what governs the timescales associated with the well known large-scale agglomeration and breakaway of vorticity from the VRS toroid, though some of the mechanisms that cause the breakaway have been shown in this thesis. That this particular phenomenon has previously been associated with the large, low-frequency fluctuations in rotor thrust characteristic to the VRS suggests that it is important to conduct research into what governs the timescales of the vortex dynamics of the VRS. Perhaps the 'Holy grails' of VRS research, though, are the discoveries of a means to detect, in real flight, when VRS is about to occur and also a means to control its effects when it does occur, such that it is safe to fly near to or within the VRS at low altitude. It is the author's opinion that the most fruitful next step in the research into early VRS detection should be an investigation into common, unambiguous signs of critical levels of wake truncation below the rotor followed by a means of detecting such flow behaviour below the rotorcraft. With regards to the control of the VRS, it would be useful to determine whether or not advanced methods of rotor control, such as higher harmonic control or individual blade control could be used to ameliorate the effects of power loss associated with the settling-with-power phenomenon and, additionally, whether these methods could be used to at least partially suppress the severe vibrations and rolling moments induced by the highly unsteady flow field induced by the VRS. A further, perhaps more offbeat though nonetheless interesting, line of enquiry would be to investigate whether it is possible to control VRS by modifying the stability properties of the rotor's wake. That is, it would be useful to determine whether the rate of

disorganisation of the wake could be decreased to postpone wake breakdown. Or perhaps, when a rotor is in the VRS, it would be useful to determine whether an increase in the rate of disorganisation of the flow field could be achieved in order to induce the vortex toroid to breakdown more rapidly thus allowing the rotor to exit from the VRS and move into an auto-rotative state more quickly. In any case, these are just some of the aspects of this complex fluid dynamic phenomenon that have yet to be fully researched. Indeed, until a complete understanding of the physics of the VRS is obtained it will continue to keep from the helicopter pilot a useful region of his flight envelope. Perhaps, though, this thesis has brought forward the time when the pilot can descend a little faster than before.

# Bibliography


[1] Stewart, W., "Helicopter Behaviour in the Vortex-Ring Conditions," ARC, R. & M. No. 3117, November, 1951.

[2] Lock, C. N. H., Bateman, H., and Townsend, H. C. H.,"An Extension of the Vortex Theory of Airscrews with Applications to Airscrews of Small Pitch, Including Experimental Results," Aeronautical Research Committee, R&M No. 1014, September 1925.

[3] Glauert, H., "The Analysis of Experimental Results in the Windmill Brake and Vortex Ring States of an Airscrew," Aeronautical Research Committee R&M No. 1026, February 1926.

[4] D. A. Fulghum, "Marine Corp MV 22 Crash Focus Narrows," *Aviation Week and Space Technology*, May 15, 2000.

[5] Widnall, S. E., "The Stability of a Helical Vortex Filament," *Journal of Fluid Mechanics*, Vol. 54, part 4, 1972, pp. 641-663.

[6] Bhagwat, M. J. and Leishman J. G., "Stability Analysis of Helicopter Rotor Wakes in Axial Flight," *Journal of the American Helicopter Society*, Vol. 45, No. 3, 2000.

[7] Newman, S., Brown, R. E., Perry, J., Lewis, S., Orchard, M., Modha, A. "Predicting the Onset of Wake Breakdown for Rotors in Descending Flight," *Journal of the American Helicopter Society Annual Forum*, Vol.48, No.1, January, 2003.

[8] Ahlin, G.A., and Brown, R.E., "Predicting the Onset of the Vortex Ring State under Accelerated Flight Conditions," *Proceedings of the 61st Annual Forum of the American Helicopter Society*, Grapevine, Texas, June 2005.

[9] Brown, R. E., Line, A. J., and Ahlin, G. A., "Fuselage and Tail-Rotor Interference Effects on Helicopter Wake Development in Descending Flight," *Proceedings of the 60th Annual Forum of the American Helicopter Society*, Maryland, June 2004.

[10] Yaggy, P. F., and Mort, K. W., "Wind-Tunnel Tests of Two VTOL Propellers in Descent," NASA TN D-1766, March 1963.

[11] Castles, W., jr., and Gray, R. B., "Empirical Relation Between Induced Velocity, Thrust, and Rate of Descent of a Helicopter Rotor as Determined by Wind-Tunnel Tests On Four Model Rotors," NACA TN No. 2472, October 1951.

[12] Azuma, A., and Obata, A., "Induced Flow Variation of the Helicopter Rotor Operating in the Vortex Ring State," *Journal of Aircraft*, Vol. 5, No. 4, 1968, pp. 381-386.

[13] Green, R. B., Gillies, E. A., and Brown, R. E., "The Flow Field around a Rotor in Axial Descent," *Journal of Fluid Mechanics*, Vol. 534, 2005, pp. 237-261.

[14] Drees, J. M., and Hendal, W. P., "The Field of Flow Through a Helicopter Rotor Obtained from Wind Tunnel Smoke Tests," *Journal of Aircraft Engineering*, Vol. 23, No. 266, pp. 107-111.

[15] Stack, J., Caradonna, F. X., and Savas, O., "Flow Visualisations and Extended Time Histories of Rotor Vortex Wakes in Descent," *Journal of the American Helicopter Society*, Vol. 50, July 2005, pp. 279-288.

[16] Gao, Z., "New Achievements in Helicopter Aerodynamics," *Aviation Industry Publications*, 1999 (Translated from Chinese to English by Chan, W., 2003)

[17] Leishman, G. J., "Principles of Helicopter Aerodynamics," Second Edition, Cambridge University Press, Cambridge, UK, 2006.

[18] Castles, W., jr., "Flow Induced By A Rotor in Power-On Vertical Descent," NACA TN 4330, July 1958.

[19] Taghizad, A., Binet, L., Jimenez, J., and Heuze, D.,"Experimental and Theoretical Investigations to Develop a Model of Rotor Aerodynamics Adapted to Steep Descents," *Proceedings of the 58th Annual Forum of the American Helicopter Society*, Montreal, Canada, June 2002.

[20] Wang, S., "Analytical Approach to the Induced Flow of a Helicopter Rotor in Vertical Descent" *Journal of the American Helicopter Society*, January 1990.

[21] Perry, F. J., Chan, W. Y. F., Simons, I. A., Brown, R. E., Ahlin, G. A., "Modelling the Mean Flow through a Rotor in Axial Flight including Vortex Ring Conditions," *Journal of the American Helicopter Society*, Vol. 52, No. 3, July 2007, pp. 224-238

[22] Washizu, K., Azuma, A., Koo, J., and Oka, T., "Experiments on a Model Helicopter Rotor Operating in the Vortex Ring State," *Journal of Aircraft*, Vol.3, No. 3, 1966, pp. 225230.

[23] Washizu, K., Azuma, A., Koo, J., and Oka, T., "Experimental Study on the Unsteady Aerodynamics of a Tandem Rotor Operating in the Vortex Ring State," *Proceedings of the 22nd Annual Forum of the American Helicopter Society*, May 1966.

[24] Betzina, M. D., "Tiltrotor Descent Aerodynamics: A Small-Scale Experimental Investigation," *Proceedings of the 57th Annual Forum of the American Helicopter Society*, Washington D.C., May 2001.

[25] Abrego, A., Betzina, M. D., and Long, K. R., "A Small-Scale Tiltrotor Model Operating in Descending Flight," *Proceedings of the European Rotorcraft Forum*, Bristol, United Kingdom, September 2002.

[26] Lock, C. N. H., and Townsend H. C. H., "Photographs of the Flow Around a Model Screw Working in Water, Especially in the "Vortex Ring State"," *Aeronautical Research Committee*, R&M No. 1043, May 1926.

[27] Holmes, P., Lumley, J. L., and Berkooz, G., "Turbulence, Coherent Structures, Dynamical Systems and Symmetry,", *Cambridge University Press*, Cambridge, England, 1996.

[28] Brown, R. E., "Rotor Wake Modeling for Flight Dynamic Simulation of Helicopters," *AIAA Journal,* Vol. 38, No. 1, 2000, pp. 57-63.

[29] Wolkovitch, J., "Analytical Prediction of Vortex-Ring Boundaries for Helicopters in Steep Descent," *Journal of the American Helicopter Society*, Vol. 17, (3), July 1972, pp. 13-19.

[30] Leishman, G. J., Bhagwat, M. J. and Ananthan, S., "The Vortex Ring State as a Spatially and Temporally Developing Wake Instability," *Proceedings of the American Helicopter Society International Specialists Meeting on Aerodynamics, Acoustics and Test Evaluation*, San Fransisco, CA, USA, January 2002.

[31] Peters, D. A., and Chen, S., "Momentum Theory, Dynamic Inflow and the Vortex Ring-State," *Journal of the American Helicopter Society*, Vol. 27 (3), July 1982, pp. 18-24.

[32] Brand, A., Kisor, R., Blyth, R., Mason, D., and Host, C., "V-22 High Rate of Descent (HROD) Test Procedures and Long Record Analysis" *Proceedings of the 60th Annual Forum of the American Helicopter Society*, June 2004, Baltimore, Maryland.

[33] Kisor, R., Blyth, R., Brand, A., and MacDonald, T., "V-22 Low-Speed/High Rate of Descent (HROD) Test Results," *Proceedings of the 60th Annual Forum of the American Helicopter Society*, June 2004, Baltimore, Maryland.

[34] Brown, R. E., Leishman, J. G., Newman, S. J., and Perry, F. J., "Blade Twist Effects on Rotor Behaviour in the Vortex Ring State," *Proceedings of the 28th European Rotorcraft Forum*, Bristol, England, September 2002.

[35] Brown, R. E. and Line, A. J., "Efficient High-Resolution Wake Modelling using the Vorticity Transport Model," *AIAA Journal*, Vol. 43, No. 7, 2005.

[36] Ahlin, G. A., and Brown, R. E., "Investigating The Physics of the Rotor Vortex Ring State using the Vorticity Transport Model," *Proceedings of the 31st European Rotorcraft Forum*, Florence, Italy, September 2005.

[37] Ahlin, G. A., and Brown, R. E., "The Vortex Dynamics of the Rotor Vortex Ring Phenomenon," *Proceedings of the 63rd Annual Forum of the American Helicopter Society*, Virginia Beach, Virginia, June 2007.

[38] Caradonna, F. X., "Developments and Challenges in Rotorcraft Aerodynamics," *38th AIAA Aerospace Sciences Meeting,* AIAA 2000-0109, January 2000.

[39] Versteeg, H. K. and Malalasekera, W., "An Introduction to Computational Fluid Dynamics, The Finite Volume Method," Prentice Hall, 1995.

[40] Saffman, P. G., "Vortex Dynamics," *Cambridge University Press*, 1992.

[41] Line, A. J., "Computational Modelling of Helicopter High-Frequency Dynamics," Ph.D Thesis, Department of Aeronautics, Imperial College, London, U.K. 2004.

[42] Kenyon, A. R., and Brown, R. E., "Wake Dynamics and Rotor-Fuselage Aerodynamic Interactions," *Proceedings of the 63rd annual forum of the American Helicopter Society*, Virginia, May, 2007.

[43] Whitehouse, G. R., and Brown, R. E., "Modeling Rotor Wakes in Ground Effect," *Journal of the American Helicopter Society*, Vol.49, No.3, July, 2004.

[44] Whitehouse, G. R., and Brown, R. E., "Modelling a Helicopter Rotor's Response to Wake Encounters," *Aeronautical Journal*, Vol.108, No.1079, January, 2004.

[45] Strang, G., "On the Construction and Comparison of Finite Difference Schemes," *SIAM Journal of Numerical Analysis*, Vol. 5, 1968, pp.995-1011.

[46] Toro, E. F., "A Weighted Average Flux Method for Hyperbolic Conservation Laws," *Proceedings of the Royal Society of London, Series A: Mathematical and Physical Sciences,* Vol. 423, No. 1864, 1989, pp. 401-418.

[47] Brown, R. E., "Numerical Solution of the Two-Dimensional Navier -Stokes Equations Using Viscous-Convective Operator Splitting," M.Sc. Thesis, College of Aeronautics, Cranfield Inst. of Technology, Cranfield, England, U.K., 1990.

[48] Harlow, F. H. and Welsh, J. E., "Numerical Calculation of Time-Dependent Viscous Incompressible Flow of Fluid with Free Surface," *Physics of Fluids* Vol. 8, 1965, pp.2182-2189.

[49] Toro, E. F., "Some Aspects of Shock Capturing Methods for Gas Dynamics," College of Aeronautics Report, Cranfield Institute of Technology, No. 9112, June 1991.

[50] Rosenhead, L., "The Spread of Vorticity in the Wake behind a Cylinder," *Proceedings of the Royal Society London,* Series A, Vol. 127, No. 590, 1930.

[51] Moore, D. W., "Finite Amplitude Wave on Aircraft Trailing Vortices," *Aero. Quarterly,* Vol. 23, No. 307, 1972.

[52] Greengard, L. and Rokhlin V., "A Fast Algorithm for Particle Simulations," *Journal of Computational Physics,* Vol. 73, No. 1, 1987, pp. 325-348

[53] Greengard, L. and Rokhlin, V., "A Fast Algorithm for Particle Simulations," *Journal of Computational Physics,* Vol. 135, 1997, pp. 280-292

[54] Weissinger, J., "The Lift Distribution of Swept-Back Wings," *NACA Technical Memorandum,* No. 1120, March 1947.

[55] Clough, R. W., and Penzien, J., "Dynamics of Structures,", Second Edition, *McGraw-Hill International Editions*, 1993.

[56] Caradonna, F. X. and Tung, C., "Experimental and Analytical Studies of a Model Helicopter Rotor in Hover," *Vertica,* Vol. 5, 1981, pp. 149-161.

[57] Harris, F. D., "Articulated Rotor Blade Flapping Motion at Low Advance Ratio," *Journal of the American Helicopter Society,* Vol. 17, No. 1, 1972, pp. 41-48.

[58] Kim, H. W. and Brown, R. E., "Coaxial Rotor Performance and Wake Dynamics in Steady and Manoeuvring Flight," *Proceedings of the 62nd Annual Forum of the American Helicopter Society*, Arizona, May 2006.

[59] Harrington, R.D., "Full-Scale-Tunnel Investigation of the Static-Thrust Performance of a Coaxial Helicopter Rotor," NACA TN-2318, March 1951.

[60] Du, Z. and Selig, M. S., "The Effect of Rotation on the Boundary Layer of a Wind Turbine Blade," *Windpower Conference,* Bakersfield, CA, USA, 1998.

[61] Gerber, M., "Assessment of Implicit Turbulence Properties and Kinetic Energy Transfer Mechanisms for the Vorticity Transport Model used for Rotorcraft Aerodynamics," Diploma Thesis, Institut für Fluiddynamik, Eidgenössische Technische Hochschule (ETH) Zürich, Switzerland, January 2006.

[62] Frisch, U., "Turbulence," *Cambridge University Press*, 1995.

[63] Weinstein, J., and Gurgov, C., "Two-dimensional turbulent cascades," *Internal Report*, University of Pennsylvania, 2005.

[64] Morton, B. R., "The Generation and Decay of Vorticity," *Geophysical and Astrophysical Fluid Dynamics*, Vol. 28, Iss. 3 & 4, April 1984, pp. 277-308.

[65] Batchelor, G. K. "The Theory of Homogeneous Turbulence," Cambridge University Press, (1967).

[66] Ananthan, S., Leishman G. J., and Ramasamy, M., "The Role of Filament Stretching in the Free-Vortex Modeling of Rotor Wakes," 58th Annual Forum and Technology Display of the American Helicopter Society International, Montreal, Canada, June 11-13, 2002.

[67] Shariff, K., and Leonard, A., "Vortex Rings," *Annual Review of Fluid Mechanics*, Vol. 24, pp. 235-297, 1992.

[68] Brinson, P., and Ellenrieder, T., "Experimental Investigation of Vortex Ring Condition," *Proceedings of the 24th Annual European Rotorcraft Forum*, Marseilles, France, 1998.

[69] Landgrebe, A. J., "The Wake Geometry of a Hovering Helicopter Rotor and Its Influence on Rotor Performance," *Journal of the American Heli- copter Society*, Vol. 17, No.4, October 1972, pp. 2-15.

[70] Strawn, R. C. and Djomehri, M. J., "Computational Modeling of Hovering Rotor and Wake Aerodynamics," *Journal of Aircraft*, Vol. 39 (5), 2002, pp. 786 - 793.

[71] Johnson, W., "Helicopter Theory," *Dover Publications*, 1994.

[72] Huerre, P., and Monkewitz, P. A., "Local and Global Instabilities in Spatially Developing Flows," *Annual Review of Fluid Mechanics*, Vol. 22, 1990, pp. 473-537.

[73] Lock, C. N. H., "Note on the Characteristic Curve of an Airscrew or Helicopter," *National Physical Laboratory, ARC*, Reports and Memoranda No. 2673, June, 1947.

[74] Gessow, A., "Flight Investigation of Effects of Rotor-Blade Twist on Helicopter Performance in the High-Speed and Vertical-Autorotative-Descent Conditions," NACA TN No. 1666, August 1948.

[75] Felker, F. F., and McKillip, R. M., "Comparisons of Predicted and Measured Rotor Performance in Vertical Climb and ," *Proceedings of the 50th Annual Forum of the American Helicopter Society*, Washington, D.C., May 1994.

[76] Empey, R. W., and Ormiston, R. A., "Tail-Rotor Thrust on a 5.5-Foot Helicopter Model in Ground Effect," *Proceedings of the Annual Forum of the American Helicopter Society*, Washington D.C., May 1974.

[77] Leishman, G. J., Bhagwat, M. J. and Ananthan, S., "Free-Vortex Wake Predictions of the Vortex Ring State for Single-Rotor and Multi-Rotor Configurations," *Proceedings of the 58th Annual Forum of the American Helicopter Society*, Montreal, June 2002.

[78] Du, Z. and Selig, M. S., "A 3-D Stall Delay Model for Horizontal Axis Wind Turbine Performance Prediction," *ASME/AIAA Joint Wind Energy Symposium,* Austin, Texas, June 1997.

[79] Corten, G. P., "Inviscid Stall Model," *European Wind Energy Conference,* Copenhagen, Denmark, July 2001.

[80] Johnson, W., "Model for Vortex Ring State Influence on Rotorcraft Flight Dynamics," *Proceedings of the American Helicopter Society 4th Decennial Specialist's Conference on Aeromechanics*, San Francisco, California, January 2004.

[81] Brotherhood, P., "Flow Through a Helicopter Rotor in Vertical Descent," ARC, R. & M. No. 2735, July 1949.

[82] Prouty, R. W., "Helicopter Performance, Stability, and Control," *Robert E. Krieger Publishing Company,* 1986.